University of California
Santa Barbara

A multiscale biophysical platform for charting design-specific interactions of nanoparticles with model cellular membranes

A dissertation submitted in partial satisfaction
of the requirements for the degree

Doctor of Philosophy
in
Chemical Engineering

by

David J. Smith

Committee in charge:

Professor M. Scott Shell, Co-Chair
Professor L. Gary Leal, Co-Chair
Professor Samir Mitragotri, Co-Chair
Professor Frank L. H. Brown
Professor Otger Campàs

December 2018

The Dissertation of David J. Smith is approved.

Professor Frank L. H. Brown

Professor Otger Campàs

Professor M. Scott Shell, Committee Co-Chair

Professor L. Gary Leal, Committee Co-Chair

Professor Samir Mitragotri, Committee Co-Chair

December 2018

A multiscale biophysical platform for charting design-specific interactions of nanoparticles with model cellular membranes

by

David J. Smith

Acknowledgements

The Ph.D. is sometimes referred to as a roller coaster, and my Ph.D. was no different. Sometimes, it seemed like the roller coaster even dipped underwater. Indeed, when you're behind the eight ball, it can feel like you're drowning. It can become very hard to keep up with the proper skillset and publication credentials and remain competitive in a sea of applicants for awards, fellowships, grants, and funding. To be perfectly honest, when I hit around Year 3 of my Ph.D., the stress and anxiety really caught up to me. Luckily, I had a wonderful support system of mentors, peers, family, and friends to guide me the whole way through.

I would not have been able to do this without my highly supportive and extremely patient triad of Ph.D. advisors. I appreciate them humoring me in this marriage of three seemingly disparate fields of research–drug delivery and biomaterials, fluid mechanics of non-Newtonian fluids, and molecular simulations and multiscale modeling. While their brains, hearts, and courage were critical to my trek along the yellow brick road, my advisors also taught me several important skills, some concrete and some more abstract and all of which I will carry on with me for the rest of my life. They are all different (you could put each of them at a different place on the Myers-Briggs scale, for example), and each brought different things to the table in this Ph.D.

I credit Samir with the initial inspiration of my work, which nonetheless underwent many major adjustments along the course of my Ph.D. to raise both its impact and viability for funding. Samir's seminal work in nanotechnology, drug delivery, and biomaterials has been an inspiration to me and countless others. In my case, he inspired me to try to develop a better physical understanding and predictive capabilities in his work and that of others. At times, Samir also took it upon himself to secure funding for me, most notably with the UCSB Crossroads Fellowship in Materials, Mechanics, and Medicine through the

Center for Bioengineering–for that, I am very grateful. Samir was also critical in instilling in me a sense of expediency and relevance, which I hope to have carried through my own work and which has fueled my ultimate goals and passions in connecting my career closer and closer to clinical and biological applications.

Across my Ph.D., Gary has been my "sage grandpa." Our meetings were rarely when they were scheduled to be, but were often characterized by rich and wholesome scientific discussion (and sometimes went beyond that). Gary provided some of the critical fuel for pursuing a physical understanding of Samir's systems, and was critical to the incorporation of continuum theory and transport phenomena in the multiscale platform that we developed. Gary has always been a questions person, and his questions have provided unprecedented guidance to the scope of this work. Together, Gary and Samir were major factors in the cross-disciplinarity of my development as a doctoral student.

Scott was my original reason for choosing to come to UCSB. His dedication to fundamental research, pedagogy, and professional development was very evident early on, based on second-hand accounts from my predecessors in the Shell group as well as some in my own undergraduate research group and his house calls to me after I was accepted into UCSB. His focus in molecular simulations and multiscale modeling, as well as his resourcefulness and generosity of time, made all the difference transitioning into graduate school and full-time research. On a practical level, Scott also provided the financial netting to support the first few years of my Ph.D. This initial work on peptide-peptide interactions and peptide-surface interactions, in collaboration with the group of Markus Valtiner (then at the Max Planck Institute for Iron Research in Dusseldorf, Germany), was more than me just "doing my time." Rather, it was an essential experience in start-up research and confidence building, characterized by success through a few publications and unforgettable experiences like the trips to Dusseldorf and the achievement of one-to-one comparison between molecular simulations and atomic force microscopy. Initially, it was

not easy to convince Scott, in parallel with Gary and Samir, that my proposed Ph.D. work would be viable or was even correctly posed. Indeed, the work was refocused several times, and failed to be convincing enough early on for fellowship and short-term grant funding. I appreciate Scott's flexibility, and that of Gary and Samir. Perhaps what I admire most about Scott, however, is his "fit-for-purpose" advising strategy, tailoring his feedback and assistance to the skillset, ambitions, and personality of each and every one of his students. For me, that meant not only humoring me in the triple coadvisorship, but also in accommodating my tedious startup process and not just permitting, but also encouraging, the cultivation and application of techniques outside molecular simulations. The amount of emotional intelligence that Scott has transmitted to me these five years is nothing short of priceless.

With the addition of Frank and Otger to my thesis committee, I believe that we covered all bases in the expertise that was necessary for my proposed Ph.D. Frank is a world leader in the theory and simulations of lipid bilayer membranes. His knowledge and feedback have been absolutely essential to my calibration to the membrane community and production of realistic, impactful results. I got to know Otger by enrolling in his Special Topics class on Pattern Formation and Self-Organization. His broad expertise in continuum theory and, in his own fascinating research, the applications of that theory to *in vitro* and *in vivo* systems provided some early inspiration on how to bridge the gap between theory and biology.

During my Ph.D., I bonded particularly well with my colleagues in the Shell and Baron Peters groups, due to our common lab space, combined experience in molecular simulations, and extended overlap in our degrees. In the Shell group, I particularly thank Nikolai Petsev (Ph.D., 2017), Tanmoy Sanyal (2018), Brian Lynch (M.S., 2017), Jacob Monroe (2019, intended), and Nick (likely 2021) for the extensive technical and non-technical discussion, inside and outside of the lab. One of the hardest parts about leaving

UCSB will be losing regular access to these guys. In the Peters group, I particularly thank Kartik Kamat, Christian Leitold, Geoff Poon, and Ryan Mullen for the stimulating discussions, and all of the Shell and Peters group members for their jokes and banter. In the Leal group, I thank Mansi Seth for the initial crash course on making liposomes, which despite me not ending up doing experiments was an informative dabble in them, and Joe Peterson for the seemingly endless interest and brainstorming in my work and that of others. In the Mitragotri group, I thank Kat Camacho, Doug Vogus, and Anusha Pusuluri, all for their invaluable experimental perspective, relevant advice, and emotional support. I also thank the Helgeson and Squires groups, particularly my friend Alexandra Bayles, for the additional scientific feedback. Lastly, in Frank Brown's group, I would be remiss to not include Sean Cray, who like Frank was totally essential to my learning curve in membrane theory and simulation.

Of course, none of this would have been possible without the stable netting of my family. Across my life, I have been particularly inspired by three strong women: my grandmother Eleanor ("Gammy"), mom Carrie, and girlfriend of nine years Carla. Gammy was probably the most kind-hearted, caring, supportive, and inspirational person I will ever meet, and I know her eyes would be aglow for me now as they were for every achievement of her grandchildren. In care and support, my mom is a very close second, and has kept me and my brothers financially and emotionally afloat for most of our lives. As a career nurse and currently a product manager in pharmaceuticals for patient safety surveillance, my mom has been the inspiration for the biomedical applications of my work. Since we met in college, Carla and I have grown and taught each other so much. That our careers have never really crossed has been the real adventure. Carla joined me in California soon after I started at UCSB, and thanks to her charm, skill, and–most of all–grit, has quickly risen in her career and introduced me to more about Santa Barbara, California, and their people than I could ever have figured out on my

own. I am deeply indebted to Carla for the load balancing of my Ph.D. In her, I have found my true companion and a partner in ambition and worldview. She is a professional superstar and the love of my life.

My dad Kevin and brothers Ryan and Billy have also been essential to my development as a professional and human being. My dad is the most thoughtful, quirky, and hilarious person I have ever known. My favorite quotes from him–"everybody's different" and "moooooooooooderation" (moderation)–are the core of my being and how I approach others and my work. One similarity between myself and my brothers is that we have always had low confidence. That is why it is so great to see Ryan and Billy excelling now at The Vanguard Group in Pennsylvania and CTSI in Virginia. I wish them continued success in overcoming their personal barriers, just as I hope to continue overcoming mine. I also thank my dad, Ryan, and Billy for truly challenging me to become as effective a scientific communicator as possible–lest I get derailed with a joke.

There are many others here that I am leaving out, and they should know who they are. A Ph.D. can never be completed in isolation, and all of these people understand–at least peripherally–that it has many ups and many downs, abstract requirements, moving deadlines, tenuous funding, unforeseen consequences, and pleasant surprises. I thank all of them for pushing and pulling me when I needed it most.

So the roller coaster-Ph.D. analogy is somewhat true, but unlike most roller coasters, my final height was higher than my initial one. Particularly in the final year or so of my Ph.D., I think that I came out with more than enough accolades that the first four or so years seemed worth it. In this thesis, I hope that I make a convincing case for the multiscale physics-based modeling strategy in nano-pharmaceutical and -toxicological applications.

Curriculum Vitæ

David J. Smith

Education

University of California, Santa Barbara — Santa Barbara, CA
Ph.D., Chemical Engineering — Dec. 2018 *(expected)*

University of Notre Dame du Lac — Notre Dame, IN
B.S., Chemical & Biomolecular Engineering — May 2013

Professional Experience

Dept. Chem. Eng., Univ. of California, Santa Barbara — Santa Barbara, CA
Graduate Student Researcher, Dissertation Fellow (2018), UCSB Crossroads Fellow (2015)
2014-present

Pfizer Global Research and Development — Groton, CT
Employee, Student Worker Program, Drug Product Development — Jun.-Aug. 2013

Dept. Chemical & Biomolecular Eng., Univ. of Notre Dame — Notre Dame, IN
Undergraduate Researcher, NSF REU Awardee (2012), Undergraduate Research Awardee (2013)
2011-2013

Naval Surface Warfare Center, Ship Systems Eng. Station — Philadelphia, PA
Employee, Student Employment Prog., Power/Propulsion Systems — 2010-2012

Peer-Reviewed Publications

D. J. Smith, L. G. Leal, S. Mitragotri, and M. S. Shell. "A quantitative structure-property and structure-kinetic relationship for the membrane transport of sub-nanometer hydrophilic, hydrophobic, and interfacially active particles." *J. Am. Chem. Soc.*, In preparation.

D. J. Smith, L. G. Leal, S. Mitragotri, and M. S. Shell. "A multiscale framework for the membrane permeability of sub-nanometer particles." *J. Chem. Theory Comput.*, In preparation.

D. J. Smith, J. B. Klauda, and A. J. Sodt. "Simulation Best Practices for Lipid Membranes." *Living Journal of Computational Molecular Science*, Under Review.

D. J. Smith, L. G. Leal, S. Mitragotri, and M. S. Shell. "Nanoparticle Transport Across Model Cellular Membranes: When Do Solubility-Diffusion Models Break Down?" *J. Phys. D.: Applied Physics, Special Issue: Physical Interactions between Nanoparticles and Biomembranes*, 2018.

D. J. Smith, and M. S. Shell. "Can Simple Interaction Models Predict Sequence-Dependent Effects in Peptide Homodimerization?" *J. Phys. Chem. B*, 2017.

P. Stock, J. I. Monroe, T. Utzig, **D. J. Smith**, et al. "Unraveling hydrophobic interactions at the molecular scale using force spectroscopy and molecular dynamics simulations." *ACS Nano*, 2017.

D. J. Smith, J. K. Shah, and E. J. Maginn. "Molecular Dynamics Simulation Study of the Association of Lidocainium Docusate and Its Derivatives in Aqueous Solution." *Molecular Pharmaceutics*, 2015.

Conference Presentations

D. J. Smith, S. Mitragotri, L. G. Leal, and M. S. Shell. "Nanoparticle Transport across Biomembranes: Probing the Limits and Consequences of Solubility-Diffusion Theories through Multiscale Modeling." Talk. AIChE Annual Meeting, Pittsburgh, PA, Oct. 2018.

D. J. Smith, L. G. Leal, S. Mitragotri, and M. S. Shell. "A Molecular Thermodynamic Model for Nanoparticle- Membrane Interactions." Talk. AIChE Annual Meeting, San Francisco, CA, Nov. 2016.

D. J. Smith, and M. S. Shell. "Can Simple Theories Capture Sequence-Dependent Effects in Peptide Homodimerization?" Poster. Berkeley Mini Stat Mech Conference, UC Berkeley, Jan. 2016.

Outreach and Mentoring

Amgen-Clorox Chem. Eng. Graduate Student Symposium Santa Barbara, CA
Event Co-Chair 2017

Dept. Chem. Eng., Univ. of California, Santa Barbara Santa Barbara, CA
Teaching Assistant (Outstanding TA Award, Chemical Engineering, College of Engineering, 2018) 2015-2017

Graduate Simulation Seminar Series Santa Barbara, CA
Co-founder and Co-organizer (2014-2017), Advisor (2017-present) 2014-present

Center for Science and Engineering Partnerships Santa Barbara, Goleta, and Carpinteria, CA
Volunteer, Family Ultimate Science Exploration 2013-2018

Abstract

A multiscale biophysical platform for charting design-specific interactions of nanoparticles with model cellular membranes

by

David J. Smith

In this thesis, we outline the development of a multiscale physics-based platform for exploring and ultimately predicting the design-specific interaction of ∼1-10 nm particles with model cellular membranes. Nanoparticles (NP) are ever-present in foods and beverages, cosmetics, packaging, cooking products, fertilizers, pesticides, and novel pharmaceuticals, and pose significant challenges related to their increased consumer, occupational, and environmental exposure and their unique bioactivity relative to small molecules and large colloids. Thanks to rapidly advancing fabrication and characterization techniques, NPs are highly tunable in physicochemical properties such as size, surface chemistry, shape, elasticity, roughness, and crystallinity. Currently, however, the influence of these NP design parameters is highly underdeveloped, and difficult to reproducibly demonstrate in *in vivo*, *in vitro*, and even model experiments. Specifically, NP interactions with and passive transport across cellular membranes play a significant role in pharmacological and consumer product performance (biodistribution) as well as adverse outcome pathways in toxicology. We thus focus on the fundamental problem of design-specific interactions between NPs and cellular membranes, modeled to a first approximation as lipid bilayers.

To provide accurate, efficient, and robust predictions for a range of NP designs, we construct a first-of-its kind, multiscale physics-based platform linking detailed molecular dynamics (MD) simulations, continuum mechanical theory, and multi-compartment modeling. Using this platform, we examine the two most influential design parameters–size

and surface chemistry–and through two main case studies: (1) the membrane permeability of sub-nanometer particles and (2) the thermodynamic stability of larger-scale, ∼1-10 nm particle-membrane interactions. Within (1), we first simulate the NP-membrane interactions and transport in full detail to test the validity of Overton's Rule, a longstanding structure-property relationship, and the inhomogeneous solubility-diffusion (ISD) model, a microscopic mechanistic continuum model for transport. We show that Overton's Rule is overly simplified for describing transport across a fluctuating lipid bilayer membrane, yet that ISD model holds for small enough particles. Within this range of particles where the solubility-diffusion mechanism holds, we directly link the impact of particle chemistry in the MD simulations to transient (time-dependent) transport outcomes in the macroscopic multi-compartmental models. This allows us to both compare with and evaluate models used in experimental permeability assays and close the orders of magnitude gap between simulation-predicted and experimentally-calculated permeabilities. We also leverage our platform to construct improved structure-property relationships for the steady-state membrane permeability and structure-*kinetic* relationships, accounting for a wider range of particle chemistries and highlighting the imperative of time in dictating the design rules for membrane permeation.

Within case study (2), we probe larger NP-membrane interactions that implicate macroscopic membrane deformations and restructuring. Using the molecular simulations, we map out in particle size and chemistry space the putative NP-membrane interaction configurations, some of which resemble and agree with small-scale solubility-diffusion theory or large-scale membrane elastic theory (e.g. for lipid bilayer or monolayer wrapping of the NP) in stability limits and free energies and some of which require closer examination in the simulation to explain the thermodynamics. We also discover an entirely novel mechanism of interaction for ∼4 nm, rough crystalline hydrophobic particles that we call "asymmetric leaflet hopping," wherein the particle preferentially inserts in one bilayer

leaflet, forming a pre-pore in the membrane and inducing large-scale membrane curvature, and flips to the other leaflet over extended time scales. We conclude with preliminary phenomenologies to outline the phase behavior of ∼1-10 nm particles of varying chemistry, as well as other areas where our platform shows great promise. By accounting for a vast range of NP designs, natural lipid diversity (lipidomics), and variable compartmental size, boundary layer, and transient conditions, this platform has the potential to more intuitively and effectively inform systems-level physiologically-based pharmacokinetic models for NP biodistribution predictions, as well as structure-activity relationships for direct predictions of product efficacy and toxicity. The end result of this multiscale platform is that we can directly link a NP's microscopic physicochemical properties to its macroscopic outcomes in a dynamic biodistribution setting.

Contents

List of Figures

List of Tables

Chapter 1

Introduction

A critical problem in many areas of current biological and biomedical interest is the interactions of nanoparticles (NPs) with cellular membranes, as an enormous number of NPs of different varieties are becoming pervasive in therapeutics, foods & beverages, consumer products, and agriculture. A great deal of research has attempted to understand these interactions and to develop theoretical frameworks for charting the rapidly expanding suite of NP types. Among the parameters of interest, experiments suggest that the most important are the size of the NP, its shape, mechanical rigidity, and surface chemistry (e.g. hydrophobic, hydrophillic, Janus structure, etc.). Existing theories are successful in treating very small (< 1 nm) particles, which essentially partition in or outside the membrane with relatively little perturbation to it, while "large" NPs (roughly > 10 nm) can be treated by macroscopic, continuum membrane models.[1] However, a major gap exists be-tween these two limiting cases, where there are neither effective theoretical models nor basic, quantitative pictures of the mechanistic regimes of interaction. At the same time, this size range might be blamed for the most toxic of consequences.[2] Thus the development of a theoretical framework for exploring the nature of NP-membrane interactions in this critical nanoscale size regime is a crucial first step toward methods for

rapid, preliminary evaluation of factors like toxicity in existing but especially emerging NP technologies. Indeed, NPs have higher permeabilities and chemical & catalytic activity relative to colloidal chemicals,[3–7] and yet there is a major deficiency in current NP regulations.[5,8,9]

The overall goal of this thesis, which we view as an initial step toward the full complex problem, is to use multiscale physics-based modeling techniques to develop an integrated molecular-continuum-systems understanding of ∼1-10 nm NP-membrane interactions. This includes molecular simulations to delineate the distinct mechanistic regimes pertinent to nanoscale particles in their interactions with a model membrane, continuum theories (or modifications thereof) to model and explain this behavior, and systems-level modeling to determine the dynamic and macroscopic consequences of the continuum-level parameterization. We believe this thesis to be an essential step towards the broader problem of NP interactions with and also transport through cellular membranes. It provides a framework that can be subjected to well-controlled experimental studies in subsequent work, but conversely, will also produce a self-consistent, independent picture useful for clarifying conflicts in the current experimental literature.

1.1 Significance

Nanoparticles (NPs) are ubiquitous in the food, agriculture, and consumer product industries, and are increasingly attractive as new drug carriers, preservatives, and antimicrobials.[5,9–25] However, their small size leads to high permeability and chemical & catalytic activity,[3–7,26] both of which generate major concerns about toxicity.[5,8,9,27] Because advances in nanoscale fabrication[22,28–36] and manipulation[2,35,37–42] now offer the ability to custom-design NPs with an enormous array of options, a predictive methodology based on physical theory and modeling is now essential for charting potential toxicity

factors throughout the vast particle design space.

1.1.1 NP toxicity, membrane interactions, and NP design effects

On the cellular level, NPs can induce oxidative stress, interfere with signaling & gene expression, produce cytokines, damage membranes and organelles, and initiate apoptosis & ultimately cell death.[26,43,44] The consumer products industry does not appreciate how many of its active ingredients work at the intended destination,[45] while NPs are becoming increasingly diverse with advanced synthesis techniques and many design parameters that have a demonstrated impact on toxicity and performance.[46–49] Moreover, pharmacological and toxicological studies have produced conflicting results,[26] including the effects of NP size[50,51] and shape.[52,53] An integrated picture of such NP design parameters is lacking.

Here we focus on predicting NP interactions with and damage to idealized lipid membranes, as simple models of real cellular membranes that provide first-line barriers to NP contaminants. NPs can damage membranes through physical disturbance, membrane activity, and electron-ion membrane transport activity, among other chemical & physical mechanisms. NPs can thus lead to direct and indirect (e.g. through oxidation) membrane destabilization, including hole formation that can lead to leakage.[27,54,55] NPs on the 1 to 10 nm scale–including quantum dots (QDs) and Au, TiO2, FeO2, and polystyrene NPs, amongst others[2]–have particularly serious toxicity concerns. For example, clusters of such particles can accumulate in plasma membranes before entering cells.[56–58] However, thermodynamic and kinetic processes of 1-10 nm NPs with cellular membranes, including both passive diffusion and active endocytosis, are complex and diverse.

Recent efforts have sought a more fundamental understanding through idealized experimental models (including lipid bilayers, liposomes, or giant unilamellar vesicles[41,43,44,59–63])

and theoretical & simulation studies. Importantly, statistical mechanical advances now allow accurate free energy calculations from experiments and simulations in both equilibrium and nonequilibrium settings.[64–66] Simulation approaches are particularly attractive because techniques to fabricate and characterize precise NP sizes and chemistries (let alone shapes and elasticities) are expensive and time-consuming to execute in a "high-throughput" fashion. Simulations also offer the ability to measure informative behaviors like small wavelength membrane fluctuation modes and kinetic particle "pull through" events that are difficult to probe in experiment.[66–68] So far, computational studies have generated qualitative mechanisms of NP-membrane interactions[69,70] for various particle sizes,[71] chemistries,[72–75] shapes,[76,77] elasticities,[78] and functionalization (e.g., ligand chemistries,[79–81] lengths,[82] rigidities,[82] reversibility,[83] and charge[84–87]). While most of these studies did not make a detailed examination of particle effects on and potential destabilization of the membrane, a few have uncovered important clues. For example, 3 nm hydrophobic and 6 nm charged NPs induce local disorder in DPPC bilayers through inclusion (insertion) and adsorption, respectively, and furthermore negatively charged NPs globally reduce the gel-liquid phase transition temperature.[85] A Monte Carlo study showed how hydrophobic and amphiphilic particles could inflict reversible membrane damage that increases solvent permeability.[73] Another study showed that NPs enhance water permeation, ion transport, and lipid flip-flop, all of which can have toxic consequences by disrupting concentration gradients and through rearrangement of the inner and outer leaflet structure.[68]

1.1.2 The need to fill theoretical gaps

The theory of membrane-particle interactions is well-developed at the extremes of particle size, but remains murky in the "crossover" regime between them. For small

molecularly-sized moieties, the classic ideas of Overton and Uhlig still capture the main features of cross-membrane transport,[88–92] even though many theoretical refinements have since been developed.[93–97] Overton's rule states that the solute permeability is related to its membrane-solvent partition coefficient; by extension, the translocation kinetics are dominated by the thermodynamic barrier (or well) in the solute's free energy profile across the membrane. The thermodynamics are largely governed by solvation changes in moving from the aqueous to inner membrane environment,[92,97–99] but somewhat larger molecules can incur additional penalties from excluded volume effects, particularly in the interfacial region, that can be included in the theory.[100,101] Many simulation studies have tested these ideas through detailed calculations of free energy profiles and permeabilities.[88,89,94–97,97,98,100,102–115]

At the other extreme ($>$ 10 nm), continuum theory captures colloid-membrane interactions. Here simple membrane diffusion is unlikely, but spontaneous budding (wrapping followed by pinching of the membrane) is possible for particles with specific affinity for membrane head groups[116] while inclusion (membrane insertion) may occur for hydrophobic particles.[117–120] Wrapping is described by bending and stretching energetics in Canham-Helfrich elastic membrane theory:[121–124] unfavorable membrane deformations balance favorable particle adhesion, and thermodynamics scale with the bending modulus k_c and interfacial tension.[125–128] Coarse-grained, mesoscopic, and continuum simulations have tested the limits of the interactions and theory.[116,125–127,129–136] A variety of metastable and stable states have been observed in simulation that both agree and disagree with theory depending on the assumptions of a finite-sized membrane and the shape of the NP-membrane complex.[116]

The physics becomes complicated for 1-10nm particles. The free energy barrier/well is difficult to predict for a NP size comparable to the membrane thickness ($\sim$5 nm), and many venerable statistical mechanical approaches (like scaled particle theory) break

down at these large sizes. Moreover, the scaling of interaction free energies becomes highly chemistry-dependent. Hydrophilic solutes like sucrose (300 Da) are essentially impermeable, but chemical modifications can lead to membrane penetration and efficient transport.[80,137–141] Generally, hydrophilic particles do not partition and thus permeation becomes unfavorable; however, transport may still occur through dynamic opening and closing of pore fluctuations.[94,97,142–147] Such hydrophilic holes can arise from mechanical tension and electrical fields, and their population is governed by energetic cost (related to membrane edge energy and interfacial tension).[143–147] For hydrophobic particles, partitioning can occur in a pre-pore (hydrophobic hole) or inclusion (insertion), and is influenced in poorly-understood ways by hydrophobic interactions and small-wavelength membrane fluctuations.[120,148,149] Hydrophobic particles also lead to membrane expansion or compression.[117–119,150] Recent pure membrane theory has been able to include key fluctuations in lipid tilt, twist, and splay, and in a manner consistent with the standing mesoscopic descriptions that dominate at large length scales (e.g. bending and splay). A complete understanding of such effects, however, is lacking.[151–159] A core problem is that simulations at all-atom resolution are very difficult due to system size, yet macroscopic theory breaks down.[151] The picture becomes even more difficult for Janus, striped, patchy, and randomly distributed morphologies, for which passive diffusion has been found to be possible. We hypothesize that nanoscale membrane deformation processes manifest largely in lipid splay for a hydrophilic NP (forming a hydrophilic hole/pore) and in lipid tilt for a hydrophobic NP (forming a hydrophobic hole/pre-pore). This suggests appropriate simple theoretical models that can be vetted by simulations and ultimately extended to more complicated nanoscale chemistry, shape, and elasticity designs that are of increasing interest.[80,137–141]

1.2 Focus and outline

In this thesis, we focus on the impact of NP physicochemical properties for the interactions with and transport of ∼1-10 nm NPs across lipid bilayer membranes. We focus on passive interactions and transport, independent of ATP and active transport and without additional cellular machinery. We seek fundamental insights on the interaction modes and mechanisms, and ultimately *novel, physically-motivated* structure-property, structure-kinetic, and structure-activity relationships. This work will be organized as follows:

- **Chapter 2: Theoretical background**
- **Chapter 3: Nanoparticle transport across model cellular membranes: when do solubility-diffusion theories break down?** This study concerns the exploration and validation (or invalidation) of small-scale theories for the membrane permeability of sub-nanometer then nanoscale particles, using continuum theory and detailed molecular simulations.
- **Chapter 4: A multiscale framework for the membrane permeability of sub-nanometer particles.** This study concerns the linkage of microscopic continuum theories to macroscopic systems-level outcomes in multi-compartment models, for sub-nanometer particles on the hydrophilic-hydrophobic spectrum.
- **Chapter 5: A quantitative structure-property and structure-kinetic relationship for the membrane transport of sub-nanometer hydrophilic, hydrophobic, and interfacially active particles.** This study concerns the linkage of the molecular simulation results from Chapter 3 to microscopic theories and macroscopic systems-level outcomes, using the framework of Chapter 4, for sub-nanometer particles of varying lipid head group and tail group attraction.

- **Chapter 6: A unified molecular/continuum thermodynamic model for size and chemistry effects on ∼1-10 nm particle-membrane interactions.** This study concerns the initial exploration of and development of descriptive phenomenlogies for larger, ∼1-10 nm NP-membrane interactions, using the range of chemistries in Chapters 3 and 5.

- **Chapter 7: Conclusions and future work**

Bibliography

[1] Van Lehn RC, Alexander-Katz A. Penetration of lipid bilayers by nanoparticles with environmentally-responsive surfaces: simulations and theory. *Soft Matter.* 2011; 7(24): 11392.

[2] Shang L, Nienhaus K, Nienhaus GU. Engineered nanoparticles interacting with cells: size matters. *Journal of nanobiotechnology.* 2014; 12(1): 5.

[3] Arnida , Malugin A, Ghandehari H. Cellular uptake and toxicity of gold nanoparticles in prostate cancer cells: A comparative study of rods and spheres. *Journal of Applied Toxicology.* 2010; 30(3): 212–217.

[4] Colvin VL. The potential environmental impact of engineered nanomaterials. *Nature Biotechnology.* 2003; 21(10): 1166–1170.

[5] Miller G, Senjen DR. Out of the Laboratory and On To Our Plates: Nanotechnology in Food & Agriculture. *Friends of the Earth.* 2008.

[6] Nolte TM, Kettler K, Meesters JA, Hendriks AJ, Meent D. A semi-empirical model for transport of inorganic nanoparticles across a lipid bilayer: Implications for uptake by living cells. *Environmental Toxicology and Chemistry.* 2015; 34(3): 488–496.

[7] Oberdörster G, Oberdörster E, Oberdörster J. Nanotoxicology: An Emerging Discipline Evolving from Studies of Ultrafine Particles. *Environmental Health Perspectives.* 2005; 113(7): 823–839.

[8] Davenport M. Closing the Gap for Generic Nanomedicines. *Chemical & Engineering News.* 2014; 92(45): 10–13.

[9] Illuminato I. Tiny Ingredients, Big Risks: Nanomaterials Rapidly Entering Food and Farming. *Friends of the Earth.* 2014.

[10] Beija M, Salvayre R, Lauth-de Viguerie N, Marty JD. Colloidal systems for drug delivery: from design to therapy. *Trends in biotechnology.* 2012; 30(9): 485–96.

[11] Bertrand N, Wu J, Xu X, Kamaly N, Farokhzad OC. Cancer nanotechnology: The impact of passive and active targeting in the era of modern cancer biology. *Advanced Drug Delivery Reviews.* 2014; 66: 2–25.

[12] Biello D. Do Nanoparticles in Food Pose a Health Risk? *Scientific American.* 2008.

[13] Brar SK, Verma M, Tyagi RD, Surampalli RY. Engineered nanoparticles in wastewater and wastewater sludge - Evidence and impacts. *Waste Management.* 2010; 30(3): 504–520.

[14] Cheng CJ, Tietjen GT, Saucier-Sawyer JK, Saltzman WM. A holistic approach to targeting disease with polymeric nanoparticles. *Nature Reviews Drug Discovery.* 2015; 14(4): 239–247.

[15] Couvreur P, Vauthier C. Nanotechnology: Intelligent Design to Treat Complex Disease. *Pharmaceutical Research.* 2006; 23(7): 1417–1450.

[16] Danhier F, Ansorena E, Silva JM, Coco R, Le Breton A, Préat V. PLGA-based nanoparticles: An overview of biomedical applications. *Journal of Controlled Release.* 2012; 161(2): 505–522.

[17] Farokhzad OC, Cheng J, Teply BA, et al. Targeted nanoparticle-aptamer bioconjugates for cancer chemotherapy in vivo. *Proceedings of the National Academy of Sciences of the United States of America.* 2006; 103(16): 6315–6320.

[18] Farokhzad OC, Langer R. Impact of Nanotechnology on Drug Delivery. *ACS Nano.* 2009; 3(1): 16–20.

[19] Kujawa P, Winnik FM. Innovation in nanomedicine through materials nanoarchitectonics. *Langmuir : the ACS journal of surfaces and colloids.* 2013; 29(24): 7354–61.

[20] McCarthy JR, Weissleder R. Multifunctional magnetic nanoparticles for targeted imaging and therapy. *Advanced drug delivery reviews.* 2008; 60(11): 1241–51.

[21] Napier ME, DeSimone JM. Nanoparticle Drug Delivery Platform. *Polymer Reviews.* 2007; 47(3): 321–327.

[22] Petros RA, DeSimone JM. Strategies in the design of nanoparticles for therapeutic applications. *Nature reviews. Drug discovery.* 2010; 9(8): 615–27.

[23] Raj S, Sumod U, Jose S, Sabitha M. Nanotechnology in cosmetics: Opportunities and challenges. *Journal of Pharmacy and Bioallied Sciences.* 2012; 4(3): 186.

[24] Sun T, Zhang YS, Pang B, Hyun DC, Yang M, Xia Y. Engineered Nanoparticles for Drug Delivery in Cancer Therapy. *Angew. Chem. Int. Ed..* 2014; 53: 12320–12364.

[25] Zhang L, Chan JM, Gu FX, et al. Self-assembled lipid-polymer hybrid nanoparticles: A robust drug delivery platform. *ACS Nano.* 2008; 2(8): 1696–1702.

[26] Horie M, Kato H, Fujita K, Endoh S, Iwahashi H. In Vitro Evaluation of Cellular Response Induced by Manufactured Nanoparticles. *Chemical Research in Toxicology.* 2011; 25(3): 605–619.

[27] Elsaesser A, Howard CV. Toxicology of nanoparticles. *Advanced Drug Delivery Reviews.* 2012; 64(2): 129–137.

[28] Anselmo AC, Zhang M, Kumar S, et al. Elasticity of nanoparticles influences their blood circulation, phagocytosis, endocytosis and targeting. *ACS Nano.* 2015; 9(3): 3169–3177.

[29] Champion JA, Katare YK, Mitragotri S. Making polymeric micro- and nanoparticles of complex shapes. *Proceedings of the National Academy of Sciences of the United States of America.* 2007; 104(29): 11901–4.

[30] Euliss LE, DuPont JA, Gratton S, DeSimone J. Imparting size, shape, and composition control of materials for nanomedicine. *Chemical Society reviews.* 2006; 35(11): 1095–1104.

[31] Ge J, Lei J, Zare RN. Protein inorganic hybrid nanoflowers. *Nature Nanotechnology.* 2012; 7(7): 428–432.

[32] Jackson AM, Myerson JW, Stellacci F. Spontaneous assembly of subnanometre-ordered domains in the ligand shell of monolayer-protected nanoparticles. *Nature materials.* 2004; 3(5): 330–336.

[33] King NP, Sheffler W, Sawaya MR, et al. Computational Design of Self-Assembling Protein Nanomaterials with Atomic Level Accuracy. *Science.* 2012; 336(6085): 1171–1174.

[34] Niu W, Chua YAA, Zhang W, Huang H, Lu X. Highly Symmetric Gold Nanostars: Crystallographic Control and Surface-Enhanced Raman Scattering Property. *Journal of the American Chemical Society.* 2015: 150813155008007.

[35] Rolland JP, Maynor BW, Euliss LE, Exner AE, Denison GM, DeSimone JM. Direct fabrication and harvesting of monodisperse, shape-specific nanobiomaterials. *Journal of the American Chemical Society.* 2005; 127(28): 10096–10100.

[36] Seo D, Yoo C, Chung I, Park S, Ryu S, Song H. Shape Adjustment between Multiply Twinned and Single-Crystalline Polyhedral Gold Nanocrystals: Decahedra, Icosahedra, and Truncated Tetrahedra. *Journal of Physical Chemistry C.* 2008; 112(7): 2469–2475.

[37] Carney RP, Astier Y, Carney TM, Voïtchovsky K, Jacob Silva PH, Stellacci F. Electrical method to quantify nanoparticle interaction with lipid bilayers. *ACS Nano.* 2013; 7(2): 932–942.

[38] Chen KL, Bothun GD. Nanoparticles meet cell membranes: Probing nonspecific interactions using model membranes. *Environmental Science and Technology.* 2014; 48(2): 873–880.

[39] Glatzel T, Garcia R, Schimmel T. Advanced atomic force microscopy techniques II. *Beilstein Journal of Nanotechnology.* 2014; 5: 2326–2327.

[40] Hoo CM, Starostin N, West P, Mecartney ML. A comparison of atomic force microscopy (AFM) and dynamic light scattering (DLS) methods to characterize nanoparticle size distributions. *Journal of Nanoparticle Research.* 2008; 10(S1): 89–96.

[41] Roiter Y, Ornatska M, Rammohan AR, Balakrishnan J, Heine DR, Minko S. Interaction of lipid membrane with nanostructured surfaces. *Langmuir.* 2009; 25(11): 6287–6299.

[42] Shan Y, Ma S, Nie L, et al. Size-dependent endocytosis of single gold nanoparticles. *Chem. Commun..* 2011; 47: 8091–8093.

[43] Le Bihan O, Bonnafous P, Marak L, et al. Cryo-electron tomography of nanoparticle transmigration into liposome. *Journal of Structural Biology.* 2009; 168(3): 419–425.

[44] Zhang S, Nelson A, Beales PA. Freezing or wrapping: the role of particle size in the mechanism of nanoparticle-biomembrane interaction. *Langmuir : the ACS journal of surfaces and colloids.* 2012; 28(35): 12831–7.

[45] Levin J, Momin SB. How much do we really know about our favorite cosmeceutical ingredients? *The Journal of clinical and aesthetic dermatology.* 2010; 3(2): 22–41.

[46] Brunner TJ, Wick P, Manser P, et al. In Vitro Cytotoxicity of Oxide Nanoparticles: Comparison to Asbestos, Silica, and the Effect of Particle Solubility. *Environ. Sci. Technol..* 2006; 40(14): 4374–4381.

[47] Magrez A, Kasas S, Salicio V, et al. Cellular Toxicity of Carbon-Based Nanomaterials. *Nano Letters.* 2006; 6(6): 1121–1125.

[48] Sayes CM, Wahi R, Kurian PA, et al. Correlating nanoscale titania structure with toxicity: A cytotoxicity and inflammatory response study with human dermal fibroblasts and human lung epithelial cells. *Toxicological Sciences.* 2006; 92(1): 174–185.

[49] Sayes CM, Fortner JD, Guo W, et al. The Differential Cytotoxicity of Water-Soluble Fullerenes. *Nano Letters.* 2004; 4(10): 1881–1887.

[50] Chithrani BD, Ghazani AA, Chan WCW. Determining the size and shape dependence of gold nanoparticle uptake into mammalian cells. *Nano Letters.* 2006; 6(4): 662–668.

[51] Pan Y, Neuss S, Leifert A, et al. Size-Dependent Cytotoxicity of Gold Nanoparticles. *Small.* 2007; 3(11): 1941–1949.

[52] Chithrani BD, Chan WCW. Elucidating the mechanism of cellular uptake and removal of protein-coated gold nanoparticles of different sizes and shapes. *Nano Letters.* 2007; 7(6): 1542–1550.

[53] Gratton SEA, Ropp PA, Pohlhaus PD, et al. The effect of particle design on cellular internalization pathways. *Proceedings of the National Academy of Sciences of the United States of America.* 2008; 105(33): 11613–8.

[54] Hong S, Bielinska AU, Mecke A, et al. Interaction of poly(amidoamine) dendrimers with supported lipid bilayers and cells: Hole formation and the relation to transport. *Bioconjugate Chemistry.* 2004; 15(4): 774–782.

[55] Kim IY, Joachim E, Choi H, Kim K. Toxicity of silica nanoparticles depends on size, dose, and cell type. *Nanomedicine: Nanotechnology, Biology, and Medicine.* 2015; 11(6): 1407–1416.

[56] Jiang X, Röcker C, Hafner M, Brandholt S, Dörlich RM, Nienhaus GU. Endo- and exocytosis of zwitterionic quantum dot nanoparticles by live hela cells. *ACS Nano.* 2010; 4(11): 6787–6797.

[57] Shang L, Stockmar F, Azadfar N, Nienhaus GU. Intracellular thermometry by using fluorescent gold nanoclusters. *Angewandte Chemie - International Edition.* 2013; 52(42): 11154–11157.

[58] Yang L, Shang L, Nienhaus GU. Mechanistic aspects of fluorescent gold nanocluster internalization by live HeLa cells. *Nanoscale.* 2013; 5(4): 1537–43.

[59] Mashaghi S, Jadidi T, Koenderink G, Mashaghi A. *Lipid nanotechnology*; Vol. 14 . 2013.

[60] Strobl FG, Seitz F, Westerhausen C, et al. Intake of Silica Nanoparticles by Giant Lipid Vesicles : Influence of Particle Size and Thermodynamic Membrane State. *Beilstein Journal of Nanotechnology.* 2014: 2468–2478.

[61] Sullan RMA, Li JK, Hao C, Walker GC, Zou S. Cholesterol-dependent nanomechanical stability of phase-segregated multicomponent lipid bilayers. *Biophysical Journal.* 2010; 99(2): 507–516.

[62] Tahara K, Tadokoro S, Kawashima Y, Hirashima N. Endocytosis-like uptake of surface-modified drug nanocarriers into giant unilamellar vesicles. *Langmuir.* 2012; 28(18): 7114–7118.

[63] Van Lehn RC, Ricci M, Silva PHJ, et al. Lipid tail protrusions mediate the insertion of nanoparticles into model cell membranes. *Nature communications.* 2014; 5: 4482.

[64] Chipot C, Pohorille A. *Free energy calculations: Theory and applications in chemistry and biology.* Berlin Heidelberg: Springer-Verlag 2007.

[65] Hummer G, Szabo A. Free energy surfaces from single-molecule force spectroscopy. *Accounts of Chemical Research.* 2005; 38(7): 504–513.

[66] Park S, Schulten K. Calculating potentials of mean force from steered molecular dynamics simulations. *Journal of Chemical Physics.* 2004; 120(13): 5946–5961.

[67] BaÅ§tuÇğ T, Chen PC, Patra SM, Kuyucak S. Potential of mean force calculations of ligand binding to ion channels from Jarzynski's equality and umbrella sampling. *The Journal of chemical physics.* 2008; 128(15): 155104.

[68] Song B, Yuan H, Pham SV, Jameson CJ, Murad S. Nanoparticle permeation induces water penetration, ion transport, and lipid flip-flop. *Langmuir.* 2012; 28(49): 16989–17000.

[69] Ding Hm, Ma Yq. Theoretical and Computational Investigations of Nanoparticle-Biomembrane Interactions in Cellular Delivery. *Small.* 2015; 11(9-10): 1055–1071.

[70] Zhang S, Gao H, Bao G. Physical Principles of Nanoparticle Cellular Endocytosis. *ACS Nano.* 2015; 9(9): 8655–8671.

[71] Lin X, Li Y, Gu N. Nanoparticle's size effect on its translocation across a lipid bilayer: A molecular dynamics simulation. *Journal of Computational and Theoretical Nanoscience.* 2010; 7(1): 269–276.

[72] D'Rozario RSG, Wee CL, Wallace EJ, Sansom MSP. The interaction of C60 and its derivatives with a lipid bilayer via molecular dynamics simulations. *Nanotechnology.* 2009; 20(11): 115102.

[73] Pogodin S, Werner M, Sommer JU, Baulin VA. Nanoparticle-induced permeability of lipid membranes. *ACS Nano.* 2012; 6(12): 10555–10561.

[74] Qiao R, Roberts AP, Mount AS, Klaine SJ. Translocation of C 60 and Its Derivatives Across a Lipid Bilayer. *Nanoletters.* 2007; 7(3): 614–619.

[75] Lin J, Zhang H, Chen Z, Zheng Y. Penetration of lipid membranes by gold nanoparticles: Insights into cellular uptake, cytotoxicity, and their relationship. *ACS Nano.* 2010; 4(9): 5421–5429.

[76] Vácha R, Martinez-Veracoechea FJ, Frenkel D. Receptor-mediated endocytosis of nanoparticles of various shapes. *Nano letters.* 2011; 11(12): 5391–5.

[77] Yang K, Ma YQ. Computer simulation of the translocation of nanoparticles with different shapes across a lipid bilayer. *Nature nanotechnology.* 2010; 5(8): 579–583.

[78] Yi X, Shi X, Gao H. Cellular uptake of elastic nanoparticles. *Physical Review Letters.* 2011; 107(9): 1–5.

[79] Li Y, Zhang X, Cao D. A spontaneous penetration mechanism of patterned nanoparticles across a biomembrane. *Soft matter.* 2014; 10(35): 6844–56.

[80] Li Y, Li X, Li Z, Gao H. Surface-structure-regulated penetration of nanoparticles across a cell membrane. *Nanoscale.* 2012; 4(12): 3768.

[81] Van Lehn RC, Ricci M, Silva PH, et al. Lipid tail protrusions mediate the insertion of nanoparticles into model cell membranes. *Nature Communications.* 2014; 5(1): 4482.

[82] Ding Hm, Ma Yq. Role of physicochemical properties of coating ligands in receptor-mediated endocytosis of nanoparticles. *Biomaterials.* 2012; 33(23): 5798–802.

[83] Ding HM, Tian Wd, Ma YQ. Designing nanoparticle translocation through membranes by computer simulations. *ACS nano.* 2012; 6(2): 1230–8.

[84] Rocha EL, Caramori GF, Rambo CR. Nanoparticle translocation through a lipid bilayer tuned by surface chemistry. *Physical chemistry chemical physics : PCCP.* 2013; 15(7): 2282–90.

[85] Prates Ramalho JP, Gkeka P, Sarkisov L. Structure and phase transformations of DPPC lipid bilayers in the presence of nanoparticles: Insights from coarse-grained molecular dynamics simulations. *Langmuir.* 2011; 27(7): 3723–3730.

[86] Gkeka P, Angelikopoulos P, Sarkisov L, Cournia Z. Membrane Partitioning of Anionic, Ligand-Coated Nanoparticles Is Accompanied by Ligand Snorkeling, Local Disordering, and Cholesterol Depletion. *PLoS Computational Biology.* 2014; 10(12): e1003917.

[87] Lin J, Alexander-Katz A. Cell membranes open "doors" for cationic nanoparticles/biomolecules: insights into uptake kinetics. *ACS nano.* 2013; 7(12): 10799–808.

[88] Finkelstein A. Water and nonelectrolyte permeability of lipid bilayer membranes. *The Journal of general physiology.* 1976; 68(2): 127–135.

[89] Missner A, Kügler P, Antonenko YN, Pohl P. Passive transport across bilayer lipid membranes: Overton continues to rule. *Proceedings of the National Academy of Sciences of the United States of America.* 2008; 105(52): E123.

[90] Orsi M, Essex JW. Chapter 4. Passive Permeation Across Lipid Bilayers: a Literature Review. In *Royal Society of Chemistry*no. 20 76–90 2010.

[91] Overton E. Ueber die osmotischen Eigenschaften der Zelle in ihrer Bedeutung für die Toxikologie und Pharmakologie. *Zeitschrift für Physikalische Chemie.* 1897; 22U(1): 383–406.

[92] Uhlig HH. The Solubilities of Gases and Surface Tension. *The Journal of Physical Chemistry.* 1937; 41(9): 1215–1226.

[93] Diamond JM, Katz Y. Interpretation of nonelectrolyte partition coefficients between dimyristoyl lecithin and water. *The Journal of membrane biology.* 1974; 17(2): 121–154.

[94] Fuertes G, Giménez D, Esteban-Martín S, Sánchez-Muñoz OL, Salgado J. A lipocentric view of peptide-induced pores. *European Biophysics Journal.* 2011; 40(4): 399–415.

[95] Marrink SJ, Berendsen HJC. Simulation of water transport through a lipid membrane. *The Journal of Physical Chemistry.* 1994; 98(15): 4155–4168.

[96] Nagle JF, Mathai JC, Zeidel ML, Tristram-Nagle S. Theory of passive permeability through lipid bilayers. *The Journal of general physiology.* 2008; 131(1): 77–85.

[97] Paula S, Volkov AG, Van Hoek AN, Haines TH, Deamer DW. Permeation of protons, potassium ions, and small polar molecules through phospholipid bilayers as a function of membrane thickness. *Biophysical journal.* 1996; 70(1): 339–348.

[98] Mälkiä A, Murtomäki L, Urtti A, Kontturi K. Drug permeation in biomembranes: In vitro and in silico prediction and influence of physicochemical properties. *European Journal of Pharmaceutical Sciences.* 2004; 23(1): 13–47.

[99] Markin VS, Volkov AG. The gibbs free energy of ion transfer between two immiscible liquids. *Electrochimica Acta.* 1989; 34(2): 93–107.

[100] Mitragotri S, Johnson ME, Blankschtein D, Langer R. An analysis of the size selectivity of solute partitioning, diffusion, and permeation across lipid bilayers. *Biophysical journal.* 1999; 77(3): 1268–1283.

[101] Tieleman D, Marrink S, Berendsen H. A computer perspective of membranes: molecular dynamics studies of lipid bilayer systems. *Biochimica et Biophysica Acta (BBA) - Reviews on Biomembranes.* 1997; 1331(3): 235–270.

[102] Bemporad D, Luttmann C, Essex J. Behaviour of small solutes and large drugs in a lipid bilayer from computer simulations. *Biochimica et Biophysica Acta (BBA) - Biomembranes.* 2005; 1718(1-2): 1–21.

[103] Bemporad D, Essex JW, Luttmann C. Permeation of Small Molecules through a Lipid Bilayer: A Computer Simulation Study. *The Journal of Physical Chemistry B.* 2004; 108(15): 4875–4884.

[104] Bemporad D, Luttmann C, Essex J. Computer Simulation of Small Molecule Permeation across a Lipid Bilayer: Dependence on Bilayer Properties and Solute Volume, Size, and Cross-Sectional Area. *Biophysical Journal.* 2004; 87(1): 1–13.

[105] Bernèche S, Nina M, Roux B. Molecular dynamics simulation of melittin in a dimyristoylphosphatidylcholine bilayer membrane. *Biophysical journal.* 1998; 75(4): 1603–1618.

[106] Ingram T, Storm S, Kloss L, Mehling T, Jakobtorweihen S, Smirnova I. Prediction of micelle/water and liposome/water partition coefficients based on molecular dynamics simulations, COSMO-RS, and COSMOmic. *Langmuir.* 2013; 29(11): 3527–3537.

[107] MacCallum JL, Bennett WFD, Tieleman DP. Partitioning of amino acid side chains into lipid bilayers: results from computer simulations and comparison to experiment. *The Journal of general physiology.* 2007; 129(5): 371–377.

[108] MacCallum JL, Bennett WFD, Tieleman DP. Distribution of amino acids in a lipid bilayer from computer simulations. *Biophysical journal.* 2008; 94(9): 3393–3404.

[109] MacCallum JL, Tieleman DP. Hydrophobicity scales: A thermodynamic looking glass into lipid-protein interactions. *Trends in Biochemical Sciences.* 2011; 36(12): 653–662.

[110] MacCallum JL, Tieleman DP. Computer simulation of the distribution of hexane in a lipid bilayer: Spatially resolved free energy, entropy, and enthalpy profiles. *Journal of the American Chemical Society.* 2006; 128(1): 125–130.

[111] Marrink SJ, Berendsen HJC. Permeation Process of Small Molecules across Lipid Membranes Studied by Molecular Dynamics Simulations. *The Journal of Physical Chemistry.* 1996; 100(41): 16729–16738.

[112] Orsi M, Sanderson WE, Essex JW. Permeability of small molecules through a lipid bilayer: a multiscale simulation study. *The journal of physical chemistry. B.* 2009; 113(35): 12019–12029.

[113] Peter C, Hummer G. Ion transport through membrane-spanning nanopores studied by molecular dynamics simulations and continuum electrostatics calculations. *Biophysical journal.* 2005; 89(4): 2222–2234.

[114] Sok RM, Berendsen HJC, Gunsteren WF. Molecular dynamics simulation of the transport of small molecules across a polymer membrane. *The Journal of Chemical Physics.* 1992; 96(6): 4699–4704.

[115] Tepper HL, Voth GA. Mechanisms of passive ion permeation through lipid bilayers: Insights from simulations. *Journal of Physical Chemistry B.* 2006; 110(42): 21327–21337.

[116] Ruiz-Herrero T, Velasco E, Hagan MF. Mechanisms of budding of nanoscale particles through lipid bilayers. *Journal of Physical Chemistry B.* 2012; 116(32): 9595–9603.

[117] De Jesus AJ, Allen TW. The determinants of hydrophobic mismatch response for transmembrane helices. *Biochimica et Biophysica Acta - Biomembranes.* 2013; 1828(2): 851–863.

[118] Marsh D. Energetics of hydrophobic matching in lipid-protein interactions. *Biophysical journal.* 2008; 94(10): 3996–4013.

[119] Nielsen C, Goulian M, Andersen OS. Energetics of inclusion-induced bilayer deformations. *Biophysical journal.* 1998; 74(4): 1966–1983.

[120] Wrenn SP, Small E, Dan N. Bubble nucleation in lipid bilayers: a mechanism for low frequency ultrasound disruption. *Biochimica et biophysica acta.* 2013; 1828(4): 1192–7.

[121] Campelo F, Arnarez C, Marrink SJ, Kozlov MM. Helfrich model of membrane bending: From Gibbs theory of liquid interfaces to membranes as thick anisotropic elastic layers. *Advances in Colloid and Interface Science.* 2014; 208: 25–33.

[122] Canham PB. The minimum energy of bending as a possible explanation of the biconcave shape of the human red blood cell. *Journal of theoretical biology.* 1970; 26(1): 61–81.

[123] Helfrich W. Elastic properties of lipid bilayers: theory and possible experiments. *Zeitschrift für Naturforschung. Teil C: Biochemie, Biophysik, Biologie, Virologie.* 1973; 28(11): 693–703.

[124] Safran SA. *Statistical Thermodynamics of Surfaces, Interfaces, and Membranes.* Boca Raton, FL: Westview Press 2018.

[125] Bahrami AH, Raatz M, Agudo-Canalejo J, et al. Wrapping of nanoparticles by membranes. *Advances in Colloid and Interface Science.* 2014; 208: 214–224.

[126] Deserno M, Bickel T. Wrapping of a spherical colloid by a fluid membrane. 2002: 5.

[127] Deserno M, Gelbart W. Adhesion and Wrapping in ColloidâĹŠ Vesicle Complexes. *Journal Of Physical Chemistry B.* 2002: 5543–5552.

[128] Raatz M, Lipowsky R, Weikl TR. Cooperative wrapping of nanoparticles by membrane tubes. *Soft matter.* 2014; 10(20): 3570–7.

[129] Bahrami AH. Orientational changes and impaired internalization of ellipsoidal nanoparticles by vesicle membranes. *Soft Matter.* 2013; 9(36): 8642.

[130] Dasgupta S, Auth T, Gompper G. Shape and orientation matter for the cellular uptake of nonspherical particles. *Nano letters.* 2014; 14(2): 687–93.

[131] Dasgupta S, Auth T, Gompper G. Wrapping of ellipsoidal nano-particles by fluid membranes. *Soft Matter.* 2013; 9(22): 5473.

[132] Decuzzi P, Ferrari M. The receptor-mediated endocytosis of nonspherical particles. *Biophysical journal.* 2008; 94(10): 3790–3797.

[133] Decuzzi P, Ferrari M. The role of specific and non-specific interactions in receptor-mediated endocytosis of nanoparticles. *Biomaterials.* 2007; 28(18): 2915–22.

[134] Shillcock JC, Lipowsky R. Tension-induced fusion of bilayer membranes and vesicles. *Nature materials.* 2005; 4(3): 225–228.

[135] Zhdanov VP. Kinetics of virus entry by endocytosis. *Physical Review E.* 2015; 91(4): 042715.

[136] Zhdanov VP. Physical aspects of the initial phase of endocytosis. *Physical Review E.* 2013; 88(6): 064701.

[137] Verma A, Uzun O, Hu Y, et al. Surface-structure-regulated cell-membrane penetration by monolayer-protected nanoparticles. *Nature Materials.* 2008; 7(7): 588–595.

[138] Verma A, Stellacci F. Effect of surface properties on nanoparticle-cell interactions. *Small (Weinheim an der Bergstrasse, Germany).* 2010; 6(1): 12–21.

[139] Van Lehn RC, Alexander-Katz A. Free energy change for insertion of charged, monolayer-protected nanoparticles into lipid bilayers. *Soft Matter.* 2014; 10(4): 648–658.

[140] Van Lehn RC, Atukorale PU, Carney RP, et al. Effect of particle diameter and surface composition on the spontaneous fusion of monolayer-protected gold nanoparticles with lipid bilayers. *Nano Letters.* 2013; 13(9): 4060–4067.

[141] Van Lehn RC, Alexander-Katz A. Structure of Mixed-Monolayer-Protected Nanoparticles in Aqueous Salt Solution from Atomistic Molecular Dynamics Simulations. *The Journal of Physical Chemistry C.* 2013; 117(39): 20104–20115.

[142] Den Otter WK. Free energies of stable and metastable pores in lipid membranes under tension. *Journal of Chemical Physics.* 2009; 131(20).

[143] Glaser RW, Leikin SL, Chernomordik LV, Pastushenko VF, Sokirko AI. Reversible electrical breakdown of lipid bilayers: formation and evolution of pores. *Biochimica et biophysica acta.* 1988; 940(2): 275–287.

[144] Litster J. Stability of lipid bilayers and red blood cell membranes. *Physics Letters A.* 1975; 53(3): 193–194.

[145] Tolpekina TV, Otter WK, Briels WJ. Simulations of stable pores in membranes: System size dependence and line tension. *The Journal of Chemical Physics.* 2004; 121(16): 8014.

[146] Weaver JC, Chizmadzhev Y. Theory of electroporation: A review. *Bioelectrochemistry and Bioenergetics.* 1996; 41(2): 135–160.

[147] Wohlert J, Otter WK, Edholm O, Briels WJ. Free energy of a trans-membrane pore calculated from atomistic molecular dynamics simulations. *The Journal of Chemical Physics.* 2006; 124(15): 154905.

[148] Chandler D. Interfaces and the driving force of hydrophobic assembly. *Nature.* 2005; 437: 640–647.

[149] Jamadagni SN, Godawat R, Garde S. Hydrophobicity of Proteins and Interfaces: Insights from Density Fluctuations. *Annu. Rev. Chem. Biomol. Eng..* 2011; 2(1): 147–171.

[150] Mondal S, Khelashvili G, Shi L, Weinstein H. The cost of living in the membrane: A case study of hydrophobic mismatch for the multi-segment protein LeuT. *Chemistry and Physics of Lipids.* 2013; 169: 27–38.

[151] Bitbol AF, Constantin D, Fournier JB. Bilayer Elasticity at the Nanoscale: The Need for New Terms. *PLoS ONE.* 2012; 7(11): 1–19.

[152] De Vita R, Stewart IW. Nonlinearities in tilt and layer displacements of planar lipid bilayers. *European Physical Journal E.* 2010; 32(3): 319–326.

[153] Hamm M, Kozlov M. Elastic energy of tilt and bending of fluid membranes. *The European Physical Journal E.* 2000; 3(4): 323–335.

[154] Kozlovsky Y, Chernomordik LV, Kozlov MM. Lipid Intermediates in Membrane Fusion: Formation, Structure, and Decay of Hemifusion Diaphragm. *Biophysical Journal.* 2002; 83(5): 2634–2651.

[155] Lee A. LipidâĂŞprotein interactions in biological membranes: a structural perspective. *Biochimica et Biophysica Acta (BBA) - Biomembranes.* 2003; 1612(1): 1–40.

[156] May ER, Narang a, Kopelevich DI. Molecular modeling of key elastic properties for inhomogeneous lipid bilayers. *Molecular Simulation.* 2007; 33(9-10): 787–797.

[157] Watson MC, Penev ES, Welch PM, Brown FLH. Thermal fluctuations in shape, thickness, and molecular orientation in lipid bilayers. *The Journal of Chemical Physics.* 2011; 135(24): 244701.

[158] Watson MC, Brandt EG, Welch PM, Brown FLH. Determining Biomembrane Bending Rigidities from Simulations of Modest Size. *Physical Review Letters.* 2012; 109(2): 028102.

[159] Watson MC, Morriss-Andrews A, Welch PM, Brown FLH. Thermal fluctuations in shape, thickness, and molecular orientation in lipid bilayers. II. Finite surface tensions. *Journal of Chemical Physics.* 2013; 139(8).

Chapter 2

Theoretical background

2.1 Modeling approaches to pharmacology and toxicology

In the grand scheme of pharmacometric approaches, or modeling approaches in pharmacology, both statistics-based and kinetic approaches provide essential insights into the efficacy and toxicity of a foreign agent when introduced into the human body. Statistics-based approaches like quantitative structure-activity relationships (QSARs) implement data mining and regression strategies, amongst others, to directly connect the physicochemical properties of the administered compound to its biological, pharmacological, and toxicological impact. Kinetic approaches have the power to enhance statistical ones by describing the dynamic or time-dependent disposition of the compound of interest. More specifically, approaches like pharmacokinetics (PK) seek to describe time-dependent species concentrations in well-mixed "compartments" that physically represent groups of organs systems, organs, tissues, cells, and even organelles–in other words, PK describes "what the body does to the drug." Together with pharmacodynamics (PD), which de-

scribes the response or effect of the species as a function of its concentration–"what the drug does to the body"–pharmacokinetics/pharmacodynamics (PKPD) then describes the time-dependent effect of the compound. While the dose-response connection in particular is a difficult one, potentially implicating various biological signalling processes and hierarchical biological events, PKPD remains a parsimonious and fairly reliable tool in the pharmaceutical industry, even in the clinic, for monitoring the kinetics of a given species throughout the body and its potential connection to efficacy and toxicity across a wide range of therapies, dosing regimens, and patient populations.

2.1.1 Macroscopic/Compartmental/ODE-based modeling

In compartmental modeling, transport processes are represented as exchanges between well-mixed volumes or compartments. It is worth noting that this macroscopic approach is completely analogous to a microscopic master equation approach, with the former typically formulated in terms of species concentration while the latter is typically formulated in terms of probabilities.

Pharmacokinetics

The two-compartment pharmacokinetic (PK) model is a standard pharmaceutical industry model whereby the body is broken down into gastrointestinal, central, and peripheral compartments (Figure 2.1). The gastrointestinal tract is relevant if the drug is administered orally (*per os*/p.o.), and transfer to the rest of the system is often modeled as irreversible. The central compartment represents the bloodstream and all well-perfused tissues (i.e. tissues that are quickly serviced by the bloodstream). In this sense, it is a rough indicator of blood plasma drug concentration. For intravenous drug (iv) administration, the drug dosage enters the central compartment directly. The central

compartment exchanges reversibly with the peripheral compartment, which accounts for all other, poorly-perfused tissues. Excretion, often through the kidneys, is accounted for as an irreversible process from the central compartment.

Physiologically-based pharmacokinetics

Relative to simpler PK models, physiologically-based pharmacokinetic (PBPK) models (Figure 2.2) seek to better represent human physiology and the broader stratification of perfusion time scales through explicit representation of specific organs and organ systems. This often results in an order of magnitude increase in well-mixed compartments. Here, we show a 12-compartment model accounting for the diverse constitution of and kinetics to and from the venous and arterial blood, lungs, brain, heart, liver, gut, kidney, adipose or fatty tissue, bone, muscle, and all remaining organs.

A critical aspect to both PK and PBPK models is the parameterization of transfer processes between compartments. Often, these transfer process regard transport across cellular membranes. Thus, it is crucial to understand what mediates this transport, and how to design for more efficient transport as desired. Often, PBPK models make limiting assumptions about what physical process mediates the transport between compartments. More times than not, a perfusion-limited assumption is made, as the transfer of a compound through the bloodstream is in fact expected to be slower than the transfer across membranes and endothelial cells to the interstitial space and tissues. In these perfusion-limited models, the compound is assumed to be quasi-equilibrated between the bloodstream and tissue. However, this limiting case may not always be true, particularly for larger nanoparticles. For a given NP design, it is important to determine the mechanism of transfer, how this varies with NP design and cell membrane and tissue composition, and what this then means for systems-level PK and PBPK models.

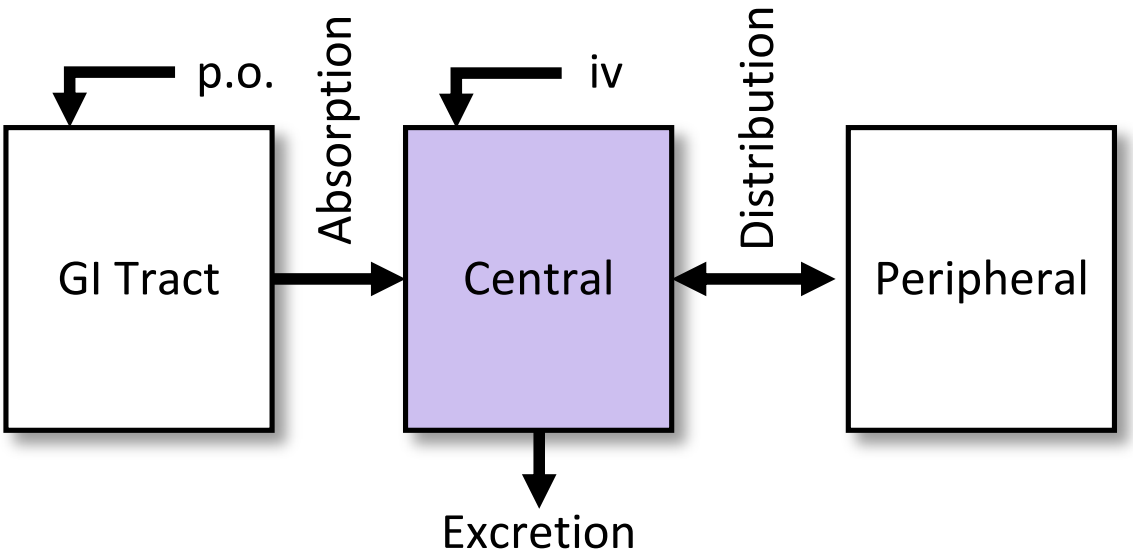

Figure 2.1: Pharmacokinetic two-compartment modeling. In the classical PK two-compartment model, an orally administered compound is introduced into the gastrointestinal tract, followed by irreversible transfer to the central compartment representing well-perfused tissue. From the central compartment, the compound transfers reversibly with poorly-perfused tissue–the peripheral compartment–and irreversibly exits the body through the relevant excretion processes.

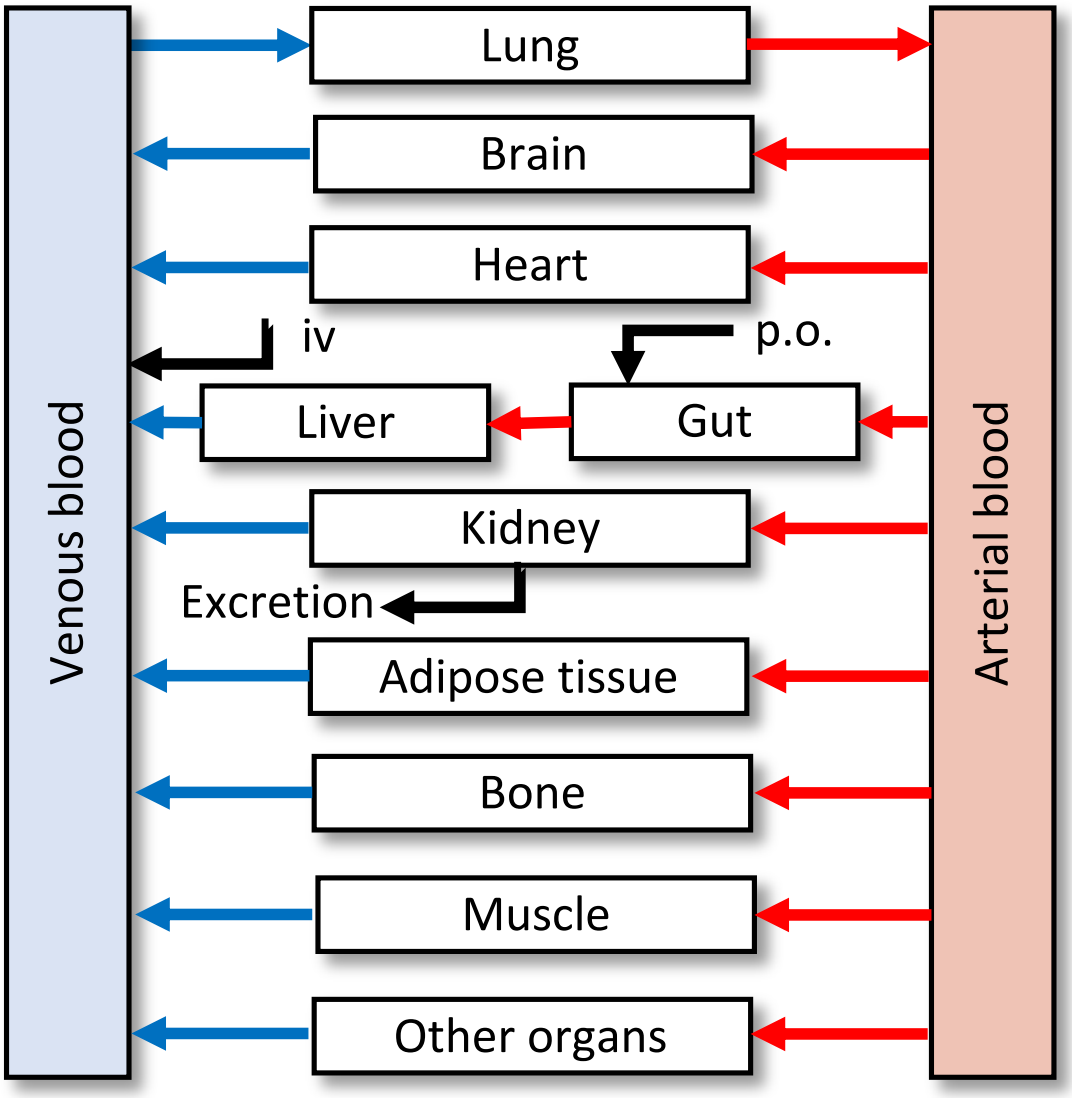

Figure 2.2: Physiologically-based pharmacokinetic modeling. PBPK models extend the PK approach for a better physical representation of the structure and dynamics within the body. The organ representations shown here are a fairly standard representation, grouping cells and tissues with a similar constitution and perfusion time scale into well-mixed compartments.

Membrane permeability assays

A common determinant of membrane permeability and screening tool in the pharmaceutical industry is the parallel artificial membrane permeability assay (PAMPA). Figure 2.3 shows a simplified schematic of a typical PAMPA setup. PAMPA loads a compound in the donor chamber (left) and measures the loading into a receiver compartment (right) on the other side of a lipid membrane assembled on a microfilter plate. Consistent stirring maintains mixing in each compartment and reduces the size and impact of unstirred water layers (gray), diffusive boundary layers that can assemble on each side of the membrane and contribute to significant steady-state and dynamic effects on calculated permeabilites. Crucially, PAMPA is simpler than Caco-2 and MDCK assays that use cellular monolayers instead of just lipids, probing only passive diffusion down a concentration gradient and more amenable to high-throughput operation.

Results from PAMPA and other permeability assays can then be used to inform membrane and cellular transport process in a biological setting. Figure 2.4 shows one biodistribution example–transfer from the bloodstream to peripheral tissue. In a capillary architecture like this one here, red blood cells result in significant convection, but unstirred water layers (diffusive boundary layers) will likely still persist and contribute to the resistance for transfer to the peripheral tissue. In this sense, PAMPA may in fact be a relevant model for passive membrane transport down a concentration gradient. For reliable comparison, however, there are many crucial considerations, not least of which are the exact mixing conditions; membrane composition, structure, and dynamics; and system geometry.

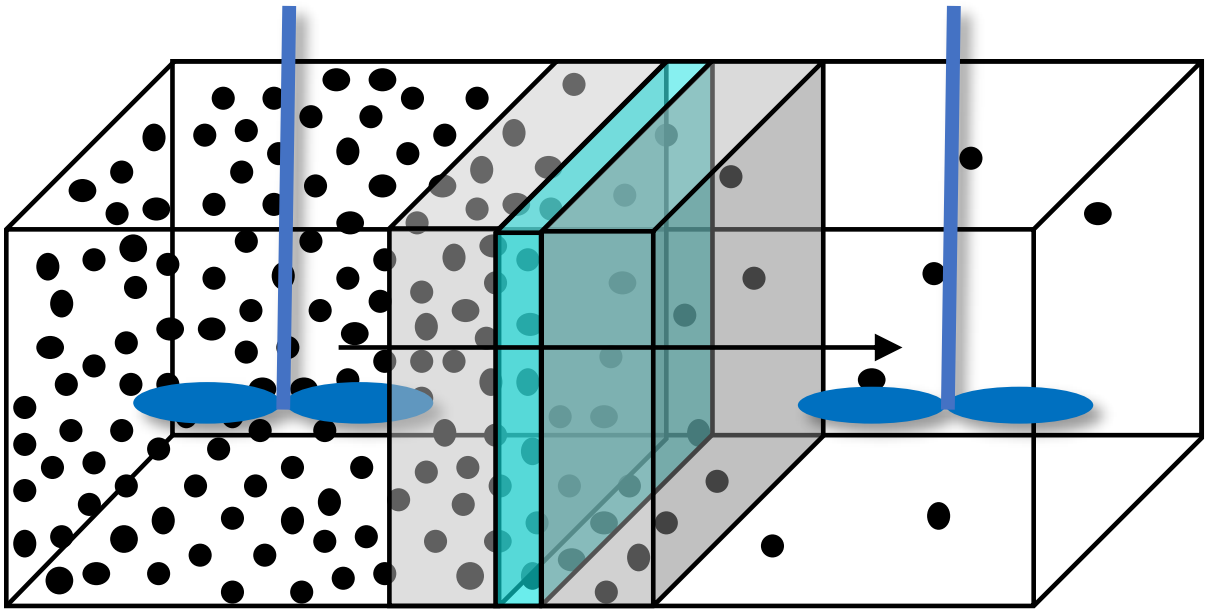

Figure 2.3: Schematic of the parallel artificial membrane permeability assay. PAMPA measures a compound's membrane permeability through bulk loading into a donor compartment, monitoring the delivery rate to the receiver compartment on the other side of the membrane. When properly operated, PAMPA is a powerful screening tool for drug candidates and other permeant products.

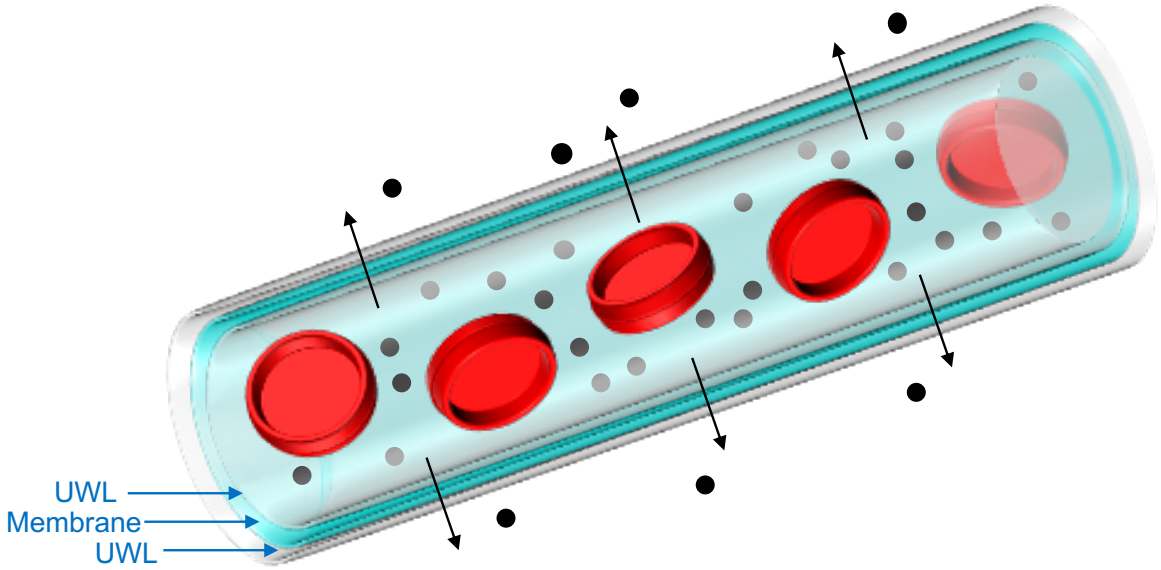

Figure 2.4: Membrane permeation in a systemic biological setting. One example of biodistribution involves transfer of a compound from the bloodstream to a peripheral tissue domain. For this example and others, a predictive capability for the compound's membrane permeability becomes a powerful tool for product screening.

2.2 Spatial variations and microscopic/PDE-based transport modeling

Unlike ODE-based compartmental modeling strategies, PDE-based transport phenomena modeling strategies can provide potentially crucial insights into the spatial variation in state variables like species concentration.

2.2.1 General engineering approach

An important conservation equation in mass transfer is the species balance:

$$\frac{\partial C_i}{\partial t} = -\nabla \cdot J + r_i(C_i) \tag{2.1}$$

where $C_i \equiv C_i(\mathbf{r}, t)$ is the concentration of species i, t is time, J is the species flux, and r_i is the volumetric reaction rate. Generally speaking, the flux J can contain inertial, diffusive and external force components. In the case of diffusion and external forcing (i.e. overdamped dynamics and diffusive barrier crossing), i.e.

$$J = -D_i \nabla C_i + D_i f_i C_i \tag{2.2}$$

–where $D_i \equiv D_i(\mathbf{r})$ is the diffusivity of species i and $f_i \equiv f_i(\mathbf{r}) \equiv -\nabla G_i$ is the mean force or negative gradient of the free energy–and in the absence of convection and reaction, Equation 2.1 reduces to the Smoluchowski Equation:

$$\frac{\partial C_i}{\partial t} = -\nabla \cdot \Big(D_i \nabla C_i + D_i f_i C_i \Big) = \nabla \cdot \Big(D_i \nabla C_i + D_i \nabla G_i C_i \Big) \tag{2.3}$$

In the specific case of diffusion over a free energy landscape in a static slab geometry, system properties are constant in the x and y directions in the plane of the slab, and only vary in the z direction perpendicular to the slab. In this case, the Smoluchowksi Equation reduces to the Nernst-Planck Equation:

$$\frac{\partial C_i(z,t)}{\partial t} = \frac{\partial}{\partial z} \Big(D_{i,z}(z) \frac{\partial C_i}{\partial z} + D_{i,z} \frac{dG_i}{dz} C_i \Big) \tag{2.4}$$

The Nernst-Planck Equation is a typical microscopic equation for describing solute transport across membranes. At steady-state, for constant concentration boundary conditions, the Nernst-Planck Equation can be used to solve for the inhomogeneous solubility-diffusion (ISD) equation:

$$1/P = \int_{-d/2}^{d/2} \frac{e^{\beta G(z)}}{D_z(z)} dz \tag{2.5}$$

where d is the membrane or domain thickness. The ISD equation thus predicts the steady-state membrane permeability, given knowledge of the free energy profile $G(z)$ and diffusivity profile $D_z(z) \equiv D(z)$ across the membrane. From Equation 2.4, a prediction for the mean first passage time rate constant (inverse to the mean first passage time, or MFPT) can be obtained:

$$1/k_{MFPT} = \int_{-d/2}^{d/2} dz \frac{e^{\beta G(z)}}{D_z(z)} \int_{-d/2}^{z} dz' e^{-\beta G(z')}. \tag{2.6}$$

However, Equations 2.4, 2.5, and 2.6 all implicitly assume a translational z coordinate for the mechanistic description, which may not be appropriate for larger particles that themselves may involve show structural and orientational rearrangements and may implicate macroscopic membrane deformations. In the work that follows, we test the validity of the ISD equation for a range of systems.

2.3 Continuum theory of membranes: a brief discussion

Lipid bilayer membranes have diverse applications in soft matter physics, pharmacology, and consumer products, and are first approximants to biological membranes. Lipid bilayers are structures consisting of two molecularly-thick layers, or leaflets, on the scale of nanometers in aqueous solvent. In these structures, molecules are oriented with their polar head groups pointing outward towards the solvent and their nonpolar tail groups pointing inward towards the other leaflet. The dominant driving forces in their formation and stability include (1) hydrophobic and dispersion interactions, wherein the lipid tail groups maximize their contacts with each other and minimize their contacts with water, decreasing area per lipid and (2) head group electrostatic/excluded-volume

repulsion and tail group conformational entropy, which work to increase the area per lipid.[1] Generally, cylinder-shaped lipids form quasi-two-dimensional lamellae (macroscopic in two dimensions and nanoscopic in the third), while conical and inverse conical lipid amphiphiles more favorably form micelles and inverted micelles, respectively[2] (although this simple view of lipids has recently been of debate[3]). Lamellar lipid bilayers often exist as multilayered vesicles (also known as liposomes–basically bilayer spheres) in solution, but can also exist in model experiments as planar bilayers across an aperture (black lipid membranes, or BLMs), laying on a solid support (supported lipid bilayers/SLBs), or directly anchored by a solid substrate (tethered bilayer lipid membranes/t-BLMs). For experimental analysis of lipid membranes, bilayers are normally assembled in multilayered stacks, while in simulations, lipid membranes are often studied as planar bilayers with periodic boundary conditions.

There is an extensive continuum theoretical framework for lipid bilayer membranes. Lamellar lipid membranes are interfaces embedded in three dimensions, but are more complicated than typical liquid-liquid interfaces due to their finite thickness and preferred area per molecule depending on the lipids' molecular neighbors and composition.[4,5] They also differ from solid-solid interfaces, due to their negligible surface tension. Because of these complexities, simple interfacial theories of surface tension in terms of, e.g., an oil-water interface or even an interface with capillary fluctuations are often insufficient for membranes. Alternatively, fluid (liquid crystalline) lipid membranes are normally modeled as liquid-like laterally (without an in-plane shear modulus), and solid-like transversely (out-of-plane).

Another major continuum assumption is that the lipids are strongly surface active, and therefore are not soluble in bulk (aqueous) solvent.[5] In aqueous solution, the lipids thus form a macroscopic interface where the head groups maintain contact with the water and the tail groups are buried, in contact with each other. In a rectangular thermal

system of constant size (i.e. the canonical ensemble), the system may reach a point where the lipid-water interface is "saturated," i.e. the lipids are packed on average at their optimal area per molecule. Since the addition of more lipids would further decrease the average area per molecule to an extent that may be globally unfavorable (higher total free energy), the membrane may instead "buckle," curving the lipid-water interface to accommodate additional lipids at the same average area per molecule. In a system of constant tension (e.g. the isobaric-isothermal ensemble, where the box dimensions can change), the addition of more lipids will instead expand the area of a bilayer that on average is flat.

For continuum lipid bilayer physics, it is almost always safe to assume volume incompressibility, as negligible fluctuations in volume cost far more than typical thermal fluctuations. Area incompressibility is a less common assumption and invalid in many cases; however, area fluctuations are often assumed to exchange with thickness (peristaltic) fluctuations through a simple equation of state whereby area and thickness are inversely correlated.[5] For this reason, a Gibbs monolayer (two-dimensional surface) description is a common and often reasonable theoretical approach. Perhaps the most studied fluctuations in lipid membranes, and what separates them from most conventional solid-liquid and liquid-liquid interfaces, are in mesoscopic shape, termed undulations.[6,7] This is typically approached from the perspective of membrane curvature elasticity, where large wavelength bending modes are highly accessible via thermal fluctuations. These out-of-plane modes lead to a distinction between the projected (in-plane) area and membrane contour area; therefore, care should be taken in deconvoluting deformations in membrane curvature (bending) from those in contour area (expansion/compression). Still, other fluctuations are accessible at smaller length scales, and typically involve local lipid orientation ("tilt" relative to mesoscopic shape) and operations thereof, as in other liquid crystalline systems.[8–11]

2.4 Diffusion on a free energy landscape for a generalized reaction coordinate

In the event that the mechanistic assumptions of the ISD model are not valid, which is particularly possible for fluctuating lipid bilayer membranes, the solute transport process must be generalized in description to a reaction coordinate q from the original translational coordinate z. In this case, we return to the Smoluchowski Equation, which is typically presented in terms of the Kramers crossover function $\xi \equiv p(q,t)/exp(-G(q))$, where $p \equiv p(q,t)$ is the probability distribution function in the mechanistic coordinate q and time t and $G(q)$ is the free energy profile across that same coordinate. The Smoluchowski Equation is then written as:

$$\frac{\partial \xi_i(q,t)}{\partial t} = e^{\beta G(q)} \frac{d}{dq}\left(e^{-\beta G(q)} D_{i,q}(q) \frac{d\xi_i}{dq} \right) \tag{2.7}$$

where $D_q \equiv D_q(q)$ is the diffusivity profile across q in the q direction. The corresponding equations for the steady-state permeability and mean first passage time rate constant are therefore:

$$\begin{cases} 1/P = \int_{q_0}^{q_F} \frac{e^{\beta G(q)}}{D_q(q)} dq \\ 1/k_{MFPT} = \int_{q_0}^{q_F} dq \frac{e^{\beta G(q)}}{D_q(q)} \int_{-\infty}^{q} dq' e^{-\beta G(q')}. \end{cases} \tag{2.8}$$

where q_0 is the initial position in terms of the reaction coordinate q, q_F is the final position, and, here, the inner integral extends in lower bounds to a limitless domain of the reactant basin, due to the placement of a reflecting boundary condition at $q \to -\infty$. The appropriate q for a given NP-membrane combination and the particular interaction event of interest, however, is not obvious. Mechanistic hypothesis testing to determine the optimal q, along with testing of the ISD model, and correct representation of fluctuating

lipid bilayer membranes, require the use of detailed molecular simulations.

2.5 Solute membrane transport: *classical* microscopic picture

2.5.1 Molecular simulation of lipid membranes

Despite the extensive physical framework for lipid bilayer membranes from both continuum theory and experiments, detailed molecular simulations can be a tremendous asset to a further understanding. Molecular simulations were first applied to lipid membrane systems in the early 1990s, and have since become increasingly amenable to larger spatiotemporal scales and higher resolutions.[12] In general, molecular simulations work well for lipid membrane studies in the following instances:

- When nanometer resolution is required, and chemical detail is important (e.g. for heterogeneous membranes, and in the case of additional non-lipid components)
- For finite-sized systems where macroscopic continuum principles may not apply
- When the interior of the membrane is being probed, and the two-dimensional/thin film assumption is not a given
- When the expected mesostructure of a lipid solution is not a planar bilayer but otherwise unclear
- To test continuum mechanical assumptions (e.g. volume/area compressibility, tension, bending renormalization, structure of pores, etc.)
- To parameterize continuum theory and simulations (i.e. with spatiotemporal and macroscopic properties)

Many of these conditions are met in a study of nanoparticle-membrane interactions. In particular for nanoparticle-membrane interactions, molecular simulations can help to determine the design-specific mechanisms of interaction, given the particular system of interest (nanoparticle design and membrane composition).

We extensively outline simulation best practices for lipid membranes, and particularly molecular models for lipid membranes, in Appendix A. In this thesis, we use the implicit solvent (solvent-free) coarse-grained Dry Martini model of Arnarez et al. Coarse-graining represents chemical groups rather than individual atoms, giving orders of magnitude increases in speed relative to atomistic simulations,[13] and the implicit solvent model here removes ∼90 percent of the degrees of freedom in the system, resulting in approximately an order of magnitude speed-up in simulation. The basic prescription of the Martini model is to combine heavy (non-hydrogen) atoms into pseudoatoms based on an approximately 4:1 atom mapping. Together with the removal of aqueous solvent, this results in a precipitous drop in computational cost and the ability to simulate molecularly-specific lipid membranes at large length and time scales. We model a fluid, one-component membrane of DPPC phospholipid, due to its extensive development in CG simulations and moderate prevalence in real biological membranes.[14–17] Figure 2.5 shows the Dry Martini model for a zwitterionic DPPC lipid bilayer. Positively-charged choline groups are drawn in blue, negatively-charged phosphates are drawn in gold, glycerol backbone groups are drawn in pink, and acyl chain tail groups are drawn in cyan.

2.5.2 Our combined molecular model

We combine the Dry Martini model with our custom-made nanoparticle model (Figure 2.6). Our model accounts for several crucial nanopaticle design parameters, in an independent and controllable manner. We are able to vary particle size, chemistry, shape,

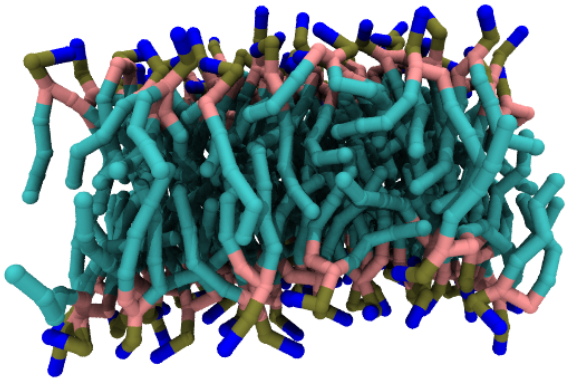

Figure 2.5: Model of the lipid bilayer membrane. Shown here is the 12-site model for DPPC in the Dry Martini force field, assembled into a planar lipid bilayer. This small bilayer is comprised of 128 lipids, and spans approximately 6.4, 6.4, and 4.5 nm in the x, y, and z directions respectively.

and elasticity through changes to particle structure, Lennard-Jones interactions, and inter-bead force constants. We build nanoparticles as aggregates of generic Dry Martini bead types that cover a range of hydrophobic and hydrophilic chemical groups principally through variations in the nanoparticle-lipid head group and nanopaticle-lipid tail group interactions. We also introduce new bead types to model passive wrapping and pinch off events driven by highly specific "ligand-receptor" interactions (strong head group interactions). Dry Martini was parameterized to experimental membrane properties and partitioning free energies, and therefore performs very well in capturing nanoscale interactions and membrane mechanics, which dominate the properties of interest here. All-in-all, our combined platform and models capture the essential ingredients of fundamental NP-membrane interactions, from simple membrane partitioning (validated with atomistic findings)[18–20] to inclusion and wrapping (validated with continuum theory).[21–32]

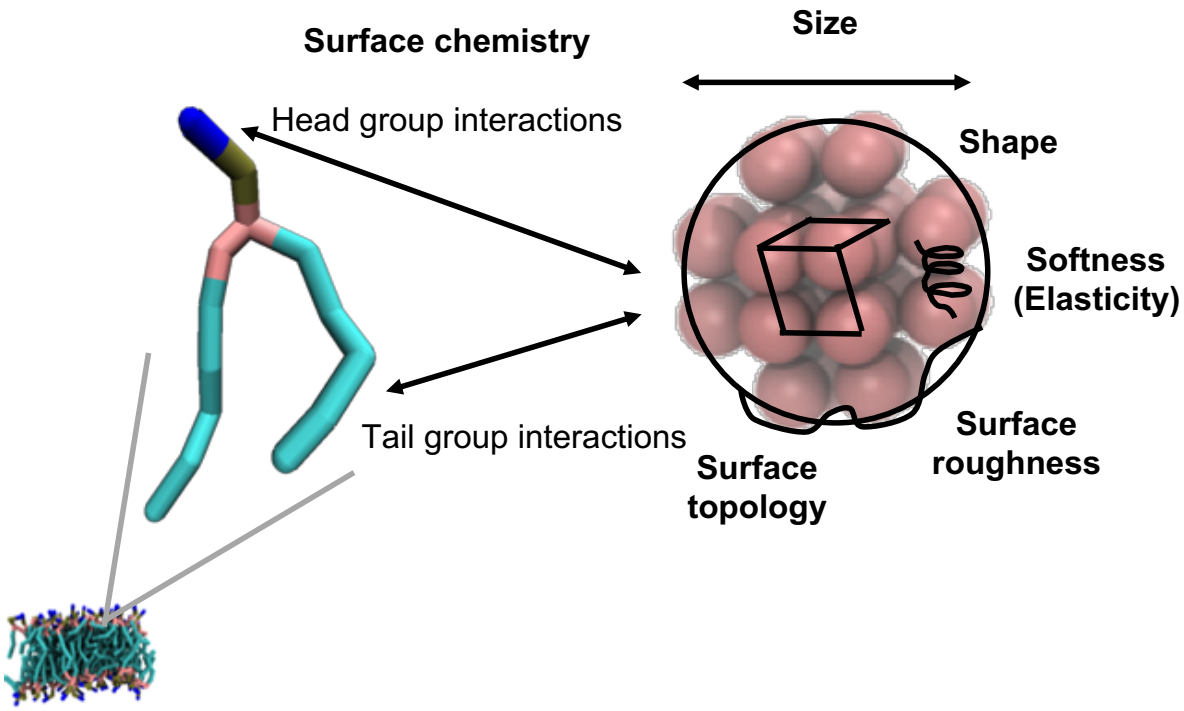

Figure 2.6: Tunability of NP design in our molecular model. A promising capability in molecular modeling is the ability to make precise and orthogonal variations in system design parameters and study the effect of those variations. Our combined nanoparticle-membrane model allows for variations in nanoparticle size, shape, elasticity, surface roughness and topology, and lipid head and tail group interactions, along with variations in the composition of the membrane itself.

2.5.3 Free energy calculations and advanced sampling

To validate the ISD model and, if it fails, to fit an improved mechanistic microscopic continuum model, the determination of free energy and diffusivity profiles is essential. The calculation of converged free energies and diffusivities often requires extensive sampling in molecular simulations. Particularly for nanoparticle-membrane interactions, the larger constituents and therefore slower dynamics of this system, along with the fluctuating nature of soft matter systems like lipid membranes, this sampling presents challenges. Most nanoparticle-membrane events of interest are currently still considered to be rare events in that they occur on time scales that are prohibitively long given current computing resources. However, one source of simulation speed-up is the coarse-grained model. Another source of speed-up lies in advanced sampling strategies that bias the system and, in data processing, rigorously correct and unweight for the imposed bias. One particular technique that we use here is umbrella sampling.[33] Umbrella sampling is fast-converging and bypasses dynamic complications like solute-interface coupling that can produce odd results due to slow-relaxing degrees of freedom.[34–37] Along with free energy calculations, umbrella sampling facilitates the determination of diffusivity profiles with the very same simulation data set. Thus, both unbiased MD and umbrella sampling MD can be used to study a wide range of nanoparticle-membrane interactions and validate the ISD model. For more rigorous mechanistic hypothesis testing where the ISD is questioned or shown to be inadequate, other rare events methods are necessary.

2.6 Our unique multiscale approach

Here, we focus on the interesting regime of ∼1-10 nm nanoparticle-membrane interactions. To capture basic chemistry-mediated aspects of interactions, we modulate nanoparticle-lipid head and -lipid tail group interactions. The preliminary state diagrams

from the MD simulations are presented in Figure 2.7. In this thesis, we break this state diagram down by devising reduced, highly-predictive models for the following problems:

- Outlining the range and limits of standing solubility-diffusion theories (mechanistic models like the ISD model) for the lipid bilayer transport of small-scale, sub-nanometer particles
- Coupling microscopic solubility-diffusion theories with macroscopic systems-level models for dynamical insights into the membrane transport of small-scale solutes in an experimental or physiological setting
- Coupling MD simulations, microscopic solubility-diffusion theories, and macroscopic systems-level models for dynamical insights and subsequently improved, physically inspired quantitative structure-property and structure-kinetic relationships for the membrane transport of small solutes
- Reducing MD simulations into continuum phenomenologies, if not rigorous continuum kinetic mechanistic models, for nanoscale and larger NP-membrane interactions

We couple these MD simulations with continuum mechanics and multi-compartment modeling, which allows us to confirm molecular-scale mechanisms, incorporate macroscopic experimental elements like unstirred water layers, and access experimentally-relevant time scales (Figure 2.8). In the experimental sense, our multiscale platform augments and improves upon existing and developing approaches in industry, leveraging molecular-scale resolution and high-performance computing to determine where reductions and simplifications can be made. Compared with the current simulation landscape in nanoparticle-membrane interactions, our approach is unique through the combination of (1) a robust platform supporting a wide range of generic particle designs; (2) the study of behaviors on multiple particle scales that integrates molecular and mesoscopic pictures of

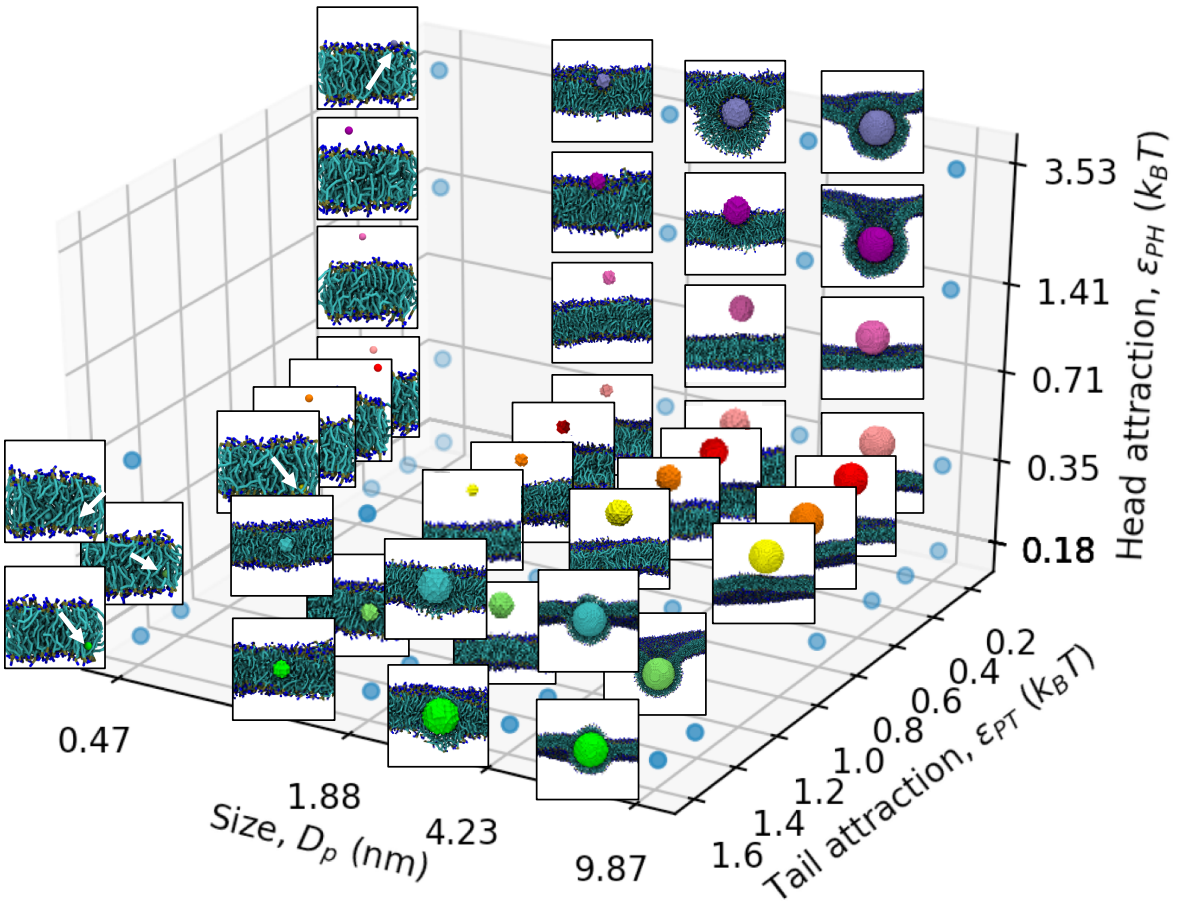

Figure 2.7: NP-membrane state diagram for particles of varying size and surface chemistry. Shown here are the results from the preliminary MD simulations of ∼1-10 nm nanoparticles of varying size (diameter D_p), particle-lipid head group affinity (ϵ_{PH}), and particle-lipid tail group affinity (ϵ_{PT}) with a single-component, fluid-phase DPPC lipid bilayer. The exploration of this space reveals a variety of interaction modes and mechanisms that we outline in more detail across this thesis.

particle-membrane interactions (rather than focusing on predominantly small or large-scale behavior, as previously shown[29,38]); and (3) the close coupling with continuum theory and systems-level modeling, therefore carrying the microscopic results through to their macroscopic consequences in an experimental setting.

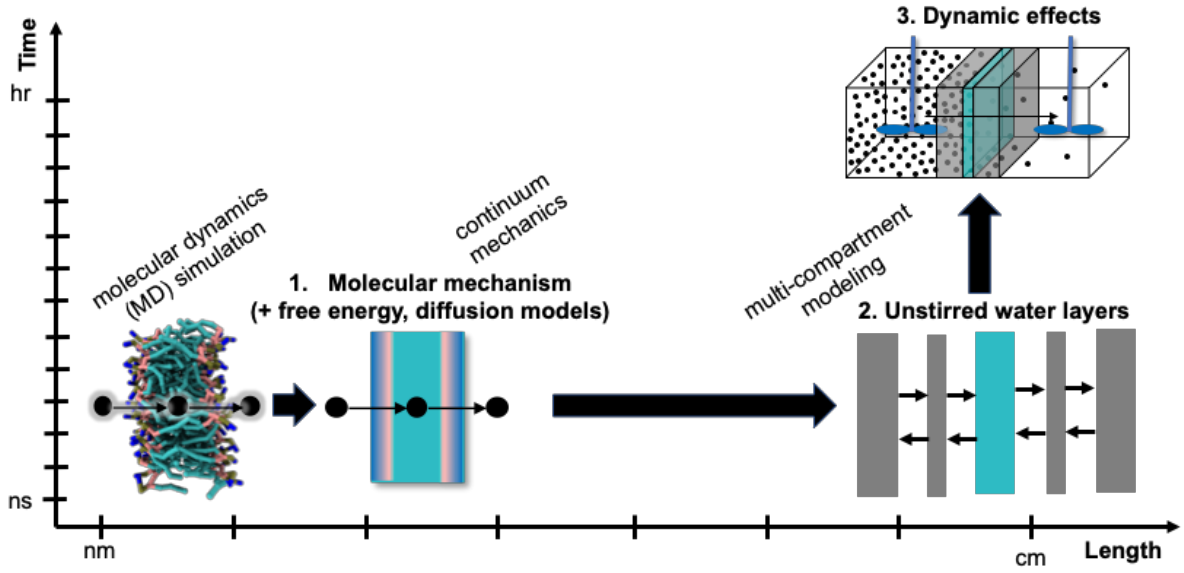

Figure 2.8: Our combined multiscale framework for NP interactions with and transport across lipid membranes. To directly connect simulations on the nanoscale with experiments (cm in length scales, hr in time) for the nanoparticle-membrane interaction problem, we link our detailed MD simulations to continuum mechanical theory through mechanistic models, then link to macroscopic systems by using our continuum theories to parameterize systems-level models that incorporate crucial components like unstirred water layers and more closely model experiments like typical membrane permeability assays. Our platform is first-of-its-kind, and has the potential to tackle a wide range of problems in nanoparticle-membrane interactions.

Bibliography

[1] Ben-Shaul A. Molecular Theory of Chain Packing, Elasticity and Lipid-Protein Interaction in Lipid Bilayers. In *Handbook of Biological Physics*; Vol. 1 359–401 1995.

[2] Israelachvili JN. *Intermolecular and Surface Forces*. Waltham, MA: Elsevier 2011.

[3] Sodt AJ, Venable RM, Lyman E, Pastor RW. Nonadditive Compositional Curvature Energetics of Lipid Bilayers. *Physical Review Letters.* 2016; 117(13): 1–6.

[4] Diamant H. Model-free thermodynamics of fluid vesicles. *Physical Review E.* 2011; 84(6): 061123.

[5] Safran SA. *Statistical Thermodynamics of Surfaces, Interfaces, and Membranes*. Boca Raton, FL: Westview Press 2018.

[6] Canham P. The minimum energy of bending as a possible explanation of the biconcave shape of the human red blood cell. *Journal of Theoretical Biology.* 1970; 26(1): 61–81.

[7] Helfrich W. Elastic properties of lipid bilayers: theory and possible experiments. *Zeitschrift fur Naturforschung. Teil C: Biochemie, Biophysik, Biologie, Virologie.* 1981; 28(11): 693–703.

[8] Hamm M, Kozlov M. Elastic energy of tilt and bending of fluid membranes. *The European Physical Journal E.* 2000; 3(4): 323–335.

[9] May ER, Narang A, Kopelevich DI. Role of molecular tilt in thermal fluctuations of lipid membranes. *Physical Review E.* 2007; 76(2): 021913.

[10] Watson MC, Penev ES, Welch PM, Brown FLH. Thermal fluctuations in shape, thickness, and molecular orientation in lipid bilayers. *The Journal of Chemical Physics.* 2011; 135(24): 244701.

[11] Watson MC, Morriss-Andrews A, Welch PM, Brown FLH. Thermal fluctuations in shape, thickness, and molecular orientation in lipid bilayers. II. Finite surface tensions. *The Journal of Chemical Physics.* 2013; 139(8): 084706.

[12] Venable RM, Brown FL, Pastor RW. Mechanical properties of lipid bilayers from molecular dynamics simulation. *Chemistry and Physics of Lipids.* 2015; 192: 60–74.

[13] Ding Hm, Ma Yq. Theoretical and Computational Investigations of Nanoparticle-Biomembrane Interactions in Cellular Delivery. *Small.* 2015; 11(9-10): 1055–1071.

[14] Arnarez C, Uusitalo JJ, Masman MF, et al. Dry Martini, a Coarse-Grained Force Field for Lipid Membrane Simulations with Implicit Solvent. *Journal of Chemical Theory and Computation.* 2015; 11(1): 260–275.

[15] Marrink SJ, Risselada HJ, Yefimov S, Tieleman DP, Vries AH. The MARTINI Force Field: Coarse Grained Model for Biomolecular Simulations. *The Journal of Physical Chemistry B.* 2007; 111(27): 7812–7824.

[16] Marrink SJ, Vries AH, Mark AE. Coarse Grained Model for Semiquantitative Lipid Simulations. *The Journal of Physical Chemistry B.* 2004; 108(2): 750–760.

[17] Spector AA, Yorek MA. Membrane lipid composition and cellular function. *Journal of lipid research.* 1985; 26(9): 1015–1035.

[18] Jakobtorweihen S, Zuniga AC, Ingram T, Gerlach T, Keil FJ, Smirnova I. Predicting solute partitioning in lipid bilayers: Free energies and partition coefficients from molecular dynamics simulations and COSMOmic. *The Journal of Chemical Physics.* 2014; 141(4): 045102.

[19] MacCallum JL, Bennett WFD, Tieleman DP. Distribution of amino acids in a lipid bilayer from computer simulations. *Biophysical journal.* 2008; 94(9): 3393–3404.

[20] Mazzobre MF, Román MV, Mourelle AF, Corti HR. Octanol-water partition coefficient of glucose, sucrose, and trehalose. *Carbohydrate Research.* 2005; 340(6): 1207–1211.

[21] Bahrami AH, Raatz M, Agudo-Canalejo J, et al. Wrapping of nanoparticles by membranes. *Advances in Colloid and Interface Science.* 2014; 208: 214–224.

[22] Bahrami AH. Orientational changes and impaired internalization of ellipsoidal nanoparticles by vesicle membranes. *Soft Matter.* 2013; 9(36): 8642.

[23] Dasgupta S, Auth T, Gompper G. Shape and orientation matter for the cellular uptake of nonspherical particles. *Nano letters.* 2014; 14(2): 687–93.

[24] Dasgupta S, Auth T, Gompper G. Wrapping of ellipsoidal nano-particles by fluid membranes. *Soft Matter.* 2013; 9(22): 5473.

[25] Decuzzi P, Ferrari M. The receptor-mediated endocytosis of nonspherical particles. *Biophysical journal.* 2008; 94(10): 3790–3797.

[26] Decuzzi P, Ferrari M. The role of specific and non-specific interactions in receptor-mediated endocytosis of nanoparticles. *Biomaterials.* 2007; 28(18): 2915–22.

[27] Deserno M, Bickel T. Wrapping of a spherical colloid by a fluid membrane. 2002: 5.

[28] Deserno M, Gelbart W. Adhesion and Wrapping in Colloid Vesicle Complexes. *Journal Of Physical Chemistry B.* 2002: 5543–5552.

[29] Ruiz-Herrero T, Velasco E, Hagan MF. Mechanisms of budding of nanoscale particles through lipid bilayers. *Journal of Physical Chemistry B.* 2012; 116(32): 9595–9603.

[30] Shillcock JC, Lipowsky R. Tension-induced fusion of bilayer membranes and vesicles. *Nature materials.* 2005; 4(3): 225–228.

[31] Zhdanov VP. Kinetics of virus entry by endocytosis. *Physical Review E.* 2015; 91(4): 042715.

[32] Zhdanov VP. Physical aspects of the initial phase of endocytosis. *Physical Review E.* 2013; 88(6): 064701.

[33] Torrie G, Valleau J. Nonphysical sampling distributions in Monte Carlo free-energy estimation: Umbrella sampling. *Journal of Computational Physics.* 1977; 23(2): 187–199.

[34] Ahn YN, Gupta A, Chauhan A, Kopelevich DI. Molecular transport through surfactant-covered oil-water interfaces: role of physical properties of solutes and surfactants in creating energy barriers for transport. *Langmuir : the ACS journal of surfaces and colloids.* 2011; 27(6): 2420–36.

[35] Gupta A, Chauhan A, Kopelevich DI. Molecular modeling of surfactant covered oil-water interfaces: Dynamics, microstructure, and barrier for mass transport. *The Journal of Chemical Physics.* 2008; 128(23): 234709.

[36] Gupta A, Chauhan A, Kopelevich DI. Molecular transport across fluid interfaces: Coupling between solute dynamics and interface fluctuations. *Physical Review E.* 2008; 78(4): 041605.

[37] Kopelevich DI. One-dimensional potential of mean force underestimates activation barrier for transport across flexible lipid membranes. *Journal of Chemical Physics.* 2013; 139(13).

[38] Bahrami AH, Raatz M, Agudo-Canalejo J, et al. Wrapping of nanoparticles by membranes. *Advances in Colloid and Interface Science.* 2014; 208: 214–224.

Chapter 3

Nanoparticle transport across model cellular membranes: when do solubility-diffusion models break down?

3.1 Abstract

The interactions of nanoparticles (NPs) with cellular membranes and subsequent transport processes have major implications for the biology, toxicology, and pharmacology of nanoscale materials. Moreover, understanding and predicting the behaviors of diverse nanoparticle designs in a physiological setting is of increasing technological and regulatory importance. Still, the current complexity of experiments and lack of a consensus in modeling and simulation preclude a clear picture of relevant NP-membrane interaction modes and mechanisms, particularly for particles on the ∼1-10 nm scale. Here, we leverage detailed coarse-grained molecular dynamics simulations with advanced sampling

strategies to uncover the thermodynamic driving forces and possible kinetic pathways of approximately 0.5-2.0 nm hydrophilic, hydrophobic, and "interfacially active" particles with model lipid bilayer membranes. Using the simulations, we test the applicability of well-established theoretical models for the permeability of small molecule transport–Overton's Rule and the inhomogeneous solubility-diffusion model–and conclude that the former is overly-simplified for fluctuating lipid bilayers, while the latter breaks down at the larger particle sizes due to the influence of other physics like membrane undulations. We place this work in the context of recent simulation studies, and conclude with critical physical and methodological insights to guide future thermodynamic and kinetic studies of NP-membrane interactions.

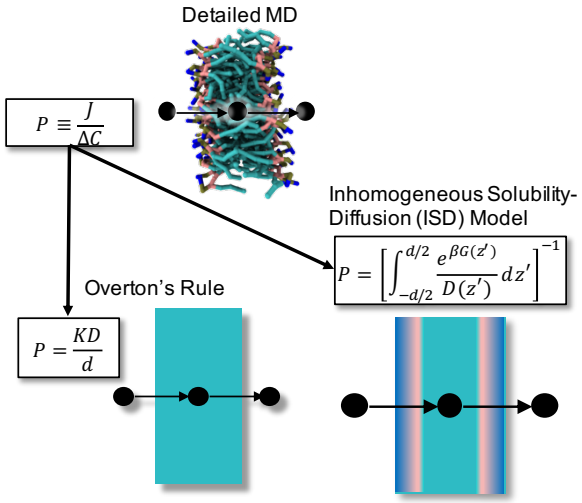

Figure 3.1: Evaluating solubility-diffusion theories for nanoparticle transport across model cell membranes with detailed molecular dynamics simulation.

3.2 Introduction

Despite the pervasiveness of nanoparticles (NPs) in industrial applications, an understanding of their pharmacological and toxicological properties is lacking. The past few

decades have witnessed an explosion in techniques for NP fabrication.[1–5] and characterization.[5–9] The technological promise of NPs is highlighted by their presence in foods and beverages, fertilizers and pesticides, cooking products, packaging, textiles, consumer products, and, perhaps most importantly, pharmaceuticals.[4,10–16] At the same time, NPs can pose many possible sources of toxicity[15–18] due to their steric effects compared to small molecules and their higher chemical & catalytic activity and permeability relative to traditional colloids.[16,19–23] Some of the most serious toxicity concerns are attributed to NPs on the 1 to 10 nm scale,[8] including quantum dots and Au, TiO_2, FeO_2, and polystyrene NPs, amongst others. There is a serious deficiency in current NP regulations,[15–17] and there have been several calls over the past decade for federal regulatory agencies like the FDA to develop new, NP-specific protocols that take the complexities of NP dosage into account.[18]

It is unclear if biodistribution principles that work well for small solutes also apply to NPs. A major problem of both pharmacological and toxicological interest is the physical interaction of NPs with cellular membranes, including NP transport across them. From a pharmacological perspective, membrane transport is a critical bottleneck in drug delivery, and from a toxicological perspective, membrane disruption is one physical process implicated in greater adverse outcome pathways.[18,24] Passive transport is highly desirable from a therapeutic perspective, as it avoids endosomal pathways and the drug can more directly reach its target. Overton's Rule (the Meyer-Overton Rule, or the solubility-diffusion model) is a venerable and long-standing ($>$ 100-year-old) small solute model that provides an incredibly simple structure-property relation for the passive membrane permeability P, relating the solute diffusive flux across the membrane J to its

concentration difference from one side of the membrane to the other ΔC:

$$P = J/\Delta C = \frac{KD_c}{d_c}. \tag{3.1}$$

Here, K is the partition coefficient, D_c is the diffusivity across the membrane core, and d_c is the membrane core thickness. Overton's Rule assumes that the membrane is a static, homogeneous slab, with properties (e.g. K) approximated for a bulk nonpolar solvent (e.g. octanol) interfacing with water. The solute is assumed to cross the membrane by a simple diffusive mechanism.[25] Crucially, Overton's Rule describes qualitative trends in the membrane transport of a wide range of small molecules–the higher the membrane partitioning, the faster the membrane transport. It has also been largely upheld in experiment for small molecules.[25–27] While some nanoscale (∼1-10 nm) chemically-structured (e.g. striped and patchy hydrophilic-hydrophobic) particles have been found in recent experiments to passively and efficiently transport across membranes,[28] there is evidence to suggest that Overton's Rule and the mechanism it implies will break down once particles reach this size range. The primary issue is that NP transport relies on a picture involving, as often described, "(direct) penetration," "passive diffusion," "simple diffusion," or "passive permeation",[13,29] where it is unclear what exact mechanism such terms are describing and particularly if these NP transport processes leave the equilibrium membrane structure unaltered. Especially with the possibility of disruptive membrane pore formation,[28] it seems likely for nanoscale NPs that, in addition to the partition coefficient, properties like NP size, surface chemistry, shape, and softness[10,18,30] and their impact on the local details of the membrane must be taken into account.

Here, we use coarse-grained molecular dynamics (MD) simulations with advanced sampling to critically evaluate the applicability of existing small-scale membrane interaction models like Overton's Rule for particles in the 1-10 nm range with a range of particle

surface chemistries. The size and surface chemistry (e.g. hydrophilic, hydrophobic) of NPs have been shown in experiment as the most consequential,[18] and so we specifically simulate rigid spherical particles with varied size and chemistry, assessing their interaction with single-component phospholipid bilayer membranes. We evaluate existing models like Overton's Rule by directly comparing permeability predictions with simulation-computed driving forces and experimental permeabilities. Our hypothesis is that, at some NP length scale that could be chemistry-dependent, nondisruptive simple diffusion (i.e. transport that does not alter membrane structure) will no longer be possible and the small-scale permeability models will fail. We therefore seek to identify precise mechanisms by which these NPs passively transport, and whether or not competing interaction modes and mechanisms (e.g. solubilization, adsorption, insertion, hydrophilic/hydrophobic pore formation, wrapping, budding, micellization) are relevant for a given NP design. To do so, we conduct detailed molecular thermodynamic analysis through order parameters calculated from the simulations. Our goals are to: (1) determine exactly where nondisruptive simple diffusion and the permeability models break down in size-chemistry space, (2) obtain physical intuition behind the relevant interaction modes and mechanisms, and (3) establish careful methodological techniques for future simulation studies of NP-membrane interactions. In the process, we establish physically-motivated models for NP-membrane interactions from the molecular scale up.

Detailed molecular simulations have been an invaluable tool for NP-membrane interactions in overcoming spatiotemporal experimental limitations and by providing complete microstate information at rates increasingly competitive with less-detailed statistical modeling techniques.[31,32] Molecular simulations have deconvoluted the precise effects of NP size,[33] chemistry,[34–37] shape,[38,39] elasticity,[40] and functionalization (e.g., ligand chemistries,[41–43] lengths,[44] rigidities,[44] reversibility,[45] and charge[46–49]), generating qualitative mechanisms and in some cases quantitative measures (e.g. free energies, permeabilities,

rate constants) of NP-membrane interactions.[29,50] In particular, simulations have sought to inform recent experimental findings on the effect of NP chemical nanostructuring.[41–43,51,52] Still, it has been difficult to glean general mechanistic principles in terms of NP design, especially at modest particle sizes and even for particles of homogeneous chemistry, and therefore determine appropriate theoretical models for thermodynamic and kinetic predictions.

Simulations allow for direct calculation of quantities relevant to a more general version of Overton's Rule, the so-called inhomogeneous solubility-diffusion (ISD) model. The ISD model has for several decades captured the full thermodynamic and kinetic picture in small solute membrane transport.[53] Unlike Overton's Rule, the model describes motion along and the ensemble of states across the entire permeation reaction coordinate. Assuming overdamped dynamics (a reasonable assumption for most physiological problems[54]), motion along solely a translational coordinate (z), and steady-state conditions, the ISD permeability follows:[55]

$$1/P \equiv R \equiv \int_{-d/2}^{d/2} \frac{e^{\beta G(z)}}{D(z)} dz \tag{3.2}$$

where R is the total resistance, G is the free energy profile for moving the particle across the membrane (potential of mean force, or PMF), $\beta \equiv 1/k_B T$, and D is the one-dimensional particle diffusivity profile. Thus, for a permeability prediction, the ISD model requires the free energy (solubility) and diffusivity profiles to be determined, both accessible from simulation. The ISD model recovers Overton's Rule if the free energy and diffusivity profiles are flat across the membrane. Other, multi-layered models recover Overton's Rule in this instance as well.[56] While Overton's Rule and the ISD model are often associated with simple diffusion alone,[25] we further stipulate that they imply no macroscopic membrane deformations during NP transport, including cavities and

out-of-plane deformations. Otherwise, the transport process would implicate other slow membrane and internal solute (e.g. orientational, conformational) degrees of freedom. Indeed, the ISD model does assume a separation of timescales, in that the translational motion is the slowest degree of freedom and other degrees of freedom relax quickly, acting as a thermal bath.

The above models work well for small molecules, but the actual mechanism for NP interactions and transport will largely depend on the particle size. Figure 3.2 outlines this problem of relative length scales. While chemically nanostructured particles are physiologically promising, it is unclear what the relevant interaction mechanisms are even for homogeneous NP chemistries. Part of the challenge has been the diversity of models and methods investigated in the literature. The appropriate physical approach will depend largely on the relative sizes of the NP, which we specify by diameter D_p, and membrane thickness d. Continuum theories are well-established at the small ($D_p << d$) and large ($D_p >> d$) solute length scales; permeability models (i.e. the theories described above) work for small particles, while membrane continuum elastic theories work well in the large particle limit.[57–60] Yet these small and large-scale limits are dominated by very different mechanisms, and there is a major theoretical gap for particles in between. We expect Overton's Rule, the ISD model, and the nondisruptive simple diffusive mechanism to work for small solutes, but to break down for a wide range of NPs in the 1-10 nm range ($D_p \sim d$) due to internal membrane distortions. Furthermore, we do not expect membrane wrapping, associated with continuum elastic theories, to be relevant for these small particles due to the high curvature deformations that it would entail. One mechanistic question concerns the relevance of solute (NP) conformation and orientation. Another question is whether or not the NP mechanisms involve significant membrane deformations to accommodate the particle. While pore formation is unstable at zero tension and zero applied electric field, and transient pore formation will be rare,[61–64] mechanisms could involve unstable,

metastable, or even stable states with particle induced pores and pre-pores, as well as particle fusion with out-of-plane membrane deformations, for ease of interaction and transport.[43,52,65,66]

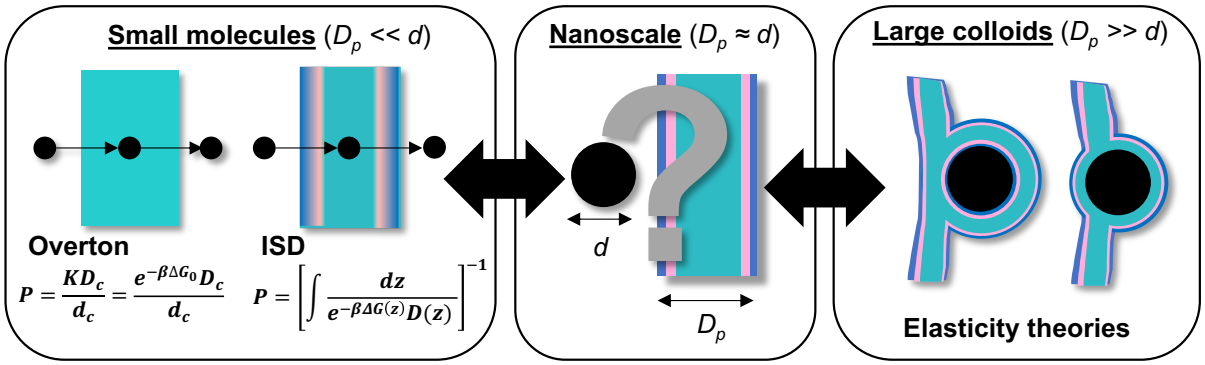

Figure 3.2: Spectrum of theoretical models for NP-membrane interactions. For small-scale particles ("small molecules," $D_p << d$), solubility-diffusion models are well-established for predicting permeability (here, ΔG_0 is the overall free energy change related to the partition coefficient). For large-scale particles ("large colloids," $D_p >> d$), membrane elastic continuum theories describe the interaction thermodynamics and kinetics. When the particle diameter is comparable to the membrane thickness (i.e. for approximately 1-10 nm nanoparticles), there is a complete lack of theory for membrane interactions and transport, and it is unclear exactly where small-scale permeability theories break down.

Even for small solutes, alternative reaction coordinates may be essential to modeling permeability. Recent simulations have suggested that solute orientation may matter in particular for amphiphiles, and for larger and more flexible solutes;[67,68] Parisio et al. developed permeability expressions in response, and the ISD model is recovered in the case of fast solute reorientation.[68] Other studies have investigated the influence of solute protonation state,[69] membrane deformation,[70] and solute-membrane/solute-solvent coordination.[71] These additional degrees of freedom can potentially identify hidden barriers in the free energy landscape, induce memory effects when their relaxation time scales rival that of membrane permeation, and significantly impact transport rate constant estimates.[67,71] In the first small-solute study that has considered long-range correlations

in time and space, Comer and Chipot found that, for a solute as simple as methanol, even the classical diffusion assumption is violated by subdiffusive motion in the membrane interior associated with solute combination with membrane voids. Anomalous diffusion could therefore be relevant for NPs, and it has in fact been found in early studies that, while neutral NPs may diffuse in the plane of the membrane upon insertion, charged NPs undergo superdiffusive motion on the membrane surface.[72] In some cases, anomalous diffusion is the result of projecting a multi-dimensional diffusion process onto a single coordinate, and selection of the appropriate alternative projection will remove the apparent anomalies.[71,73]

There is still much to be explored, and standardization and consolidation of theory and simulations across these many variables would facilitate a more unified and predictive picture. In this work, we thus develop a general simulation model of NP-membrane interactions that allows a systematic exploration of particle size and other effects to precisely pinpoint the breakdown of existing theories.

3.3 Methods

3.3.1 Membrane molecular model

This study aims to evaluate the breakdown of Overton's Rule and the ISD model and the potential competition of nondisruptive simple diffusion with mechanisms involving multiscale membrane deformations. Coarse-grained MD is a technique that can provide a reasonable balance of chemical specificity with efficiency, capturing a range of phenomena in the 1-10 nm particle range. Here, we use the Dry Martini force field, an implicit solvent coarse-grained model developed by Arnarez et al.[74] that for membrane systems achieves an order of magnitude increase in efficiency relative to explicit solvent coarse-grained MD by

completely removing the solvent degrees of freedom. Dry Martini is a combined bottom-up and top-down model that uses atomistic simulation parameters to fit bonded interactions and experimental partition free energies to fit nonbonded interactions. Relative to explicit solvent Martini, entropic contributions to hydrophobic interactions are effectively masked by shuttling such driving forces into energetics, resulting in an attenuation of nonpolar-nonpolar affinities relevant to lipid-lipid interactions. Dry Martini thus retains essential physical properties like bilayer self-assembly, phase behavior, mechanics, and thermal fluctuations, and has been validated for a host of membrane properties.[74] We specifically model DPPC membranes due to their prevalence in egg lecithin membranes used in vesicle experiments,[75,76] as a major component of pulmonary surfactant,[77] and due to their status as a benchmarking system for membrane simulations.[78–82] All MD simulations are run with either a 128-lipid, approximately 6.4x6.4 nm "confined" or 2048-lipid, approximately 26x26 nm "modest-sized" planar bilayer (Figure 3.3). The "confined" membrane is used for the 0.47 nm NP studies while the "modest" membrane is used for the 1.88 nm NP ones. While the primary factor in whether or not small-scale theories should apply is the NP length scale and remaining NP design, system (membrane) size effects will also play a role; this is demonstrated for the spectrum of 0.47 nm NPs by the use of both membranes (not shown in this thesis). Additional details about the membrane model, including extensive structural, thermodynamic, and dynamic validation of Dry Martini for DPPC, can be found in Appendix B.

3.3.2 Particle molecular model

Beyond the membrane model, we create a NP force field that uses Dry Martini bead types (representing different chemical groups) with additional groups for enhanced breadth of chemistry. NPs of different sizes are then built as multi-bead particles from these

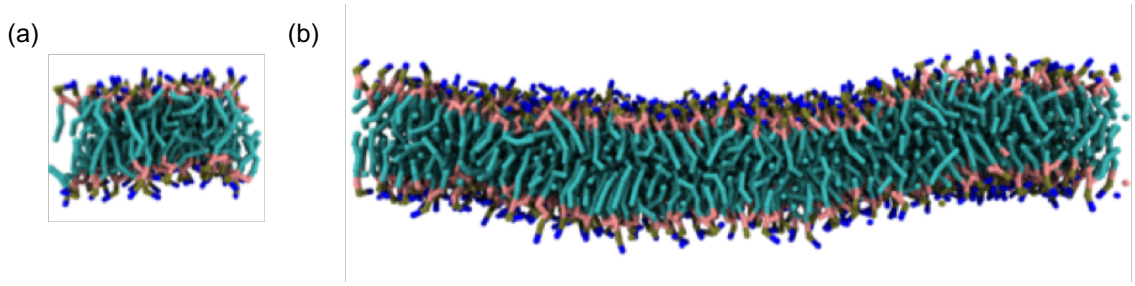

Figure 3.3: Membranes used in this study. Final simulation snapshot in xz-plane of planar lipid bilayer membranes after assembly and equilibration: (a) "confined," 128-lipid ($\sim 6.4x6.4$ nm) membrane and (b) a "modest," 2048-lipid ($\sim 26x26$ nm) membrane. The "modest" membrane shows significant large-scale out-of-plane deformations (undulations) at equilibrium.

fundamental groups, allowing controllability of size and shape via particle diameter and structure (in all cases here, maintaining a roughly spherical shape), surface chemistry via chemical group type, and softness via intra-particle bond stiffness (in all cases in the present study, set high for practical rigidity). In the simulation community, there are two main approaches to generic NP models: (1) single sites with varying excluded volume[60,83,84] and (2) building particles from particles.[33–38,42,44–47,49,49,51,52,85–88,88–91] We implement the latter method, due to its ease of incorporation into standard simulation packages (i.e. without toying with effective, longer-ranged interactions) and its practicality in incorporating intrinsic NP roughness. Figure 3.4 shows the two particle sizes used in this study. The procedure of building NPs out of 0.47 nm sites is for maximal consistency with the Dry Martini model. Above the infinitely smooth single-site 0.47 nm NPs, our procedure of building NPs from a simple cubic lattice generates designs of roughly constant surface roughness (R_{rms} of approximately 0.14 nm, based on the formula of Girasole et al.[92] and surface sites defined as those within approximately two molecular diameters of the circumscribed sphere).

Specifically, we develop a spectrum of chemical groups that mainly vary in their Lennard-Jones interaction between the NP and both the phospholipid heads and tails,

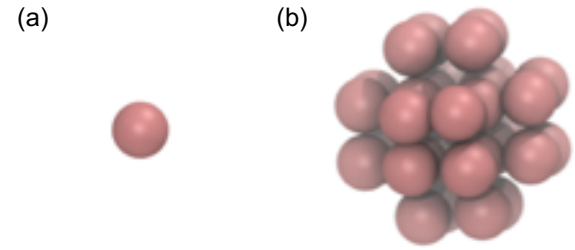

Figure 3.4: Particle constructs used in this study. Here, we study NP-membrane interactions at two particle sizes: (a) a "molecular-scale," single bead (0.47 nm in diameter) one and (b) a "nanoscale," 32-bead (1.88 in diameter) one cut from a simple cubic lattice. "Nanoscale" NPs are kept rigid through the use of intraparticle bonds of stiffness 1250 kJ/mol-nm^2 and equilibrium bond length 0.47 nm (the molecular diameter) for nearest neighbors; diagonal bonds are included for even further stiffness. Intraparticle nonbonded interactions are turned off.

defined as the choline $(NC3)^+$ functional group (Dry Martini $Q0^+$ group) and acyl chains (Dry Martini C1 group), respectively. Table 3.1 and Figure 3.5, panel (a), summarize the NP chemical groups and their interaction parameters implemented in this study. The three general classes of NP surface chemistries are thus "hydrophobic" (strong attraction to lipid tail groups and weak attraction otherwise), "hydrophilic" (weak attraction to both lipid head and tail groups), and "interfacially active" (an extension of the Dry Martini hydrophilic species, but with enhanced attraction specifically to lipid head groups that effectively mimics opposite-charge electrostatics or even ligand-receptor interactions). This simplistic picture of NP surface chemistry is not meant to explicitly connect to specific molecular species, yet spans the relevant range of groups so as to capture basic chemistry-mediated aspects of NP-membrane interactions. All molecular diameters in this case are set at 0.47 nm, and remaining epsilons and sigmas for the NP and membrane models can be found by referencing the Dry Martini force field.[74]

3.3.3 Simulation setup and details

In all MD simulations here and in this thesis, we use the fast and open-source GROMACS 4.6.5 package.[93] Membranes are initially templated into a starting planar lipid bilayer via the *insane.py* algorithm.[94] The bilayer is assembled in a periodic box in the xy-plane, and the transverse (z) direction is set to be approximately equal to the other dimensions. This is followed by 500 steps of steepest descent energy minimization to remove bad contacts, and a 30 ns NPT (constant number of particles, pressure, and temperature) simulation using the Berendsen thermostat at the target temperature and Berendsen isotropic barostat at 0.0 bar. This procedure ensures an equilibrated bilayer at the start of the membrane and NP-membrane production runs during which data is gathered. NPs in this study are combined with an equilibrated membrane at a fixed starting z-separation (5 nm for 0.47 nm NPs and typically 10 nm for 1.88 nm NPs) and first simulated using unbiased MD in the $NP_z\gamma T$ (constant number of particles, transverse pressure, tension, and temperature) ensemble (the "multiphase" ensemble) for 100 ns to observe, if possible, any spontaneous or mildly activated interaction modes and mechanisms.

Simulations are performed with a time step of 0.04 ps, saving every 2500 steps (100 ps). Nonbonded interactions (Lennard-Jones and Coulombic) are shifted and truncated from 0.9 to 1.2 nm and 0.0 to 1.2 nm, respectively. For Coulombic interactions, a relative permittivity of 15 is used. Temperatures are maintained at 341 K, well above the gel-to-liquid phase transition temperature, to ensure a fluid phase bilayer. Temperature control is managed by a Langevin thermostat with a time constant of 25.0 ps, which sets the drag coefficient. In the limit that the friction forces change much more than the systematic PMF forces do, Langevin dynamics reduces to overdamped/Brownian dynamics.[95] With the intuition that liposomes and real cell membranes in water are

characterized by low to negligible tension,[96] here we use semiisotropic pressure coupling where in-plane and out-of-plane pressures are set to be equal, thus enforcing a tensionless condition via $\gamma = \frac{L_z}{2}\left(P_z - \frac{(P_x+P_y)}{2}\right)$,[97] where L_z is the transverse box length, P_z is the transverse pressure (zz normal component of the pressure tensor), and P_x and P_y are the lateral pressures (controlled jointly by the barostat). In accordance with the Dry Martini prescription, the lateral and transverse pressures ($P_{xy} \equiv \frac{(P_x+P_y)}{2}$ and P_z) are independently set to 0 bar. We use a Parrinello-Rahman barostat with a lateral and transverse compressibilities of 3x10^{-4} and 0 bar^{-1} and a time constant of 8.0 ps for both xy and z. To prevent drift, the center of mass motion of the entire system is removed after every frame.

We also use umbrella sampling to facilitate the exploration of states along the particle permeation reaction coordinate and to determine free energy and diffusivity profiles to high accuracy.

3.3.4 Advanced sampling and free energies

To systematically sample the full NP-membrane reaction coordinate, we use umbrella sampling.[98] Briefly, this approach biases the system through use of a harmonic restraint on the collective variable defined as the particle-bilayer center-of-mass separation $\Delta z_+ \equiv \bar{z}_{NP} - \bar{z}_{mem}$ (the "global displacement"), where $\bar{z}_{NP}$ is the center of mass z-coordinate of the NP, while $\bar{z}_{mem}$ is that of the entire membrane (calculated using all lipid sites). This metric is more precise than the generic z used in the ISD model, and accounts for the NP position relative to the membrane. For a given NP-membrane system, a set of simulations ("umbrellas") are performed for different set point values of Δz_+. In all cases, a constant-velocity pulling scheme (i.e. steered MD) is used to set up initial configurations for umbrella sampling, pulling in the z-direction at a rate of 0.01 nm/ps and with a spring

constant of 1000 kJ/mol-nm^2. Configurations are saved every 10 ps (0.1 nm), and a subset of these configurations are then equilibrated and sampled for equilibrium free energies.

The umbrellas are then combined and "reweighted" to produce unbiased properties and free energies with the Multistate Bennett Acceptance Ratio algorithm, specifically using the pymbar package.[99] PMFs are determined by default along Δz_+, the coordinate used for umbrella sampling, but also for physically-motivated coordinates related to the local membrane environment and particle-membrane coordination.

We note that several other advanced sampling strategies have been leveraged for studies of NP-membrane interactions, including constrained MD, metadynamics, bias-exchange metadynamics, the oscillating forward-reverse method, the adaptive biasing force algorithm, and multiple-walker adaptive biasing force.[100] We use umbrella sampling for its accuracy, robustness, and convenience in terms of both its establishment as a conventional tool in modern simulation packages and its theoretical correspondence to the Generalized Langevin Equation in a harmonic potential, which is used to determine position-dependent diffusivities.[100]

3.3.5 Diffusivity profile calculations

We determine diffusivity profiles from the very same set of umbrella sampling simulations as those used for the free energies, specifically via the Hummer positional autocorrelation extension of the Woolf-Roux estimator:[101]

$$D(\Delta z_+) = \frac{\left\langle \delta z_+^2 \right\rangle^2}{\int_0^\infty \left\langle \delta z_+(t)\delta z_+(0) \right\rangle dt} \tag{3.3}$$

where $\delta z_+ \equiv \Delta z_+ - \left\langle \Delta z_+ \right\rangle$ is the global displacement fluctuation about the umbrella mean value and t is the lag time. This expression works well for a stiff spring for the

umbrella biasing, such that the remaining forces act as a thermal bath for the solute translational motion.[100] The bulk of the calculation involves production of the positional correlation function in the equation denominator which, depending on the umbrella positions in the global displacement coordinate, can decay over several different orders of magnitude in time. Following the convention of Lee et al.,[100] integrals of the positional correlation function were cut off when the function drops to 5% its original value at t=0. The full diffusivity profile is interpolated using the individual umbrella results at intervals equal to the those of the PMF.

3.3.6 Resistivity, total resistance, and permeability calculations

Resistivity profiles are determined by linearly interpolating diffusivity profiles at the positions corresponding to the closer-spaced PMF outputs from the Multistate Bennett Acceptance Ratio algorithm, then combining the diffusivity profile and PMF information via:

$$\mathbb{R}(z_+) = \frac{e^{G(z_+)}}{D(z_+)} \tag{3.4}$$

where $\mathbb{R}$ is the local resistance (resistance per unit length). When integrated over the entire membrane domain, $\mathbb{R}$ equals the overall resistance R as defined in Equation 3.2.

3.3.7 Partition coefficient and permeability calculations

The membrane partition coefficient is an important experimental quantity closely tied to the PMF. In simulation, a size-independent metric characterizing favorable or unfavorable membrane interaction is determined by the equilibrium equation for concentrations

within and outside of the membrane:

$$K^{c,c} \equiv \frac{C_i^I}{C_i^{II}} \tag{3.5}$$

where $K^{c,c}$ is the size-independent partition coefficient, C_i is the solute (NP) concentration, I refers to the membrane phase, and II refers to the solvent (water) phase. If the PMF is flat outside the membrane, the partition coefficient can be defined as:[102]

$$K^{c,c} \equiv K \equiv \frac{1}{L_I} \int exp(-\beta G(\Delta z_+)) d\Delta z_+ \tag{3.6}$$

where L_I is the transverse length scale of the membrane. Thus, $logK > 0$ indicates a membrane-favorable NP, while $logK < 0$ indicates a membrane-unfavorable one.

3.4 Results and Discussion

3.4.1 The ISD model correctly predicts < 0.5 nm NP permeability

For molecular-scale, 0.47 nm NPs with a conventional 128-lipid (approximately 6.4 by 6.4 nm) simulation-scale membrane model, it is expected that nondisruptive simple diffusion is the main interaction mechanism and the solubility-diffusion models should apply. As the full spectrum of membrane partitioning states is inaccessible via unbiased MD simulations for most chemistries at this NP size, we use umbrella sampling to bias the system along various positions of the particle-bilayer center-of-mass separation $\Delta z_+ \equiv \overline{z}_{NP} - \overline{z}_{mem}$ (the "global displacement"), where $\overline{z}_{NP}$ is the center of mass z-coordinate of the NP, while $\overline{z}_{mem}$ is that of the entire membrane (calculated using all lipid sites). This metric is more precise than the generic z used in the ISD model, and

accounts for the NP position relative to the membrane. Figure 3.5 presents PMFs for different particle chemistries, while Table 3.1 summarizes their most important features; in all cases, they look similar to small molecule transport studies, as expected due to the small particle size.

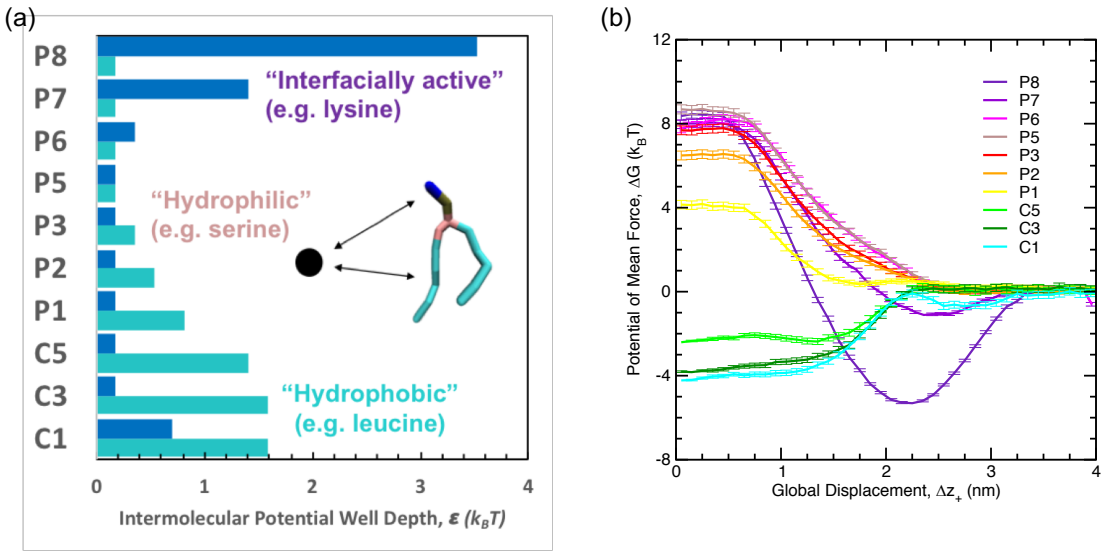

Figure 3.5: Transmembrane PMFs for spectrum of NP chemistries at 0.47 nm size. (a) Particle chemistries in our molecular model (b) PMFs were determined by umbrella sampling along the global displacement coordinate in the half space of the membrane–solvent system, assuming PMF symmetry. Free energies for these molecular-scale solute permeation processes vary on the order of thermal fluctuations or more, with the PMF shape ultimately determined by the particle chemistry.

Table 3.1: Summary of 0.47 nm NP PMFs computed in this work in comparison to prior efforts. Small-scale NP results from this study (gray) are compared with amino acid side chain analogs in a POPC bilayer/water system and others (all converted to k_BT at 341 K, the temperature of this study). All standard Dry Martini bead types serve as single-particle proxies for the common organic solvents reported in parentheses, and Lennard-Jones intermolecular potential well depths with lipid head and tail groups are reported for the species in the customized NP force field. PMFs in the upper portion of the table are ordered roughly by free energy change to the membrane interface, while those in the lower portion are ordered by their free energy change to the membrane center. *DOPC bilayer[103] [a]Residue charged at this location [b]Residue neutral at this location [#]DPPC bilayer[104]

Chemistry (proxy for)	**Chemistry type**	ϵ_{PH} (k_BT)	ϵ_{PT} (k_BT)	ΔG **to interface** (k_BT)	ΔG **to center** (k_BT)
LYS*	charged (+)	–	–	-8.3[a]	8.9[b]
P8	interfacially active	3.53	0.176	-5.3	8.4
THR*	polar	–	–	-1.9	6.2
P7	interfacially active	1.41	0.176	-1	8

SER*	polar	–	–	-0.3	7
P6	interfacially active	0.353	0.176	0.6	7.8
P5 (acetamide)	polar	0.176	0.176	0.8	8.7
P3 (acetic acid)	polar	0.176	0.353	0.6	7.7
P2 (ethanol)	polar	0.176	0.529	0.6	6.5
P1 (propanol)	polar	0.176	0.811	0.5	4.1
Methanol[#]	polar	–	–	–	8.1
Benzene[#]	aromatic	–	–	–	-1.7
Ethane[#]	nonpolar	–	–	–	-2
C5 (methylethylsulfide)	nonpolar	0.176	1.41	0.1	-2.4
ALA*	nonpolar	–	–	-3	-3.7
C3 (chloropropane)	nonpolar	0.176	1.59	0.1	-3.8
C1 (butane)	nonpolar	0.705	1.59	-0.1	-4.2
PHE*	aromatic	–	–	-6.6	-5.7
VAL*	nonpolar	–	–	-5.4	-6.1

Hydrophobic (C1 through C5) NPs show a relatively monotonic drop in free energy upon entry into the membrane tail group region (core), with a well depth ranging from about 2.5 to 4 k_BT, indicating spontaneous partitioning into the membrane. The C3 and C5 PMFs are qualitatively similar to some small hydrophobes and aliphatic amino acid side chain analogs such as 1,3,5-trichlorobenzene and alanine.[105] One minor nuance is a preliminary shallow well for the C1 NP system at the membrane head group region (interface), due to the attenuated head group attraction for the C1 chemistry in the

Dry Martini model. The PMF barrier, here resulting mainly from the diminished C1 NP-lipid interactions between the head and tail group regions, is also common for small hydrophobes, aliphatics, and aromatics like ethane, hexane and benzene.[104,106,107] In this sense, the C1 chemistry behaves like an aromatic or van der Waals-dominated molecule.

Hydrophilic (P1 through P5) NPs show a monotonic rise in free energy, with a barrier at $\Delta z_+ = 0$ ranging from about 4 to 8 k_BT. These PMFs are typical of small hydrophilic molecules. In addition to a central barrier of more or less equal height to the hydrophilic P5 case, the interfacially active (P6 through P8) NPs also show a free energy minimum at the membrane interface ($\Delta z_+ \sim 2.25$ nm), with a depth ranging from about 0 to 5.5 k_BT, indicating spontaneous adsorption onto the membrane. The qualitative shape of the interfacially active PMFs is prevalent amongst amphiphilic small molecule drugs.[105] One difference between our interfacially active NPs and amphiphiles, however, involves the positions of the PMF features–most amphiphiles situate themselves inside the head group interface to favorably interact with both the head and tail groups, while the P6 through P8 chemistries here have a specific affinity to the choline headgroup, and therefore act effectively as an ion (e.g. amino acid side chain analog like lysine). In Table 3.1, we show that this latter comparison is also quantitatively reasonable, along with other amino acid side chain analogies to the NP chemistries studied here.

Figure 3.6 shows, for all 0.47 nm NP systems, the diffusivity profiles as well as the combined thermodynamic and dynamical information via the local resistance profile. Diffusivity profiles (panel (a)) typically show a one to two order of magnitude decrease in diffusivity upon membrane penetration, from $\sim 10^{-4}$ cm^2/s to around 10^{-6} to 10^{-5} cm^2/s. We find that NP chemistry does not play a statistically significant role in dynamics at this NP (and membrane) length scale. Local resistance profiles (panel (b)) show that the hydrophobic NPs are able to maintain a very low local resistance across the entire global displacement coordinate despite perturbed diffusivities inside the membrane,

primarily due to their thermodynamic propensity for membrane insertion (Figure 3.5, panel (b)). Hydrophilic NPs experience a dramatic (approximately five order of magnitude) increase in resistance upon insertion, both dynamically- and thermodynamically-mediated (i.e. by both $D(\Delta z_+)$ and $G(\Delta z_+)$), and interfacially active NPs additionally show a thermodynamically-mediated drop in local resistance at the membrane interface.

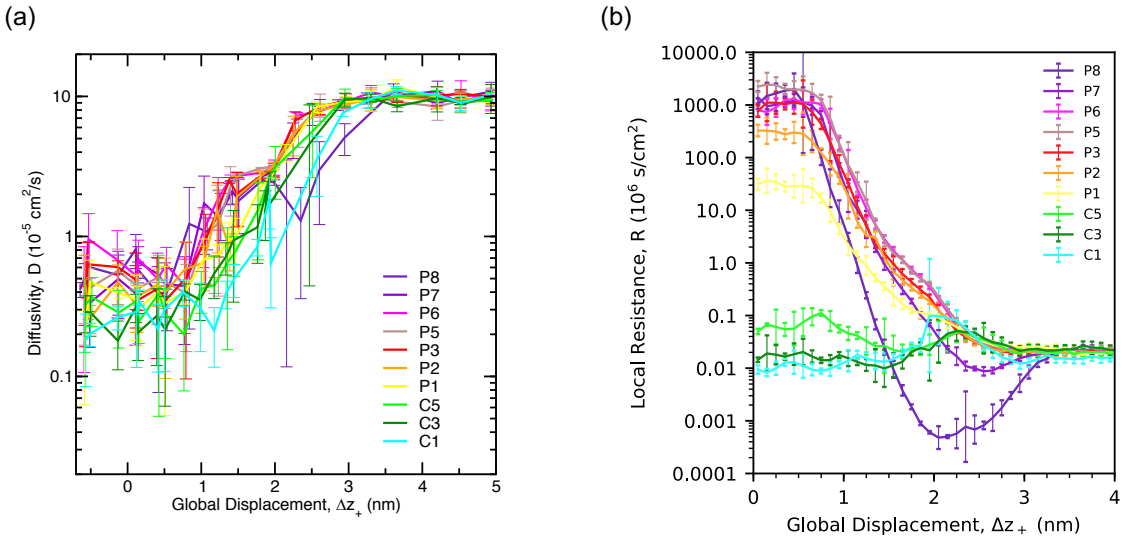

Figure 3.6: Transmembrane diffusivity and local resistance profiles for spectrum of NP chemistries at 0.47 nm size. (a) Diffusivity profiles were calculated via Equation 3.3 and (b) local resistance profiles via Equation 3.4 along the global displacement coordinate in the half space of the membrane-solvent system. Diffusivities drop one to two orders of magnitude upon membrane penetration, and profiles are relatively insensitive to NP chemistry. While small nonpolar NPs maintain a fairly low resistance across the entire membrane, polar NPs experience a several orders of magnitude increase upon membrane penetration, and interfacially active NPs additionally experience lower resistance at the interface.

Free energy and resistivity information is further reflected in the partition coefficient K (Figure 3.7) and permeability P (Figure 3.8). Practically for the partition coefficient, the right-hand-side expression in Equation 3.6 depends largely on the integral cutoff. The integral cutoff, and therefore also L_I, is here chosen to be that which corresponds

to a convergence of K after capturing the interfacially adsorbed states relevant to the P8 through P6 NPs. Based on this criterion and the notable leveling of all cumulative integrals chemistry-wide, L_I was uniformly set to 3.5 nm (Figure 3.7). Values are positive for the hydrophobic and interfacially active particles, indicating favorable membrane interactions, and negative for hydrophilic particles, indicating unfavorable membrane interactions.

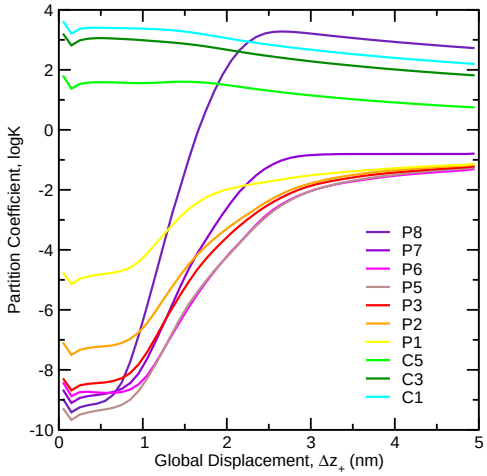

Figure 3.7: Partition coefficient cumulative integral profiles across global displacement coordinate for 0.47 nm NPs. Profiles are cut off at 3.5 nm, where all appear to level off. The cutoff is essentially set at the membrane interface, leaving the region below the cutoff to define the "homogeneous membrane slab" assumed in the Meyer-Overton Rule.

Figure 3.8 plots P against K for the 0.47 nm NPs studied here as well as for solutes of similar size in experiment. The Overton's Rule prediction, shown as the orange line, uses the average membrane diffusivity of the 0.47 nm NPs in the implicit solvent coarse-grained model; as such, it provides a comparison principally for the simulation predictions based on the ISD model. In general, Figure 3.8 shows that, the more membrane favorable (the higher the K), the faster the membrane transport (the higher the P), but also that

the relationship is more complicated than Overton's Rule. Quantitatively, Overton's Rule predicts permeability for the hydrophobic NPs within an order of magnitude, but it significantly errs for the hydrophilic and interfacially active NPs. The higher sensitivity of P to K for the hydrophilic NPs is consistent with other findings and attributable to the rising free energy barrier to permeation.[68] However, while P may be single-valued along K for a range of hydrophobes and hydrophiles, for the NP set here, it is multi-valued due to the inherent degeneracy of "membrane-favorable" NPs–the truly hydrophobic (C5 through C1) particles with a high affinity to the membrane core region and the interfacially active (P8 through P6) ones with a high affinity to the interface. Despite the net favorable membrane interaction of interfacially active NPs, their major contribution to the resistance comes from the membrane core region, driving their permeabilities to be lower than the hydrophobes and between three and five orders of magnitude lower than the Overton prediction. Overton's Rule (and even generalizations based on the ISD model[108]) cannot capture these types of degeneracies in permeability with the partition coefficient.

The failure of the experimental data sets in Figure 3.8 to map to linear trends of their own, which would be expected for similarly-sized solutes, shows that Overton's Rule is overly simplified for these studies as well. Interestingly, experimental acetamide and acetic acid permeabilities lie within about one order of magnitude of their Dry Martini proxies P5 and P3, respectively. In general, however, the experimental permeabilities in Figure 3.8 should not be quantitatively compared with the Overton or ISD permeabilities from this study. One reason is that the implicit solvent coarse-grained model dynamics are inherently faster relative to atomistic simulations, and thus are not necessarily an accurate representation of experimental dynamics. There is also potential for errors in the experimental measurements: the lag time in solute transport from the donor to receiver compartment often leads to experimental underestimates relative to the steady-state

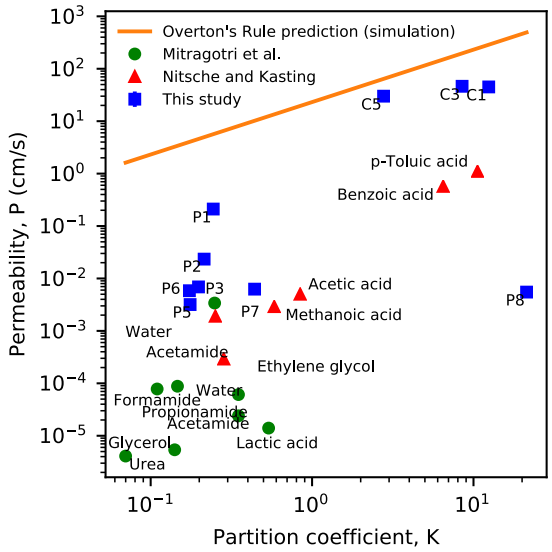

Figure 3.8: Experimental and simulation analysis of the ISD model and Overton's Rule for approximately 0.47 nm NPs. Small-scale NP permeability results from this study (blue squares), implementing the ISD model, are compared with compilations of lecithin vesicle experiments (Mitragotri et al.,[109] green circles, and Nitsche and Kasting,[75] red triangles). Overton's prediction (orange line), using the average particle diffusivity inside the membrane across all chemistries and a membrane thickness of 4.35 nm, is shown to be overly simplified by overpredicting all ISD permeabilities and by not distinguishing interfacially active NPs from hydrophobic ones.

permeability value. This effect has been underscored in recent studies,[110,111] and can be particularly pathological for solutes with favorable membrane interactions, for which the membrane acts not as a barrier but as a sink. As a result, simulation values can generally lie orders of magnitude higher than those from experiment. Lastly, compounds of similar K should still be compared with caution, as this metric can attain similar values for solutes that interact favorably with the membrane in distinctly different regions (in the head or tail group region or between the two, as in the case of P8, C1, and benzoic acid, respectively).

We further confirm ISD model validity by probing its assumptions. To confirm classical diffusion, we follow the prescription of previous approaches,[106] calculating the free energy change traversed over a correlation distance of the NP. We find that, while the NPs and regions with the highest free energy slopes may traverse up to $\sim$1.5 k_BT in the most extreme cases (i.e. P8 around Δz_+ =1.25 nm), for most others, the result is well below thermal fluctuations, in general validating classical diffusion and the ISD free energy and diffusivity mappings onto Δz_+. In terms of the stiff spring assumption (permitting use of Eqn. 3.3), our results show that an order of magnitude increase in spring stiffness generally has less than an order of magnitude effect on diffusivities (Figure 3.9). Diffusivities have only a linear effect on the ISD model while free energy effects are exponential. The use of umbrella restraints in the first place leads to only about a factor of three reduction of the NP diffusivity at far separation ($\Delta z_+ \sim$5 nm) relative to the bulk NP diffusivity ($\sim$ $2.9x10^{-4}$ cm^2/s, calculated from the particle mean-squared displacement in bulk solution). While the Langevin thermostat here could destroy long-range spatiotemporal correlations necessary for observation of anomalous diffusion,[73] improved hydrodynamics thermostats could be coupled with Dry Martini in a more rigorous future study.[112]

In terms of mechanism, we show for the 0.47 nm NP systems no statistically significantly variations in membrane shape upon NP-membrane interaction–the membrane, on average,

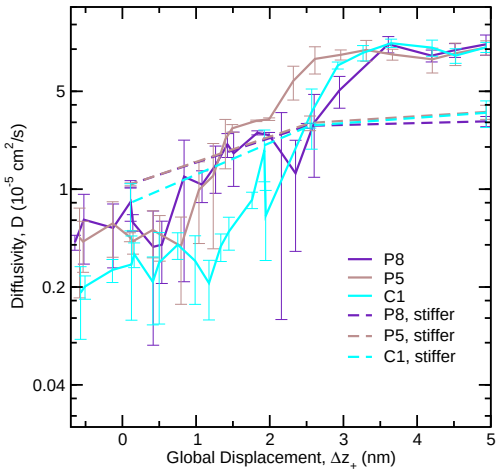

Figure 3.9: Stiff spring check for 0.47 nm NP dynamics. For the 0.47 nm P8, P5, and C1 systems, the biasing potential stiffness was increased at sample points by one order of magnitude. The observed effect was less than an order of magnitude effect on the resulting diffusivities, resulting in minimal consequences for ISD permeability predictions.

is always flat. While the implicit solvent coarse-grained model limits the observation of behaviors like explicit hydration and dehydration and the facilitation of membrane transport by water wires,[25] there should otherwise be no hindrance to the observation of alternative mechanisms, including those involving membrane deformations or defects.

To summarize, in the study of 0.47 nm NPs, we find for a comprehensive range of single-site spherical particle surface chemistries that (1) nondisruptive simple diffusion is an appropriate model for the membrane transport mechanism, (2) the ISD model is both practical and valid as a transport model for detailed molecular simulations, and (3) Overton's Rule is overly-simplified. These findings are robust across the range of NP chemistries studied. Nondisruptive simple diffusion appears to be reasonable because the membrane is undisturbed in terms of global and local shape and internal coordinates are absent for single-bead NPs. Confirmation of the ISD model is provided through

semi-quantitative experimental comparison as well as evaluation of the classical diffusion assumption. A major reason the classical diffusion assumption holds is precisely because NP permeation, for all chemistries, is effectively nondisruptive to the membrane and devoid of internal degrees of freedom. Because Overton's Rule neglects in particular the influence of the membrane interfacial region and its relevance to solutes like amphiphiles, it does not quantitatively capture the permeability dependence on chemistry, even at this small NP size.

3.4.2 The ISD model breaks down for NPs > 0.5 nm due to membrane deformations

To study the sensitivity of nondisruptive simple diffusion and the ISD model to larger NP sizes, we consider NPs with diameters four times larger (1.88 nm) for three surface chemistries: P8, P5, and C1. At this scale, P8 NPs are analogous in chemistry to charged monolayer-protected gold and P5 to silica or some equivalent. C1 NPs, at this size, are fullerene-like, due to their membrane partitioning through strong van der Waals interaction. To accommodate these larger NPs, we use a 2048-lipid, approximately 26 by 26 nm bilayer. We note that this system scale-up leads to about a three order of magnitude increase in computing time, and proper sampling for these systems will lead to a further time increase. This reality prevents the immediate operation of simulations in high-throughput (as before, for a variety of NP designs). We find in preliminary unbiased MD simulations that the C1 NP rapidly and symmetrically inserts into the membrane core, while the P8 NP rapidly adsorbs with significant local deformation of the membrane interface and the P5 does not appear to interact on any reasonable unbiased MD time scale.

In the calculation of global displacement PMFs relevant to the ISD model via umbrella

sampling, significant complications emerge. Figure 3.10 shows final snapshots from representative umbrellas that indicate systematic membrane out-of-plane deformations (undulations) along Δz_+. Undulations fall in two major categories: (1) protrusion for C1 and P8 NPs, where at intermediate particle-bilayer separations, the membrane deflects towards the particle due to the gain in NP-membrane interaction that outweighs bending, and (2) retraction for P5 and P8 NPs, where at low displacements, the membrane deflects away from the particle because the cost of bending is still more favorable than particle penetration. Both types of undulations have been observed in previous NP-membrane simulation studies,[70,113,114,114–117] and are part of the greater phenomenon of solute-interfacial coupling (defying the adiabatic assumption that permeation follows solely a displacement coordinate and the remaining coordinates act as a thermal bath).

Across the global displacement sampling coordinate, we track membrane deflection through the metric $z_+(r_c) \equiv \overline{z}_{PO_4}(r_{2D} < r_c) - \overline{z}_{PO_4}(r_{2D} \to \infty)$, which effectively calculates the local membrane height in the vicinity of the inserted or projected NP relative to the far-field value (at $r_{2D} \sim L/2$, where L is the box length). Here, we calculate $z_+(r_c)$ in real space and polar coordinates due to the small to intermediate membrane sizes implemented in this study, but note that other studies have used a Fourier mode of z_+[70,113] and also calculated the membrane mean curvature explicitly.[115] Figure 3.11, panel (a), shows the results of this analysis. At intermediate NP-membrane separations, protrusion for the hydrophobic and interfacially active NPs is manifested in a positive deflection for $z_+(r_c)$, and at close separations, retraction for the hydrophilic and interfacially active NPs is manifested in a negative deflection. Systematic correlations between the membrane undulations and global displacement show that the nondisuptive simple diffusion mechanism and ISD model break down.

Effectively, these undulations lead to significant deviations between the global displacement Δz_+ and a more locally-defined variant between the NP and a proximal membrane

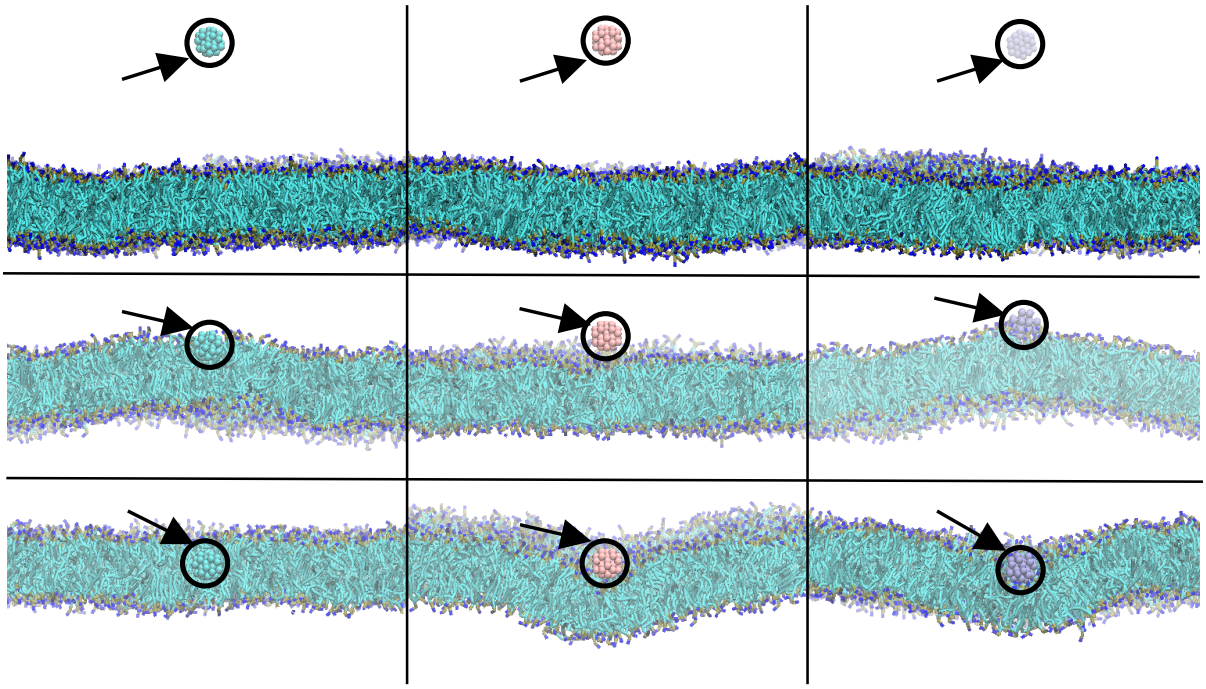

Figure 3.10: Final snapshots from representative umbrella sampling simulations of 1.88 nm NPs. Shown are the final configurations after 200 ns for the 1.88 nm (from left to right) C1, P5, and P8 particles and (from top to bottom) decreasing values of the NP-membrane global displacement set point (particles marked with black circles and arrows for clarity). For the C1 and P8 particles, the membrane protrudes towards the NP at intermediate separations, and for the P5 and P8 particles at close separation, the membrane retracts.

patch in the xy-plane: the local displacement $\Delta z_+(r_c) \equiv \overline{z}_{NP} - \overline{z}_{PO_4}(r_{2D} < r_c)$, where $\overline{z}_{PO_4}$ is the average height of the lipid phosphate groups, r_{2D} is the radial in-plane distance from the inserted or projected NP center, and r_c is some radial cutoff (set to 1.5 nm for resolution of the local membrane environment but also for sufficient lipid statistics). Figure 3.11, panel (b) shows the comparison for these two metrics, which are equivalent for a static, planar interface but can vary significantly for a fluctuating, deformable one. Off-diagonal contributions reflect protrusion and retraction when below and above the diagonal, respectively.

The global displacement PMFs are consequently a result of integrating the corresponding local displacement PMFs over the distribution of $\Delta z_+(r_c)$ values that satisfy a given Δz_+ constraint. This leads to physical tunneling through barriers and the smearing of the PMF from $\Delta z_+(r_c)$ to Δz_+ (Fig 3.11, panel (c)). Here, we find a barrierless PMF for the C1 case in both Δz_+ and $\Delta z_+(r_c)$; a surprisingly low barrier for the P5 case across Δz_+ with a steeper apparent PMF in $\Delta z_+(r_c)$; and the complete absence of intermediate and central barriers in the P8 case in Δz_+ that otherwise exist in $\Delta z_+(r_c)$. Some of these results have been found in several previous studies; for example, with hydrophilic solutes, undulations can lead to lower, narrower barriers, and with hydrophobic solutes, they can lead to shallower minima.[105,118] Because sampling was collected in the global displacement coordinate, local displacement sampling is poor in regions where protrusion and retraction are relevant.

Figure 3.11, panel (d) shows the correlation between undulations and global displacement for the 1.88 nm C1 NP system via the 2D ($\Delta z_+, z_+(r_c)$) PMF post-processed from the original umbrella sampling simulations in Δz_+. The blue curve tracks the minimum free energy pathway. The protrusion event appears as an abrupt transition, with $z_+(r_c)$ proceeding from rest ($\sim$0) to fully protruded ($\sim$2.3 nm) over the course of less than a 0.5 nm change in Δz_+. This result compares well with the deflection observed in a

similar study with a fullerene-sized (∼1.1 nm) C1 particle in explicit solvent, wherein the membrane deflects maximally at slightly less (∼1.4 nm) than observed here, and at lower displacement (3 nm vs. ∼4.5 nm here).[70] The main difference is that the larger NP here comes in contact with the membrane at a larger separation and contains a larger number of interaction sites with the membrane that can afford greater deflection. Retraction events for P5 and P8 are, by nature, more gradual, as the membrane can continuously deform while the particle is constrained at closer and closer separations (not shown).

The results here show qualitative agreement with self-consistent field theory studies that do not a priori assume the appropriate reaction coordinate. In the field theory studies, significant out-of-plane deformations including NP-induced membrane pre-pore, pore, and stalk formation are observed. Because these studies use the string method, the results are in fact more general, and rigorously determine minimum free energy pathways between the non-interacting and symmetrically inserted states (and therefore, presumably, the mechanism for transport).[65,66] These studies also show free energy discontinuities in translational ($\overline{z}_{NP}$) PMFs.

Yet solute-interfacial coupling can also lead to dynamical effects that may falsely suggest that the ISD model applies. Dynamical effects are relevant if the undulation timescale is comparable to or slower than motion along Δz_+.[113] By overlaying undulation-displacement PMFs with a sample 100 ns unbiased MD trajectory of the corresponding NP-membrane system in red (Fig. 3.11, panel (d)), we see that the membrane insertion of the C1 NP deviates from the expected minimum free energy pathway in blue. The membrane protrudes to only about 1/3 of its maximum value from the umbrella sampling simulations. While the free energy landscape of this dynamical pathway is not entirely sampled, the pathway presumably crosses a higher free energy barrier than the minimum free energy one.[113] Dynamic effects were also observed for P8 NP adsorption (not shown). These results can deceptively lead to the perception that the pathway maps to Δz_+ alone

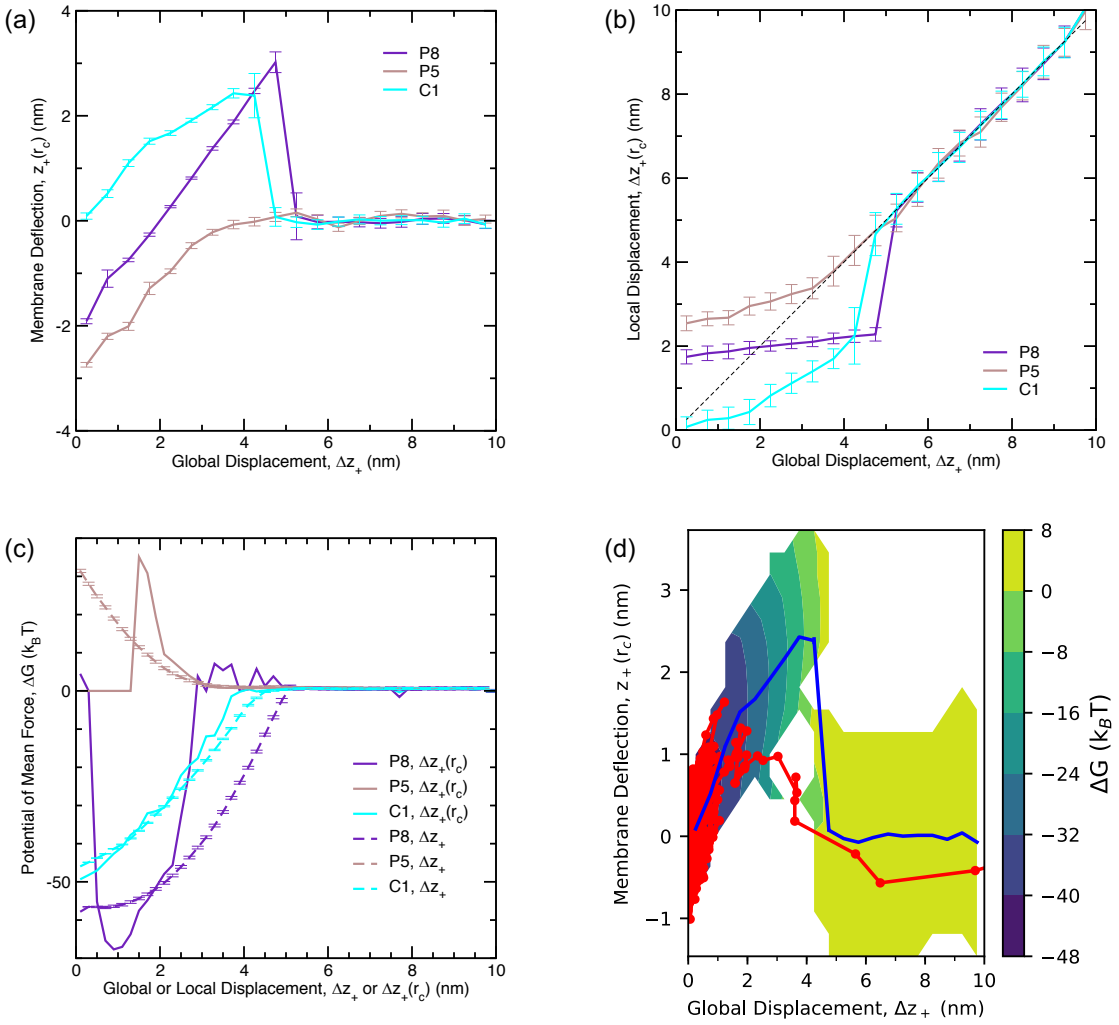

Figure 3.11: Correlations between undulations and displacement for 1.88 nm NPs. For 1.88 nm interfacially active, hydrophilic, and hydrophobic NPs, (a) deviations between global displacement Δz_+ and local displacement $\Delta z_+(r_c)$ demonstrate protrusion and retraction events that lead to (b) smearing of $\Delta z_+(r_c)$ PMFs to generate those in Δz_+. (c) The 2D free energy projection into global displacement (x-axis) and membrane deflection (y-axis) for the 1.88 nm hydrophobic NP shows that processes like membrane insertion may still dynamically deviate (red) from the minimum free energy pathway (blue).

and the ISD model applies; in reality, however, this is a cancellation of nonadiabatic and dynamic errors.

In a last attempt to study the ISD model, we artificially restrain the membrane to eliminate membrane undulations and improve sampling along Δz_+. We follow the prescription of Kopelevich, imposing out-of-plane (z-directional) harmonic restraints on the individual lipids at their phosphate groups to ensure one macroscopic configuration for every Δz_+.[70] Figure 3.12 shows the Δz_+ PMFs resulting from this restrained membrane umbrella sampling scheme, compared with the original unrestrained membrane results. Restraints on the membrane result in an apparently more stable symmetric insertion for the C1 NP ($\sim$-75 k_BT compared to -45 k_BT), consistent with a reduction in PMF smearing across a spectrum of membrane configurations, and also possibly a suppressed entropic penalty for NP insertion. Restraints also result in a much higher barrier for the P5 NP ($\sim$80 k_BT compared to 30 k_BT) due to NP penetration rather than membrane retraction as before. The PMF for the P8 NP shows both a well and a barrier, with the former much shallower than the unrestrained membrane case ($>$ -20 k_BT compared to $\sim$-60 k_BT) and the latter much higher than the restrained membrane P5 case ($\sim$130 k_BT). This PMF suggests (1) that the membrane restraints frustrate P8 NP adsorption and do not capture the corresponding stable state and (2) that the membrane even defies the lipid restraints upon NP penetration. Indeed, we find in the latter case that the lipids are attempting to make contact with the NP via their head groups (not shown). This result further suggests that particle-mediated pore transport may be the most viable mechanistic pathway for 1.88 nm interfacially active and even hydrophilic NP transport (in agreement with the field theory studies[65,66]), but that the mechanism requires substantial activation, as previously suspected.

The use of membrane restraints has several limitations that prevent direct validation of the ISD model. With membrane restraints, the resulting Δz_+ sampling coordinate

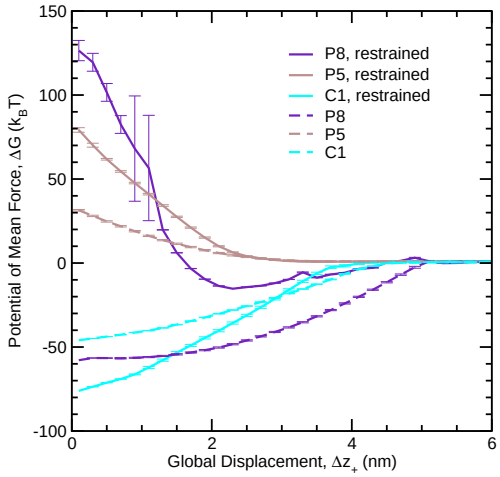

Figure 3.12: "Transmembrane" PMFs from restrained membrane umbrella sampling simulations of 1.88 nm NPs. Displayed are PMFs with and without position restraints on the membrane lipids. The use of membrane restraints reveals otherwise hidden barriers and the unfavorability of nondisruptive simple diffusion for the P8 and P5 particles, while also more clearly capturing the symmetrically inserted stable state for the C1 NP.

is artificial, and not guaranteed to be a mechanistically-relevant reaction coordinate. This is particularly obvious in the event that protrusion is physically relevant and if the NP is prone to induce deformations in the membrane leaflets upon insertion or in the bilayer as a whole upon adsorption.[105] Even with membrane restraints, one notable slow degree of freedom that remains is NP orientation. We find that, despite the particles' 90-degree rotational symmetry, they do not properly exchange between equivalent states, especially inside the membrane; this prevents convergence of the global displacement PMF. Furthermore, the use of position restraints has energetic and entropic consequences for the natural, unbiased physics, including the suppression of membrane fluctuations and therefore smaller entropic driving forces across the interaction states. Indeed, we find that the position restraints are doing significant work to hold the lipids in place. Lastly, the restraining procedure does not even guarantee capturing the unbiased stable states of interaction. In fact, some lipid out-of-plane deformation might be most favorable for C1 symmetric insertion in the unrestrained and unbiased system, and as seen with P8, restraints can prevent full adsorption.

These results are intrinsically coupled with membrane size. Here, we study two sizes of membranes–one "modest-sized", and one "confined." It is well known that the membrane scale-up process inherently reduces the membrane bending modulus (via membrane "softening")[119] and permits larger membrane deformations. In fact, we also observe retraction and protrusion phenomena for the 0.47 nm NP systems upon membrane scale-up. There are two major reasons why simulating larger membranes is generally better. First, recent simulations have reported that the membrane must be large enough to accommodate the necessary distortions for solute penetration. A $6x6$ nm membrane, while practically expedient in simulation, may suppress these distortions.[67] Second, the target experimental system is typically a macroscopic lipid bilayer. In biological membranes, cytoskeleton pinning points dictate an experimentally relevant length scale

of 100 to 500 nm,[120,121] beyond which the membrane is effectively periodic. While the larger membrane sizes in this study (∼26 nm) are more reasonable than most, results can be further extrapolated to experiments via adjustments in the bending modulus and range of permissible undulations. To the authors' knowledge, this is the first instance of providing a system size recommendation for simulations of NP-membrane interactions.

In the study of 1.88 nm NPs with modest-sized membranes, we find that both nondisruptive simple diffusion as a mechanistic picture and the ISD model for kinetic permeabilities break down. The key evidence for the breakdown is provided by the solute-interfacial coupling, wherein $z_+(r_c)$ systematically varies with Δz_+. Significant deformations are required by the membrane, both in direct insertion in the hydrophobic NP case and insertion into a bilayer pore, which is a likely approximant to the transport mechanism for the hydrophilic and interfacially active NP cases. At intermediate segments along the permeation pathway, the membrane may also protrude to meet the NP. The global displacement coordinate is generally not a good one for mechanistic interpretation. We have shown that this coordinate is size-dependent and degenerate, and self-consistent field theory studies have shown that translational (specifically, $\overline{z}_{NP}$) PMFs can vary discontinuously across the permeation pathway.[65] For this scale of NPs, permeability predictions made with the ISD model will likely lead to overpredictions due to tunneling and therefore lower apparent free energy barriers relative to the minimum free energy pathways.[70] On a practical note, comparably slow or slower degrees of freedom like membrane deformation modes and NP orientation can lead to unreasonably slow free energy convergence, and possibly even dynamical deviations from the undetermined kinetic pathways that can additionally increase apparent free energy barriers and can therefore appear to close the gap in permeability predictions.[113] However, it is generally not the case that the restraining method of Kopelevich will apply.

Based on these results, we recommend that studies evaluating the ISD model and Δz_+

projection techniques a priori for NPs 2 nm and above be revisited. Recent studies have implemented the ISD model for NPs much larger than C60 fullerenes (up to 6 nm) that significantly disrupt membranes and even induce undulations upon insertion. Resulting permeability estimates, ranging from 10^{-15} to 1 cm/s and that are not currently amenable to experimental comparison, are thus questionable.[114,117] Another study even uses free energy barriers and transition state theory estimates for absolute kinetic rate constants.[122] Transition state theory is often insufficient for NP-membrane interactions because it assumes classical and adiabatic dynamics as well as no recrossing of the transition state when recrossing may be relevant and velocities may even be undefined.[95] For proper kinetic (mechanistic and rate) insights from simulations, more rigorous techniques and alternative reaction coordinates are required.

3.4.3 Better coordinates may exist for > 0.5 nm NP-membrane interactions

If nondisruptive simple diffusion is not the mechanism and ISD model is not applicable, then what is? In the pursuit of physically-motivated reaction coordinates to add intuition to the more aphysical "string" coordinates in other work, we simply examine a few alternatives to displacement and membrane shape through post-processing the same simulation data from the unrestrained membrane umbrella sampling simulations. We can define coordination metrics N_1 and N_2 for the membrane with the upper and lower hemisphere of the NP (above the below the NP centroid), respectively. We can then define a total coordination number $N_+ \equiv N_1 + N_2$ and coordination number asymmetry $N_- \equiv N_1 - N_2$. We define coordination metrics N_+^{head} and N_-^{head} specifically for NP interactions with the lipid head groups and N_+^{tail} and N_-^{tail} for the tail groups. The use of coordination metrics is inspired by the work of Ghaemi et al.[71] and Van Lehn et al.[43]

The latter showed through usage of a lipid tail-water coordination number metric that the membrane insertion of $D_p \sim d$ NPs is an activated event involving spontaneous lipid out-of-plane fluctuations into the solvent and interacting with the NP. NP-tail group interactions are thus hypothesized to be crucial to the description of hydrophobic NP insertion, while head group interactions could describe interfacially active NP adsorption.

Figure 3.13 shows via a 2D PMF and dynamical trajectory for the 1.88 nm C1 NP system that N_+^{tail} and N_-^{tail} together connect reactant and product basins with a potentially relevant pathway for NP-membrane insertion. For a NP starting above the membrane, the interaction proceeds as follows: (1) initial interaction, resulting in $N_+ > 0$ and $N_- < 0$ due to preferential coordination of the particle lower hemisphere and (2) progression to the symmetrically inserted stable state, resulting in a further increase in N_+ and an increase in N_- towards 0. For completion of membrane transport, the system completes a diamond shape in (N_+, N_-) space through (3) a decrease in N_+ and a further increase in N_- and, finally, (4) a further decrease in N_+ and a decrease in N_-. The PMF also elucidates a thermodynamic and potentially kinetically-relevant barrier. P8 NP results for N_+^{head} and N_-^{head} are shown in panel (b).

Table 3.2 summarizes the 1.88 nm NP with unrestrained membrane PMF results, in terms of their global wells and barriers for the order parameters investigated in this study. It is important to note that all PMFs result from post-processing the simulation data sampled in Δz_+; more precise and potentially more accurate results can be obtained for the other order parameters by biasing them directly. Nonetheless, this efficient and straightforward post-processing routine further confirms NP-membrane stable states–through generally small free energy differences between PMF wells across coordinates–and reveals hidden free energy barriers that may be relevant to interaction mechanisms. The 1.88 nm C1 NP Δz_+ well depth found in this study agrees well with those of fullerene and Au NPs in others.[33,114,117] The apparent P5 barrier for the unrestrained membrane system

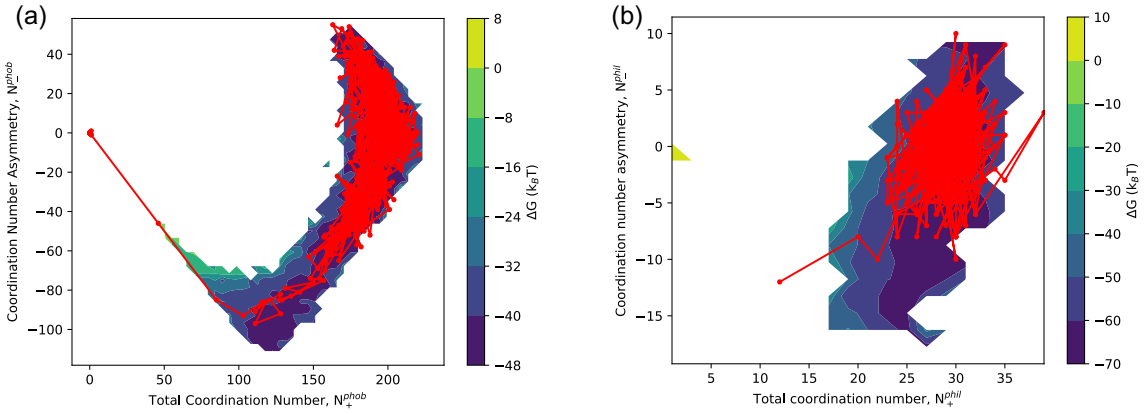

Figure 3.13: PMF and dynamical trajectory for 1.88 nm C1 NP membrane insertion/P8 NP membrane adsorption in the space of total coordination number and coordination number asymmetry. (a) Show here is the free energy projection onto N_+^{tail} (x-axis) and N_-^{tail} (y-axis). Superimposed (in red) is the dynamical trajectory from the 100 ns unbiased MD simulation, demonstrating a physically intuitive process of NP membrane insertion. (b) Corresponding results for P8 in terms of N_+^{head} (x-axis) and N_-^{head} (y-axis).

is notably small due to tunneling, but the result from restrained membrane simulations agrees well with a study of hydroxylated fullerenes.[34] To the authors' knowledge, the P8 results do not quantitatively correspond to any recent study, but are qualitatively analogous to those of charged NPs.[114,117] Results, however, can be highly dependent on the type and spatial range of interactions.

Table 3.2: Thermodynamic comparisons for 1.88 nm NPs in this study from analysis in different candidate reaction coordinates. Major features of the one- and two-dimensional PMFs–the global well $\Delta G(q_{min})$ and global barrier $\Delta G(q^{\ddagger})$–are displayed for the 1.88 nm C1, P5, and P8 NPs and multiple trial coordinates (in k_BT). The comparison adds confidence to the capturing of relevant interaction states, but also further suggests that, in some cases, smearing over wells and barriers is taking place.

NP	Δz_+	$\Delta z_+(r_c)$	$(\Delta z_+, z_+(r_c))$	N_+^{tail}	(N_+^{tail}, N_-^{tail})	N_+^{head}	(N_+^{head}, N_-^{head})
C1	-46.0/ –	-49.3/ –	∼-48/ ∼6	-49.3/ 8.4	∼-48/ ∼8	–	–
P5	–/ 31.4	–/ ??	–/ ∼32	–	–	–	–
P8	-57.8/ 0.9	-67.7/ 7.1	∼-60/ ∼10	–	–	-64.7/ 3.5	∼-70/ ∼10

Here, we find that alternative coordinates aid in the physical interpretation of 1.88 nm NP-membrane interactions for multiple NP chemistries. Regardless of the qualitative mechanism, in which membrane out-of-plane deformations are essential, these metrics uncover hidden barriers and suggest possible interaction pathways while still capturing free energy differences to the final stable states. As shown by the work of Ghaemi et al., Van Lehn et al., Ting and coworkers, and this study, metrics involving particle-lipid coordination and collective membrane degrees of freedom could be quite

promising.[43,65,66,71] Previous studies have shown that direct biasing in alternative coordinates can both eliminate memory (non-classical) effects and lead to faster free energy convergence.[71] We have shown that the global displacement translational coordinate is often a poor choice for NPs larger than typical small molecules, and can even be a poor choice of sampling for small molecules as well, including ions with a strong electrostatic component to the membrane interaction and aspherical, flexible solutes that can reorient and deform.[25,105,118] There are several rigorous works for solute-membrane interactions that analyze the utility of a local displacement coordinate for sampling, and it has been shown to be both reliable for avoiding major system size effects & tunneling and accessible through conventional MD packages.[118] However, in our results, we show that even the local displacement PMFs sometimes do not uncover barriers (e.g. C1 in Table 3.2), and are not quite system size invariant. The consideration of NP orientation seems to be an outstanding issue in the literature, and we defer the relevant analysis to a future study. We recommend coordination-based metrics for their physical relevance, size independence, and low uncertainty.

3.5 Conclusions

Despite the pervasiveness of NPs and explosion of NP fabrication and characterization techniques in recent years, a fundamental understanding of NP interactions with biological membranes and models thereof is lacking. In analogy to the current regulatory landscape, NP-membrane simulations have often assumed that NPs behave the same way as small molecules–namely, in their interaction modes and mechanisms.[85,106,114,117,123,124] In this study, we leverage MD simulations with advanced sampling to study NP-membrane interactions, specifically in the breakdown of the nondisruptive simple diffusion mechanism, the ISD model, and Overton's Rule for the membrane transport of rigid spherical NPs

of varying size and surface chemistry. As expected, a breakdown of these traditional small-scale theories occurs at larger NP length scales. In general, the well-known Overton's Rule is overly simplified for NP transport across a fluctuating lipid bilayer membrane, and therefore systematically overpredicts membrane permeabilities. From the NP size and surface chemistry ranges and resolutions studied here, we conclude that the nondisruptive simple diffusion mechanism and ISD model break down between around 0.5 and 2 nm diameter solutes, across several common chemistries (interfacially active, hydrophilic, and hydrophobic). For 0.5 nm NPs and below, NPs interact with and cross membranes with minimal disruption, and ISD permeability predictions are in semi-quantitative agreement with experiments. Around 2 nm particles, significant complications emerge owing to the coupling of the NP with the large-scale membrane undulations as well as poor NP rotatability; the ISD model is no longer a mechanistically accurate description, regardless of NP chemistry. Implementation of the ISD model for NPs larger than 0.5 nm will likely result in overpredictions of the permeability due to tunneling that smears the translational free energy profiles and reduces the apparent free energy barrier relative to the minimum free energy pathway. These order parameters fluctuate on timescales comparable to or slower than the NP translational motion, preventing free energy convergence along the global displacement coordinate and suggesting the incorporation of additional order parameters into the determination of mechanistic pathways and kinetic rates. Alternative coordinates like coordination-based metrics provide a gateway to understanding interaction and transport mechanisms through capturing major interaction states and elucidating otherwise hidden barriers in the critical 1-10 nm subspace of NP design.

While these complications have been recognized in several recent studies,[67,70,71,105,113,118] we demonstrate here exactly how and where these complications lead to a breakdown of small-scale theories and provide guidelines for future studies. It has been difficult in previous simulation studies to glean general, design-dependent principles for NP-membrane

interactions. In the present systematic study, we provide insights into relevant pathways and fates for a broad subset of NP-membrane interactions. We see that, at homogeneous chemistry even for modest NP sizes, membrane interaction modes and minimum free energy pathways start to significantly diverge, with some requiring significant activation. We show that undulations are a more general phenomenon affecting nearly all types of NPs. While we do not implement more rigorous kinetic techniques here, we use extensive free energy calculations and molecular thermodynamic analysis to construct one- and two-dimensional PMFs that provide relative populations of states, correlations between coordinates, and physical intuition of NP-membrane interaction. We suggest strategies moving forward based on viable reaction coordinates and realistic membrane models for future studies.

To build upon the simulation work here and by others, we advise that major attention be paid to the relevant thermodynamic states and kinetic pathways in NP-membrane interactions. There are a host of more complicated NP designs at this length scale that are experimentally promising. Presently, however, the proper determinations via simulations should involve convergence on the equilibrium distribution of states, which is a nontrivial task for the 1-10 nm range of particles due to unclear interaction modes and mechanisms. Existing small- and large-scale theories can be a helpful guide, providing free energy estimates and bounds for thermodynamic stability (e.g. binodals), and where these theories break down will require the largest attention. Once the major states are benchmarked with theory (in terms of the relevant order and design parameters), more rigorous techniques (e.g. committor analysis, transition path sampling, likelihood maximization, etc.[95,125]) can leverage information of possible transition states and pathways to determine minimum free energy pathways, rate estimates, and the relevance of dynamic effects.

Here, our focus was on the underlying physics of NP interactions with and transport across membranes, including the associated molecular driving forces. As such, a major

capability of this detailed, physics-based simulation strategy is that it can capture factors beyond simple empirical structure-property relations and the metrics that they fit. It has been difficult to discern the precise effects of solute size and chemistry on the thermodynamics and dynamics of membrane permeation.[53] The mechanistic insight of this MD approach should be useful to the development of design principles for > 0.5 nm NPs. Due to the experimental difficulty of these determinations, simulations are a highly promising alternative, and will be increasingly so with advances in high performance computing.

3.6 Acknowledgements

The authors gratefully acknowledge the support of the Department of Defense Defense Threat Reduction Agency (HDTRA1-15-1-0045) and NSF (project DMR-1312548). The content of the publication does not necessarily reflect the position or policy of the Federal Government, and no official endorsement should be inferred. At UCSB, the authors acknowledge the Center for Scientific Computing for computing resources through NSF Grant CNS-0960316 and the Center for Bioengineering for the Crossroads Fellowship in Materials, Mechanics, and Medicine. SM acknowledges support from the Duncan and Suzanne Mellichamp Chair Fund. LGL acknowledges support from the Schlinger Professorship endowment at UCSB.

Bibliography

[1] Anselmo AC, Zhang M, Kumar S, et al. Elasticity of nanoparticles influences their blood circulation, phagocytosis, endocytosis and targeting. *ACS Nano.* 2015; 9(3): 3169–3177.

[2] Champion JA, Katare YK, Mitragotri S. Making polymeric micro- and nanoparticles of complex shapes. *Proceedings of the National Academy of Sciences of the United States of America.* 2007; 104(29): 11901–4.

[3] Jackson AM, Myerson JW, Stellacci F. Spontaneous assembly of subnanometre-ordered domains in the ligand shell of monolayer-protected nanoparticles. *Nature materials.* 2004; 3(5): 330–336.

[4] Petros RA, DeSimone JM. Strategies in the design of nanoparticles for therapeutic applications. *Nature reviews. Drug discovery.* 2010; 9(8): 615–27.

[5] Rolland JP, Maynor BW, Euliss LE, Exner AE, Denison GM, DeSimone JM. Direct fabrication and harvesting of monodisperse, shape-specific nanobiomaterials. *Journal of the American Chemical Society.* 2005; 127(28): 10096–10100.

[6] Chen KL, Bothun GD. Nanoparticles meet cell membranes: Probing nonspecific interactions using model membranes. *Environmental Science and Technology.* 2014; 48(2): 873–880.

[7] Shan Y, Ma S, Nie L, et al. Size-dependent endocytosis of single gold nanoparticles. *Chem. Commun..* 2011; 47: 8091–8093.

[8] Shang L, Nienhaus K, Nienhaus GU. Engineered nanoparticles interacting with cells: size matters. *Journal of nanobiotechnology.* 2014; 12(1): 5.

[9] Liu J, Weller GER, Zern B, et al. Computational model for nanocarrier binding to endothelium validated using in vivo, in vitro, and atomic force microscopy experiments. *Proceedings of the National Academy of Sciences of the United States of America.* 2010; 107(38): 16530–16535.

[10] Bertrand N, Wu J, Xu X, Kamaly N, Farokhzad OC. Cancer nanotechnology: The impact of passive and active targeting in the era of modern cancer biology. *Advanced Drug Delivery Reviews.* 2014; 66: 2–25.

[11] Brar SK, Verma M, Tyagi RD, Surampalli RY. Engineered nanoparticles in wastewater and wastewater sludge - Evidence and impacts. *Waste Management.* 2010; 30(3): 504–520.

[12] Raj S, Jose S, Sabitha M. Nanotechnology in cosmetics : Opportunities and challenges. 2016: 1–10.

[13] Sun T, Zhang YS, Pang B, Hyun DC, Yang M, Xia Y. Engineered Nanoparticles for Drug Delivery in Cancer Therapy. *Angew. Chem. Int. Ed..* 2014; 53: 12320–12364.

[14] Biello D. Do Nanoparticles in Food Pose a Health Risk? *Scientific American.* 2008.

[15] Illuminato I. Tiny Ingredients, Big Risks: Nanomaterials Rapidly Entering Food and Farming. *Friends of the Earth.* 2014.

[16] Miller G, Senjen DR. Out of the Laboratory and On To Our Plates: Nanotechnology in Food & Agriculture. *Friends of the Earth.* 2008.

[17] Davenport M. Closing the Gap for Generic Nanomedicines. *Chemical & Engineering News.* 2014; 92(45): 10–13.

[18] Elsaesser A, Howard CV. Toxicology of nanoparticles. *Advanced Drug Delivery Reviews.* 2012; 64(2): 129–137.

[19] Arnida , Malugin A, Ghandehari H. Cellular uptake and toxicity of gold nanoparticles in prostate cancer cells: A comparative study of rods and spheres. *Journal of Applied Toxicology.* 2010; 30(3): 212–217.

[20] Horie M, Kato H, Fujita K, Endoh S, Iwahashi H. In Vitro Evaluation of Cellular Response Induced by Manufactured Nanoparticles. *Chemical Research in Toxicology.* 2011; 25(3): 605–619.

[21] Colvin VL. The potential environmental impact of engineered nanomaterials. *Nature Biotechnology.* 2003; 21(10): 1166–1170.

[22] Nolte TM, Kettler K, Meesters JA, Hendriks AJ, Meent D. A semi-empirical model for transport of inorganic nanoparticles across a lipid bilayer: Implications for uptake by living cells. *Environmental Toxicology and Chemistry.* 2015; 34(3): 488–496.

[23] Oberdörster G, Oberdörster E, Oberdörster J. Nanotoxicology: An Emerging Discipline Evolving from Studies of Ultrafine Particles. *Environmental Health Perspectives.* 2005; 113(7): 823–839.

[24] Gerloff K, Landesmann B, Worth A, Munn S, Palosaari T, Whelan M. The Adverse Outcome Pathway approach in nanotoxicology. *Computational Toxicology.* 2016: 1–9.

[25] Missner A, Pohl P. 110 Years of the Meyer-Overton Rule: Predicting Membrane Permeability of Gases and Other Small Compounds. *ChemPhysChem.* 2009; 10(9-10): 1405–1414.

[26] Li S, Hu PC, Malmstadt N. Imaging Molecular Transport across Lipid Bilayers. *Biophysical Journal.* 2011; 101(3): 700–708.

[27] Missner A, Kügler P, Antonenko YN, Pohl P. Passive transport across bilayer lipid membranes: Overton continues to rule. *Proceedings of the National Academy of Sciences of the United States of America.* 2008; 105(52): E123.

[28] Verma A, Uzun O, Hu Y, et al. Surface-structure-regulated cell-membrane penetration by monolayer-protected nanoparticles. *Nature Materials.* 2008; 7(7): 588–595.

[29] Ding Hm, Ma Yq. Theoretical and Computational Investigations of Nanoparticle-Biomembrane Interactions in Cellular Delivery. *Small.* 2015; 11(9-10): 1055–1071.

[30] Gao H. Probing mechanical principles of cell-nanomaterial interactions. *Journal of the Mechanics and Physics of Solids.* 2014; 62(1): 312–339.

[31] Lee CT, Comer J, Herndon C, et al. Simulation-Based Approaches for Determining Membrane Permeability of Small Compounds. *Journal of Chemical Information and Modeling.* 2016; 56(4): 721–733.

[32] Swift RV, Amaro RE. Back to the Future: Can Physical Models of Passive Membrane Permeability Help Reduce Drug Candidate Attrition and Move Us Beyond QSPR? *Chemical Biology & Drug Design.* 2013; 81(1): 61–71.

[33] Lin X, Li Y, Gu N. Nanoparticle's size effect on its translocation across a lipid bilayer: A molecular dynamics simulation. *Journal of Computational and Theoretical Nanoscience.* 2010; 7(1): 269–276.

[34] D'Rozario RSG, Wee CL, Wallace EJ, Sansom MSP. The interaction of C60 and its derivatives with a lipid bilayer via molecular dynamics simulations. *Nanotechnology.* 2009; 20(11): 115102.

[35] Pogodin S, Werner M, Sommer JU, Baulin VA. Nanoparticle-induced permeability of lipid membranes. *ACS Nano.* 2012; 6(12): 10555–10561.

[36] Qiao R, Roberts AP, Mount AS, Klaine SJ. Translocation of C 60 and Its Derivatives Across a Lipid Bilayer. *Nanoletters.* 2007; 7(3): 614–619.

[37] Lin J, Zhang H, Chen Z, Zheng Y. Penetration of lipid membranes by gold nanoparticles: Insights into cellular uptake, cytotoxicity, and their relationship. *ACS Nano.* 2010; 4(9): 5421–5429.

[38] Vácha R, Martinez-Veracoechea FJ, Frenkel D. Receptor-mediated endocytosis of nanoparticles of various shapes. *Nano letters.* 2011; 11(12): 5391–5.

[39] Yang K, Ma YQ. Computer simulation of the translocation of nanoparticles with different shapes across a lipid bilayer. *Nature nanotechnology.* 2010; 5(8): 579–583.

[40] Yi X, Shi X, Gao H. Cellular uptake of elastic nanoparticles. *Physical Review Letters.* 2011; 107(9): 1–5.

[41] Li Y, Zhang X, Cao D. A spontaneous penetration mechanism of patterned nanoparticles across a biomembrane. *Soft matter.* 2014; 10(35): 6844–56.

[42] Li Y, Li X, Li Z, Gao H. Surface-structure-regulated penetration of nanoparticles across a cell membrane. *Nanoscale.* 2012; 4(12): 3768.

[43] Van Lehn RC, Ricci M, Silva PH, et al. Lipid tail protrusions mediate the insertion of nanoparticles into model cell membranes. *Nature Communications.* 2014; 5(1): 4482.

[44] Ding Hm, Ma Yq. Role of physicochemical properties of coating ligands in receptor-mediated endocytosis of nanoparticles. *Biomaterials.* 2012; 33(23): 5798–802.

[45] Ding HM, Tian Wd, Ma YQ. Designing nanoparticle translocation through membranes by computer simulations. *ACS nano.* 2012; 6(2): 1230–8.

[46] Rocha EL, Caramori GF, Rambo CR. Nanoparticle translocation through a lipid bilayer tuned by surface chemistry. *Physical chemistry chemical physics : PCCP.* 2013; 15(7): 2282–90.

[47] Prates Ramalho JP, Gkeka P, Sarkisov L. Structure and phase transformations of DPPC lipid bilayers in the presence of nanoparticles: Insights from coarse-grained molecular dynamics simulations. *Langmuir.* 2011; 27(7): 3723–3730.

[48] Gkeka P, Angelikopoulos P, Sarkisov L, Cournia Z. Membrane Partitioning of Anionic, Ligand-Coated Nanoparticles Is Accompanied by Ligand Snorkeling, Local Disordering, and Cholesterol Depletion. *PLoS Computational Biology.* 2014; 10(12): e1003917.

[49] Lin J, Alexander-Katz A. Cell membranes open "doors" for cationic nanoparticles/biomolecules: insights into uptake kinetics. *ACS nano.* 2013; 7(12): 10799–808.

[50] Zhang S, Gao H, Bao G. Physical Principles of Nanoparticle Cellular Endocytosis. *ACS Nano.* 2015; 9(9): 8655–8671.

[51] Van Lehn RC, Atukorale PU, Carney RP, et al. Effect of particle diameter and surface composition on the spontaneous fusion of monolayer-protected gold nanoparticles with lipid bilayers. *Nano Letters.* 2013; 13(9): 4060–4067.

[52] Van Lehn RC, Alexander-Katz A. Pathway for insertion of amphiphilic nanoparticles into defect-free lipid bilayers from atomistic molecular dynamics simulations. *Soft Matter.* 2015; 11(16): 3165–3175.

[53] Marrink SJ, Berendsen HJC. Permeation Process of Small Molecules across Lipid Membranes Studied by Molecular Dynamics Simulations. *The Journal of Physical Chemistry.* 1996; 100(41): 16729–16738.

[54] Purcell E. Life at low Reynolds number. 1977.

[55] Awoonor-Williams E, Rowley CN. Molecular simulation of nonfacilitated membrane permeation. *Biochimica et Biophysica Acta (BBA) - Biomembranes.* 2016; 1858(7): 1672–1687.

[56] Nagle JF, Mathai JC, Zeidel ML, Tristram-Nagle S. Theory of passive permeability through lipid bilayers. *The Journal of general physiology.* 2008; 131(1): 77–85.

[57] Bahrami AH, Raatz M, Agudo-Canalejo J, et al. Wrapping of nanoparticles by membranes. *Advances in Colloid and Interface Science.* 2014; 208: 214–224.

[58] Dasgupta S, Auth T, Gompper G. Shape and orientation matter for the cellular uptake of nonspherical particles. *Nano letters.* 2014; 14(2): 687–93.

[59] Deserno M, Gelbart W. Adhesion and Wrapping in Colloid Vesicle Complexes. *Journal Of Physical Chemistry B.* 2002: 5543–5552.

[60] Ruiz-Herrero T, Velasco E, Hagan MF. Mechanisms of budding of nanoscale particles through lipid bilayers. *Journal of Physical Chemistry B.* 2012; 116(32): 9595–9603.

[61] Hamilton RT, Kaler EW. Alkali metal ion transport through thin bilayers. *The Journal of Physical Chemistry.* 1990; 94(6): 2560–2566.

[62] Glaser RW, Leikin SL, Chernomordik LV, Pastushenko VF, Sokirko AI. Reversible electrical breakdown of lipid bilayers: formation and evolution of pores. *Biochimica et biophysica acta.* 1988; 940(2): 275–287.

[63] Litster J. Stability of lipid bilayers and red blood cell membranes. *Physics Letters A.* 1975; 53(3): 193–194.

[64] Weaver JC, Chizmadzhev Y. Theory of electroporation: A review. *Bioelectrochemistry and Bioenergetics.* 1996; 41(2): 135–160.

[65] Ting CL, Frischknecht AL. Activated pathways for the directed insertion of patterned nanoparticles into polymer membranes. *Soft Matter.* 2013; 9(40): 9615–9623.

[66] Ting CL, Wang ZG. Minimum free energy paths for a nanoparticle crossing the lipid membrane. *Soft Matter.* 2012; 8(48): 12066.

[67] Comer J, Schulten K, Chipot C. Diffusive Models of Membrane Permeation with Explicit Orientational Freedom. *Journal of Chemical Theory and Computation.* 2014; 10(7): 2710–2718.

[68] Parisio G, Stocchero M, Ferrarini A. Passive Membrane Permeability: Beyond the Standard Solubility-Diffusion Model. *Journal of Chemical Theory and Computation.* 2013; 9(12): 5236–5246.

[69] Bonhenry D, Tarek M, Dehez F. Effects of phospholipid composition on the transfer of a small cationic peptide across a model biological membrane. *Journal of Chemical Theory and Computation.* 2013; 9(12): 5675–5684.

[70] Kopelevich DI. One-dimensional potential of mean force underestimates activation barrier for transport across flexible lipid membranes. *Journal of Chemical Physics.* 2013; 139(13).

[71] Ghaemi Z, Minozzi M, Carloni P, Laio A. A Novel Approach to the Investigation of Passive Molecular Permeation through Lipid Bilayers from Atomistic Simulations. *The Journal of Physical Chemistry B.* 2012; 116(29): 8714–8721.

[72] Chen P, Huang Z, Liang J, et al. Diffusion and Directionality of Charged Nanoparticles on Lipid Bilayer Membrane. *ACS Nano.* 2016; 10(12): 11541–11547.

[73] Chipot C, Comer J. Subdiffusion in Membrane Permeation of Small Molecules. *Scientific Reports.* 2016; 6(1): 35913.

[74] Arnarez C, Uusitalo JJ, Masman MF, et al. Dry Martini, a Coarse-Grained Force Field for Lipid Membrane Simulations with Implicit Solvent. *Journal of Chemical Theory and Computation.* 2015; 11(1): 260–275.

[75] Nitsche JM, Kasting GB. Permeability of fluid-phase phospholipid bilayers: Assessment and useful correlations for permeability screening and other applications. *Journal of Pharmaceutical Sciences.* 2013; 102(6): 2005–2032.

[76] Orsi M, Sanderson WE, Essex JW. Permeability of small molecules through a lipid bilayer: a multiscale simulation study. *The journal of physical chemistry. B.* 2009; 113(35): 12019–12029.

[77] Veldhuizen R, Nag K, Orgeig S, Possmayer F. The role of lipids in pulmonary surfactant. *Biochimica et Biophysica Acta (BBA) - Molecular Basis of Disease.* 1998; 1408(2-3): 90–108.

[78] Klauda JB, Venable RM, Freites JA, et al. Update of the CHARMM All-Atom Additive Force Field for Lipids: Validation on Six Lipid Types. *Journal of Physical Chemistry B.* 2010; 114(23): 7830–7843.

[79] Marrink SJ, Risselada HJ, Yefimov S, Tieleman DP, Vries AH. The MARTINI Force Field: Coarse Grained Model for Biomolecular Simulations. *The Journal of Physical Chemistry B.* 2007; 111(27): 7812–7824.

[80] Marrink SJ, Vries AH, Mark AE. Coarse Grained Model for Semiquantitative Lipid Simulations. *The Journal of Physical Chemistry B.* 2004; 108(2): 750–760.

[81] Poger D, Caron B, Mark AE. Validating lipid force fields against experimental data: Progress, challenges and perspectives. *Biochimica et Biophysica Acta (BBA) - Biomembranes.* 2016; 1858(7): 1556–1565.

[82] Tieleman D, Marrink S, Berendsen H. A computer perspective of membranes: molecular dynamics studies of lipid bilayer systems. *Biochimica et Biophysica Acta (BBA) - Reviews on Biomembranes.* 1997; 1331(3): 235–270.

[83] Bahrami AH, Raatz M, Agudo-Canalejo J, et al. Wrapping of nanoparticles by membranes. *Advances in Colloid and Interface Science.* 2014; 208: 214–224.

[84] Curtis EM, Bahrami AH, Weikl TR, Hall CK. Modeling nanoparticle wrapping or translocation in bilayer membranes. *Nanoscale.* 2015; 7(34): 14505–14514.

[85] Gkeka P, Sarkisov L, Angelikopoulos P. Homogeneous Hydrophobic Hydrophilic Surface Patterns Enhance Permeation of Nanoparticles through Lipid Membranes. *The Journal of Physical Chemistry Letters.* 2013; 4(11): 1907–1912.

[86] Li Y, Zhang X, Cao D. Nanoparticle hardness controls the internalization pathway for drug delivery. *Nanoscale.* 2015; 7(6): 2758–2769.

[87] Li Y, Zhang X, Cao D. A spontaneous penetration mechanism of patterned nanoparticles across a biomembrane. *Soft Matter.* 2014; 10(35): 6844.

[88] Van Lehn RC, Alexander-Katz A. Fusion of ligand-coated nanoparticles with lipid bilayers: Effect of ligand flexibility. *Journal of Physical Chemistry A.* 2014; 118(31): 5848–5856.

[89] Van Lehn RC, Alexander-Katz A. Membrane-Embedded Nanoparticles Induce Lipid Rearrangements Similar to Those Exhibited by Biological Membrane Proteins. *The Journal of Physical Chemistry B.* 2014; 118(44): 12586–12598.

[90] Van Lehn RC, Alexander-Katz A. Structure of Mixed-Monolayer-Protected Nanoparticles in Aqueous Salt Solution from Atomistic Molecular Dynamics Simulations. *The Journal of Physical Chemistry C.* 2013; 117(39): 20104–20115.

[91] Yang K, Ma YQ. Computer simulation of the translocation of nanoparticles with different shapes across a lipid bilayer. *Nature Nanotechnology.* 2010; 5(8): 579–583.

[92] Girasole M, Pompeo G, Cricenti A, et al. Roughness of the plasma membrane as an independent morphological parameter to study RBCs: A quantitative atomic force microscopy investigation. *Biochimica et Biophysica Acta - Biomembranes.* 2007; 1768(5): 1268–1276.

[93] Hess B, Uppsala S, Lindahl E. GROMACS 4: Algorithms for Highly Efficient, Load-Balanced, and Scalable Molecular Simulation. *J. Chem. Theory Comput..* 2008; 4(3): 435–447.

[94] Wassenaar TA, Ingólfsson HI, Böckmann RA, Tieleman DP, Marrink SJ. Computational Lipidomics with insane : A Versatile Tool for Generating Custom Membranes for Molecular Simulations. *Journal of Chemical Theory and Computation.* 2015; 11(5): 2144–2155.

[95] Peters B. *Reaction Rate Theory and Rare Events.* Amsterdam: Elsevier1st ed. 2017.

[96] Ulander J, Haymet ADJ. Permeation across hydrated DPPC lipid bilayers: simulation of the titrable amphiphilic drug valproic acid. *Biophysical journal.* 2003; 85(6): 3475–3484.

[97] Kirkwood JG, Buff FP. The Statistical Mechanical Theory of Surface Tension. *The Journal of Chemical Physics.* 1949; 17(3): 338–343.

[98] Torrie G, Valleau J. Nonphysical sampling distributions in Monte Carlo free-energy estimation: Umbrella sampling. *Journal of Computational Physics.* 1977; 23(2): 187–199.

[99] Shirts MR, Chodera JD. Statistically optimal analysis of samples from multiple equilibrium states. *Journal of Chemical Physics.* 2008; 129(12).

[100] Lee CT, Comer J, Herndon C, et al. Simulation-Based Approaches for Determining Membrane Permeability of Small Compounds. *Journal of Chemical Information and Modeling.* 2016; 56(4): 721–733.

[101] Hummer G. Position-dependent diffusion coefficients and free energies from Bayesian analysis of equilibrium and replica molecular dynamics simulations. *New Journal of Physics.* 2005; 7.

[102] Jakobtorweihen S, Zuniga AC, Ingram T, Gerlach T, Keil FJ, Smirnova I. Predicting solute partitioning in lipid bilayers: Free energies and partition coefficients from molecular dynamics simulations and COSMOmic. *The Journal of Chemical Physics.* 2014; 141(4): 045102.

[103] MacCallum JL, Bennett WFD, Tieleman DP. Partitioning of amino acid side chains into lipid bilayers: results from computer simulations and comparison to experiment. *The Journal of general physiology.* 2007; 129(5): 371–377.

[104] Bemporad D, Essex JW, Luttmann C. Permeation of Small Molecules through a Lipid Bilayer: A Computer Simulation Study. *The Journal of Physical Chemistry B.* 2004; 108(15): 4875–4884.

[105] Neale C, Pomès R. Sampling errors in free energy simulations of small molecules in lipid bilayers. *Biochimica et Biophysica Acta (BBA) - Biomembranes.* 2016; 1858(10): 2539–2548.

[106] Bedrov D, Smith GD, Davande H, Li L. Passive Transport of C60 Fullerenes through a Lipid Membrane: A Molecular Dynamics Simulation Study. *The Journal of Physical Chemistry B.* 2008; 112(7): 2078–2084.

[107] MacCallum JL, Tieleman DP. Computer simulation of the distribution of hexane in a lipid bilayer: Spatially resolved free energy, entropy, and enthalpy profiles. *Journal of the American Chemical Society.* 2006; 128(1): 125–130.

[108] Menichetti R, Kanekal KH, Kremer K, Bereau T. In silico screening of drug-membrane thermodynamics reveals linear relations between bulk partitioning and the potential of mean force. *The Journal of Chemical Physics.* 2017; 147(12): 125101.

[109] Mitragotri S, Johnson ME, Blankschtein D, Langer R. An analysis of the size selectivity of solute partitioning, diffusion, and permeation across lipid bilayers. *Biophysical journal.* 1999; 77(3): 1268–1283.

[110] Dickson CJ, Hornak V, Pearlstein RA, Duca JS. Structure Kinetic Relationships of Passive Membrane Permeation from Multiscale Modeling. *Journal of the American Chemical Society.* 2017; 139(1): 442–452.

[111] Ghaemi Z, Alberga D, Carloni P, Laio A, Lattanzi G. Permeability Coefficients of Lipophilic Compounds Estimated by Computer Simulations. *Journal of Chemical Theory and Computation.* 2016; 12(8): 4093–4099.

[112] Zgorski A, Lyman E. Toward Hydrodynamics with Solvent Free Lipid Models: STRD Martini. *Biophysical Journal.* 2016; 111(12): 2689–2697.

[113] Ahn YN, Gupta A, Chauhan A, Kopelevich DI. Molecular transport through surfactant-covered oil-water interfaces: role of physical properties of solutes and surfactants in creating energy barriers for transport. *Langmuir : the ACS journal of surfaces and colloids.* 2011; 27(6): 2420–36.

[114] Gupta R, Rai B. Effect of Size and Surface Charge of Gold Nanoparticles on their Skin Permeability: A Molecular Dynamics Study. *Scientific Reports.* 2017; 7(October 2016): 45292.

[115] Thake THF, Webb JR, Nash A, Rappoport JZ, Notman R. Permeation of polystyrene nanoparticles across model lipid bilayer membranes. *Soft Matter.* 2013; 9(43): 10265.

[116] Li Y, Chen X, Gu N. Computational investigation of interaction between nanoparticles and membranes: Hydrophobic/hydrophilic effect. *Journal of Physical Chemistry B.* 2008; 112(51): 16647–16653.

[117] Gupta R, Rai B. Penetration of Gold Nanoparticles through Human Skin: Unraveling Its Mechanisms at the Molecular Scale. *The Journal of Physical Chemistry B.* 2016; 120(29): 7133–7142.

[118] Nitschke N, Atkovska K, Hub JS. Accelerating potential of mean force calculations for lipid membrane permeation: System size, reaction coordinate, solute-solute distance, and cutoffs. *The Journal of Chemical Physics.* 2016; 145(12): 125101.

[119] Peliti L, Leibler S. Effects of Thermal Fluctuations on Systems with Small Surface Tension. *Physical Review Letters.* 1985; 54(15): 1690–1693.

[120] Morone N, Fujiwara T, Murase K, et al. Three-dimensional reconstruction of the membrane skeleton at the plasma membrane interface by electron tomography. *The Journal of Cell Biology.* 2006; 174(6): 851–862.

[121] Ritchie K, Iino R, Fujiwara T, Murase K, Kusumi A. The fence and picket structure of the plasma membrane of live cells as revealed by single molecule techniques (Review). *Molecular Membrane Biology.* 2003; 20(1): 13–18.

[122] Nangia S, Sureshkumar R. Effects of nanoparticle charge and shape anisotropy on translocation through cell membranes. *Langmuir.* 2012; 28(28): 17666–17671.

[123] Fiedler SL, Violi A. Simulation of nanoparticle permeation through a lipid membrane. *Biophysical Journal.* 2010; 99(1): 144–152.

[124] Gupta R, Rai B. Molecular dynamics simulation study of translocation of fullerene C 60 through skin bilayer: effect of concentration on barrier properties. *Nanoscale.* 2017; 9(12): 4114–4127.

[125] Peters B. Reaction Coordinates and Mechanistic Hypothesis Tests. *Annual Review of Physical Chemistry.* 2016; 67(1): 669–690.

Chapter 4

A multiscale framework for the membrane permeability of sub-nanometer particles

4.1 Abstract

The lipid membrane permeability of a compound is an all-important quantity to its physics of biodistribution and to pharmacological, toxicological, and product design principles. Still, the consequences of the permeability for dynamic mass transfer outcomes in a complex *in vivo*, *in vitro*, or even model membrane experiment are difficult to discern. An integrated multiscale picture, driving large-scale systems biology models with parameters calculated from a microscopic mechanistic model, can provide relevant experimental insight. Using compartmental kinetic models of membrane transport with semiquantitative correspondence to the full transport problem (given by the Nernst-Planck Equation), we are able to span multiple decades of time to arrive at a better understanding of both steady-state and transient effects. We demonstrate how several standard experimental

methods for calculating the permeability assume a pseudo-steady-state approximation that in reality is only applicable in the limit of hydrophilic chemistry, larger donor and receiver compartment volumes, infinitesimally-small unstirred water layers, and an intermediate range of experimental time scales. Outside of these conditions, we provide a predictive chemistry-, volume-, layer-, and time-specific correction factor for exchanging between transient experimental permeability measurements and steady-state simulation predictions. We also directly explain the correspondence between two kinetic metrics–the membrane permeability and mean first passage time rate constant–and show how these metrics are consistent in the steady-state results that they suggest. This framework provides a link between simulation and experimental permeability measurements and preliminary design rules for membrane transport optimization in both a steady-state and transient setting.

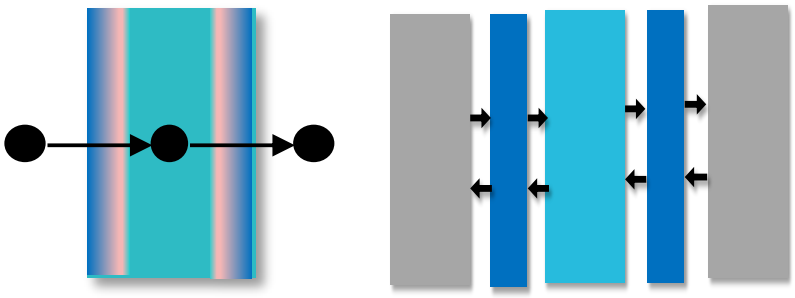

Figure 4.1: A multiscale framework linking steady-state microscopic theories for nanoparticle membrane transport to transient macroscopic models.

4.2 Introduction

The lipid membrane permeability of a compound is an all-important quantity to its physics of biodistribution and to pharmacological, toxicological, and product design principles.[1,2] Passive permeation down a concentration gradient (more generally, a chemical potential gradient) is the predominant mechanism for the membrane transport and biodistribution of foreign substances,[3] and the primary pathway of absorption for between 80 and 95 percent of commercial drugs.[4,5] As a result, membrane permeability has a high correlation to blood-brain barrier and gastrointestinal permeability.Permeability screening has contributed to as much as a 30 percent reduction in pharmacokinetics-related drug attrition.[6] The permeability is defined as:

$$P \equiv J^{ss}/\Delta C \tag{4.1}$$

where P is in units of length per time (often, cm/s), J^{ss} is the steady-state diffusive flux and ΔC is the concentration driving force (difference from one side of the membrane to the other). Due to the importance of the membrane permeability, *in vitro* assays like the parallel artificial membrane permeability assay (PAMPA), the human epithelial colorectal adenocarcinoma (CaCo-2) assay, and the Madin-Darby Canine Kidney (MDCK) assay have become fairly standard in the pharmaceutical industry and in pharmacological research.[7] In PAMPA, an artificial membrane is assembled on a microfilter, while in CaCo-2 and MDCK, an entire cellular monolayer is assembled. Caco-2 is the most widespread in industry, while PAMPA is gaining traction due to its simplicity and amenability to high-throughput operation.[8–10]

Both simulation and experiment can be an asset to membrane permeability studies, but quantitative agreement between the two has been a major challenge that has threatened their cross-validation, and consequently permeant classification[11] and drug and product

development. In many cases, simulation-predicted permeabilities are several orders of magnitude higher than those measured in experiment,[10,11] for reasons both related and unrealted to compound chemistry and other design parameters. Over time, these large discrepancies have been attributed to several simulation and experimental reasons. One major reason is the structure of the permeation layer in experiment; in the case of CaCo-2 and MDCK assays, this consists of entire cells (therefore implicating a variety of membrane and cellular transport pathways) , while in PAMPA it can consist of unclear,[10] sometimes 3D reticulated[12] membrane structures even when the lipid composition is the same as in the simulations. Compared to single lipid bilayer transport processes probed in typical simulations, these assays often introduce additional resistances in series (e.g. multilamellar membranes) and in parallel (e.g. paracellular transport pathways across tight junctions) as well as active transport processes that consume ATP. For assays like PAMPA, the additional resistances in series lead to systematic reductions in the measured permeabilities. In experiments, the material and porosity of the microfilter on which the membrane sits and the apolar solvent used to dissolve the lipid mixture can also play a role.[7] On the simulation side, the poor convergence of free energy profiles for permeation across the membrane,[13,14] potentially linked to a broader problem with the classical diffusion model[14–17] and the general mechanistic picture of permeation,[9,13,16–20] can lead to order of magnitude deviations (often overestimates) from true values.[13]

Critical to experimental permeability measurements, and therefore simulation-experiment comparison, is the continuum or compartmental model that facilitates the permeability definition and measurement.[20,21] PAMPA and Caco-2 studies typically assume a reversible or irreversible two-compartmental description in which the bulk permeant transfers from the donor to receiver compartment across the membrane. In the reversible description, there is permeant backflow from the receiver to donor compartment, leading to an equilibrium balancing of concentrations; in the irreversible description, there is

not. The permeability can consequently be calculated using the initial growth rate of the receiver compartment concentration C_R, scaled by the receiver compartment volume V_R, membrane area A, and initial donor compartment concentration C_0:[9,10]

$$P^{PAMPA,1} \equiv \left.\frac{dC_R}{dt'}\right|_{t=0} \frac{V_R}{AC_0} \tag{4.2}$$

where t is time. The two-compartment model inherently assumes that the membrane itself is at steady-state (a "pseudo-steady-state approximation," or PSSA)–as soon as the diffusant enters the membrane, it exits out the other side.[9,22] The validity of this assumption is highly compound-dependent, as it has been noted that, for hydrophilic compounds, the membrane typically acts solely as a barrier, while for hydrophobic compounds, the membrane acts as a trap.[9] Thus, for a dynamical permeation process involving hydrophobic particles, one would expect a transient stage in which particles accumulate in the membrane. This dynamic loading is believed to contribute to massive underpredictions in permeability for hydrophobic compounds (several orders of magnitude between the permeability definitions of Equations 4.1 and 4.2), and to opposite permeability trends with hydrophobicity/hydrophilicity scales relative to the steady-state predictions (which have a qualitative scaling similar to Overton's Rule,[23] i.e. permeability increasing with hydrophobicity). Inversely, for hydrophilic compounds, minimal accumulation in the membrane means that transient permeability estimates tend to be closer to their steady-state values.[9] To the authors' knowledge, implications of the PSSA have not been thoroughly discussed, let alone analyzed, for size variations of the donor and receiver compartments, for various observation time scales, and for compounds that interact with the membrane in alternative ways.[12]

Additionally, one factor discussed for some time in experiment but less frequently in simulation-experiment comparisons is unstirred water layers (UWLs), diffusive boundary

layers adjacent to the membrane in both the donor and receiver reservoirs.[7] UWLs can increase the permeation resistance typically by three or more orders of magnitude,[7] and will constitute a significant layer of resistance for hydrophobic compounds in particular or highly permeable compounds in general, especially in a dynamic scenario (e.g. when Equation 4.2 is used[9]). UWLs are present in both experimental and *in vivo* scenarios. *In vivo*, UWLs are believed to be roughly 30 to 100 μm consistent with efficient mixing at the surface of the GI tract,[7,24] or at most 1000 μm consistent with the convective mixing of circulating erythrocytes at the blood-brain barrier.[25] UWLs can plague experimental measurements and lead to widely varying estimates of the permeability.[7,26] For PAMPA experiments, the absence of stirring will lead to UWLs up to 1500 to 4000 μm (0.15 to 0.4 cm), such that reported permeabilities are never greater than $(15 - 30) \times 10^{-6}$ cm/s.[7] Hydrodynamic models have correlated the experimental thickness of UWLs to the speed of stirring in the relevant compartment, e.g. $L_{UWL} \sim \nu^{-c}$ where L_{UWL} is the UWL thickness, ν is the stirring speed, and c is a fitting exponent.[7] Through highly efficient individual-well magnetic stirring at speeds > 110 rpm, Avdeef et al demonstrated for the first time the capability to lower UWLs to the near-*in vivo* range and in some cases down to 13 μm, measuring permeabilities as high as 3500×10^{-6} (3.5×10^{-3}) cm/s.[7] Still, unchecked stirring can lead to problems of its own, including instabilities in phospholipid vesicles that constitute the membrane used for permeability measurement.[27] The fact that multiple recent studies have closed the simulation-experiment permeability gap to as little as one order of magnitude[13,14] is very promising; however, near-quantitative agreement between the two does not guarantee the correct physical representation, and therefore transferability and robustness in extrapolating to different compounds and conditions. In fact, close quantitative agreement with experiment could be due to a cancellation of errors; experiments show large variability even amongst themselves,[10] and the fact that the simulation factors discussed above can both increase and decrease permeability

predictions over several orders of magnitude requires close examination.

Here, we leverage multiscale modeling to extensively examine transient effects, which are chemistry-, volume-, layer-, and time-dependent and can lead to several orders of magnitude difference between apparent and steady-state permeabilities. Multiscale physics-based modeling can provide significant insight to the membrane transport problem in a way that phenomenological or descriptor-based models cannot.[1] Multiscale modeling can by definition span multiple time scales, crucially to experimental ones, while also incorporating system complexity.[1,9] Due to their pervasiveness in several facets of membrane transport, we believe that transient effects are a crucial factor to be considered in aggregate with other insightful and influential analyses on the permeability problem. Indeed, the importance of transient effects in real biodistribution has initiated the consideration of quantitative "structure-kinetic" relationships (QSKRs) that take the residence time of the compound into account.[3,28] Several methods have been proposed to account for the discrepancy between transient and steady-state kinetics, including a "retention factor" by which to scale the transient estimate due to dynamic membrane loading and a "lag time" prescription after which the permeability can be more accurately measured. We argue that these suggestions necessitate a closer look at the dynamical transport process. Two major questions emerge from the transient problem: (1) how can one predict the systematic experimental errors, due to transient effects and otherwise, in the calculation of steady-state permeabilities and (2) which kinetic measurement, the steady-state or transient one, is more relevant to membrane transport and biodistribution applications? The answer to both questions involves a delicate analysis of chemistries, volumes, UWLs, and time scales.

We outline our general approach in Figure 4.2. We specifically model the slab geometry of PAMPA, where UWLs can be considerable, and examine simple toy compounds on the hydrophilic-hydrophobic spectrum. Through a continuum mechanistic model (Nernst-

Planck equation) for the detailed membrane transport, we link the physiochemical properties of the compounds and the membrane system to steady-state permeability predictions via Equation 4.1. This link can be thought of as a quantitative structure-property relationship (QSPR). We then reduce the continuum model to a spatially discrete one that can scale from the times common in simulation to those essential to experiments. Therefore, we can give practical transient permeability estimates per Equation 4.2. These estimates, with the incorporation of the UWLs, allow for transient correction to steady-state predictions (a QSKR) and a 1:1 comparison with experiment (assuming other simulation and experimental factors are accounted for). Thus, we systematically demonstrate how compound, size, hydrodynamic, and dynamic effects combine. The intuition is that this combined information can ultimately be used to make reliable predictions of biological activity (via a quantitative structure-activity relationship or QSAR). Here, we build on the work of Ghaemi et al.[9] and Dickson et al.[3] However, unlike previous studies that have examined transient effects, we seek a broader range of compound chemistries and compartmental volumes,[3] a larger range of time scales,[9] and the systematic incorporation of UWLs. Furthermore, we modify our macroscopic models to account for the proper scaling in this geometry, and uniquely show semiquantitative correspondence of the discrete kinetic problem with the detailed transport one.

Implementation of the above framework first requires a microscopic continuum mechanistic model for membrane permeation, i.e. identification of a mechanistic reaction coordinate q (or set of coordinates $(q_1, q_2, ..., q_n)$) and characterization of the free energy and dynamic landscapes $G(q)$ and $D(q)$ across that (those) coordinate(s). We have recently shown that the inhomogeneous solubility-diffusion (ISD) model is a reasonable approximant for sub-nanometer particles.[18] The ISD model formulates the steady-state membrane permeability as a function of the transverse z coordinate perpendicular to the

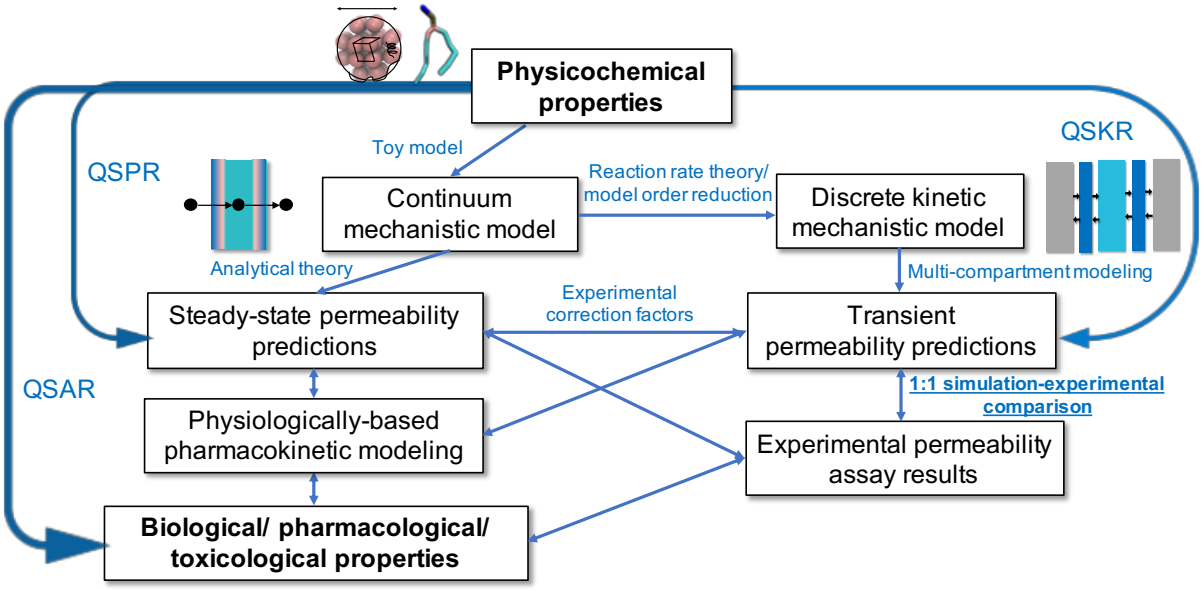

Figure 4.2: A multiscale QSPR/QSKR/QSAR framework for particle transport across lipid membranes

plane of the membrane:

$$P^{ISD} \equiv P^{ISD}(G(z), D(z)) = \left[\int_{-d/2}^{d/2} \frac{e^{\beta G(z)}}{D(z)} dz \right]^{-1}. \tag{4.3}$$

To study a family of compounds with varying hydrophilicity/hydrophobicity, we develop a toy model for the potential of mean force (PMF, or $G(z)$). The model is based on a Gaussian function $G(z) = -\alpha e^{\frac{-z^2}{2*\sigma^2}}$ where α gives the particle's negative free energy in the membrane center. In other words, α is a measure of hydrophobicity–$\alpha < 0$ for hydrophiles, $\alpha = 0$ for intermediate hydrophilicity/hydrophobicity, and $\alpha > 0$ for hydrophobes. σ is the standard deviation of the Gaussian function and a characteristic length scale of the PMF. This toy model qualitatively captures a range of compounds with molecular weights below 100, including acetamide, methanol, acetic acid, and methylamine (all $\alpha < 0$) as well as methylacetate, benzene, and ethane (all $\alpha > 0$).[29] Here, we also assume negligible variations in solute dynamics within the membrane $D(z)$–specifically, we set

the diffusivity profile to be constant D. Detailed molecular simulations have shown that this is a reasonable approximation for small solutes (diameter $<\sim$ 1 nm; molecular weight < 100), as the transverse diffusivities will typically only vary at most by an order of magnitude, generally dropping as the solute enters the membrane.[18,29,30]

In addition to the gap in permeabilities between simulation and experiment, the discussion of the optimal (fastest) permeant is currently a confusing one in the literature. The key problem lies in the precise definition of the kinetic metric for optimization, for which there are two major candidates. The first is P. Maximizing the ISD permeability (Equation 4.3) is a nontrivial process in general; however, assuming a constant diffusivity, the result is that the permeability is maximized for an infinitely deep PMF (i.e. infinitely hydrophobic particle). This qualitative result is the same as Overton's Rule[23] and its multi-layered generalizations,[21] and is thus consistent with statements that bilayer translocation or crossing is faster for hydrophobic molecules than for hydrophilic ones.[17,31,32] However, this steady-state design rule appears to be at odds with the other kinetic metric: the mean first passage time (MFPT) rate constant k_{MFPT}. k_{MFPT} is the inverse of the MFPT, and is defined microscopically for solutes obeying the inhomogeneous solubility-diffusion mechanism as:

$$k_{MFPT}^{ISD} = \Big[\int_{-d/2}^{d/2} dz' \frac{e^{\beta G(z')}}{D(z')} \int_{-d/2}^{z'} dz'' e^{-\beta G(z'')} \Big]^{-1}. \tag{4.4}$$

This result is derived for diffusive barrier crossing with reflecting source side and absorbing receiver side boundary conditions, specifically restricted to the domain of the membrane. k_{MFPT} is a single-particle metric that has been shown to pertain to both steady-state and transient scenarios.[33] Recently, studies have accurately argued that, for a constant diffusivity, k_{MFPT} is maximized for a flat free energy profile (i.e. intermediate hydrophilicity/hydrophobicity).[34,35] While the relationship between the permeability and mean

first passage time has been established,[36] its implications for rational design principles in passive permeation across membranes is still clouded. It would help to clarify these concepts as well. In what follows, we also provide a transparent explanation of the two kinetic metrics P and k_{MFPT}, including their relationship and apparent inconsistencies between them.

4.3 Theory and Methods

4.3.1 Microscopic theory: continuum mechanistic model and MFPT relation to steady-state permeability

For a compound or class of compounds satisfying the mechanistic assumptions of the inhomogeneous solubility-diffusion model, the corresponding Nernst-Planck equation is[37,38]

$$\frac{\partial C}{\partial t} = \frac{\partial}{\partial z}\left(D(z)\frac{\partial C}{\partial z} + \frac{d\beta G(z)}{dz}C\right) \tag{4.5}$$

where $C \equiv C(z,t)$ is the particle concentration (on a continuous basis in time t and space z). This equation in terms of concentration is directly analogous to the Smoluchowski and Fokker-Planck equations in terms of probabilities of a single particle.[36,39] At steady-state, this equation becomes

$$\frac{d}{dz}\left(D(z)\frac{dC}{dz} + \frac{d\beta G(z)}{dz}C\right) = 0 \tag{4.6}$$

For sink conditions (small times when the concentration or mass in the receiver compartment, and therefore back flow from the receiver to donor compartment, are negligible[40]), constant concentration boundary conditions $C|_{z=-d/2} = C_0$ and $C|_{z=d/2} = 0$ are often

assumed,[36,41] where C_0 is the time-independent donor side concentration and the receiver side concentration is zero. Effectively, the concentration profiles beyond the membrane are flat–i.e., the donor and receiver compartments are well-mixed. These boundary conditions result in a steady-state constant flux condition that does not reach thermodynamic equilibrium. Solving for the steady-state concentration profile leads to[36,41]

$$C(z) \equiv C^{ss}(z) = \frac{-C_0 e^{-\beta G(z)} \left(\int_{d/2}^{z} \frac{e^{\beta G(z')}}{D(z')} dz' \right)}{\int_{-d/2}^{d/2} \frac{e^{\beta G(z'')}}{D(z'')} dz''} \tag{4.7}$$

where C^{ss} is the time-independent steady-state concentration on a continuous basis in space. This concentration profile provides the route to calculating P^{ISD} (Equation 4.3). By definition, at steady-state, both the number of particles loaded in the membrane (the "hold up")

$$N = \int_V C(V) dV = A \int C(z') dz' \tag{4.8}$$

and the membrane efflux times the area JA reach stable values. The ratio of these quantities gives a characteristic transport time scale, which Hardt[33] has shown to be precisely the mean first passage time:

$$\tau \equiv N/JA \equiv k_{MFPT}. \tag{4.9}$$

Inserting Equation 4.8 into Equation 4.9 then gives

$$k_{MFPT} = \frac{J}{\int_{-d/2}^{d/2} C(z') dz'} \tag{4.10}$$

Combining Equations 4.4 and 4.10 and inserting Equation 4.3 for the permeability, Votapka et al.[36] derived the "MFPT in ISD relation" describing the steady-state relationship between these two kinetic metrics for solutes that obey the inhomogeneous solubility-diffusion mechanism:

$$P^{ISD} = \frac{k_{MFPT}^{ISD} \int_{-d/2}^{d/2} e^{-\beta G(z')} dz'}{2}. \tag{4.11}$$

Finally, combining Equations 4.1 and 4.11 and leveraging the definition of the size-independent membrane partition coefficient[42] $K^{c,c} \equiv K = \frac{1}{d} \int_{-d/2}^{d/2} e^{-\beta G(z')} dz'$:

$$k_{MFPT} = \frac{2J}{Kd\Delta C} = \frac{2P}{Kd} \tag{4.12}$$

This is essentially the macroscopic definition of the MFPT rate constant. In comparison with Equation 4.1, it thus becomes clear that, while the permeability normalizes the diffusive flux by the concentration difference, the MFPT rate constant additionally normalizes by the membrane thickness and the thermodynamic partitioning into the membrane. In other words, the permeability includes the effect of bulk thermodynamic partitioning in the membrane.[17] This has been mentioned by others,[36,43] but its consequences have not been transparently discussed. It is important not to overstate the consequences of Equation 4.11, which will only hold when the ISD model does. For more complicated transport mechanisms, like those that involve lateral movement within the membrane, the relationship between P and k_{MFPT} will be more complex.[19]

4.3.2 Macroscopic theory: multi-compartment modeling and PAMPA definitions for permeability

In the transient case, direct numerical evaluation of the full Nernst-Planck equation (Equation 4.5) for arbitrary/nontrivial free energy and diffusivity profiles out to experimentally-relevant time scales is exceedingly difficult due to computational efficiency and stability issues. These issues stem from exponential concentration variations over sub-nanometer membrane length scales combined with macrsocopically-sized donor and receiver compartments as well as time-dependent boundary conditions. While the right-hand side of Equation 4.5 can be recast as a Hermitian operator and seemingly evaluated as a Sturm-Liouville problem, realistic inhomogeneous, time-dependent boundary conditions prevent a typical analytical or numerical solution by means of separation of variables and eigenfunction expansion. Therefore, we seek a simpler, alternative approach that still avoids severe physical assumptions.

Compartmental models (analogous to chemical master equation models in terms of probabilities[9,17,44,45]) are a simpler route to accessing the relevant length and time scales and obtaining at least semiquantitative predictions. Multi-compartment modeling reduces the continuum model to discrete states in which the states (compartments) are assumed to be well-mixed, and works well as a description when the states represent the dominant features or regions of the continuum mechanistic model. Compartmental modeling has proven to be extremely powerful in the pharmaceutical industry via the approaches of pharmacokinetics,[46] physiologically-based pharmacokinetics,[47,48] and quantitative systems pharmacology,[49–54] and has recently been implemented in several recent modeling studies of specifically lipid membrane transport.[9,17,20,21] Nagle et al.[21] developed steady-state expressions for the membrane permeability from discrete representations of hydrophilic, hydrophobic, and amphiphilic permeants. Their hydrophilic and hydrophobic solute

transport models consist of four compartments with three layers between them, while the amphiphilic model consists of six compartments with five layers. These more detailed, chemistry-specific permeability expressions agree qualitatively with Overton's Rule.[23] The same authors also examined a continuum model and found qualitative agreement there as well.[21] In a recent study, Su et al.[34] examined design rules in terms of k_{MFPT}^{ISD} for a family of hydrophilic/hydrophobic spherical particles, suggesting a five-compartment, four-layer model with two states in the solvent on each side of the membrane, two states at the membrane-aqueous interfaces, and one state in the membrane core.

Two-compartment models

In this study, we principally examine three multi-compartment model variants (Figure 4.3).

The first is a two-compartment model with states representing the donor and receiver compartments and the intervening layer representing the membrane. We make the traditional assumption of mass action kinetics, that the rate of transfer between compartments is proportional to the concentration in the compartment of origin. Additionally, in a slab geometry like PAMPA, we expect the transfer rate to be proportional to the membrane area, and not the original compartment volume. Indeed, a critical parameter in pharmacokinetic studies is the permeability-surface area product "PS," incorporating the transport across capillary membranes on a surface area basis.[40,55–58] Thus, the rate of reversible mass transfer between these compartments is assumed to be proportional to the permeability and membrane area. These considerations produce the following system

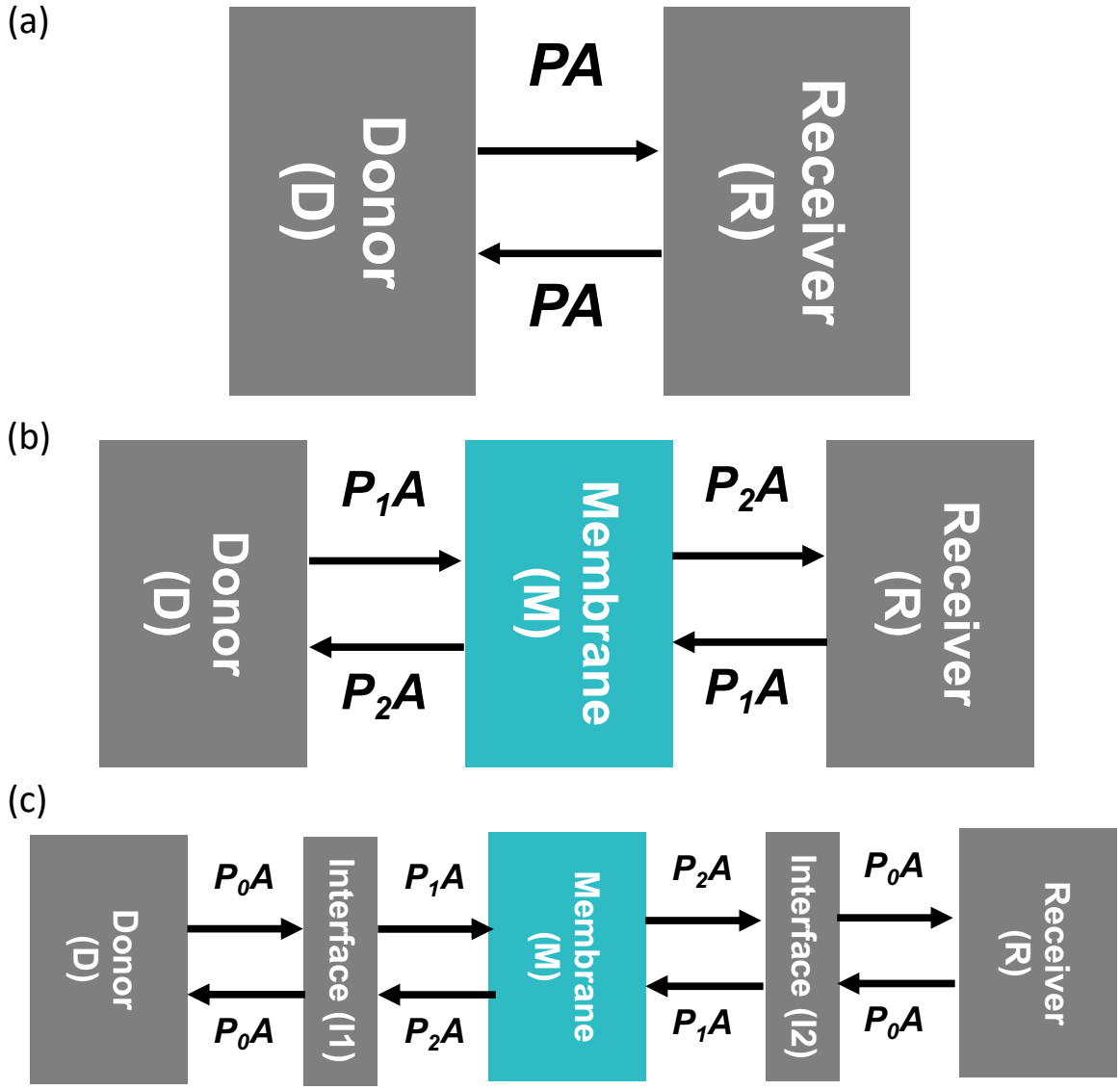

Figure 4.3: Multi-compartment models used in this study. Here, we study three multi-compartment model variants: (a) the standard PAMPA two-compartment model, (b) a three-compartment model with an explicit membrane compartment, and (c) a five-compartment model additionally with interfacial compartments that account for the lag across UWLs from the donor to membrane and membrane to receiver compartments. Transfer between adjacent compartments is reversible, and proportional to the relevant permeability and membrane cross-sectional area.

of equations for the species balance:

$$\begin{cases} \frac{dC_D}{dt} = -\frac{PA}{V_D}(C_D - C_R) \\ \frac{dC_R}{dt} = \frac{PA}{V_R}(C_D - C_R) \end{cases} \tag{4.13}$$

where C_D and C_R are the donor and receiver compartment solute concentrations and V_D and V_R are the donor and receiver compartment volumes. The analytical receiver compartment result for $C_D|_{t=0} = C_0$ and $C_R|_{t=0} = 0$ is $C_R = \frac{C_0 V_D}{V_D+V_R}\Big[1 - exp\Big(-\frac{PA(V_D+V_R)t}{V_D V_R}\Big)\Big]$, which can be used to obtain Equation 4.2 as an exact expression for and common definition of the PAMPA permeability.[9,10] Equation 4.2 is an initial [growth] rate definition, exact for the two-compartment model at $t = 0$ and roughly applicable at small times. The equation is also valid in the irreversible case.

Other permeability definitions have attempted to extend past sink conditions to larger times and finite-sized compartments, still in the context of the two-compartment description.[7,12,40] One particular definition accounts for finite-sized compartments at any time point (not just the initial) by normalizing the receiver concentration rate of change, not by the initial donor concentration, but by the instantaneous difference in concentrations between the emptying donor and filling receiver:

$$P^{PAMPA,2}(t) \equiv \left.\frac{dC_R}{dt'}\right|_t \frac{V_R}{A(C_D(t) - C_R(t))}. \tag{4.14}$$

This definition explicitly stems from Equations 4.13, and can be confirmed with the solutions to $C_D(t)$ and $C_R(t)$ outlined above. Thus, Equation 4.14 extends the available time for a permeability measurement by accounting for dynamic donor compartment unloading and receiver compartment filling.

A two-compartment model works well for permeation-limited kinetics, wherein particle biodistribution in a more complicated *in vivo* system is limited by permeation across

hydrophobic regions like cellular/lipid membranes and not by convection through the bloodstream (perfusion) or diffusion in the hydrophilic intracellular and extracellular environments. In a permeability assay, a two-compartment model assumes that membrane transport is the rate-limiting step. More specifically, a two-compartment model works well for a microscopic free energy profile with a singular free energy barrier (i.e. hydrophilic particles). However, two compartments is not enough when the particles interact favorably with the membrane (with one or more free energy wells along it, e.g. hydrophobic particles). In this case, the particles dynamically load in the membrane, and there is a distinction between the steady-state permeability $J^{ss}/\Delta C$ and normalized flux $J/\Delta C$ in general. In other words, the two-compartment model and PSSA used in most permeability assays is only appropriate for hydrophilic particles.

Three-compartment models

One way to account for hydrophobes is through a three-compartment model with an explicit membrane compartment (second model in Figure 4.3). The reduction of the continuum of interaction states along the membrane normal to three discrete states separated by two layers (primarily made up of higher density lipid[59]) results in two main kinetic parameters of interest, namely (1) a rate constant for transport from the aqueous exterior to membrane interior and (2) a rate constant for escape from the membrane to the water compartments. The rate of reversible mass transfer between compartments is again assumed to be proportional to permeabilities and membrane areas, resulting in the

following system of equations:

$$\begin{cases} \frac{dC_D}{dt} = -\frac{A}{V_D}(P_1 C_D - P_2 C_M) \\ \frac{dC_M}{dt} = -\frac{A}{V_M}(2P_2 C_M - P_1(C_D + C_R)) \\ \frac{dC_R}{dt} = -\frac{A}{V_R}(P_1 C_R - P_2 C_M). \end{cases} \tag{4.15}$$

Here, C_M is the solute membrane concentration, V_M is the membrane compartment volume, and $P_1 A$ and $P_2 A$ are the permeability-surface area products from the donor or receiver to membrane compartment (corresponding to membrane entry) and the membrane to donor or receiver compartment (corresponding to membrane escape), respectively. The development of a realistic three-compartment model is nontrivial due to the reduction of physical space to discrete states; the parameters V_M, P_1, and P_2 and physical cutoffs between compartments are often difficult to determine. The piecewise permeabilities P_1 and P_2 for membrane entry and escape, respectively, are determined by a modified version of the ISD model wherein the integral limits correspond to the layers between the compartments and the free energies are normalized with respect to their values at the start of each step:

$$\begin{cases} P_1 \equiv \left[e^{-\beta G(-d/2)} \int_{-d/2}^{0} \frac{e^{\beta G(z)}}{D(z)} dz \right]^{-1} \quad \textit{(entry)} \\ P_2 \equiv \left[e^{-\beta G(0)} \int_{-0}^{d/2} \frac{e^{\beta G(z)}}{D(z)} dz \right]^{-1} \quad \textit{(escape).} \end{cases} \tag{4.16}$$

We expect that the kinetics depend on *relative* free energy features and not global ones. While seemingly unorthodox, this correction to the normalization allows for the incorporation of relative free energies, rather than global ones that would be the consequence of a single free energy normalization. In other words, this parameterization accounts for both the ease of entering free energy wells and the difficulty of exiting them, as well as the difficulty of climbing free energy barriers and the ease of leaving them. We

have shown that, at steady-state, the MFPT rate constant and permeability are related, and specifically that the permeability accounts for the holdup when the rate constant does not (Equation 4.11). As we already assume mass action kinetics in our model (i.e., $\frac{dC_i}{dt} \propto C_i$), the inclusion of the holdup $\approx C_M(t \to \infty)V_M$ would not only "double-count" for both the concentration in the origin compartment and steady-state loading in the relevant membrane monolayer, but its implicit steady-state assumption would also defeat the purpose of a transient analysis. Thus, we formulate piecewise permeabilities that are normalized with respect to the holdup by dividing the piecewise ISD permeabilities effectively by the thermodynamic partitioning in each compartment (i.e. $e^{-\beta G(-d/2)}$ and $e^{-\beta G(0)}$) As one will see in the Results section, this parameterization is essential to account for single-particle kinetics that are also proportional to membrane area. At steady-state, this framework becomes consistent with other chemical kinetics approaches in that the ratio of piecewise rate constants (or in our case, the piecewise permeabilities) determines the thermodynamic partitioning.[17,21]

It is crucial to justify this model formulation in relation to traditional and recent multi-compartment modeling efforts. Perhaps the most relevant, Dickson et al.[3] recently adapted a compartmental modeling framework for a family of drug molecules for which the assumed mechanism was a three-step process consisting of (1) solubilization in one leaflet of the membrane, (2) flip flop to the other leaflet, and (3) exit from the membrane to the other side. Their framework instead fits MFPT rate constants from detailed molecular simulations that they determine through a Markov state modeling approach,[60] but in our case can be determined with our microscopic mechanistic model. For our

three-compartment model, this becomes:

$$\begin{cases} k_1^{sim} = \left[\int_{-d/2}^{0} dz \frac{e^{\beta G(z)}}{D(z)} \int_{-d/2}^{z} dz' e^{-\beta G(z')} \right]^{-1} & \textit{(entry)} \\ k_2^{sim} = \left[\int_{0}^{d/2} dz \frac{e^{\beta G(z)}}{D(z)} \int_{0}^{z} dz' e^{-\beta G(z')} \right]^{-1} & \textit{(escape)} \end{cases} \tag{4.17}$$

where k_1^{sim} is the MFPT rate constant for membrane entry and k_2^{sim} is the rate constant for membrane escape. Piecewise permeabilities are then obtained by normalizing those rate constants with respect to the surface area of the relevant barrier and the volume of the relevant reactant basin, both from the molecular simulation:

$$\begin{cases} P_D = k_1^{sim} \frac{V_D^{sim}}{A^{sim}} \\ P_M^r = P_M^f \equiv P_M = k_2^{sim} \frac{V_M^{sim}}{A^{sim}} \\ P_R = k_1^{sim} \frac{V_R^{sim}}{A^{sim}} \end{cases} \tag{4.18}$$

where P_D is the permeability from the donor to membrane compartment, P_M is the permeability from the membrane to donor or receiver compartment (P_M^r specifically referring to membrane to donor and P_M^f referring to membrane to receiver), P_R is the permeability from the receiver to membrane, A^{sim} is the membrane area in their molecular simulations, and V_D^{sim}, V_M^{sim}, and V_R^{sim} are the simulation donor, membrane, and receiver compartment volumes. Rate constants for the experimental model are then assembled with the permeabilities and the relevant areas and volumes of the experimental system:

$$\begin{cases} k_1^f = P_D \frac{A}{V_D} \\ k_2^r = k_2^f \equiv k_2 = P_M \frac{A}{V_M} \\ k_1^r = P_R \frac{A}{V_R}. \end{cases} \tag{4.19}$$

where k_1^f is the forward rate constant from the donor to membrane compartment, k_2

equals the forward (k_2^f) and backward (k_2^r) rate constant from the membrane to donor or receiver, and k_1^r is the reverse rate constant from the receiver to membrane. The rate constants are consequently implemented in a multi-compartment model of the form:

$$\begin{cases} \frac{dC_D}{dt} = -\frac{1}{V_D}(k_1^f C_D V_D - k_2 C_M V_M) \\ \frac{dC_M}{dt} = -\frac{1}{V_M}\Big(2k_2 C_M V_M - (k_1^f C_D V_D + k_1^r C_R V_R)\Big) \\ \frac{dC_R}{dt} = -\frac{1}{V_R}(k_1^r C_R V_R - k_2 C_M V_M). \end{cases} \tag{4.20}$$

As the compartmental volumes in the above formulation then cancel in the species balance (by, for example, $k_1^f C_D V_D = P_D A C_D$), the framework of Dickson et al. and others[40] also effectively accounts for this area but not compartmental volume dependence. However, like the two-compartment model, the normalization technique of Dickson et al., using volumes and areas from the simulation and experimental systems, assumes permeation-limited kinetics. In fact, the origin of this normalization technique in Equations 4.18 and 4.19 can be traced back to a limiting case of the MFPT rate constant for a large, singular barrier (e.g. a hydrophilic particle):[22,44]

$$k_{MFPT}^{ISD} \approx \Big[\int_{\cup} dz' e^{-\beta G(z')} \int_{\cap} dz \frac{e^{\beta G(z)}}{D(z)}\Big]^{-1} \quad \textit{(singular barrier)} \tag{4.21}$$

where $\cup$ refers to the reactant basin and $\cap$ refers to the barrier (for a hydrophile, the membrane). Because the integrals are separable, the second integral is the ISD equation (i.e. $P^{ISD^{-1}}$) and the first, for a flat origin compartment PMF, gives a length scale corresponding to the origin compartment volume divided by the area of the barrier (e.g. $(\frac{A}{V_D})^{-1}$). The assumptions in this parameterization procedure are not expected to hold for hydrophobes, wherein the diffusion through the flat portions of the PMF preceding the well will be rate-limiting. The length scale of the transport should not be incorporated as a scale factor to the rate constant, but technically as an additional resistance in series

with the intrinsic membrane resistance.

Five-compartment models

In reality, UWLs extend the flat portions of the PMFs outside of the membrane to macroscopic length scales, resulting in significant resistance for hydrophobes and possibly additional dynamical effects that are not captured in a two- or three-compartment model. From a practical standpoint, UWLs can lead to lags in particle entrance to the membrane and in membrane exit to the receiver. Furthermore, it is generally a poor assumption that the donor and receiver compartments on each side of the membrane are themselves well-mixed; as a result of the UWLs, significant concentration gradients can form on each side of the membrane. Thus, we also examine a five-compartment model that includes membrane-water interfacial compartments on each side of the membrane (third model in Figure 4.3):

$$\begin{cases} \frac{dC_D}{dt} = -\frac{P_0 A}{V_D}(C_D - C_{I1}) \\ \frac{dC_{I1}}{dt} = -\frac{A}{V_{I1}}((P_0 + P_1)C_{I1} - (P_0 C_D + P_2 C_M)) \\ \frac{dC_M}{dt} = -\frac{A}{V_M}(2P_2 C_M - P_1(C_{I1} + C_{I2})) \\ \frac{dC_{I2}}{dt} = -\frac{A}{V_{I2}}((P_0 + P_1)C_{I2} - (P_0 C_R + P_2 C_M)) \\ \frac{dC_R}{dt} = -\frac{P_0 A}{V_R}(C_R - C_{I2}). \end{cases} \tag{4.22}$$

Here, C_{I1} and C_{I2} are the solute concentrations on the donor-side and receiver-side membrane-water interface, V_{I1} and V_{I2} are the corresponding interfacial volumes, and $P_0 A$ is the permeability-surface area product from the donor to proximal interfacial compartment or vice versa or receiver to distal interfacial compartment or vice versa (symmetric because of the flat free energy profiles). As for P_1 and P_2, P_0 is determined by a modified ISD equation, resulting in the simple expression $P_0 = D/L_{UWL}$, where we

are assuming that the UWLs are of equal length. Interfacial compartments allow for the separation of UWL from membrane layers and deconvolute the effects of each.

Apparent kinetics from compartmental models

The PAMPA permeability definitions above provide an excellent means for normalizing the apparent permeabilities for each compound/compartmental modeling combination and therefore testing the validity of the two-compartment model and PSSA. For the three- and five-compartment models, we define a time-dependent normalized apparent permeability in analogy to the two-compartment model (Equation 4.2):

$$\hat{P}^{app}(t) \equiv \frac{P^{app}(t)}{P^{ss,isd}} = \left.\frac{dC_R}{dt}\right|_t \frac{V_R}{AC_0P^{ss,isd}} \tag{4.23}$$

where P^{app} is the apparent membrane permeability and $\hat{P}^{app}$ is the normalized analog (= 1 at steady-state and ≈ 1 at pseudo-steady state). $\hat{P}^{app}$ is thus a gauge of steady-state and provides a means of normalizing simulation result relative to a more realistic experiment and vice versa. Similarly, we define a normalized apparent permeability on the basis of PAMPA permeability definition 2 (Equation 4.14):

$$\hat{P}^{app,2}(t) \equiv \frac{P^{app2}(t)}{P^{ss,isd}} = \left.\frac{dC_R}{dt}\right|_t \frac{V_R}{A(C_D - C_R)P^{ss,isd}} \tag{4.24}$$

In analogy to the normalized apparent permeability, we also define a normalized apparent rate constant:

$$\hat{k}^{app}(t) \equiv \frac{k^{app}(t)}{k_{MFPT}} = \left.\frac{dC_R}{dt}\right|_t \frac{V_R}{V_DC_0k_{MFPT}} \tag{4.25}$$

where k^{app} is the apparent rate constant and $\hat{k}^{app}$ is the normalized version. The k^{app} definition will also level off at steady-state.. However, as we will show, the value at

which it levels off will depend strongly on the volume of origin compartment. In a way, this additional apparent metric serves as validation for our compartmental modeling framework in terms of piecewise permeabilities, which are instead origin compartment size-independent.

A completely general and physically-reasonable model is by no means obvious here. We believe that the framework we have developed above strikes a balance amongst the complexities in developing a physically-relevant compartmental model for this problem. Furthermore, we find our framework promising due to its qualitative insights and semiquantitative correspondence to the full transport problem (Equation 4.5).

4.4 Results and Discussion

4.4.1 Steady-state results

Figure 4.4 below shows free energy profiles and steady-state results for three hypothetical compounds in the family of toy Gaussian PMFs: "hydrophilic" ($\alpha = -1$), "intermediate" ($\alpha = 0$), and "hydrophobic" ($\alpha = 1$). Hydrophilic and hydrophobic compounds are characterized by a singular free energy barrier and well, respectively, while intermediate compound profiles are flat (panel a). Together with the [flat] diffusivity profiles, the free energy profiles determine the steady-state transmembrane nondimensionalized concentration profiles $\Phi \equiv C/C_0$ (panel b), for which the α parameter leads to exponential features in the profiles compared to the linear concentration profile for the intermediate compound. (We assume $D = 10^{-5}\ cm^2/s$ and $d = 5\ nm$, and the influence of the flat diffusivity profiles on the concentration profiles in Equation 4.7 falls out.) The resulting ISD permeability $P^{ISD}(\alpha)$ (panel c) thus scales supra-linearly with α, varying over several orders of magnitude from very hydrophilic compounds to intermediate ones.

From intermediate to hydrophobic, the rise is less steep, a result of the lesser influence of exponentiated negative free energies than exponentiated positive ones that has been observed in previous studies.[9,17] The steady-state permeabilities for the family of toy Gaussian PMFs thus agrees qualitatively with Overton's Rule (the higher the α, the better). As described earlier, the incorporation of bulk thermodynamic partitioning into the permeability metric mediates this Overton Rule agreement. Alternatively, the mean first passage time rate constant k_{MFPT}^{ISD} (panel d) is symmetric and peaked about $\alpha = 0$, a result that comes from the additional thermodynamic normalization relative to P^{ISD}. On a single-particle level, the intermediate compound (flat free energy profile) crosses the membrane fastest due to the absence of both barriers and "traps" (wells). More hydrophobic compounds enter the membrane quickly, but exit slowly; hydrophiles exit quickly, but enter slowly. This design chart on a k_{MFPT}^{ISD} basis (again, panel (d)) qualitatively explains the results of Su et al.,[34] amongst others.[35] Which steady-state design rule matters depends on the phenomenon of interest–single particle or bulk transport.

In terms of the steady-state membrane transport problem, the interest from a pharmacological and engineering perspective is often in bulk transport. The steady-state flux J^{ss}, and thus the macroscopic dynamics and thermodynamics of particle transport, depends on both the choice of compound (e.g. α) and the dosage (e.g. C_D); in other words, $J^{ss}(\alpha, C_D) \approx P(\alpha)C_D$. Figure 4.5 illustrates this design chart for the family of Gaussian PMFs. There are several practical reasons why α and C_D cannot simply be increased without bound. One is toxicity–from a biological standpoint, cell death will spike above a threshold particle concentration. For a toxicity limit, we use 4×10^{-3} mg/mL, drawn from a recent experimental study of fullerenes.[61] An additional, explicitly physical constraint is membrane free volume–as the membrane only has so much free space, above a threshold particle concentration, the membrane will saturate. Lipid membranes are highly anisotropic in the transverse (z) direction, leading to a highly variable free

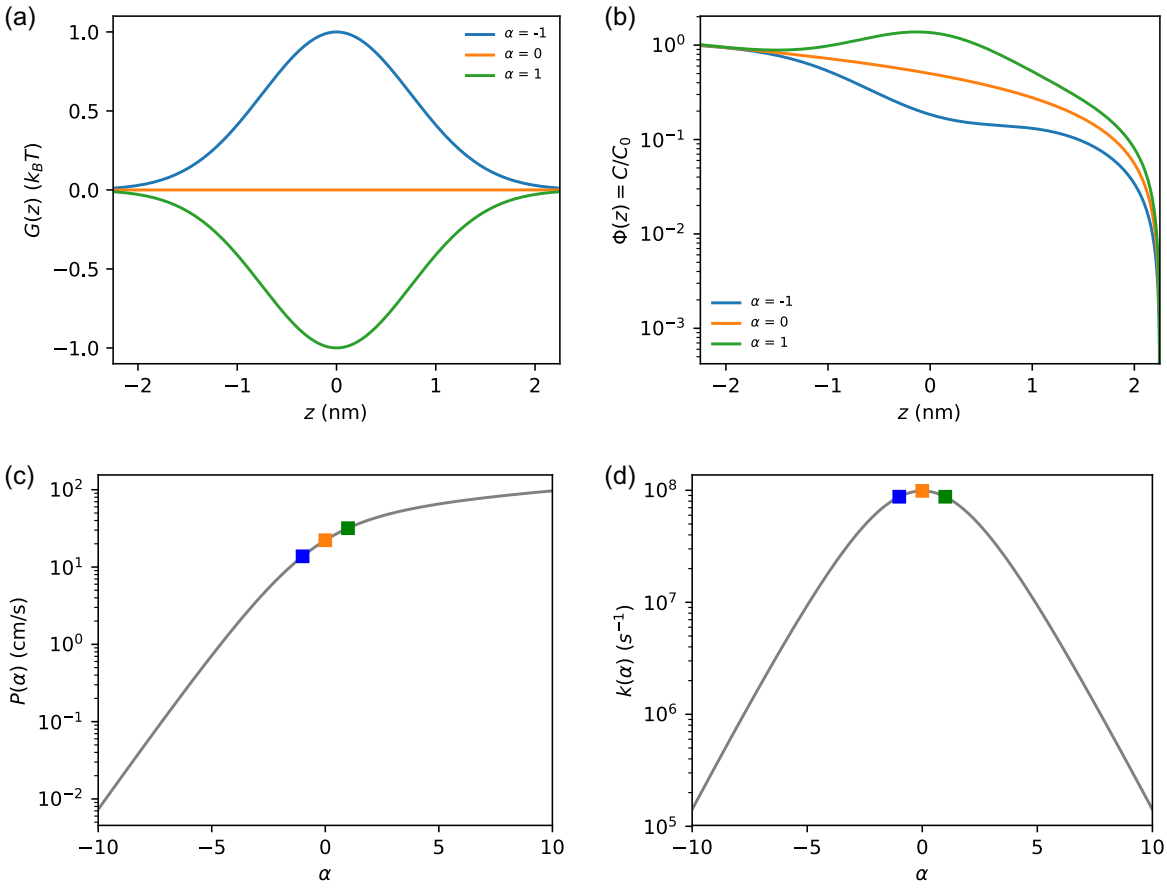

Figure 4.4: Free energies and steady-state design rules for toy Gaussian PMFs. (a) free energy profiles, or PMFs; (b) normalized steady-state concentration profiles; (c) permeability and (d) mean first passage time rate constant variations with hydrophobicity. In panels (c) and (d), hydrophilic, intermediate, and hydrophobic chemistry case studies are marked in blue, orange, and green, respectively.

volume $f(z) \equiv \frac{V_{acc}(z)}{V_{tot}}$ (where V_{acc} is the accessible volume and V_{tot} is the total volume) that is dependent on the position along the membrane and probe volume.[62] We therefore quantify a membrane "filling limit" on both a pointwise and integral basis. We model a typical lipid membrane free volume profile with an additional toy Gaussian model $f(z) = 0.01e^{\frac{-z^2}{2\sigma^2}}$, where the membrane has a maximal free volume of 1% in the center of the membrane that quickly decays on each side. This model is inspired by the result of Marrink and Berendsen for probe volumes of diameter 0.4 and 0.6 nm.[62] We define a pointwise metric $\psi(z;\alpha,C_D)$ that quantifies the free volume filled at every position along the membrane and an integral metric $\Psi(\alpha,C_D)$ that quantifies the free volume filled in the entire membrane. Figure 4.5 shows how these practical constraints manifest themselves on the design chart. The pointwise metric is stricter in that, for increasing α and C_D, the steady-state system reaches a state where the free volume at one point along the membrane is completely depleted before reaching a state where the entire membrane is filled. In the pointwise full state, the particular state along the membrane that is full should start to rearrange lipids in the transverse direction, leading to severe membrane structural deformations. The integral metric constraint shows that, at higher hydrophobicity and/or concentration, the entire membrane is filled and will start to more seriously deform. These toxicity and free volume constraints are just a few practical constraints on particle transport, and provide a starting point for safer design rules.

Still at steady-state, particle transport can be complicated by diffusion through UWLs. The influence of UWLs at steady-state is straightforward, and a consequence of resistances in series via the equation $P^{ISD,eff} = \left[\frac{L_{UWL,1}}{D_{UWL}} + \int_{-d/2}^{d/2} \frac{e^{\beta G(z')}}{D(z')} dz' + \frac{L_{UWL,2}}{D_{UWL}}\right]^{-1}$, where $P^{ISD,eff}$ is the effective steady-state permeability, $L_{UWL,1}$ and $L_{UWL,2}$ are the UWL thicknesses on the donor and receiver side of the membrane respectively, and D_{UWL} is the diffusivity across the UWLs (here, equal to that across the membrane for simplicity). The second term on the right hand side is the inverse intrinsic membrane permeability from the ISD

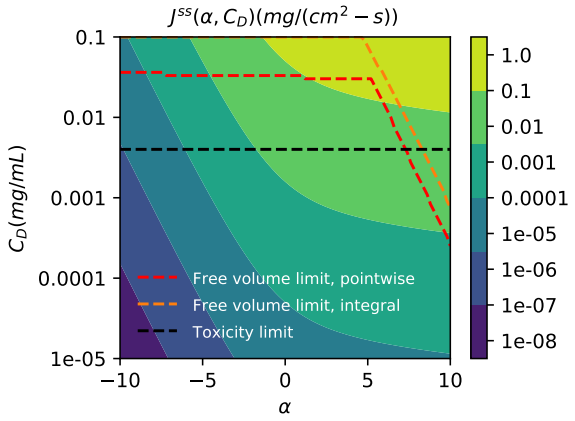

Figure 4.5: Steady-state membrane transport design chart for family of toy Gaussian PMFs. We illustrate the hypothetical yet practical scenario in which the permeant design optimization on the basis of hydrophobicity α and donor compartment concentration C_D should consider physical and biological constraints such as free volume and cytotoxicity, respectively. Free volume constraints are reported as the values in (α, C_D) space in which either a single point in the membrane or the membrane as a whole saturates with particles, while the toxicity limit is reported as a threshold aqueous concentration above which fullerenes have been found to be cytotoxic.

model. Figure 4.6 shows that, as a consequence of this equation, normalized steady-state permeabilities will decrease several orders of magnitude, but as the resistances across the UWLs are chemistry-independent, compound permeabilities will never cross. From the intrinsic value P^{ISD} to the effective value $P^{ISD,eff}$ at a standard UWL thickness of 10 μm, permeabilities drop from approximately three orders of magnitude, depending on the compound/chemistry. The effect on the mean first passage time rate constant is analogous, and UWLs do not disrupt $k_{MFPT}^{ISD,eff}$ ranking either.

As we will also show, this idealized steady-state membrane transport problem is several stages removed from a realistic physical model for PAMPA, let alone biology. One major reason is the influence of dynamical effects and their influence on different interaction states in the membrane and with UWLs.

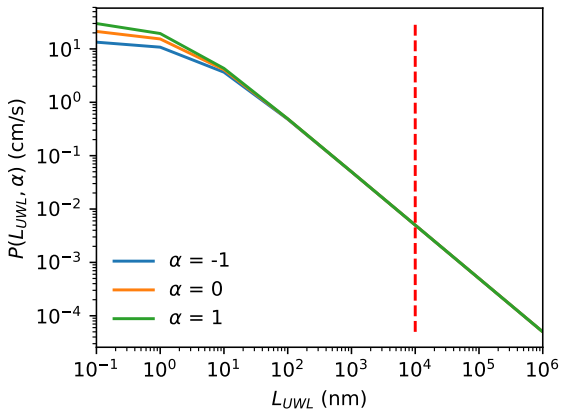

Figure 4.6: Steady-state membrane transport variations with resistance of UWLs. Unstirred waters layers limit the permeability achievable at steady-state through the addition of mass transfer resistances in series. By comparing the hydrophilic, intermediate, and hydrophobic chemistry case studies ($\alpha = -1$, $\alpha = 0$, and $\alpha = 1$, respectively), one can see the blurring of chemical differences in permeability and significant perturbations thereof (10 $\mu m = 10^4$ nm shown as a vertical dashed red line).

4.4.2 Transient results

To account for dynamic loading in the membrane that is especially important for hydrophobic compounds at small times, as well as finite-size effects that arise at long times, we fit the three-compartment model outlined in Section 4.3.2 with our toy Gaussian model compounds. Results from this model with experimentally-relevant donor and receiver compartment volumes ($V_D : V_M : V_R = 10^8 : 1 : 10^8$, corresponding to donor and receiver volumes of $\sim$1 cm) are shown in Figure 4.7 for several decades in real time. Concentrations appear in panels (a) through (c). Over a very short period of time ($\sim$100 ns), the membrane dynamically loads with solute (as shown by the normalized membrane concentration Φ_M), loading at the highest initial rate for the hydrophobic compound (again, $\alpha = 1$), but leveling off the fastest for the hydrophilic compound ($\alpha = -1$). The leveling of membrane concentrations corresponds to a pseudo-steady-state, i.e. the rate of particles entering the membrane compartment nearly equals the rate

leaving, despite the fact that the donor compartment is still dynamically unloading and the receiver compartment loading. The variations in the donor and receiver compartment concentrations Φ_D and Φ_R is difficult to see due to their large volumes and therefore stable concentrations, but they eventually equalize over much larger times (∼1 s), both at approximately one half the original concentration supply in the donor compartment. Subtle chemistry-specific effects can be seen with the hydrophobic particles unloading the fastest from the donor compartment. The receiver side concentration is interesting, with multiple intersection points between chemistries at small and large times: for very small times (∼ 1 ns), the hydrophiles actually penetrate the membrane the fastest, while for a large intermediate range of times ($\sim 100\ ns - 1\ s$), the hydrophobes surpass them, with the hydrophiles eventually winning out at very large times due to their smaller thermodynamic loading in the membrane. These results are by no means trivial, and are also sensitive to the precise range of chemistries and compartment size.

The effect of the system dynamics on the apparent kinetics is therefore striking (Figure 4.7, panels (d) through (f)). At small times during the membrane loading, the normalized apparent rate constant and normalized apparent permeabilities are well below their predicted steady-state values from Figure 4.4–in other words, $\hat{k}^{app}$, $\hat{P}^{app}$, and $\hat{P}^{app,2}$ are all $<< 1$. The apparent rate constants never reach even close to their steady-state predictions, due to the influence of the large donor (origin) compartment volume. It is important to reiterate that we parameterize our compartmental models with piecewise permeabilities. The size effects on the rate constants that are explicitly built into the models of Dickson et al and others[3,40] can be considered a byproduct of our permeability-based models. In terms of permeabilities, all compounds have a large intermediate time window (over several orders of magnitude from ∼100 ns to 1 s) where the apparent permeability reaches very close to the steady-state values predicted in Figure 4.4. In this time window, steady-state is a reasonable approximation and it should appear in

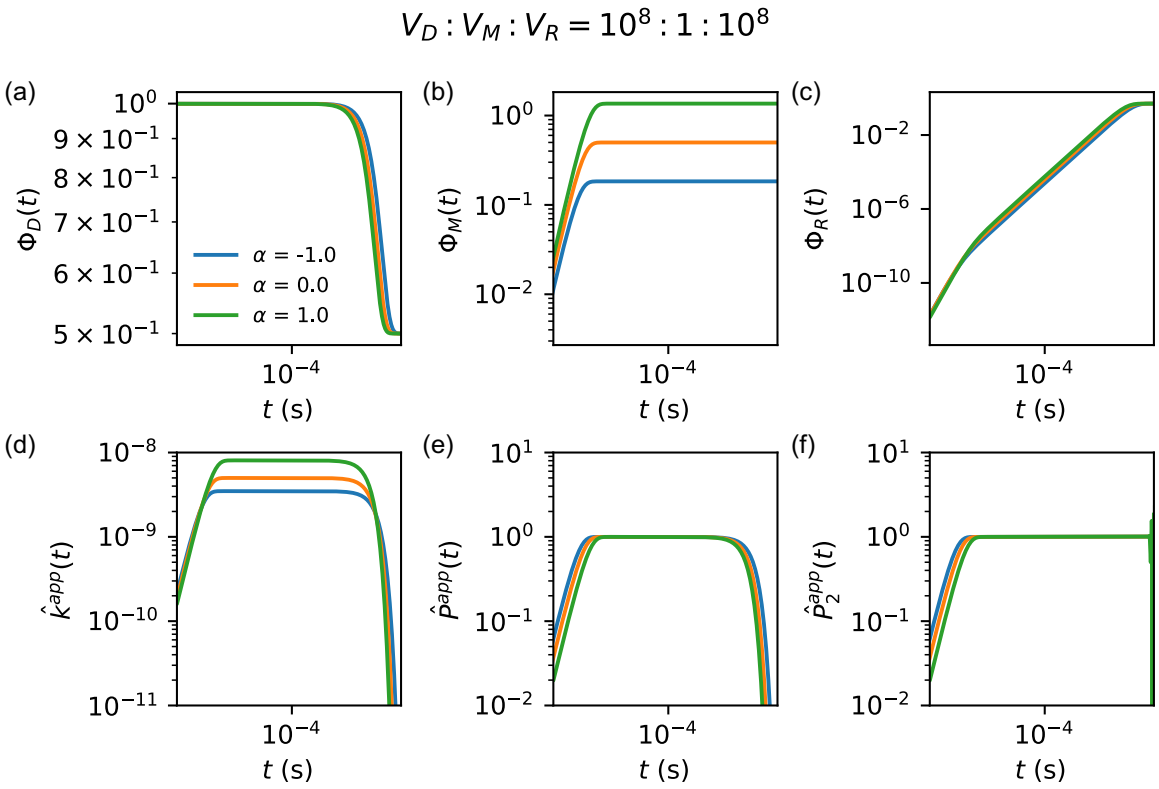

Figure 4.7: Three-compartment PAMPA model for family of toy Gaussian PMFs. Reported for the three chemistry case studies for the three-compartment model are normalized concentration profiles for the (a) donor, (b) membrane, and (c) receiver compartments, as well normalized apparent kinetic metrics in terms of the (d) apparent rate constant and apparent permeability (PAMPA definitions (e) 1 and (f) 2). The results, reported over several decades in time, show a short-time loading regime in the membrane compartment, intermediate period of pseudo-steady-state, and long-time equilibration regime, all of which are chemistry-dependent.

PAMPA measurements in which ISD simulation design rules apply. However, this pseudo-steady-state window is chemistry-dependent; the smallest available window occurs for the hydrophobic particle that gets dynamically trapped in the membrane (influencing small times) and also favorably and more quickly achieves equilibrium loading in the membrane (influencing large times). PAMPA permeability definition 2 extends the available time for a steady-state measurement by accounting for dynamic donor compartment unloading and receiver compartment filling.

At steady-state, UWLs cannot change permeability rankings and qualitative design rules, but in a transient setting, their effect is more complicated. Figure 4.8 shows results for the five-compartment model accounting for the donor, membrane, receiver, and interfaces that are separated from their adjacent donor and receiver compartments by the UWLs ($V_D : V_{I1} : V_M : V_{I2} : V_R = 10^8 : 1 : 1 : 1 : 10^8$). Transfer rates across the UWLs reflect their macroscopic thickness, which we have set here to approximately the minimal values obtainable with stirring from Avdeef et al. ($\sim$10 μm).[7] Normalized concentration results are essentially indistinguishable except in the membrane compartment, wherein the hydrophobe loads more quickly and higher overall, lagging in time to pseudo-steady state behind the intermediate and hydrophilic compounds as for the three-compartment model. For the normalized apparent permeability, this results in a thinner plateau in time for the hydrophobe before which the interfacial and membrane compartments are loading and after which equilibrium is basically achieved. However, for all compounds, the apparent permeabilities never reach their steady-state ISD predictions, and are in fact three to four orders of magnitude below it. This can at least partly be explained by the additional resistances in series provided by the UWLs (Figure 4.6). Again, permeability definition 2 expands the long-time limit of the pseudo-steady plateau. For the normalized apparent rate constant, a similar plateau to the first apparent permeability is observed, with values even smaller relative to the intrinsic membrane k_{MFPT} than in the three-compartment

model due to the additional UWLs.

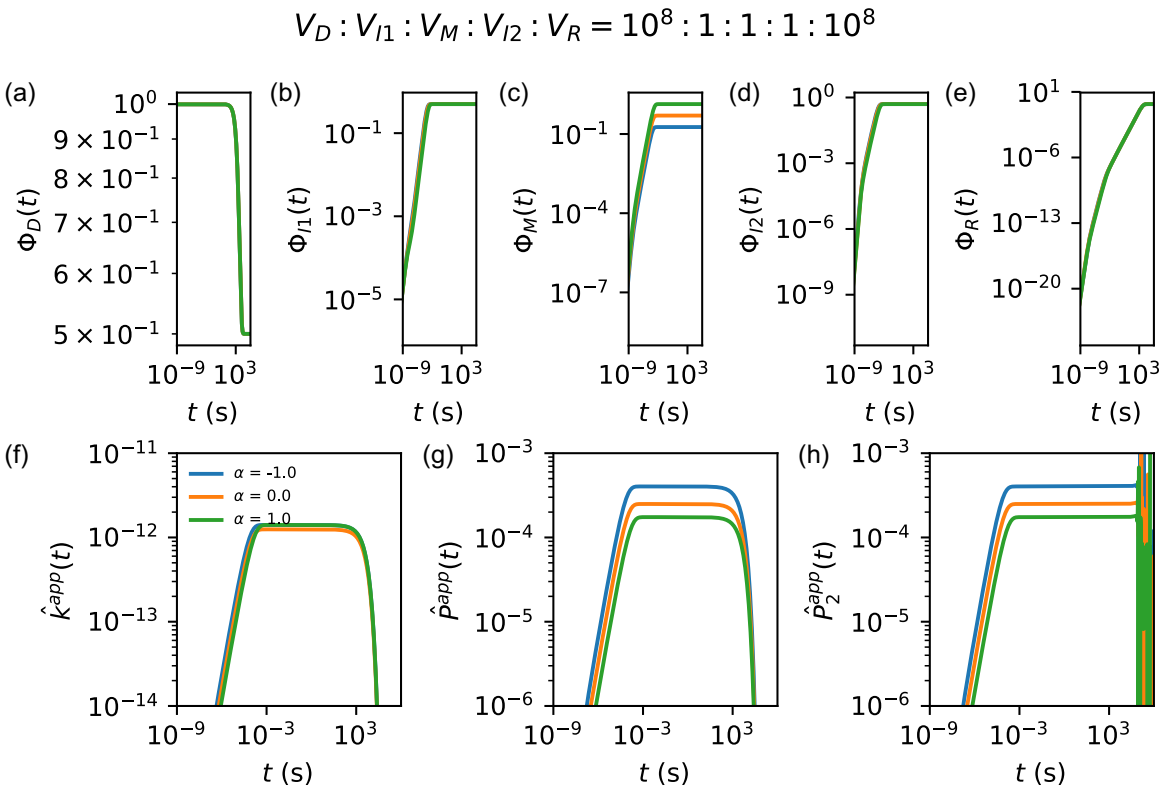

Figure 4.8: Five-compartment PAMPA model for family of toy Gaussian PMFs with UWLs. Reported for the three chemistry case studies for the five-compartment model are normalized concentration profiles for the (a) donor, (b) proximal interfacial, (c) membrane, (d) distal interfacial, and (e) receiver compartments, as well as normalized apparent kinetic metrics in terms of the (f) apparent rate constant and apparent permeability (PAMPA definitions (g) 1 and (h) 2). Results reported over several decades in time show short-time loading in the intermediate membrane and interfacial compartments, an intermediate pseudo-steady-state, and long-time equilibration, with chemical differences more subtle due to the smearing effect of the UWLs.

Another critical note is the exact range of times. While the three-compartment model (idealized condition of perfect convection in the donor and receiver chambers and no UWLs) shows pseudo-steady behavior spanning ∼100 ns to seconds, the five-compartment (incorporating reasonably-sized UWLs) shows pseudo-steady behavior spanning ∼100 μs to approximately hours. The exact sizes of the UWLs, along with the compound (e.g.

chemistry α), have a profound effect on the temporal range of pseudo-steady behavior. To obtain a more quantitative view of the characteristic time scales in this problem, we report the results of an eigenvalue analysis of the system of ODEs for the five-compartment model and three particle chemistry systems. In Figure 4.9, panel (a), we report the second and third slowest time scales in each system resulting form the eigenvalue analysis (specifically, the inverses of the eigenvalues[22]) and beyond the slowest time scale corresponding to the equilibrium solutions. This reveals that, while for the modest chemistries here the precise chemical effect on the time scales is small, the thickness of the UWLs plays a major role. Specifically, this illustrates the shifting of the PSSA regime from ∼100 ns to seconds in the absence of UWLs (three-compartment model) to ∼100 μs to ∼hours with 10 μm UWLs (five-compartment model). This should necessitate great caution in the conduct and normalization of PAMPA experiments. Below the PSSA regime, dynamic loading in the membrane and at the interfaces will result in severe underpredictions of the steady-state permeabilities; above this regime, the first apparent permeability prediction will severely underpredict $P^{ss,isd}$, but in so far as the experimental system can detect minute differences in donor and receiver compartment concentrations, the second apparent permeability prediction will still represent steady-state.

The five-compartment model can then be used to generate transient design rules (i.e. a QSKR) for the membrane transport of hydrophilic/hydrophobic compounds. Expanding the above analysis to a wider range of the α parameter to include larger free energy features relevant to MW < 100 compounds like acetamide, ethane, and beyond, picking normalized apparent permeability results (here, just definition 1) out at various time scales (10^{-1}, 10, 10^3, and 10^4 s, corresponding to the markers along the 10 μm line in Figure 4.9, panel (a)), and rescaling these values with the corresponding steady-state permeabilities, we generate an apparent permeability design chart that is a transient version of Figure 4.4. Panel (b) of Figure 4.9 shows the result of this analysis. At small times (10^{-1} s, pink

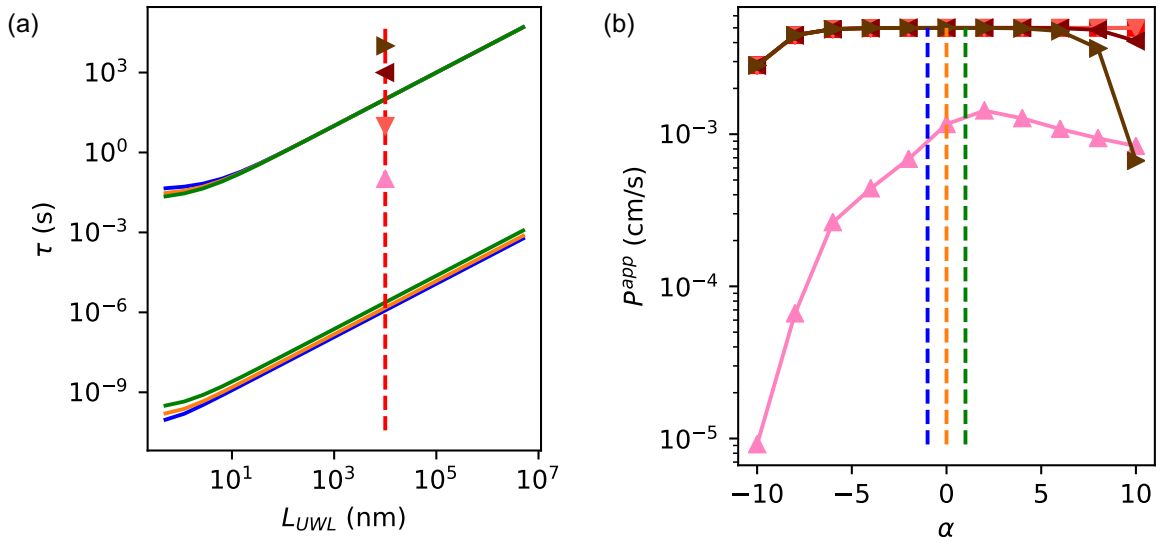

Figure 4.9: Transient design rules from five-compartment PAMPA model for family of toy Gaussian PMFs with UWLs. Reported here are (a) the second and third slowest time scales from eigenvalue analysis of system of ODEs, as a function of chemistry and UWL thickness and (b) a quantitative structure-kinetic relationship obtained by rescaling the normalized apparent permeability measurements from PAMPA definition 1 with the corresponding steady-state permeabilities as a function of hydrophobicity for various times (pink upward-pointing arrows: 10^{-1} s; light red downward-pointing arrows: 10 s; dark red leftward-pointing arrows: 10^3 s; brown rightward-pointing arrows: 10^4 s; chemistry case studies marked by vertical dashed lines in same colors as before). Overton's Rule is not qualitatively recovered at 10^{-1} s, as pseudo-steady-state is not yet achieved for all chemistries, but is recovered at 10 s; at 10^3 s, equilibration starts to impact hydrophobes, resulting in an intermediate apparent permeability optimum, while at 10^4 s, equilibration significantly impacts hydrophobes, as they actually appear slower than hydrophiles.

curve with upward pointing arrows), the interfaces and membrane are loading; pre-steady apparent permeabilities are consequently several orders of magnitude below the steady-state predictions that incorporate the series resistance of UWLs and qualitatively follow Overton's Rule. The 10^{-1} s results, however, do not agree with Overton's Rule, as the loading process is particularly detrimental to the most hydrophobic particles ($\alpha >> 0$) As a result, there is an apparent permeability optimum, which appears to agree with the dynamic results of Nakamura and Osakai[12]–some intermediate hydrophobicity appears to provide the fastest permeant. This also explicitly demonstrates the need of an incubation time or "lag time" before steady-state permeability measurements; however, the precise time for a given chemistry (and experimental setup, i.e. V_D, V_R, L_{UWL1}, and L_{UWL2}) is nontrivial. Then, for 10 s (light red curve with downward pointing arrows) and 1000 s (dark red curve with leftward pointing arrows, i.e. ~ 17 min), apparent permeabilities reach very close to their steady-state values, corresponding to the $\sim 10^{-2}$ to 10^{-3} cm/s range (with D and d defined as before) that is comparable to experiments with the same size UWLs.[7] Qualitative agreement with Overton's Rule, however, is very fleeting. By 10^4 s (brown curve with rightward pointing arrows, ~ 2.8 hr), equilibrium effects impact measurements using permeability definition 1, particularly hydrophobic compounds. As a result, apparent permeabilities calculated at very long times with definition 1 may appear to trend very differently from Overton's Rule–hydrophobic compounds are actually slowest, with some intermediate optimum here as well. Permeability definition 2 (not shown) is more stable at longer times in that it preserves steady-state scalings by adjusting the concentration driving force across the membrane. Thus, so long as a sufficient lag time is prescribed in experiments to allow for dynamic loading, permeability definition 2 is the preferred theoretical model for experimental permeability estimates.

4.5 Conclusions

The transient multiscale modeling analysis here provides a major link between simulation-predicted and experimentally-measured permeabilities, by providing realistic chemistry-, size-, layer-, and time-specific corrections, in some cases over orders of magnitude, to simulation values. We thus demonstrate that simulation-experiment correspondence is highly sensitive to compound chemistry, donor and receiver volumes, UWLs, and the time scale of measurement, and that proper treatment of these factors are essential to closing the gap between simulation and experiment. There are major temporal impacts on PAMPA measurements, especially at small and large times, systematically reducing apparent permeability values and even altering qualitative design rules that are essential to optimizing product performance and reducing drug attrition. At small times, we clearly show on the particle hydrophilicity/hydrophobicity scale that apparent permeability for an intermediately hydrophobic particle system is optimal, due to the dynamic membrane loading for all chemistries and moderate membrane entry and escape properties of the intermediate hydrophobicity. At large times, it may appear, depending on the apparent permeability definition, that again some intermediate chemistry is optimal; however, this is an artifact of one apparent permeability model definition for experimental assays, and another experimental model definition properly accounts for the donor and receiver compartment equilibration and diminishing mass transfer driving force. Thus, above small times, pseudo-steady-state estimates can be obtained in experiment using the latter apparent permeability definition. The exact ranges of pre-steady and post-steady behavior for the former permeability definition in real time depends sensitively on the size of the UWLs, with key transitions occurring anywhere from milliseconds to hours. Given that PAMPA and Caco-2 incubation times can vary between 15 min for highly permeable molecules and 15 hours for poorly permeable molecules,[10] the findings here seem highly

relevant to experiment and highlight the importance of compartment stirring to minimize the effect of UWLs and reduce them to biologically-relevant length scales. If anything, the results obtained here emphasize the crucial importance in experimental studies of removing the biasing in assaysand, particularly, to measure at different time points.[63] The results here also clearly show, consistent with previous findings and prescriptions, that stirring can reduce UWLs and thus significantly shift the range of permissible measurement times down to values that make permeability assays more amenable to high-throughput operation.

Given that we have extensively addressed our first aim in predicting the systematic experimental errors in steady-state permeabilities, primarily through the incorporation of UWLs and transient effects, per our second aim, what are the consequences for permeant design rules and which kinetic measurement–steady-state vs. transient–is more relevant to membrane transport and biodistribution? To a large extent, this question comes down to the intended application. From a bulk transport perspective and for a macroscopic system, the steady-state permeability, achieved for a wide spectrum of time scales (Figure 4.7, panels (e) and (f); Figure 4.8, panels (g) and (h)), appears relevant in the sense that, the more hydrophobic the compound, the more efficient the transient delivery (Figure 4.7, panel (c); Figure 4.8, panel(e)). This is perhaps unsurprising, given the dominance of the permeability over the rate constant in systems-level models and prescriptions like Overton's Rule.However, from a single particle perspective, for a short time of observation, or for a microscopic donor or receiver compartment, the transient permeability, qualitatively consistent with the single-particle MFPT rate constant, may be more relevant in the sense that an intermediate chemistry that efficiently enters and exits the membrane leads to the most efficient transient delivery. Here, we provide some limiting cases–very dilute in particle, short time of observation, small donor or receiver–where optimization on the basis of the steady-state permeability may not be relevant for the dynamical experimental

system. Our general framework allows for the evaluation of the relevant transient design rules beyond the limiting cases, where the exact interplay of particle chemistry, donor and receiver volume, UWL thickness, and time of observation may be very nontrivial.

We stress again that the best and most physically-reasonable model of the experimental system is not obvious here. The best model depends largely on the exact corresponding experimental system. Nonetheless, we have a large degree of confidence in our PAMPA model due to the extensive cross-testing of compartmental approaches and baselining to the full transport problem. Perhaps in the future, an adaptive spatiotemporal solution to the Fokker-Planck (Nernst-Planck) Equation (Equation 4.5), leveraging recent advancements in the spectral parameter power series method[64] and distributed approximating functionals,[65,66] may be feasible for this more complicated problem. These techniques are not immediately amenable to this problem due to its complicated drift and diffusion expressions and inhomogeneous boundary conditions. That said, Ghysels et al[20] alternatively takes a Fokker-Planck/Smoluchowski approach for single particle probabilities in transverse+radial membrane transport using a delta function initial condition and homogeneous boundary conditions, which may be promising. Stable methods for numerically and adaptively integrating the Nernst-Planck equation, to span experimentally-relevant time scales and large UWLs while also retaining the high spatial resolution necessary to resolve subtle chemical differences (i.e. differences in $G(z)$ and $D(z)$) would also be highly desirable.

The proper capturing of system size effects on the membrane transport problem is in general a theoretically and physically nontrivial concept. In the case of permeability assays, a gradient diffusion approach like the one outlined here (i.e. grounded in a diffusion or Nernst-Planck equation, $flux \sim (\nabla D(z) - F(z))C(z,t)$) seems to make sense. However, in the case of infinite dilution and no stirring (perhaps in biology), a self-diffusion approach may in fact be the most reasonable. Rate constants in this case could be assembled

from the k_{MFPT} approach, in a similar way to the Kramers escape problem where the reflecting boundary condition is extended to the start of the donor compartment. Average MFPTs could then be approximated by a weighted average over various starting positions in the donor and receiver compartments (nonequilibrium initial distribution, not an equilibrium one).[67] In this approach, the rate constants would be highly sensitive to the volume of the origin compartment–in fact, rate constants would be doubly corrected with respect to volume due both the Kramers and Shoup/Szabo corrections. This would therefore have a significant effect on apparent permeabilities and rate constants. It is not clear, however, why this method would be objectively the best. Alternatively, it may be instructive to also examine hydrophilic versus hydrophobic particle transport from the perspective of a diffusion control (or lack thereof). Indeed, one can imagine constructing a reaction-diffusion metric like the Dahmkohler number II weighing the time scale of diffusion through the bulk fluid (donor or receiver compartments) against the time scale of "reaction" (membrane transport). In this case, the framework of ten Wolde and Bolhuis,[68] in the form of a Collins-Kimballs rate constant,[69] may make sense. In this case, however, the diffusive rate constant will not account for compartmental size effects, as the only length scale it will depend on is the range of interaction (i.e. characteristic length scale of the PMF). All in all, the important note is that none of this deliberation matters for hydrophilic compounds for which size effects are minimal.

Here, we do not comprehensively consider all factors in simulation-experiment discrepancy. While we do not consider the effect of membrane composition, this initial work and the toy models herein are fairly generalizable to various bilayer types. We also do not consider the problems of experimental membrane structures, microfilter material and porosity, and lipid solvent, as these matters are difficult to address from simulation side and lamellar bilayers are biologically important in their own right. On the simulation side, the toy free energy models we use here are by definition converged, and we have restricted

ourselves to a region of particle/membrane space where we have confirmed that the ISD model (classical diffusion over a mechanistic z coordinate) applies. The hope is that the insights obtained here can be combined with other simulation and experimental studies for a more holistic framework for cross-validation and permeability predictions. Furthermore, multiscale physics-based modeling is more than capable of taking these additional factors and complexities into account.[1] This includes even membrane phase–free volume theories[70] may be helpful here.

It is tempting to try to apply the principles obtained here and elsewhere[36] to design rules for nanoparticles. Recent advances in the experimental chemical nanopatterning[71] and recent simulation studies[35,72,73] of ∼1-10 nm particles–e.g. (1) varying hydrophobic content of Janus nanoparticles, (2) varying number of hydrophobic/hydrophilic stripes at fixed hydrophobicity, and (3) varying assortment (homogeneous vs. heterogeneous arrangement) at fixed hydrophobicity–have implicated the discussion of both P^{ISD} and k^{ISD}_{MFPT}, claiming for example that a flatter PMF is better for transport. However, as we have shown that ISD is not an appropriate physical framework for the lipid membrane interactions and transport >∼1 nm particles,[18] we advocate the development of proper molecular mechanistic models first. The work of Sun et al,[13] Chipot and Comer,[15] Parisio et al,[17] Jambeck and Lyubartsev,[74] and Van Lehn et al[75] provide an excellent reference for this. Sun et al[13] in particular provide a generalization of the ISD model to alternative mechanistic coordinates. Lastly, Parisio et al.[17] provides a prescription for incorporating more complicated mechanisms into discrete compartmental/chemical master equation models.

This multiscale framework has much potential. An immediate application is connecting more detailed molecular mechanistic models to this continuum transport and discrete kinetic framework for more relevant membrane transport analysis of realistic compounds–for example, compounds that interact with membranes at their interface. Here, we

also focused mainly on chemistry effects for simple sub-nanometer particles through a structure-property-like parameter α. However, we address more detailed chemical effects linked to our molecular mechanistic analysis in Chapter 3 by designing and applying a novel structure-property correlation in Chapter 5.

A final interesting point concerns concentration effects and cooperativity. In all of this work, we have assumed infinite dilution and noninteracting particles (or pseudo-first order kinetics,[40] as the sites in each compartment are "in excess"). These are not an unreasonable starting point.[33,40,67] However, the consideration of concentration effects on free energies, diffusivities, and overall mechanisms is an interesting one. Gupta and Rai[76] studied the effect of fullerene concentration specifically on $G(z)$, observing a deepening then shallowing of the free energy profile (thermodynamically- and potentially kinetically-relevant cooperativity then anti-cooperativity) with increasing concentration. This study and other compounds and conditions could potentially produce plots like Figure 4.5 with nontrivial variations. This information could then be leveraged for their (anti-)cooperativities for better design of pharmaceuticals and consumer products.

4.6 Acknowledgements

The authors gratefully acknowledge the support of the Department of Defense Defense Threat Reduction Agency (HDTRA1-15-1-0045) and NSF (project DMR-1312548). The content of the publication does not necessarily reflect the position or policy of the Federal Government, and no official endorsement should be inferred. At UCSB, the authors acknowledge the Center for Scientific Computing for computing resources through NSF Grant CNS-0960316 and the Center for Bioengineering for the Crossroads Fellowship in Materials, Mechanics, and Medicine. SM acknowledges support from the Duncan and Suzanne Mellichamp Chair Fund. LGL acknowledges support from the Schlinger

Professorship endowment at UCSB.

Bibliography

[1] Amaro RE, Mulholland AJ. Multiscale methods in drug design bridge chemical and biological complexity in the search for cures. *Nature Reviews Chemistry.* 2018; 2(4): 0148.

[2] Swift RV, Amaro RE. Back to the Future: Can Physical Models of Passive Membrane Permeability Help Reduce Drug Candidate Attrition and Move Us Beyond QSPR? *Chemical Biology & Drug Design.* 2013; 81(1): 61–71.

[3] Dickson CJ, Hornak V, Pearlstein RA, Duca JS. Structure Kinetic Relationships of Passive Membrane Permeation from Multiscale Modeling. *Journal of the American Chemical Society.* 2017; 139(1): 442–452.

[4] Kerns EH, Di L, Petusky S, Farris M, Ley R, Jupp P. Combined application of parallel artificial membrane permeability assay and Caco-2 permeability assays in drug discovery. *Journal of Pharmaceutical Sciences.* 2004; 93(6): 1440–1453.

[5] Mandagere AK, Thompson TN, Hwang KK. Graphical model for estimating oral bioavailability of drugs in humans and other species from their Caco-2 permeability and in vitro liver enzyme metabolic stability rates. *Journal of Medicinal Chemistry.* 2002; 45(2): 304–311.

[6] Kola I, Landis J. Can the pharmaceutical industry reduce attrition rates? *Nature reviews. Drug discovery.* 2004; 3(August): 1–5.

[7] Avdeef A, Nielsen PE, Tsinman O. PAMPA: a drug absorption in vitro model. *European Journal of Pharmaceutical Sciences.* 2004; 22(5): 365–374.

[8] Sun H, Nguyen K, Kerns E, et al. Highly predictive and interpretable models for PAMPA permeability. *Bioorganic and Medicinal Chemistry.* 2017; 25(3): 1266–1276.

[9] Ghaemi Z, Alberga D, Carloni P, Laio A, Lattanzi G. Permeability Coefficients of Lipophilic Compounds Estimated by Computer Simulations. *Journal of Chemical Theory and Computation.* 2016; 12(8): 4093–4099.

[10] Orsi M, Essex JW. Chapter 4. Passive Permeation Across Lipid Bilayers: a Literature Review. In *Royal Society of Chemistry*no. 20 76–90 2010.

[11] Bennion BJ, Be NA, McNerney MW, et al. Predicting a Drug's Membrane Permeability: A Computational Model Validated With in Vitro Permeability Assay Data. *The Journal of Physical Chemistry B.* 2017; 121(20): 5228–5237.

[12] Nakamura M, Osakai T. Evaluation of the artificial membrane permeability of drugs by digital simulation. *European Journal of Pharmaceutical Sciences.* 2016; 91: 154–161.

[13] Sun R, Han Y, Swanson JMJ, et al. Molecular transport through membranes : Accurate permeability coefficients from multidimensional potentials of mean force and local diffusion constants Molecular transport through membranes : Accurate permeability coefficients from multidimensional potent. 2018; 072310.

[14] Tse CH, Comer J, Wang Y, Chipot C. Link between Membrane Composition and Permeability to Drugs. *Journal of Chemical Theory and Computation.* 2018; 14(6): 2895–2909.

[15] Chipot C, Comer J. Subdiffusion in Membrane Permeation of Small Molecules. *Scientific Reports.* 2016; 6(1): 35913.

[16] Comer J, Schulten K, Chipot C. Diffusive Models of Membrane Permeation with Explicit Orientational Freedom. *Journal of Chemical Theory and Computation.* 2014; 10(7): 2710–2718.

[17] Parisio G, Stocchero M, Ferrarini A. Passive Membrane Permeability: Beyond the Standard Solubility-Diffusion Model. *Journal of Chemical Theory and Computation.* 2013; 9(12): 5236–5246.

[18] Smith DJ, Leal LG, Mitragotri S, Shell MS. Nanoparticle transport across model cellular membranes: when do solubility-diffusion models break down? *Journal of Physics D: Applied Physics.* 2018; 51(29): 294004.

[19] De Vos O, Venable RM, Van Hecke T, Hummer G, Pastor RW, Ghysels A. Membrane Permeability: Characteristic Times and Lengths for Oxygen and a Simulation-Based Test of the Inhomogeneous Solubility-Diffusion Model. *Journal of Chemical Theory and Computation.* 2018; 14(7): 3811–3824.

[20] Ghysels A, Venable RM, Pastor RW, Hummer G. Position-Dependent Diffusion Tensors in Anisotropic Media from Simulation: Oxygen Transport in and through Membranes. *Journal of Chemical Theory and Computation.* 2017; 13(6): 2962–2976.

[21] Nagle JF, Mathai JC, Zeidel ML, Tristram-Nagle S. Theory of Passive Permeability through Lipid Bilayers. *The Journal of General Physiology.* 2008; 131(1): 77–85.

[22] Peters B. *Reaction Rate Theory and Rare Events.* Amsterdam: Elsevier1st ed. 2017.

[23] Overton E. Ueber die osmotischen Eigenschaften der Zelle in ihrer Bedeutung für die Toxikologie und Pharmakologie. *Zeitschrift für Physikalische Chemie.* 1897; 22U(1): 383–406.

[24] Lennernaäs H. Human Intestinal Permeability. *Journal of Pharmaceutical Sciences.* 1998; 87(4): 403–410.

[25] Pardridge WM. *Peptide drug delivery to the brain.* New York: Raven Press 1991.

[26] Missner A, Pohl P. 110 Years of the Meyer-Overton Rule: Predicting Membrane Permeability of Gases and Other Small Compounds. *ChemPhysChem.* 2009; 10(9-10): 1405–1414.

[27] Flaten GE, Skar M, Luthman K, Brandl M. Drug permeability across a phospholipid vesicle based barrier: 3. Characterization of drug membrane interactions and the effect of agitation on the barrier integrity and on the permeability. *European Journal of Pharmaceutical Sciences.* 2007; 30(3-4): 324–332.

[28] Schoop A, Dey F. On-rate based optimization of structure kinetic relationship: surfing the kinetic map. *Drug Discovery Today: Technologies.* 2015; 17: 9–15.

[29] Bemporad D, Essex JW, Luttmann C. Permeation of Small Molecules through a Lipid Bilayer: A Computer Simulation Study. *The Journal of Physical Chemistry B.* 2004; 108(15): 4875–4884.

[30] Lee CT, Comer J, Herndon C, et al. Simulation-Based Approaches for Determining Membrane Permeability of Small Compounds. *Journal of Chemical Information and Modeling.* 2016; 56(4): 721–733.

[31] Li S, Hu PC, Malmstadt N. Imaging Molecular Transport across Lipid Bilayers. *Biophysical Journal.* 2011; 101(3): 700–708.

[32] Li S, Hu P, Malmstadt N. Confocal Imaging to Quantify Passive Transport across Biomimetic Lipid Membranes. *Analytical Chemistry.* 2010; 82(18): 7766–7771.

[33] HARDT S. The diffusion transit time; a simple derivation. *Bulletin of Mathematical Biology.* 1981; 43(1): 89–99.

[34] Su CF, Merlitz H, Rabbel H, Sommer JU. Nanoparticles of Various Degrees of Hydrophobicity Interacting with Lipid Membranes. *The Journal of Physical Chemistry Letters.* 2017; 8(17): 4069–4076.

[35] Gkeka P, Sarkisov L, Angelikopoulos P. Homogeneous Hydrophobic Hydrophilic Surface Patterns Enhance Permeation of Nanoparticles through Lipid Membranes. *The Journal of Physical Chemistry Letters.* 2013; 4(11): 1907–1912.

[36] Votapka LW, Lee CT, Amaro RE. Two Relations to Estimate Membrane Permeability Using Milestoning. *The journal of physical chemistry. B.* 2016; 120(33): 8606–16.

[37] Diamond JM, Katz Y. Interpretation of nonelectrolyte partition coefficients between dimyristoyl lecithin and water. *The Journal of membrane biology.* 1974; 17(2): 121–154.

[38] Marrink SJ, Berendsen HJC. Simulation of water transport through a lipid membrane. *The Journal of Physical Chemistry.* 1994; 98(15): 4155–4168.

[39] Zwanzig R. *Nonequilibrium Statistical Mechanics.* New York: Oxford University Press 2001.

[40] Krämer SD. Quantitative aspects of drug permeation across in vitro and in vivo barriers. *European Journal of Pharmaceutical Sciences.* 2016; 87: 30–46.

[41] Awoonor-Williams E, Rowley CN. Molecular simulation of nonfacilitated membrane permeation. *Biochimica et Biophysica Acta (BBA) - Biomembranes.* 2016; 1858(7): 1672–1687.

[42] Jakobtorweihen S, Zuniga AC, Ingram T, Gerlach T, Keil FJ, Smirnova I. Predicting solute partitioning in lipid bilayers: Free energies and partition coefficients from molecular dynamics simulations and COSMOmic. *The Journal of Chemical Physics.* 2014; 141(4): 045102.

[43] Parisio G, Stocchero M, Ferrarini A. Passive Membrane Permeability: Beyond the Standard Solubility-Diffusion Model. *Journal of Chemical Theory and Computation.* 2013; 9(12): 5236–5246.

[44] Peters B. Reaction Coordinates and Mechanistic Hypothesis Tests. *Annual Review of Physical Chemistry.* 2016; 67(1): 669–690.

[45] Van Kampen NG. *Stochastic Processes in Physics and Chemistry, 3rd Ed.* Amsterdam, The Netherlands: Elsevier 2007.

[46] Ruiz-Garcia A, Bermejo M, Moss A, Casabo VG. Pharmacokinetics in drug discovery. *Journal of Pharmaceutical Sciences.* 2008; 97(2): 654–690.

[47] Gerlowski LE, Jain RK. Physiologically Based Pharmacokinetic Modeling: Principles and Applications. *Journal of Pharmaceutical Sciences.* 1983; 72(10): 1103–1127.

[48] Rowland M, Peck C, Tucker G. Physiologically-Based Pharmacokinetics in Drug Development and Regulatory Science. *Annual Review of Pharmacology and Toxicology.* 2011; 51(1): 45–73.

[49] Leil TA, Bertz R. Quantitative systems pharmacology can reduce attrition and improve productivity in pharmaceutical research and development. *Frontiers in Pharmacology.* 2014; 5(NOV): 1–6.

[50] Vicini P, Van Der Graaf PH. Systems pharmacology for drug discovery and development: Paradigm shift or flash in the pan? *Clinical Pharmacology and Therapeutics.* 2013; 93(5): 379–381.

[51] Van Hasselt JG, Van Der Graaf PH. Towards integrative systems pharmacology models in oncology drug development. *Drug Discovery Today: Technologies.* 2015; 15: 1–8.

[52] Danhof M. Systems pharmacology âĂŞ Towards the modeling of network interactions. *European Journal of Pharmaceutical Sciences.* 2016; 94: 4–14.

[53] Snowden TJ, Graaf PH, Tindall MJ. Model reduction in mathematical pharmacology: Integration, reduction and linking of PBPK and systems biology models. *Journal of Pharmacokinetics and Pharmacodynamics.* 2018; 45(4): 537–555.

[54] Allen RJ, Musante CJ. A mathematical analysis of adaptations to the metabolic fate of fructose in essential fructosuria subjects. *American Journal of Physiology-Endocrinology and Metabolism.* 2018; 315(3): E394–E403.

[55] Zhuang X, Lu C. PBPK modeling and simulation in drug research and development. *Acta Pharmaceutica Sinica B.* 2016; 6(5): 430–440.

[56] Shinoda W. Permeability across lipid membranes. *Biochimica et Biophysica Acta (BBA) - Biomembranes.* 2016; 1858(10): 2254–2265.

[57] Carpenter TS, Kirshner DA, Lau EY, Wong SE, Nilmeier JP, Lightstone FC. A Method to Predict Blood-Brain Barrier Permeability of Drug-Like Compounds Using Molecular Dynamics Simulations. *Biophysical Journal.* 2014; 107(3): 630–641.

[58] Agoram BM, Demin O. Integration not isolation: Arguing the case for quantitative and systems pharmacology in drug discovery and development. *Drug Discovery Today.* 2011; 16(23-24): 1031–1036.

[59] Tieleman D, Marrink S, Berendsen H. A computer perspective of membranes: molecular dynamics studies of lipid bilayer systems. *Biochimica et Biophysica Acta (BBA) - Reviews on Biomembranes.* 1997; 1331(3): 235–270.

[60] Scherer MK, Trendelkamp-Schroer B, Paul F, et al. PyEMMA 2: A Software Package for Estimation, Validation, and Analysis of Markov Models. *Journal of Chemical Theory and Computation.* 2015; 11(11): 5525–5542.

[61] Rouse JG, Yang J, Barron AR, Monteiro-Riviere NA. Fullerene-based amino acid nanoparticle interactions with human epidermal keratinocytes. *Toxicology in Vitro.* 2006; 20(8): 1313–1320.

[62] Marrink SJ, Sok RM, Berendsen HJC. Free volume properties of a simulated lipid membrane. *The Journal of Chemical Physics.* 1996; 104(22): 9090–9099.

[63] Heikkinen AT, Mönkkönen J, Korjamo T. Kinetics of cellular retention during Caco-2 permeation experiments: role of lysosomal sequestration and impact on permeability estimates. *The Journal of pharmacology and experimental therapeutics.* 2009; 328(3): 882–92.

[64] Kravchenko VV, Porter RM. Spectral parameter power series for Sturm-Liouville problems. *Mathematical Methods in the Applied Sciences.* 2009; 219(8): n/a–n/a.

[65] Zhang DS, Wei GW, Kouri DJ, Hoffman DK. Distributed approximating functional approach to the Fokker Planck equation: Eigenfunction expansion. *The Journal of Chemical Physics.* 1997; 106(12): 5216–5224.

[66] Wei GW, Zhang DS, Kouri DJ, Hoffman DK. Distributed approximating functional approach to the Fokker-Planck equation: Time propagation. *Journal of Chemical Physics.* 1997; 107(8): 3239–3246.

[67] Shoup D, Szabo A. Role of diffusion in ligand binding to macromolecules and cell-bound receptors. *Biophysical Journal.* 1982; 40(1): 33–39.

[68] Vijaykumar A, Ten Wolde PR, Bolhuis PG. The magnitude of the intrinsic rate constant: How deep can association reactions be in the diffusion limited regime? *Journal of Chemical Physics.* 2017; 147(18).

[69] Collins FC, Kimball GE. Diffusion-controlled reaction rates. *Journal of Colloid Science.* 1949; 4(4): 425–437.

[70] Amsden B. Solute Diffusion within Hydrogels. Mechanisms and Models. *Macromolecules.* 1998; 31(23): 8382–8395.

[71] Verma A, Uzun O, Hu Y, et al. Surface-structure-regulated cell-membrane penetration by monolayer-protected nanoparticles. *Nature Materials.* 2008; 7(7): 588–595.

[72] Li Y, Zhang X, Cao D. A spontaneous penetration mechanism of patterned nanoparticles across a biomembrane. *Soft Matter.* 2014; 10(35): 6844.

[73] Li Y, Li X, Li Z, Gao H. Surface-structure-regulated penetration of nanoparticles across a cell membrane. *Nanoscale.* 2012; 4(12): 3768.

[74] Jämbeck JPM, Lyubartsev AP. Exploring the Free Energy Landscape of Solutes Embedded in Lipid Bilayers. *The Journal of Physical Chemistry Letters.* 2013; 4(11): 1781–1787.

[75] Van Lehn RC, Ricci M, Silva PH, et al. Lipid tail protrusions mediate the insertion of nanoparticles into model cell membranes. *Nature Communications.* 2014; 5(1): 4482.

[76] Gupta R, Rai B. Molecular dynamics simulation study of translocation of fullerene C 60 through skin bilayer: effect of concentration on barrier properties. *Nanoscale.* 2017; 9(12): 4114–4127.

Chapter 5

A quantitative structure-property and structure-kinetic relationship for the membrane transport of sub-nanometer hydrophilic, hydrophobic, and interfacially active particles

5.1 Abstract

An understanding of the biodistribution and consequently the biological activity of a compound is essential to harnessing the efficacy and reducing the toxicity of active ingredients in pharmaceuticals and consumer products. A common route to linking a compound's physicochemical properties to its activity is through quantitative structure-

activity relationships (QSARs), which when linked with quantitative structure-property relationships (QSPRs) like those for the lipid membrane permeability and quantitative structure-kinetic relationships (QSKRs) that additionally account for a property's time dependence provide a potent statistical approach to prediction making. Still, when purely statistical, these models often suffer from transferability issues, suggesting that they are bypassing and lack a fundamental mechanistic understanding of the physics of biodistribution. The interactions with and transport across cellular membranes is an essential physical step and important predictor of biodistribution outcomes and could be key to *in vitro-in vivo* extrapolation. In this study, we design a novel, physically-grounded QSPR and QSKR for the passive lipid membrane transport of sub-nanometer particles of a wide range of chemistries. We build off of two recent studies where (1) we simulated the membrane transport process in full molecular detail to construct adequate continuum mechanistic models and parameterize those models and (2) we built an integrated multiscale platform that links high-resolution microscopic features of membrane transport to the macroscopic dynamical outcomes. We thus directly link molecular dynamics simulation, continuum mechanical theory, and multi-compartment systems modeling. Returning to the results from a previous molecular dynamics study of ∼0.5 nm particles (Chapter 3), we provide a QSPR for the permeability in terms of two intuitive molecular interaction parameters: particle-lipid head group and tail group interaction energy well depths (ε_{PH} and ε_{PT}). For the data set, which includes hydrophilic/hydrophobic compounds and an essential proportion of compounds that adsorb to the membrane interface, our QSPR provides a fit ($R^2 \approx 0.91$) far superior to Overton's Rule and many standing QSPRs. As in Chapter 4, we show that the design rules suggested by the results are highly dependent on compound chemistry, system dimensions, the influence of diffusive boundary layers, and time, the latter of which motivates the construction of membrane interaction QSKRs. This work is directly relevant to model

experiments like permeability assays, and can more broadly provide essential insights into the assumptions and construction of standard systems-level models in industry like physiologically-based pharmacokinetic models. Our combined platform has the long-term potential to extend to more advanced pharmaceutical concepts (like allometry and lipidomics) as well as more complicated membrane interaction and transport phenomena.

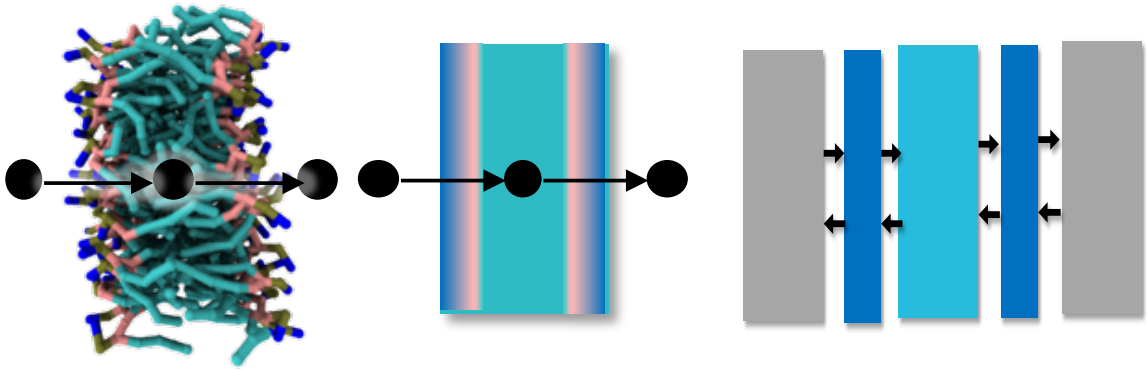

Figure 5.1: Linking detailed molecular dynamics simulation, steady-state continuum theory, and transient multi-compartment modeling for the development of new quantitative structure-property and structure-kinetic relationships in nanoparticle membrane transport.

5.2 Introduction

Phase II clinical trials are a crucial time in the drug development process to gauge a compound's efficacy and toxicity. This stage is currently a major bottleneck and source of failure, suffering from an ~80% failure rate and eating up billions of dollars in development costs. At the preclinical stage, it is becoming increasingly important to understand and predict the biodistribution properties of a multitude of compounds to reduce the pool of

compound candidates, maximize efficacy, and minimize toxicity.

Modeling and simulations strategies can be a major asset to the preclinical development process, and can potentially add mechanistic understanding of compound biodistribution. Two relevant types of modeling strategies are systems biological and pharmacological modeling. Within systems biological approaches, statistical approaches have shown predictive power for small solutes, amino acid side chain analogs, and drugs through the utility of quantitative structure-activity relationship (QSAR) models. In fact, the membrane permeability is a major determinant of biodistribution that highly correlates with gastrointestinal absorption and blood-brain barrier permeability. Models have been specifically designed for experimental membrane permeabilities (quantitative structure-permeability relationship, or QSPR, models), using molecular weights, polar surface areas, partition coefficients, and hydrogen bond counts, and further applying permeability predictions to oral availability, intestinal absorption, skin permeation, and brain permeability.However, QSAR approaches have several shortcomings, including accuracy, a strong dependency on their training sets (i.e. they are not transferable), and providing no information on the underlying atomistic mechanisms. In general, the development of QSARs based on statistics alone is difficult due to the inherent complex, multifactorial, and multiscale nature of biology and human physiology. Specifically in terms of a compound's interactions with and transport across biological membranes, a given particle and membrane combination may be characterized by an ensemble of microstates and nontrivial kinetic mechanisms that interconnect them. This, along with the sheer number of compound design variable combinations, makes solute-membrane interactions difficult to simplify using dimensionality reduction techniques.

Alternatively, pharmacological models and more generally multiscale physics-based modeling techniques provide a dynamical picture, potentially multiscale, of the compound's disposition in the body. Even for membrane interactions and transport, it seems that the

detailed molecular physics are crucial to explanatory and predictive principles. Molecular dynamics (MD) simulation has also been used in conjunction with QSAR models to improve the latter, providing descriptors like drug-solvent interactions, molecular weight, reference solvent metrics, and free energy barriers to be used for higher-accuracy models. A prime example is the membrane-interaction method developed by Hopfinger and coworkers.QSAR models are mutually beneficial to physics-based simulations, as they are less expensive, so the MD and QSAR methods are complementary. In this sense, we seek to augment statistical models with multiscale physics-based modeling. Yet besides the progress of Menichetti et al., most physics-based QSAR strategies do not seek general principles about the impact of compound design parameters on the membrane interactions and transport. A general and systematic study in this regard seems highly desirable.

In Chapter 3 and one of our previous studies,[1] we determined that the inhomogeneous solubility-diffusion (ISD) model and its assumption of a sole translational reaction coordinate z was sufficient in explaining the transport mechanism and continuum of interaction states of sub-nanometer ($\sim 0.5\ nm$) particles of varying chemistry (hydrophobic, hydrophilic, and interfacially active) with model cellular membranes, approximated as a single-component lipid bilayer. The ISD model states that P is a function of the solute diffusivity profile across the membrane $D(z)$ and the corresponding free energy profile, or potential of mean force (PMF), $G(z)$:

$$P^{ISD} \equiv P^{ISD}(G(z), D(z)) = \Big[\int_{-d/2}^{d/2} \frac{e^{\beta G(z)}}{D(z)} dz \Big]^{-1} \tag{5.1}$$

where d is the membrane thickness. All compounds were characterized by a drop in diffusivity while crossing the membrane, while free energy profiles varied with chemistry– hydrophiles with a singular barrier, hydrophobes with a singular well, and interfacially active particles with both a central barrier and additional wells at the membrane interface.

We determined that the ISD model was reasonable on the basis that there is a surprisingly low-dimensional space of relevant order parameters (devoid of internal particle degrees of freedom due to the simplicity and length scale of our model), and that the membrane was not systematically deforming along the translational degree of freedom in a statistically significant manner (e.g. in its membrane height and lipid orientation fields). Furthermore, we confirmed the reasonability of the mechanistic assumptions in the dynamical sense, as the transverse particle diffusivity profiles were relatively well converged, and relatively insensitive to the external biasing (i.e. the stiffness of the force constants holding the umbrella configurations in place during advanced sampling). Because the translational reaction coordinate, for this size of particles, was the slowest, and classical diffusion appeared reasonable, the ISD model was confirmed as a physical model for particle membrane transport in this range of particle designs ($<\sim$ 1 nm and particle-lipid head and tail group interaction well depths ranging from $\varepsilon_{PH} = 0$ to 3.4 k_BT and $\varepsilon_{PT} = 0$ to 1.2 k_BT, respectively).

In Chapter 4, we also determined the imperative of integrating the previously mentioned microscale analysis with macroscopic systems-level models for contextualization of the experimental and biological membrane transport problems. One major contributor to this discrepancy lies in the difference in model assumptions between simulation and experiment. While simulations results are often obtained using a steady-state assumption, experimental results can be susceptible to significant transient effects that can even lead to the observation of trends opposite from simulation. We previously integrated the ISD model with multi-compartment models for a range of sub-nanometer solutes on the hydrophilic/hydrophobic scale, incorporating the influence of compartmental size, unstirred water layers, and time that can collectively lead to orders of magnitude discrepancies between simulation-predicted permeabilities and apparent permeabilities from experiment. Crucially, we showed the potential difference in permeant design rules

based on the steady-state or transient context.

Here, we revisit the studies in Chapters 3 and 4 to provide major explanations and corrections to simulation-calculated steady-state permeabilities for comparison with transient permeability assay experiments. Despite the confirmation of molecular-scale mechanism in Chapter 3, simulation and experimental permeabilities in some cases varied by several orders of magnitude. Furthermore, we found that the QSPR mediating the comparison was inherently flawed, projecting simulation and experimental permeabilities onto an overly simplified physicochemical property of the solute-membrane system (i.e. octanol-water partition coefficient). Closing the gap between these measurements is essential to a proper understanding of the particle design dependence of membrane transport and to overcoming the high attrition rate of drug and consumer product formulations.

In this chapter, we thus outline two major steps to improved connectivity between simulation and experiment: (1) a novel and high-performing two-parameter QSPR to predict permeabilities of a large portion of permeant compound space from molecular interaction parameters and (2) a thorough and generalizable compartmental analysis of common macroscopic assumptions and conditions. Figure 5.2 outlines our general approach, an augmented workflow of our work in Chapter 4 that includes the MD simulations of Chapter 3. First, a QSPR is obtained by linking the physicochemical properties of the NP-membrane system to a particle-based model, reducing the molecular simulation systems to a continuum mechanistic model (e.g. the ISD model), and formulating an expression for the membrane permeability from the continuum model which is then calculated with the molecular simulation results. A quantitative structure-*kinetic* relationship (QSKR) is then obtained by converting the continuum mechanistic model to a discrete kinetic or multi-compartment model that accounts for unstirred water layers, which when fit with common experimental permeability definitions provides a transient permeability estimate

that is a dynamically corrected version of the steady-state permeability and is more comparable to permeability assay experiments. Both the QSPR and QSKR-predicted permeabilities can then be used to guide assumptions for PBPK-type models in a complex physiological setting, or even provide direct, time-dependent parameterization of membrane transport processes. All of this information can ultimately be used to better predict biological, pharmacological, and toxicological properties, ultimately providing a novel QSAR approach. By consolidating previously fragmented techniques and principles on different spatiotemporal scales, we arrive at a rigorous, consistent, and relevant platform for dictating practical design rules for a wide range of chemical compounds.

QSPRs are both a major asset and an implicit bias in the permeability comparisons between simulation and experiment. These correlations provide a low-dimensional mapping onto which simulation and experimental results can be projected and compared. However, QSPRs can be misleading and detrimental if the assumed projection parameters do not represent the dominant physical driving forces in the real phenomenon of interest. In our previous permeability comparison, one problem was the inherent QSPR assumption that membrane permeability should monotonically vary with membrane partition coefficient in the first place. In fact, Overton's Rule

$$P^{Overton} \equiv \frac{K^{o/w} D_c}{d_c} \tag{5.2}$$

where $P^{Overton}$ is the Overton-predicted permeability, $K^{o/w}$ is the octanol-water partition coefficient, D_c is the solute diffusivity, and d_c is the thickness of the hydrophobic membrane core region, was shown in our previous work to be overly simplified in that it reduces a fluctuating and anisotropic lipid bilayer membrane to a static homogeneous slab, when in reality small-scale particles can interact with the membrane in different ways (e.g. with the lipid tail groups, head groups, or in between). We showed this by consistently calculating

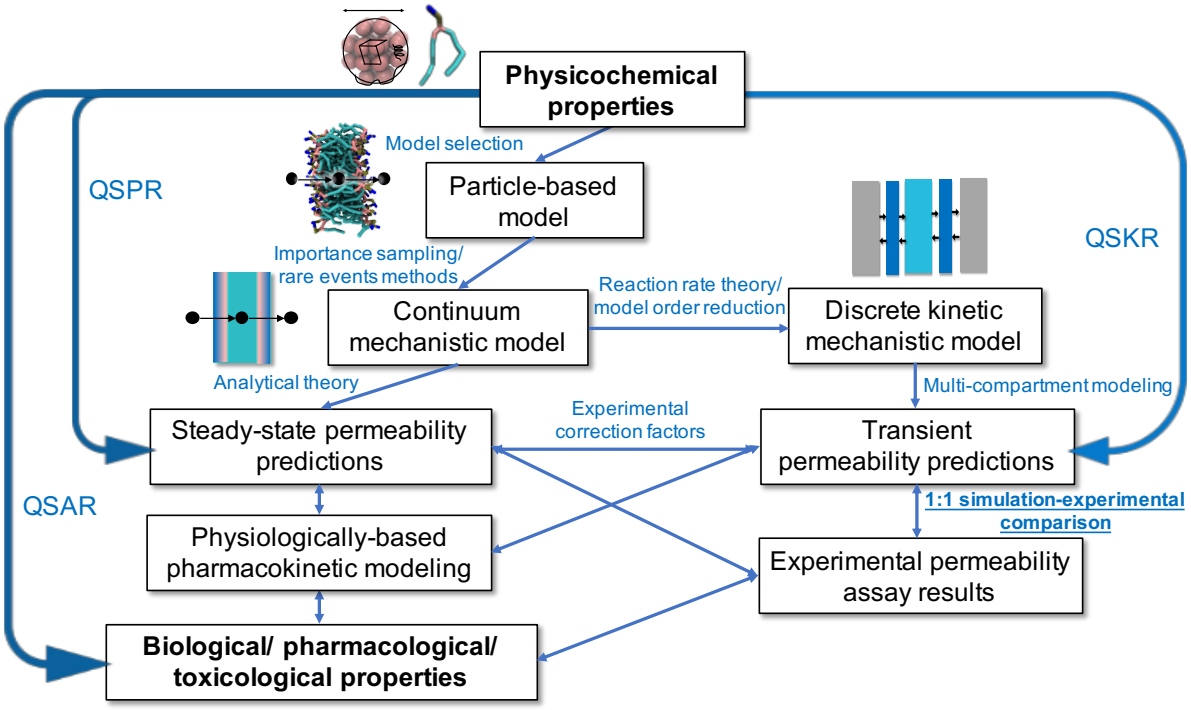

Figure 5.2: A multiscale QSPR/QSKR/QSAR framework for particle transport across lipid membranes, augmented with molecular simulations. In this study, we augment the work of Chapter 4 with a detailed particle-based model, i.e. molecular dynamics simulation. This paradigm allows for the validation of the molecular-scale mechanism of membrane transport, the continuum model for which is then used for steady-state permeability predictions (i.e. a QSPR) and also fed into a discrete kinetic or multi–compartment model for transient permeability predictions (a QSKR). These kinetic predictions can then be compared with one another, fed into physiologically-based pharmacokinetic models, and used to construct more effective models for bioactivity (QSARs).

a size-independent partition coefficient $K^{c,c} \equiv K = \frac{1}{d}\int_{-d/2}^{d/2} e^{-\beta G(z')}dz'$, which has been shown to strongly correlate with $K^{o/w}$, as well as an average transmembrane diffusivity $\bar{D}$ for D_c and different estimates for d_c including the entire thickness d, all calculated from the simulation results. As a QSPR, Overton's Rule does not account for compounds that adsorb to or, more generally, that interact with the membrane interfacial/head-group region. This includes a large set of the small compound space, including amphiphiles, charged molecules, and, particularly, small molecule drugs. We have shown in our previous work that the ISD model permeabilities evaluated with simulation results do not map well to the single dimension of $logK$, principally due to these adsorbing particles with $logK$ values similar to hydrophobes that insert in the membrane core but with permeabilities several orders of magnitude below those hydrophobes.

The main goal in developing effective QSPRs is to relate a compound via its essential quantifiable descriptors to predict all structural, thermodynamic, and kinetic properties of interest, in an accurate, efficient, and transferable manner. For particle membrane transport, quantitative structure-*permeability* relationships (themselves sometimes known as QSPRs) should naturally incorporate primary descriptors pertaining to the particle and membrane and secondary descriptors that relate to the solute-membrane interactions, amongst others. This results in, for example, $P = P(size, surfacechemistry, shape, elasticity, etc.)$. For solutes that satisfy the physical criteria of the ISD model (i.e. nondisruptive simple diffusion across the membrane), the problem comes down to mapping the descriptors to $D(z)$ and $G(z)$. Marrink and Berendsen lead the early charge in principles for solute-membrane QSPRs, showing that solubility and permeability are well correlated with hydrophobicity/solubility in the high density lipid tail group region and that small solute ($MW < 50$) permeability is more strongly dependent on solute size than that of larger solutes ($50 < MW < 300$).

Figure 5.3 outlines some common QSPR approaches to linking a solute's physicochem-

ical properties to its steady-state permeability. Our intended approach is in blue.

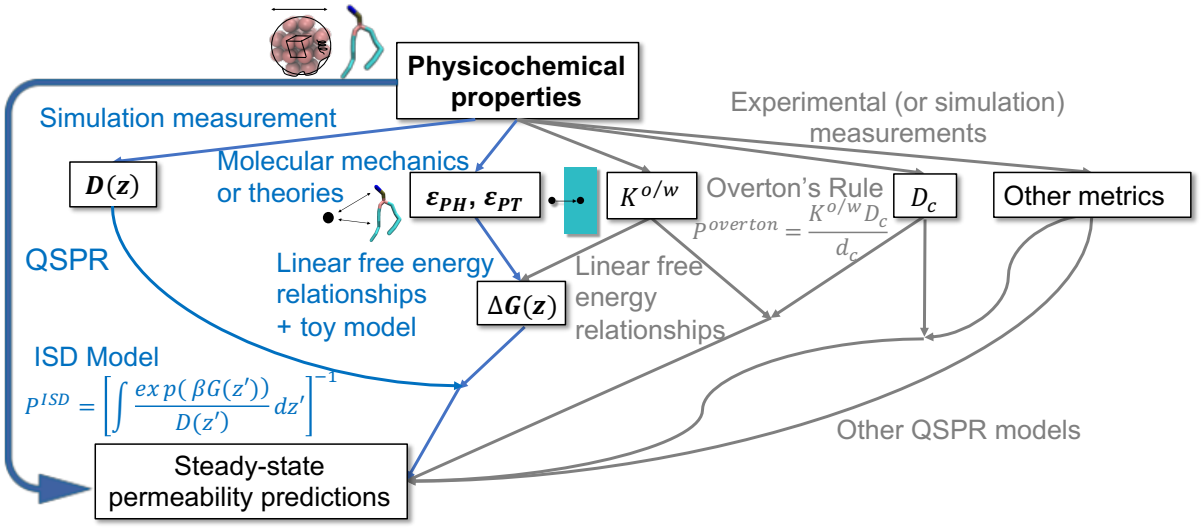

Figure 5.3: Comparison of approaches to QSPRs. Here, we present our approach and those of others to quantitative structure-permeability relationships for the membrane transport of small molecule compounds. While others often construct statistical models with various combinations of structural, thermodynamic, and dynamic properties of the particle and membrane, here we directly calculate free energy and diffusivity profiles over the mechanistically-proven coordinate for a physically-relevant prediction of the permeability, which can then be related back to the physicochemical properties of the system.

Here, we draw inspiration from the work of Neale and Pomès, which sought to classify a large set of molecular-scale compounds in their thermodynamics with lipid membranes. The authors developed a semiquantitative classification of ISD PMF ($G(z)$) types based on their major features, including the number and location of free energy features and relative heights of those features. Figure 5.4 surveys some of the PMF types in this classification system. As indicated above, we seek to represent a larger amount of compound space than the typical hydrophobic/hydrophilic scale by accounting for compounds that favorably interact with lipid head groups. In terms of the Neale-Pomès library of compounds, this significantly expands our exploration of PMF space, from ~25 to 85 percent of typical

small compounds.

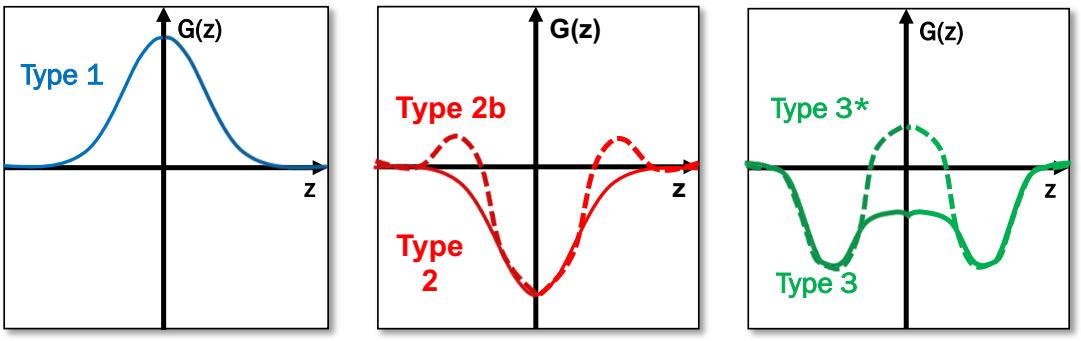

Figure 5.4: Semiquantitative PMF classifications from the work of Neale and Pomès. Type 1 PMFs are characterized by a singular free energy feature–a central barrier–while Type 2 PMFs inversely feature a singular central free energy well. Type 2b PMFs are characterized by a central well and two intermediate barriers, while Type 3 PMFs have two intermediate wells separated by a central barrier lower in free energy than the initial and final states and Type 3* PMFs have two intermediate wells separated by a barrier higher than the initial and final states.

The above matters necessitate a follow up study to Chapter 3 that includes (1) an updated, better fitting QSPR for our data set and (2) an analysis of transient effects that can potentially impact the principles obtained via steady-state assumptions.

5.3 Methods

5.3.1 Molecular simulations

As in Chapter 3, the study here concerns the modeling of the lipid bilayer membrane transport for sub-nanometer particles of a spectrum of chemistries. In Chapter 3, we used MD simulation to explore these sub-nanometer particles, specifically (1) confirming the inhomogeneous solubility-diffusion model as a mechanistic description of sub-nanometer particle membrane transport and (2) parameterizing the ISD model with simulation-calculated free energies and diffusivities. Figure 3.5, panel (a) illustrates the particle part of this model. Different chemistries were modeled through modulation of the Lennard-Jones

well depths ϵ for the particle-lipid head group and particle-lipid tail group interactions. Specifically, hydrophilic, hydrophobic, and "interfacially active" particles were designed with weak head and tail group interactions, weak head and strong tail group interactions, and strong head and weak tail group interactions, respectively. For further details, see Chapter 3 and the corresponding publication.[1]

5.3.2 Quantitative structure-property relationship (QSPR)

We fit the PMFs calculated from the MD simulations to a phenomenological "triple-Gaussian" PMF model (Figure 5.5) that generally includes five fitting parameters:

$$G = G(z; \varepsilon_{PH}, \varepsilon_{PT}) = -\alpha_1 e^{-\frac{z^2}{2{\sigma_1}^2}} - \alpha_2 \left[e^{-\frac{(z-z_2)^2}{2{\sigma_2}^2}} + e^{-\frac{(z+z_2)^2}{2{\sigma_2}^2}} \right] \tag{5.3}$$

where α_1 and α_2 are the heights of the central and interfacial PMF features, σ_1 and σ_2 are roughly the widths of those features, and z_2 is the offset of the two interfacial Gaussian functions (equal and opposite) from the central Gaussian. In this model, α_1 and α_2 effectively represent transfer free energies from the external aqueous environment to the membrane center and membrane interface, respectively. This provides a more explicit picture of the classification scheme of Neale and Pomès in that effectively 85 percent of their PMF types can be explicitly mapped to (α_1, α_2) space (assuming that σ_1, σ_2, and z_2 are roughly constant across compounds). Indeed, we find upon model optimization that the additional three parameters can be discarded without significant impact on permeability predictions, due to the lower relative variance of these fitting parameters across compounds relative to α_1 and α_2.

Furthermore, we have found that the transfer free energy features map well to a

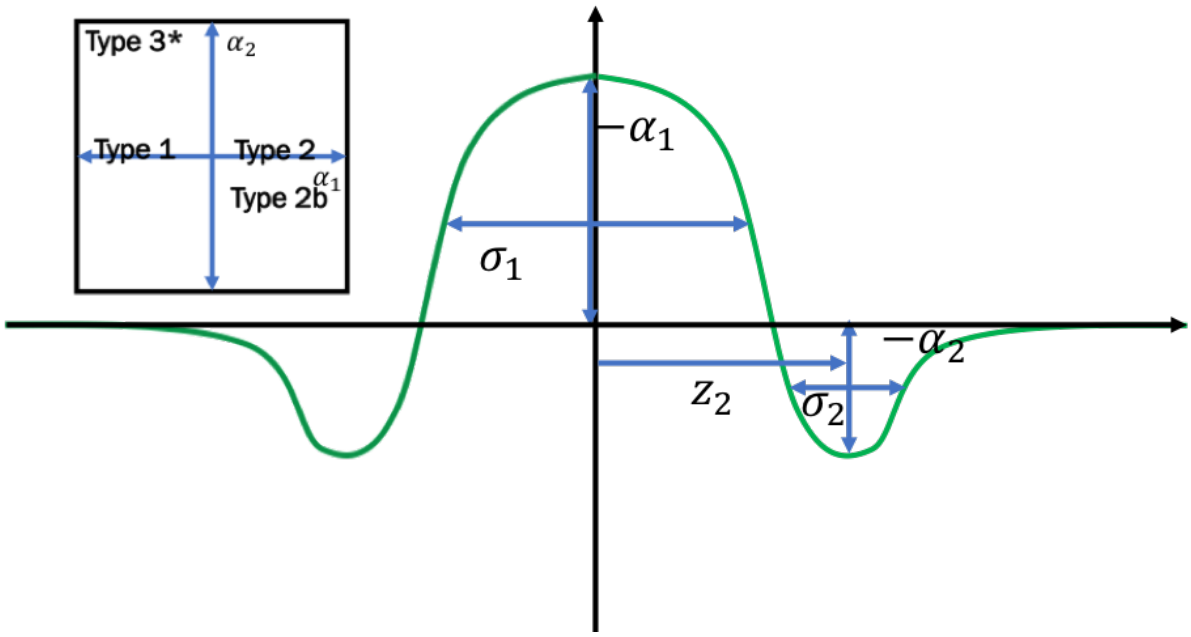

Figure 5.5: "Triple Gaussian" model for the transmembrane PMFs of small hydrophilic, hydrophobic, and "interfacially active" particles. The intuition behind this phenomenological PMF model is, unlike Overton's Rule and transport across a layer of hydrocarbons, to account both lipid head and tail groups in the anisotropic lipid bilayer structure. This PMF model accounts for a wider range of transmembrane PMFs, specifically covering Types 1, 2, 2b, and 3* in the Neale-Pomès library (inset).

bilinear regression model of the molecular interaction parameters:

$$\begin{cases} \alpha_1 = c_{11}\varepsilon_{PH} + c_{21}\varepsilon_{PT} + c_{31} \\ \alpha_2 = c_{12}\varepsilon_{PH} + c_{22}\varepsilon_{PT} + c_{32} \end{cases} \tag{5.4}$$

where c_{11}, c_{21}, c_{31}, c_{12}, c_{22}, and c_{32} are regression fitting parameters. The consequences of these linear free energy relationships (LFERs) are twofold: (1) a bidirectional thermodynamic paradigm for predicting transfer free energies from molecular interaction parameters and vice versa, and (2) a direct and simple QSPR relating the permeability to the molecular interactions:

$$P(\varepsilon_{PH}, \varepsilon_{PT}) = \Big[\int_{-d/2}^{d/2} \frac{e^{\beta G(z;\varepsilon_{PH},\varepsilon_{PT})}}{\bar{D}(z)} dz \Big]^{-1} \tag{5.5}$$

where $\bar{D}(z)$ is the average diffusivity profile across all compounds. We found in Chapter 3 that the ∼0.5 nm particle diffusivity profiles were roughly chemistry-independent (within statistical error), and given that the diffusivity profile contributes only linearly to the permeability while the free energy profile contributes exponentially, the assumption of a chemistry-independent diffusivity profile appears reasonable. As the diffusivity profiles vary almost two orders of magnitude across the reaction coordinate, we found that incorporating the z-dependence of the diffusivity still led to a much better fit than both a chemistry-independent and constant diffusivity (as in Overton's Rule). An analogous QSPR for the mean first passage time (MFPT) rate constant $k_{MFPT}(\varepsilon_{PH}, \varepsilon_{PT})$ can be constructed using Equation 4.4 and the free energy and diffusivity profile models (see Chapter 4 for more details).

5.3.3 Multi-compartment modeling

As in Chapter 4, we also directly link the microscopic analysis to a macroscopic compartment model of membrane transport. The uniqueness here, however, lies in the use of a real family of free energy and diffusivity profiles, as opposed to a toy model. As $G(z)$ and $D(z)$ are fit using the molecular simulations, we directly connect MD to continuum theory and compartmental models. Here, we augment the five-compartment model of Chapter 4 to seven compartments (six layers), accounting not only for the donor (D), receiver (R), membrane core (C), and membrane-water interfaces (I_1 and I_2), but also for the membrane head group regions (H_1 and H_2) in which the hydrophobic and "interfacially active" particles non-negligibly reside (Figure 5.6). Transfer between all compartments is reversible and assumed to follow the law of mass action, and the rate is additionally proportional to piecewise permeabilities P_i and the cross-sectional area A of the slab geometry. Transfer across the UWLs occurs between the donor and first interfacial compartments or between the second interfacial and receiver compartments, with a permeability $P_0 \equiv D_0/L_{UWL}$ determined by diffusion over a flat free energy and diffusivity landscape (and thus inversely proportional to the UWL thickness). Other transfer processes are parameterized by modified versions of the ISD model:

$$\begin{cases} P_1 \equiv \left[e^{-\beta G(-d_C/2-d_H} \int_{-d_C/2-d_H}^{-(d_C+d_H)/2} \frac{e^{\beta G(z)}}{D(z)} dz \right]^{-1} & \textit{(headgroup entry)} \\ P_2 \equiv \left[e^{-\beta G(-(d_C+d_H)/2)} \int_{-(d_C+d_H)/2}^{0} \frac{e^{\beta G(z)}}{D(z)} dz \right]^{-1} & \textit{(midplane entry)} \\ P_3 \equiv \left[e^{-\beta G(0)} \int_{0}^{(d_C+d_H)/2} \frac{e^{\beta G(z)}}{D(z)} dz \right]^{-1} & \textit{(midplane escape)} \\ P_4 \equiv \left[e^{-\beta G((d_C+d_H)/2)} \int_{(d_C+d_H)/2}^{d_C/2+d_H} \frac{e^{\beta G(z)}}{D(z)} dz \right]^{-1} & \textit{(headgroup escape).} \end{cases} \tag{5.6}$$

The piecewise permeabilities P_1, P_2, P_3, and P_4 correspond to headgroup region entry from the donor-or receiver-side membrane-water interface, membrane core region entry from the donor- or receiver-side headgroup region, membrane core region escape to the donor- or

receiver-side headgroup region, and headgroup region escape to the donor- or receiver-side membrane-water interface, respectively. Δx_D, d_I, d_H, d_C, and Δx_R are the thicknesses of the donor compartment, proximal and distal interfacial compartments, proximal and distal headgroup regions, membrane core, and receiver compartment, respectively. As in the previous chapter, here integral limits correspond to physical boundaries of layers between the compartments and the free energies at the start of each step are normalized with respect to the origin compartment. Again, this correction to the normalization allows for incorporation of relative free energy features, incorporating the difficulty (or ease) of escape from compartments for which a given particle experiences ease (or difficulty) of entry, and produces roughy a single-particle metric by correcting for the holdup or steady-state loading in the unmodified ISD model expression. The full system of ODEs for this compartmental modeling scheme is thus:

$$\begin{cases} \frac{dC_D}{dt} = -\frac{P_0}{\Delta x_D}\Big(C_D - C_{I1}\Big) \\ \frac{dC_{I1}}{dt} = -\frac{1}{d_I}\Big(\Big(P_0 + P_1\Big)C_{I1} - \Big(P_0 C_D + P_4 C_{H1}\Big)\Big) \\ \frac{dC_{H1}}{dt} = -\frac{1}{d_H}\Big(\Big(P_4 + P_2\Big)C_{H1} - \Big(P_1 C_{I1} + P_3 C_C\Big)\Big) \\ \frac{dC_C}{dt} = -\frac{1}{d_C}\Big(2P_3 C_C - P_2\Big(C_{H1} + C_{H2}\Big)\Big) \\ \frac{dC_{H2}}{dt} = -\frac{1}{d_H}\Big(\Big(P_4 + P_2\Big)C_{H2} - \Big(P_1 C_{I2} + P_3 C_C\Big)\Big) \\ \frac{dC_{I2}}{dt} = -\frac{1}{d_I}\Big(\Big(P_0 + P_1\Big)C_{I2} - \Big(P_0 C_R + P_4 C_{H2}\Big)\Big) \\ \frac{dC_R}{dt} = -\frac{P_0}{\Delta x_R}\Big(C_R - C_{I2}\Big) \end{cases} \tag{5.7}$$

After solving the system of ODEs, the donor and receiver concentration profiles are used to measure the flux through the membrane. As in the previous chapter, we use generalizations of two standard experimental models for the (apparent) membrane

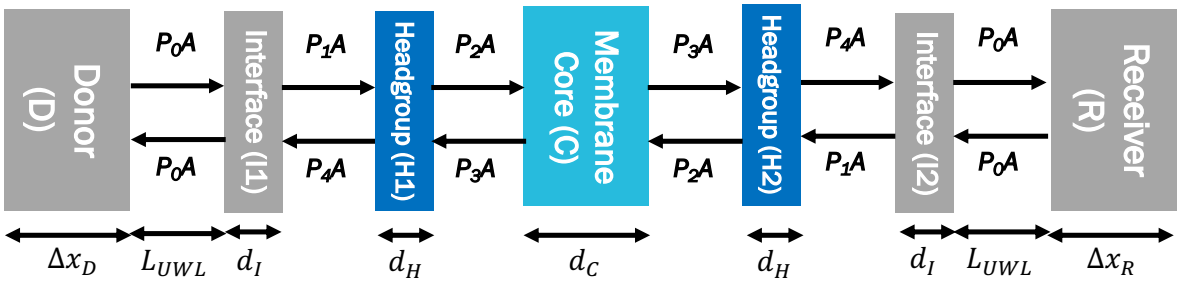

Figure 5.6: Seven-compartment PAMPA model for interfacially active, hydrohpilic, and hydrophobic compounds. The seven-compartment model here provides explicit representation of the donor and receiver bins, membrane core region, proximal and distal membrane headgroup regions, and membrane-water interfaces. Transfer between compartments is reversible, and proportional to the relevant permeability and membrane cross-sectional area, with the UWL thicknesses incorporated directly into P_0. Relative compartmental sizes are incorporated via quantitatively-relevant compartment thicknesses.

permeability:

$$\begin{cases} \hat{P}^{app}(t) \equiv \frac{P^{app}(t)}{P^{ss,isd}} = \left.\frac{dC_R}{dt}\right|_t \frac{V_R}{AC_0P^{ss,isd}} \\ \hat{P}^{app,2}(t) \equiv \frac{P^{app2}(t)}{P^{ss,isd}} = \left.\frac{dC_R}{dt}\right|_t \frac{V_R}{A(C_D-C_R)P^{ss,isd}} \end{cases} \tag{5.8}$$

5.4 Results and Discussion

5.4.1 QSPR results

Figure 5.7 shows the linear free energy relationships (LFERs), between the particle-lipid head and -lipid tail group interaction energies and the transfer free energies to the membrane core and interface, resulting from the PMF model and bilinear regression of $\alpha_1(\epsilon_{PH}, \epsilon_{PT})$ and $\alpha_2(\epsilon_{PH}, \epsilon_{PT})$. The LFERs clearly show that, for the central free energy feature (transfer free energy from the bulk water to the membrane core midplane), the tail group attraction plays an essential role–the higher the ϵ_{PT}, the higher the α_1 and deeper the central free energy minimum. For the intermediate feature (transfer free energy from

the bulk water to the membrane headgroup region), the higher the head group attraction ϵ_{PH}, the higher the α_2 and deeper the intermedate free energy minimum. We found that the bilinear regression model was essential to fitting the LFERs, as α_1 is still slightly sensitive to ϵ_{PH} and α_2 is still slightly sensitive to ϵ_{PT}.

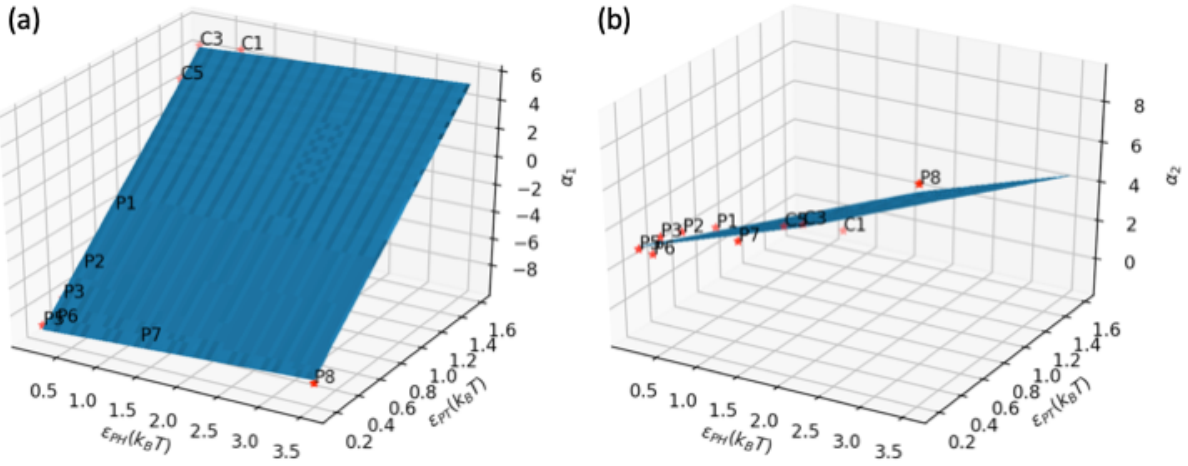

Figure 5.7: Linear free energy relationships between transmembrane transfer free energies and pairwise molecular interaction energies in our QSPR. In addition to our triple-Gaussian PMF model linking transfer free energies α_1 and α_2 the full transmembrane free energy profile, we found that (a) α_1 and (b) α_2 could also be linked back to particle-lipid head group and -lipid tail group interaction energies ϵ_{PH} and ϵ_{PT}, thus providing a direct relationship between interaction energies and the steady-state ISD permeability. Specifically, $\alpha - \epsilon$ relationships mapped well to a bilinear regression model (i.e., the data was more or less confined to a plane).

As a collective result of the LFER relating ϵ_{PH} and ϵ_{PT} to α_1 and α_2, the triple Gaussian PMF model relating α_1 and α_2 to $G(z)$, and the chemsitry-independent assumptions in the $\bar{D}(z)$, we obtain a QSPR predicting the membrane permeability as a function of the interaction energies. Figure 5.8 extends the analysis of Chapter 3, plotting P vs. K (Fig. 3.8), to this two-dimensional parameter space in ϵ_{PH} and ϵ_{PT}. We plot the QSPR in this study as well as Overton's Rule for reference. This reveals a dramatic improvement in permeability predictions whereby our QSPR closes the gap between predicted and "actual" (MD) permeabilities, particularly for particles like P7 and P8 with strong head group

interactions. Overton's Rule, in this regime, overpredicts steady-state permeabilities by several orders of magnitude. Despite the small training set in this initial exploratory QSPR study, we find that our novel QSPR attains competitively high explanatory power ($R^2 \sim 0.91$ vs. ~ 0.85 for a somewhat recent QSPR[2]).

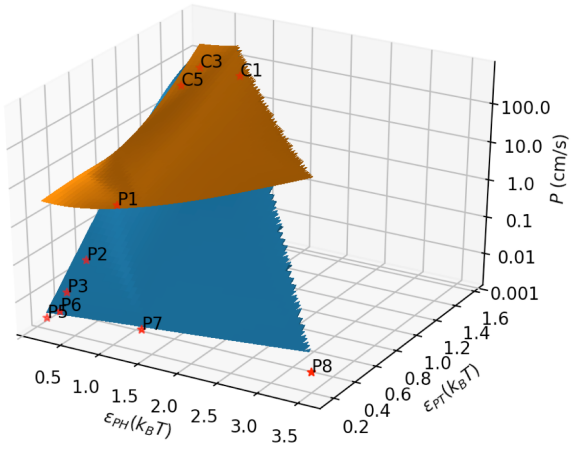

Figure 5.8: Expanding explanatory and predictive capabilities of Overton's Rule to a wider range of compound chemistries with our QSPR. Shown here, in the space of particle-lipid head group and particle-lipid tail group interactions ϵ_{PH} and ϵ_{PT}, respectively, are predictions of the steady-state permeability from our QSPR (blue) as compared with Overton's Rule (orange). Our QSPR critically accounts for particles that possess strong lipid head group affinities but not necessarily strong tail group affinities.

5.4.2 Steady-state analysis

We leverage our QSPR first for steady-state analysis in the space of particle-lipid head and tail group interactions (Figure 5.9). Panel (a) recapitulates the family of PMFs in our training set, now predicted by the QSPR (i.e. not the original MD data), ranging from Type 1 to Type 2 and Type 3* PMFs. Panel (b) plots the corresponding steady-state transmembrane normalized concentration profiles predicted by the ISD model (per Equation 4.7), revealing broad central peaks in concentration for hydrophobes in the membrane center as well as narrower headgroup region peaks for interfacially active

particles. Panel (c) is a collapsed version of our QSPR results in Figure 5.8, while panel (d) is the corresponding projection in (α_1, α_2) transfer free energy space (for ease of classification of the PMF types). Both panels show how the steady-state permeability spans several orders of magnitude. $P(\epsilon_{PH}, \epsilon_{PT})$ shows that, the higher the affinity, the higher the permeability, with P rising faster with the tail group attraction ϵ_{PT} than for the head group attraction ϵ_{PH} due in large part to the wider tail group region relative to the head group regions. Similarly, $P(\alpha_1, \alpha_2)$ shows that, the deeper the free energy wells (higher the α), the higher the permeability, with P rising faster with α_1 corresponding to the central free energy feature in the tail group region for similar reasons. Panels (e) and (f) then show the corresponding design rules for single-particle transport in terms of k_{MFPT}. An intermedium optimum appears for C type hydrophobic particles with modest tail group affinity and weak head group affinity (alternatively, modest $\alpha_1 > 0$ and $\alpha_2 \sim 0$). This optimum results from the balance of two principal processes: membrane entry, faster when entering deeper free energy wells, and membrane escape, faster when leaving high free energy barriers. From the optimal intermediate hydrophobic chemistry, increasing tail group attraction starts to penalize membrane escape more than it rewards membrane entry; decreasing tail group attraction rewards membrane escape, but penalizes membrane entry. As for the permeability, the particle-lipid head group affinity has a weaker effect than tail group affinity on k_{MFPT}. Permeabilities (representing bulk particle transport, and scaling with the thermodynamic loading in the membrane) can be linked to their corresponding MFPT rate constants through the MFPT in ISD relation (Equation 4.11). As for Chapter 4, the results here show that, by accounting for the thermodynamic loading in the membrane, the permeability metric swamps out the single-particle kinetic optimum in the MFPT rate constant.

We extend the analysis of practical engineering design rules from Chapter 4 to this family of sub-nanometer hydrophilic, hydrophobic, and interfacially active particles as

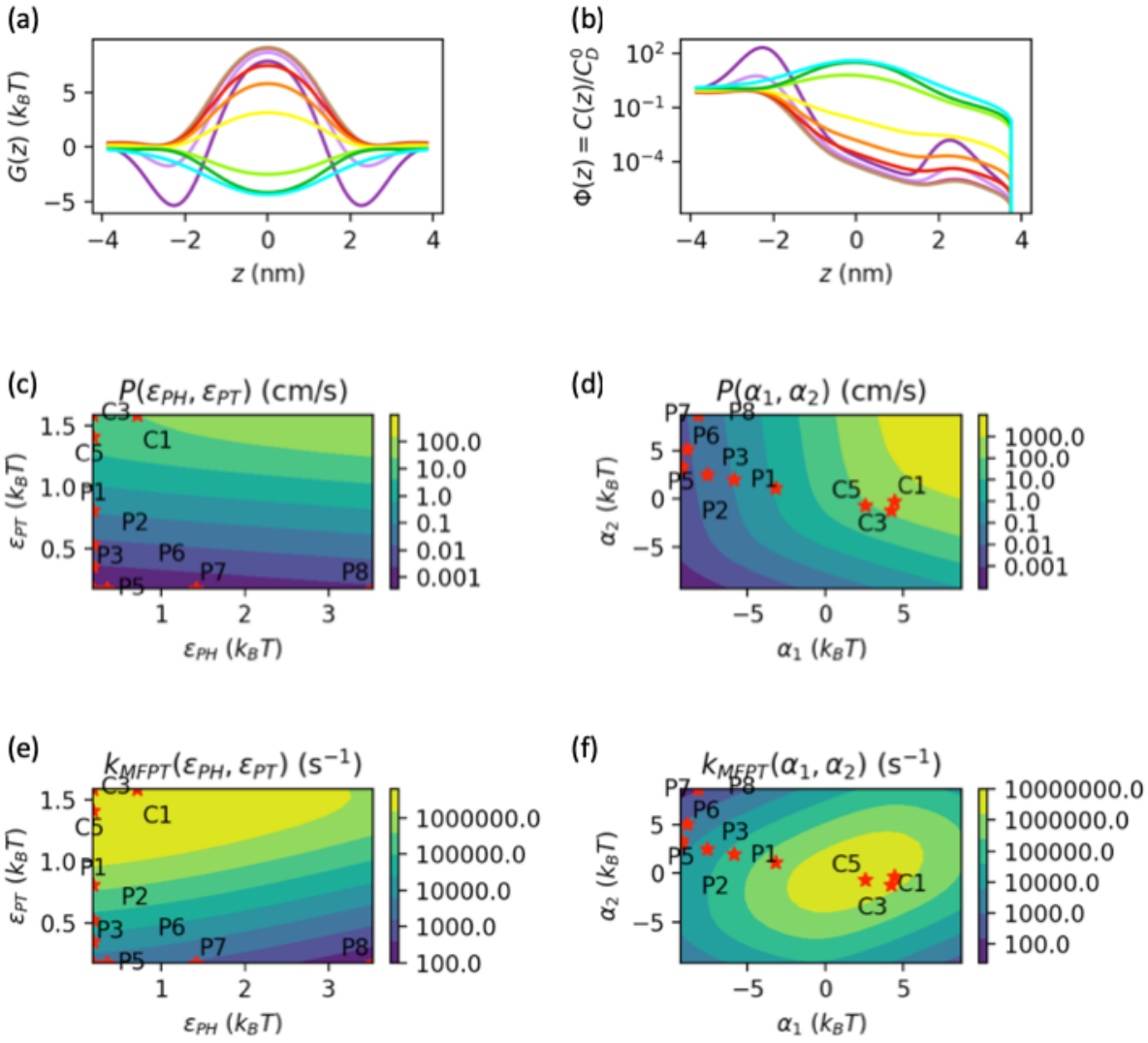

Figure 5.9: Free energies and steady-state design rules with our QSPR. Shown here are the (a) free energy and steady-state predictions from our QSPR, including (b) the normalized steady-state transmembrane concentration profiles, "permeability maps" in both (c) ϵ and (d) α space, and "MFPT rate constant maps" in (e) ϵ and (f) α space as well (for all maps, the training set is noted by red asterisks). By expanding our trained QSPR into broader design space, it becomes clear that P particularly from increased tail group affinity or a deeper central free energy well, while k_{MFPT} is optimized at some intermediate hydrophobicity beyond which the membrane serves more as a trap from a single-particle transport perspective.

well. The steady-state flux across the membrane $J^{ss}(\epsilon_{PH}, \epsilon_{PT}, C_D) \approx P(\epsilon_{PH}, \epsilon_{PT})C_D$, and therefore bulk particle transport, can be tuned with the permeant design and donor-side concentration. As shown in Figure 5.9, design affects both the single-particle kinetics as well as the thermodynamic loading. Figure 5.10 shows the steady-state flux as a function of head and tail group affinity and at a fixed donor-side concentration of 10^{-7} mg/mL. As before, design parameters–here, ϵ_{PH}, ϵ_{PT}, and C_D–cannot simply be increased without bound. As in Chapter 4, we plot the free volume "filling limit" at which an infinitesimal point in the membrane fills its available space with particles loaded at steady-state (i.e. on a pointwise basis). Practically speaking, since membrane loading is highly sensitive to ϵ_{PT}, care should be taken in selecting fast permeants solely on the basis of hydrophobicity–regardless of extensive donor-size concentration, above a critical ϵ_{PT} (increasingly sensitive with head group affinity ϵ_{PH}), at least one point within the membrane maximally loads with particles. At this critical affinity and likely much lower, the particle loading will significantly impact the membrane structure and stability. In the pointwise full state, the particular state along the membrane that is full should start to rearrange lipids in the transverse direction, leading to severe membrane structural deformations. Unlike Chapter 4, however, we do not show when the total membrane fills its total available space with particle (i.e. the integral metric), as it falls outside the range of chemistries studied here and is therefore irrelevant. Alternatively, the membrane flux can be enhanced by increasing the donor-side concentration, which in addition to hydrophobicity may impact aggregation in aqueous solution. In addition to free volume constraints, several biological considerations are also expected to influence permeant design. In Chapter 4, for example, we discussed cytotoxicity for particles like fullerenes. Interfacially active particles here are a simplified and semiquantitative representation of amphiphilic and charged particles, which themselves can have serious toxicity concerns as well as problems in overcoming biological barriers like the immune system.

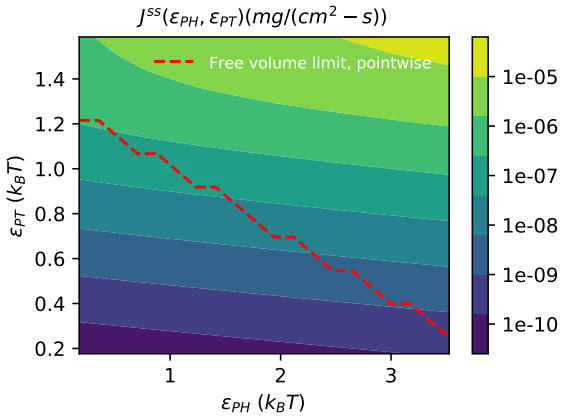

Figure 5.10: Practical steady-state design rules with our QSPR. We illustrate the hypothetical yet practical scenario in which the permeant design optimization on the basis of lipid head group affinity ϵ_{PH} and lipid tail group affinity ϵ_{PT}, along with donor compartment concentration C_D (here set to 10^{-7} mg/mL), should consider physical and biological constraints. Here, we simply show a free volume constraint line above which at least one point in the membrane fills withs its available volume with particles, therefore providing an upper limit for physical and biological effects on the membrane.

A critical step to bridging steady-state simulation results to transient scenarios like experimental permeability assays is to first capture the influence of unstirred water layers on steady-state permeability. Figure 5.11 shows the variation in permeability for the initial training set of compounds across several decades in UWL thickness. For negligible UWLs, the results without boundary layers are recovered–hydrophobic particles are the highest in permeability, followed by the interfacially active and hydrophilic particles (nearly indistinguishable from one another). Values at negligible UWL thickness vary from $\sim 10^{-3}$ to 10^{2} cm/s, or roughly five orders of magnitude. For experimentally-relevant UWL thicknesses on the order of microns, the permeability rankings are undisturbed, but the practical differences between them are negligible–permeabilities range from $\sim 10^{-3}$ to 10^{-1} cm/s, which tend to be on the upper limit of permeabilities observable in permeabilities assays like PAMPA. For still thicker UWLs, the transport problem becomes UWL diffusion-limited, and the chemistry-specific effects are negligible.

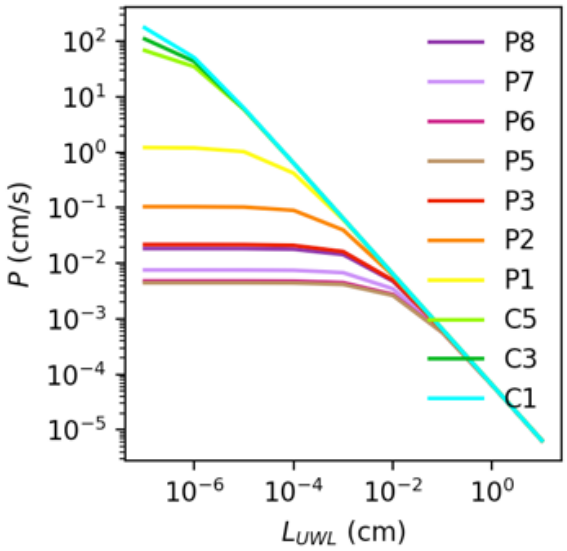

Figure 5.11: Impact of UWLs on steady-state permeabilities. At steady-state, UWLs provide additional resistances in series with the intrinsic membrane resistance. From negligible to experimentally relevant UWLs on the order of microns, effective steady-state permeabilities drop several orders of magnitude, depending on the particle chemistry, but the ranking of permeabilities is unaltered.

After correcting for the "structure-property assumption" (i.e. projecting permeabilities on head and tail group affinities instead of a single partition coefficient), there remain large discrepancies between coarse-grained simulation compounds and their direct experimental analogs. As a point of comparison, the P5 particle type in the Dry Martini model– here, with a permeability prediction of 4.46x10^{-3} cm/s–is intended to correspond to acetamide, which has been measured in PAMPA experiments with egg lecithin membranes (predominantly composed of phopholipids) at (2.9+/-0.3)x10^{-4} cm/s. The reported PAMPA value is corrected for the presence of a 120+/-40 μm UWL at least one the proximal side of the membrane. Thus, this order of magnitude discrepancy between simulation and experiment is not attributable to UWL effects at steady-state. For this reason, we also examine transient effects that have the potential to muddle steady-state measurements in experiment.

5.4.3 Transient analysis

The other critical step in bridging to experiment lies in the incorporation of dynamic effects. To address these up to experimentally relevant timescales, we turn to multi-compartment modeling. Figure 5.12 shows the result of the seven-compartment model parameterization via Equations 5.6. Panels (a), (b), (c), and (d) show the results in chemistry (particle-lipid head and -lipid tail group interaction) space for headgroup entry, core region entry, core region escape, and headgroup escape, respectively. Head group entry kinetics (panel (a)) scale strongly and proportionally with increasing head group interaction ϵ_{PH}, while tail group attraction ϵ_{PT} has a very weak effect. This is because interfacially active particles (large ϵ_{PH}) are entering a free energy well in the membrane head group region, while hydrophobic particles are gradually traveling down a free energy landscape. Inversely, tail group entry kinetics (panel (b)) scale strongly with tail group affinity and weakly with head group affinity, as hydrophobes (large ϵ_{PT}) are entering a well while interfacially active particles, along with hydrophiles, are entering a barrier. Tail group escape kinetics (panel (c)) are large for interfacially active particles, as they are again entering a well–this time on the other side of the membrane–and also exiting a barrier; kinetics are small for hydrophobes, as they are exiting their central free energy well. For head group escape kinetics (panel (d)), both head and tail group affinities have an adverse effect, as increasing ϵ_{PH} and ϵ_{PT} generally reduces the central free energy barrier, eventually to a free energy well, and adds intermediate free energy wells in the head group regions. This is clearly shown in Figure 5.7. As a result, the membrane generally acts as a trap, and effect that has been discussed here and in recent literature. However, here we also show the impact of multiple traps that are separated by an intermediate barrier. The results are therefore intuitive–for example, for a hydrophobic particle (large ϵ_{PT}, small ϵ_{PH}), (1) headgroup entry is moderate, (2) core region entry is moderate, (3)

core region escape is slow, and (4) headgroup entry is moderate. Alternatively, for an interfacially active particle (small ϵ_{PT}, large ϵ_{PH}), (1) headgroup entry is fast, (2) core region entry is slow, (3) core region escape is moderate, and (4) headgroup escape is slow. For hydrophilic particles (small ϵ_{PT} and ϵ_{PH}), entry processes are slow and escape processes are fast.

For this transient analysis, we take three case studies from the original training set–the P8 interfacially active particle, P5 hydrophilic particle, and C1 hydrophobic particle. P8 again has two free energy wells separated by a barrier (Type 3* PMF), P5 has a singular barrier (Type 1 PMF), and C1 has a singular well (Type 2 PMF). For the three case studies and varying UWL thickness, the resulting parameterization of the seven-compartment model results in vast differences in characteristic time scales. Figure 5.13 shows the two slowest time scales beyond the equilibrium solution, obtained from eigenvalue analysis of the system of ODEs (Eqns 5.7), as a function of unstirred water layer thickness L_{UWL} and chemistry. As before, time scales are determined from the inverse of the eigenvalues.[3] As we have illuminated in Chapter 4, the penultimate time scale roughly corresponds to the equilibration of the donor and receiver compartments and therefore the elimination of the membrane flux, while the third slowest time scale roughly corresponds to the achievement of pseudo-steady-state. The timescales are largely chemistry-dependent. The penultimate time scale τ_5 is largest for hydrophilic and interfacially active particles (essentially overlapping) with minimal affinity for the membrane, and smaller for hydrophobic particles that are attracted to the membrane core. The situation is different for the third slowest times scale τ_4, which is smaller for the hydrophiles and larger for the hydrophobes and interfacially active particles due to their attraction to various regions of the membrane. Together, these two time scales determine the window of pseudo-steady-state behavior before which the membrane layers are dynamically loading and after which the donor and receiver compartments are equilibrated. The time scales are also UWL-dependent–as

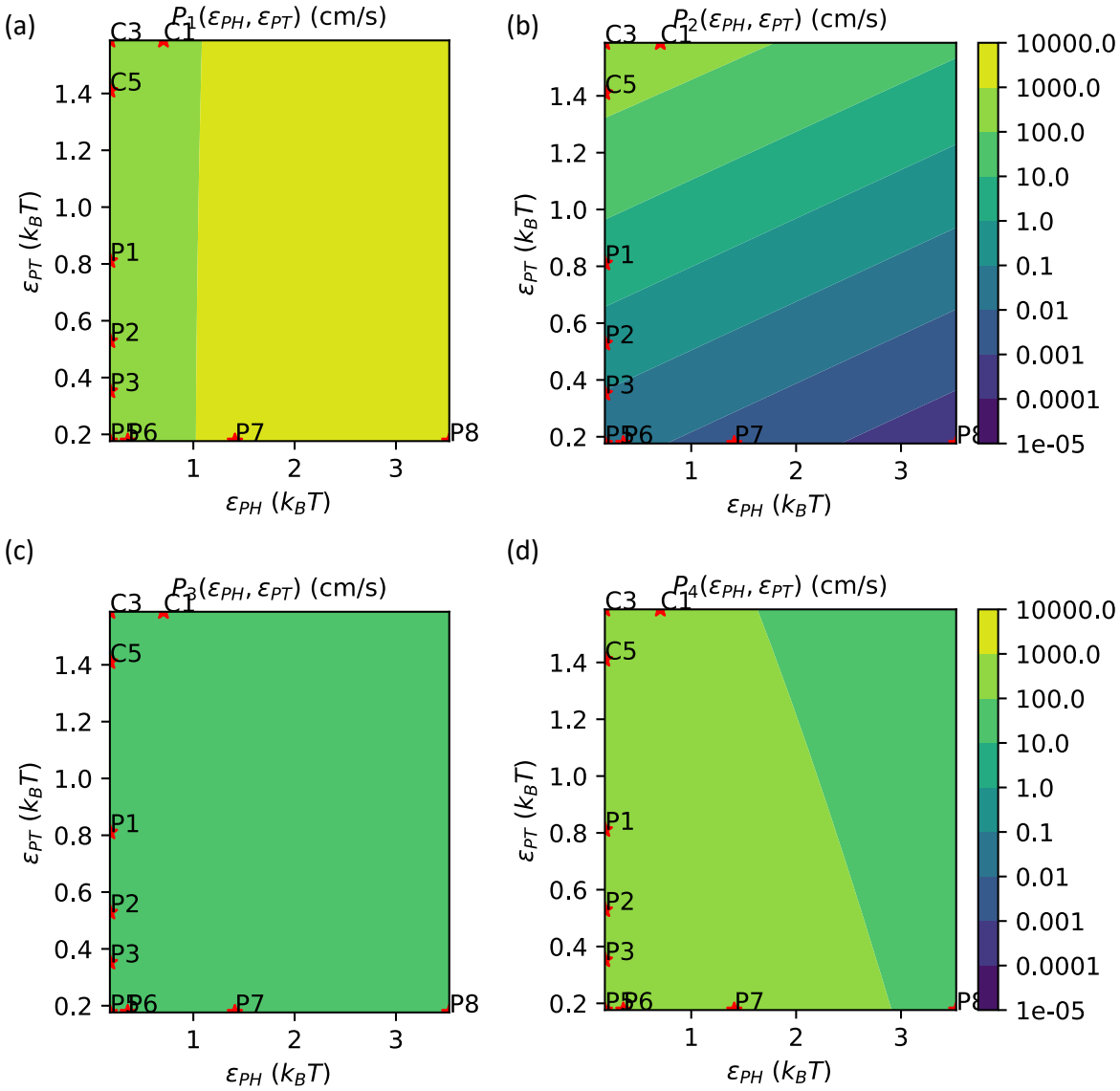

Figure 5.12: Kinetic parameterization of seven-compartment PAMPA model for interfacially active, hydrophilic, and hydrophobic compounds. Shown here are QSPR predictions of piecewise permeabilities for membrane (a) head group region entry, (b) tail group region entry, (c) tail group region escape, and (d) head group region escape, as calculated by a modified version of the ISD equation (Equations 5.6). Roughly speaking, head group entry scales with head group affinity, tail group entry scales with tail group affinity, tail group escape scales inversely with tail group affinity, and head group escape scales inversely with both head and tail group affinity.

for the steady-state permeabilities with UWLs (Figure 5.11), here the penultimate time scales become chemistry-independent at larger and larger UWL thickness.

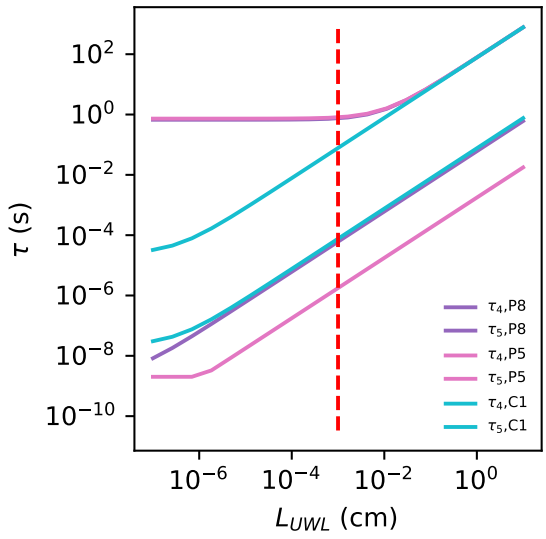

Figure 5.13: Characteristic time scales of seven-compartment PAMPA model for our QSPR with UWLs

Figure 5.14 shows the results of the seven-compartment model for the hydrophilic, hydrophobic, and interfacially active case studies, choosing (as before) 10 μm UWLs. Two critical metrics in permeant design are (1) delivery amount (panel (a)) and (2) finite-time delivery kinetics (panel (b)). These design metrics vary with chemistry. Depending on the sensitivity of the experiments, and based on the time and concentration scales studied here, it may appear that the initial growth rate of the hydrophilic particle system is closest to its corresponding steady-state value, followed by the hydrophobic and interfacially active particles (panel (b)). This is because the hydrophobic particles are dynamically loading in the membrane core and, worse off, the interfacially active particles are loading in both of the membrane headgroup regions. However, this normalized apparent permeability information does not translate to larger delivery of the hydrophilic particles to the receiver compartment at small times (panel (a)), as the absolute apparent permeability (obtained

by rescaling the normalized apparent permeability with the corresponding steady-state permeability) is still fastest for the hydrophobic particle system–in other words, the initial growth rate is still faster for hydrophobic than hydrophilic. Ultimately, the delivery of the hydrophilic particle system catches up, only for the hydrophobic particle system to pass the hydrophilic system again when it reaches its own pseudo-steady-state. When the interfacially active particle system reaches pseudo-steady-state, it catches up to the hydrophilic system. The hydrophobic particle receiver concentration is ultimately surpassed by the interfacially active and hydrophilic particle systems (slightly and more notably, respectively) at long time or equilibrium.

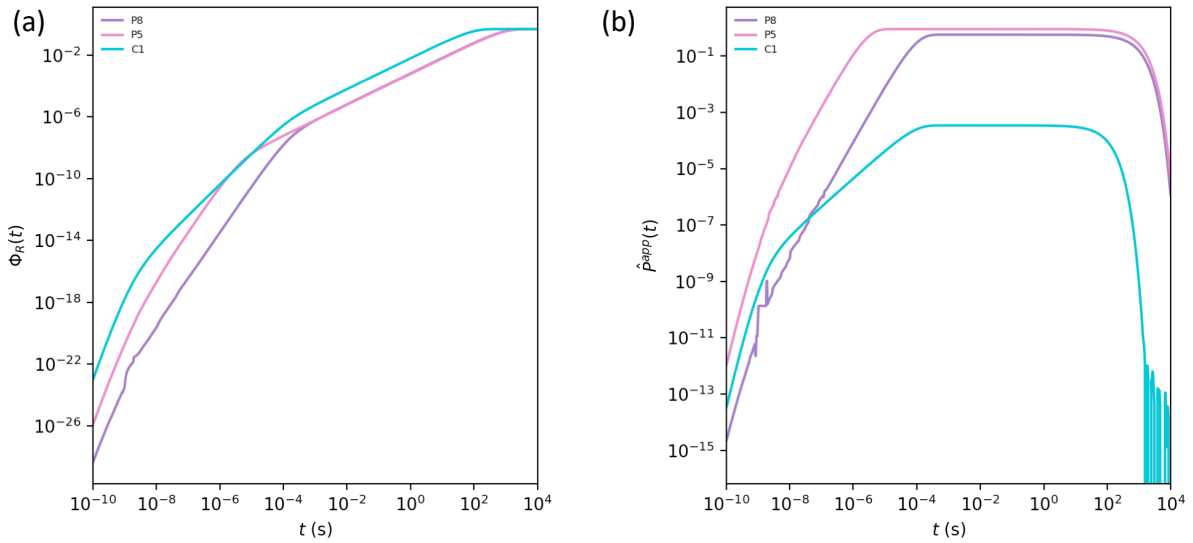

Figure 5.14: Delivery and apparent kinetics from seven-compartment PAMPA model for our QSPR with UWLs. Shown here are the results of the seven-compartment model, namely (a) the normalized receiver compartment concentration profiles and (b) the apparent permeability profiles for the interfacially active, hydrophilic, and hydrophobic chemistries. This analysis of (a) total delivery and (b) instantaneous apparent kinetics demonstrates that, while some chemistries may reach the steady-state plateau faster and for a long period of time, their intermediate delivery to the receiver compartment may still be lower than others.

The results are also otherwise strongly chemistry-dependent. From the point of view of just the donor and receiver compartments (not shown and panel (a) above, respectively), as

is the case in experiment, the hydrophobic particle equilibrates faster than the hydrophilic and interfacially active particles, whose equilibration are comparable. The benefit of this multiscale modeling study, however, is that we can also zoom into various stages of the membrane transport process. As in Chapter 4, the hydrophobic particle system loads the membrane compartment at a faster initial rate than the hydrophilic system, which plateaus and therefore reaches steady-state faster than the hydrophobic one (not shown). In the membrane, the interfacially active particle loads and equilibrates more slowly than the hydrophilic one (comparably to the hydrophobic system), principally due to its rapid and larger loading in the proximal headgroup compartment H_1. The loading of the interfacially active and hydrophobic particles in H_1 are different in magnitude, but level off around the same time scales, both higher in loading and slower in leveling off than the hydrophilic particle system. Interestingly, in the proximal interfacial compartment I_1, the hydrophilic and interfacially active particle systems achieve an intermediate plateau raised relative to the hydrophobic one. While the transfer from the donor compartment to I_1 itself is chemistry-independent, it is important to note that the next step, head group entry, is highly favorable for the interfacially active particles and, due to residual errors in our QSPR, somewhat favorable for the hydrophilic particle system as well. This adjacent sink is likely driving the higher rise in proximal interfacial compartment concentration, which for long times levels out across all chemistries. It is precisely this leveling off in I_1, which also occurs in H_1 albeit at different chemistries, that corresponds to relaxation in distal headgroup and interfacial and receiver compartments. As for the proximal side, the distal side head group concentrations level off at chemistry-dependent values, while the distal interfacial concentrations–and receiver (panel (a)) concentrations, for that matter–are essentially chemistry-independent.

As in Chapter 4, the compartmental model results here can be used to generate transient design rules or a QSKR for the membrane transport that accounts not only for

hydrophilic/hydrophobic particles but also those that adsorb to the membrane interface. We do this specifically by plotting the apparent permeabilities across the entire interpolated space of particle-lipid head group and -tail group affinity, for fixed system dimensions and different times of measurement (Figure 5.15). At small times ($\sim 1\ \mu s$, panels (a) and (b)), this QSKR shows that the apparent kinetics are in fact fastest for particles of intermediate hydrophobicity (moderate ϵ_{PT} and small ϵ_{PH}). Notably, this is in the same qualitative region as the optimum in the MFPT rate constant, which described design rules for single-particle transport (Figure 5.9, panel (e)). This small time design rule is thus a consequence of the fact that modestly hydrophobic particles can both enter and escape the membrane efficiently. At moderate times in the PSSA regime ($\sim 10^2\ s$, on the order of minutes, panels (c) and (d)), Overton's Rule is qualitatively recovered–the stronger the membrane affinity, particularly to the tail group regime, the faster the apparent kinetics. At this time, the membrane has fully loaded with particles in both its head and tail group regions, and the holdup or thermodynamic loading in the membrane feeds the outward flux to the receiver compartment. At large times post-equilibration ($\sim 10^3\ s$, on the order of hours, panels (e) and (f)), we show (as in Chapter 4) that the failing to account for falling concentration driving force in permeability definition 1 leads to a precipitous decrease in apparent kinetics, and in fact the opposite ("inverse Overton") design rule that the lower the membrane affinity, the better. Nonetheless, permeability definition 2 preserves the steady-state trends by accounting for this falling driving force.

5.4.4 QSPR Interpolation/Extrapolation

We further tested our QSPR by exploring different regions of (α_1, α_2) space, and therefore a broader interpolated and extrapolated range of PMFs. Barring solute- and membrane-based differences in the precise location of the PMF features at the headgroup

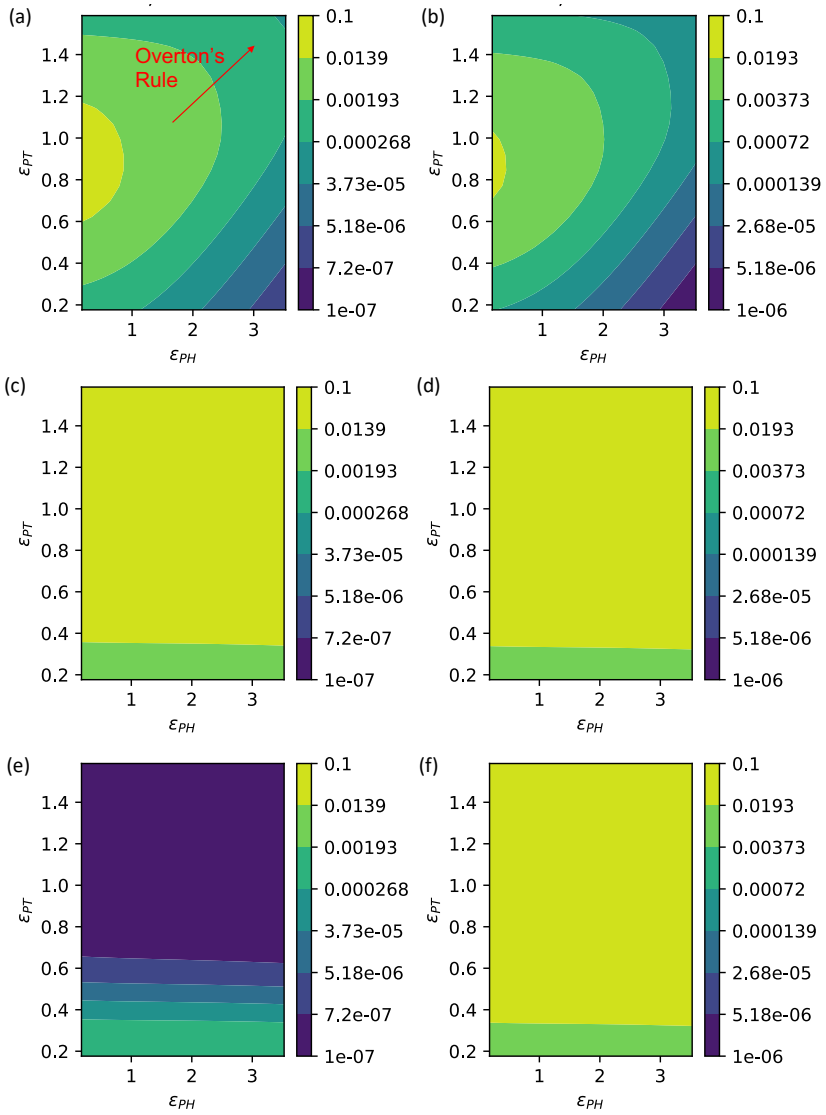

Figure 5.15: Our quantitative structure-kinetic relationship at various observation times. Shown here are the apparent permeability predictions in particle-lipid head group and particle-lipid tail group interaction space, using both PAMPA permeability definitions 1 and 2, for small times (1 μs; panels (a) and (b), respectively), intermediate times (100 s; panels (c) and (d)), and large times (1000 s; panels (e) and (f)). The transient design rule can change dramatically depending on the time of observation, with intermediately hydrophobic compounds crossing the membrane the fastest at small times, then with Overton's Rule qualitatively recovered at larger times, with definition 1 additionally breaking down as a steady-state estimator at larger times and suggesting the opposite design rule.

and core regions, many typical small solutes can be projected onto this space using transfer free energies from the corresponding translational PMFs. Figure 5.16 shows the result of this projection, plotting the thermodynamic results of Chapter 3 along with the amino acid side chain analog results of MacCallum. The projection shows that different classes of side chain analogs fall in different regions of (α_1, α_2) space–cationic arginine and lysine fall in the upper left quadrant due to their relatively barrier to cross the membrane center and intermediate wells (roughly Type 3* PMFs), while anionic aspartic acid and glutamic acid also fall in the upper left quadrant, but lower, also because of their potentially favorable headgroup interactions (Type 3*); polar serine, threonine, and glutamine in the upper left but closer to the $\alpha_2 = 0$ axis; and nonpolar and/or aromatic alanine, methionine, valine, leucine, isoleucine, phenylalanine, and tryptophan fall in the upper right quadrant due to their relatively monotonic well to cross (Type 2).

We tested our LFER specifically for a few side chain analog examples–lysine (cationic), glutamine (polar), alanine (nonpolar), isoleucine (nonpolar), and phenylalanine (aromatic)– by (1) collecting their transfer free energies from the MacCallum study, (2) backmapping those α values to the interaction energies ϵ_{PH} and ϵ_{PT} (using the relationships of Equations 5.4), and (3) plugging those values into single-site particle free energy calculations across an implicit solvent coarse-grained DPPC bilayer membrane (as in Chapter 3) (Figure 5.16). The electrostatic interactions of lysine were accounted for by building them into the head group interactions as $\epsilon_{PH}^{eff} \equiv \epsilon_{PH} - \frac{q_P e}{4\pi\epsilon_0\epsilon_r\sigma_{PH}}$. This procedure consequently provides MD-calculated transfer free energies to then test with the α values of MacCallum, thereby evaluating the LFER and QSPR. The results of this small test set are promising, but chemistry-dependent. MD-calculated transfer free energies of alanine (green square) compare well with the original values (blue upward-pointing arrow) This was expected due to the fact that the effective alanine chemistry is an interpolation of the chemistries in the original training set for the LFER/QSPR. Agreement is weaker for isoleucine and

phenylalanine, whose originally large α_1 and α_2 values provide a test for extrapolation and lead to overly dramatic interaction energies that then overpredict the transfer free energies. Glutamine and lysine are shifted, primarily downward in α_2, in their MD-calculated values. One major reason for these poor predictions results from the inability of our classical model and QSPR to capture more detailed interactions, most notably repulsive interactions. In fact, there are several amino acid side chain analogs like serine, asparagine, glutamic acid, aspartic acid, and arginine that cannot be tested here because the LFER predicts at least one negative interaction energy value. Furthermore, a mismatch between the membranes in the MacCallum study and those in this study may have a large effect on the compensation between α_1 and α_2. While the thermodynamic part of the LFER/QSPR may seem amenable to testing with comparably-sized single-site particles, testing the kinetic (permeability) part of the QSPR is practically more complicated due to the anisotropy of the side chain analogs and therefore the potential breakdown of the solubility-diffusion mechanism due at least to orientational effects. As Comer and Chipot have shown, even for methanol, the translational ISD coordinate can be prone to anomalous diffusion.

5.5 Conclusion

Here, we provide direct nexus from the physicochemical properties of a wide range of molecular-scale compounds to the compounds' membrane transport performance in a macroscopic dynamical setting. First, we provided quantitative context for a recent thermodynamic classification of solute-membrane interactions in terms of transfer free energies. Through the MD simulations and statistical techniques, we related these free energies back to the interaction energies between the particle and lipid head and tail groups, in a simple way through linear free energy relationships. This thermodynamic part

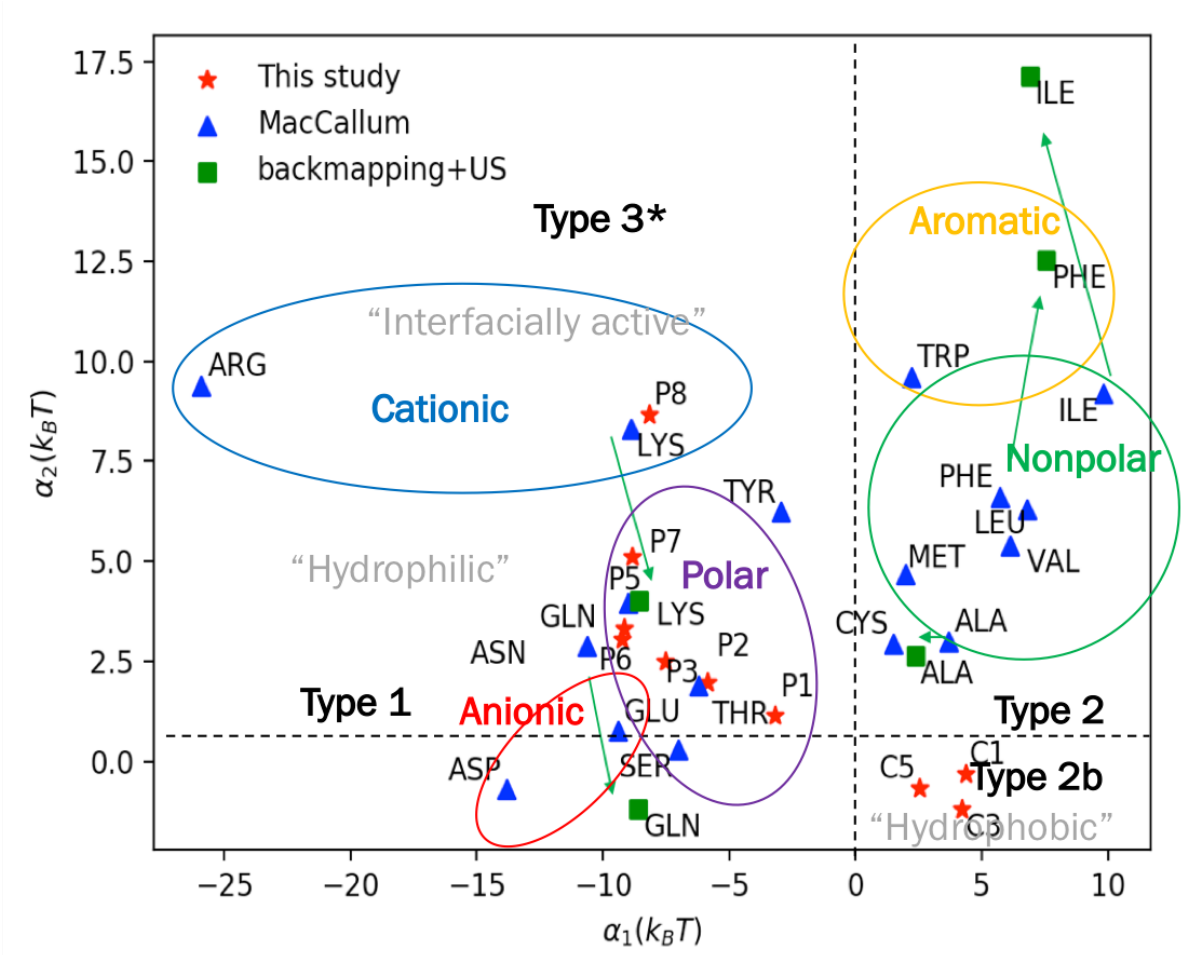

Figure 5.16: A novel 2D thermodynamic projection of common molecular compounds. Shown here are the principal free energy features for small-molecule compounds that map reasonably well to the triple Gaussian model, including the results in our study (red stars) as well as the amino acid side chain analog data set of MacCallum (blue arrow) and the results of backmapping then running free energy calculations on a subset of the MacCallum data to test the predictive capability of our combined LFER+QSAR (green square). Arrows are provided to show the deviations between the original and backmapped then calculated values.

to the model, together with a model for the transmembrane dynamics, provided a QSPR relating the particle's interaction energies to its steady-state membrane permeability. We then broke the microscopic model down into parts and applied the corresponding theoretical analysis to parameterize a macroscopic compartmental model that additionally accounts for macroscopic unstirred water layers and donor and receiver compartments. This multiscale framework, incorporating MD simulations, continuum theory, and compartmental modeling, consequently provided a QSKR where the interaction energies between the particle and lipid head and tail groups were related to time-dependent membrane transport kinetics.

5.6 Acknowledgements

The authors gratefully acknowledge the support of the Department of Defense Defense Threat Reduction Agency (HDTRA1-15-1-0045) and NSF (project DMR-1312548). The content of the publication does not necessarily reflect the position or policy of the Federal Government, and no official endorsement should be inferred. At UCSB, the authors acknowledge the Center for Scientific Computing for computing resources through NSF Grant CNS-0960316 and the Center for Bioengineering for the Crossroads Fellowship in Materials, Mechanics, and Medicine. SM acknowledges support from the Duncan and Suzanne Mellichamp Chair Fund. LGL acknowledges support from the Schlinger Professorship endowment at UCSB.

Bibliography

[1] Smith DJ, Leal LG, Mitragotri S, Shell MS. Nanoparticle transport across model cellular membranes: when do solubility-diffusion models break down? *Journal of Physics D: Applied Physics.* 2018; 51(29): 294004.

[2] Liu J, Li Y, Pan D, Hopfinger AJ. Predicting permeability coefficient in ADMET evaluation by using different membranes-interaction QSAR. *International Journal of Pharmaceutics.* 2005; 304(1-2): 115–123.

[3] Peters B. *Reaction Rate Theory and Rare Events.* Amsterdam: Elsevier1st ed. 2017.

Chapter 6

A unified molecular/continuum thermodynamic model for size and chemistry effects on ∼1-10 nm particle-membrane interactions

6.1 Abstract

Here, we leverage the power of molecular simulations to reduce the elusive and chemistry-specific picture of NP-membrane interactions to a continuum description of their structure and thermodynamics. We focus specifically on ∼1-10 nm, roughly spherical, and rigid particles of varying affinities to the lipid head and tail groups of the membrane. Through analyzing simulation-calculated order parameters, we provide a quantitative framework for several standing continuum descriptions of NP-membrane interactions as well as some completely novel descriptions. This analysis provides a predictive framework for the design-specific effects of a given nanoparticle on its stable and metastable interaction

states and general thermodynamics of interaction with lipid bilayer membranes.

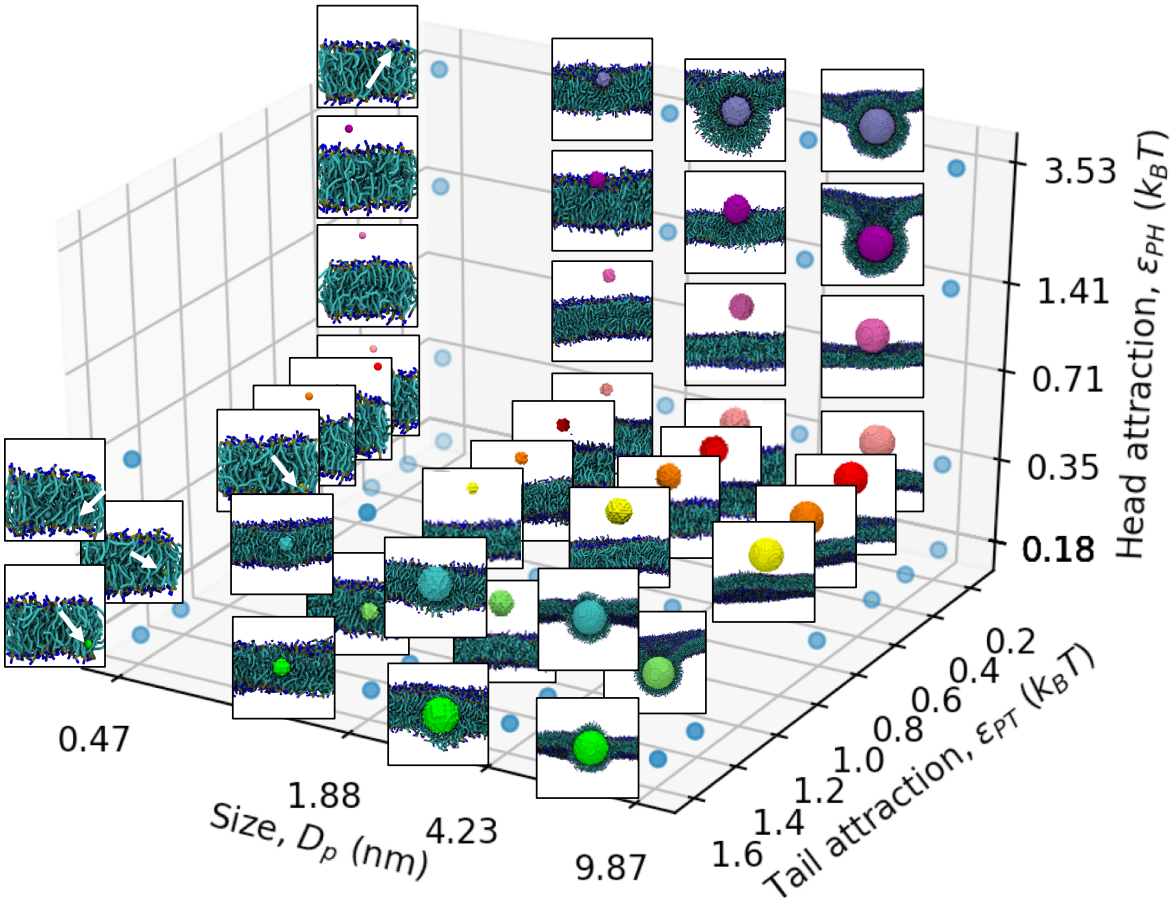

Figure 6.1: NP-membrane state diagram for particles of varying size and surface chemistry. Shown here are the results from the preliminary MD simulations of ~1-10 nm nanoparticles of varying size (diameter D_p), particle-lipid head group affinity (ϵ_{PH}), and particle-lipid tail group affinity (ϵ_{PT}) with a single-component, fluid-phase DPPC lipid bilayer. The exploration of this space reveals a variety of interaction modes and mechanisms that we outline in more detail, particularly for larger NPs, across this chapter.

6.2 Introduction

For a given NP-membrane system, a picture of the complete set of interaction states and the free energy differences and mechanisms of transport between them provides

a complete picture from which all properties can be extracted, including equilibrium populations, membrane structure, kinetic rates (of translocation, insertion, wrapping, etc.), and fundamental predictions of dynamic biodistribution outcomes. Simulation order parameters provide a clearcut method to quantitatively characterize complex molecular-scale processes in soft matter systems. The relative population of two interaction modes (or states) for a given NP-membrane system is proportional to the free energy difference between them, per the Boltzmann distribution:

$$X_i = X_0 exp(-\beta \Delta G_i) \tag{6.1}$$

where X_0 and X_i are the populations (probabilities, concentrations, etc.) of the reference state and state of interest, respectively, $\beta = 1/k_B T$, and ΔG_i is the free energy difference relative to the reference state.

Small, molecular-scale systems are significantly impacted by thermal fluctuations, and thus are often characterized by a wide spectrum of states with nonnegligible entropic driving forces. The membrane interaction of molecular-scale ($<\sim$ 1 nm), homogeneous, isotropic, and rigid solutes is well-described by the inhomogeneous solubility-diffusion (ISD) model, wherein the anisotropy of the membrane-water system is reduced using a transverse displacement coordinate, perpendicular to the plane of the membrane, and the relative solubility of the particle is described by a z-dependent partition coefficient:

$$K(z) = exp(-\beta G(z)). \tag{6.2}$$

In this ISD model, the transfer between states is described by the transverse free energy and diffusivity profiles. Transport in and out of the membrane is fast ($\sim$ns) and facile. While the precise shape of the free energy profile, and therefore maximally and minimally populated solute locations across the membrane, may vary from compound to compound,

the applicability of this model is fairly widespread in chemical space, describing a range of weak to moderate lipid head and tail group affinities for which the solubility-diffusion mechanism is appropriate. In other words, while the interaction modes (e.g. symmetric membrane insertion or insertion in the lipid head group region) may be chemistry-dependent, the mechanism (motion across the z-coordinate) is chemistry-independent.

At larger, colloidal particle scales, membrane interaction modes and mechanisms are characterized more by mild fluctuations about well-defined ground states. These interactions involve slower, more gradual processes involving collective lipid motions and large-scale membrane deformations. Interaction modes are chemistry-dependent– i.e., particles with large head group affinities interact in a fundamentally different way, involving bilayer wrapping with lipid head groups in contact with the particle, from those with large tail group affinities, involving monolayer wrapping with particle-lipid tail group contacts. While probing the kinetics of these larger-scale particle-membrane interaction processes are often prohibitive by molecular-scale physics-based modeling standards, there are some candidates for kinetically-relevant reaction coordinates. Furthermore, membrane elastic theory provides a reasonable starting point for describing the mechanics, and therefore the thermodynamic cost, of bilayer wrapping, and can potentially be extended to monolayer wrapping and other large-scale interaction processes. The Canham-Helfrich Hamiltonian (sometimes referred to as the Spontaneous Curvature Model) quantifies the cost of wrapping in terms of a bending and sometimes tension contribution from a membrane modeled as a quasi-two-dimensional elastic sheet (on a bilayer or monolayer basis, respectively). The interaction strength of NP-membrane contacts is well-described by standing theories for intermolecular forces, like Hamaker theory.

Thus, there are two disparate regimes of NP-membrane interactions that must be bridged to explain and predict the impact of a range of nanoscale solutes: the molecular scale, where fluctuations are important and solubility models work well, and the colloidal

scale, where interaction modes fluctuate about a small set of ground states and are well described by membrane elasticity. In between, the influence of relative nanoscopic particle and membrane length scales, anisotropy and chemistry of the lipid membrane, high-resolution membrane elasticity, "orthogonal" particle design parameters (e.g. shape, elasticity, molecular roughness), and energy-entropy breakdown of interaction processes are all unclear. For just particle size and chemistry variations, it is possible that the transition between the size regimes is chemistry-dependent, and also that there are regions in size-chemistry space where the theories for both regimes break down and a novel theoretical description is required.

Here, we take a fundamental physical approach to the development of a new predictive framework for NP-membrane interactions, as even a basic picture of the interaction modes and mechanisms is unclear in the critical ∼1-10 nm size regime. We take a reductionist approach, mapping out a preliminary design subspace in NP size (∼1-10 nm) and surface chemistry (weak to strong NP-lipid head and tail group interactions) using detailed molecular dynamics simulation with quantitative structural and order parameter analysis to determine the bounds of different behaviors (e.g. solubilization, bilayer and monolayer wrapping, budding, micellization, pre-pore and pore formation) and apply more rigorous sampling and free energy calculation techniques where necessary to the study of the physical pathways and driving forces. In particular, we want to pinpoint exactly where existing continuum thermodynamic theories (e.g. solubility-diffusion, large-scale membrane elasticity, etc.) are insufficient in explaining the stability and metastability limits of interaction. We conclude with a unified molecular if not continuum thermodynamic model that provides configurational and free energy predictions for the major behaviors and therefore a preliminary framework for the interplay of size and surface chemistry with NP shape, softness, roughness, and crystallinity, amongst other design parameters. This is similar to the approach of Van Lehn et al. This framework can be used to guide experimental studies,

avoiding an expensive high-throughput experimental screening protocol and narrowing the vast design space that currently mires pharmacological, toxicological, and consumer product advancements. Inversely, experiments and higher-resolution simulations can be used to confirm the most consequential results from simulation.

The goal is thus, for ∼1-10 nm NPs of varying head and tail group interaction, to quantify and classify stable (and metastable) NP-membrane interaction modes from detailed molecular simulations in terms of some simplified continuum picture (structural states of the NP-membrane complex).

6.3 Methods

6.3.1 Molecular simulations and molecular thermodynamics

As with our previous MD simulations, here we leverage the implicit solvent coarse-grained Dry Martini model along with our own particle model. Here, we first focus on the effect of size and surface chemistry on the membrane interactions through the examination of 0.47, 1.88, 4.23, and 9.87 nm particles of varying particle-head group and -tail group affinity. Particles are built by cutting spheres out of a simple cubic lattice, conferring them with nanoscale roughness. Macroscopic [spherical] shape, softness (rigid limit), roughness, and crystallinity are all kept relatively constant at first. The size of the DPPC bilayer is tuned to accommodate the various sizes of the particles–for 0.47 nm particles, we use a 128-lipid, ∼6.4 by 6.4 nm membrane, while for 1.88 and 4.23 nm particles we use a 2048-lipid, ∼26 by 26 nm membrane and for the 9.87 nm particles we use a 32768-lipid, ∼104 by 104 nm membrane.

For each particle-membrane system, we first run a preliminary 100 ns simulation with the particle and membrane initially in a non-interacting state. Over the course of the

simulation, we monitor a number of order parameters, including:

- Global and local displacement Δz and $\Delta z(r_c)$ respectively between the particle and the membrane in the transverse direction, as an indicator of the proximity between the two. The local displacement concerns the membrane position in the lateral proximity of the particle, while the global displacement concerns the average position across the entire fluctuating membrane and is therefore sensitive to large-scale undulations.

- Coordination numbers between particle and lipid head/tail groups based on their number of contacts. We include both a total (summation) metric N_+ and asymmetry (difference) metric N_- that accounts for differences in coordination between the upper and lower hemispheres of the particle N_1 and N_2, respectively. We track contacts of the particle with both the lipid head and tail groups (i.e., N_+^{head}, N_-^{head}, N_+^{tail}, and N_-^{tail}).

6.4 Results and Discussion

6.4.1 Sub-nanometer particle-membrane thermodynamics

We first review the study of ∼0.5 nm NPs, taking a closer look at the interaction modes and thermodynamics.

Figure 6.2 shows an initial probability distribution summary of the order parameter analysis across all chemistries at ∼0.5 nm size. Again, for this size of NP, we use a 128-lipid/∼6.4x6.4 nm DPPC bilayer. Probability distributions are normalized, and reflect the dynamical interaction from 0 to 100 ns in the simulations (i.e. not discarding for equilibration). The local displacement coordinate $\Delta z(r_c)$ (panel (a), using a 1 nm in-plane radial cutoff for the lipids counted in the displacement) shows that the P8 interfacially

active particle strongly adsorbs to the membrane head group regions (interface), with the P7 particle less so, and that the C1, C3, and C5 hydrophobic paricles insert stably into the membrane core (with the preliminary population qualitatively scaling with the tail group attraction and the C1 particle lower and broader due to its slightly larger head group attraction). The remaining particles (P6 through P1) do not significantly interact with the membrane over the course of the 100 ns simulations. The small-scale physics of the NP-membrane interaction is evident by the negligible differences between the local and global displacement metrics $\Delta z(r_c)$ and Δz, the latter of which (panel (b); here, determined by a 2.5 nm in-plane radial cutoff) would show if membrane deformations were relevant. This information is consistent with the coordination metric results (panels (c) through (f)). Specifically, the total head group coordination number, presented as a fraction of the maximally attainable head group coordination number across all chemistries at this size ($N_+^{head}/N_+^{head,max}$) shows strong head group binding for P8 and weak binding for P7 (panel (c)). Due to the small size of these particles and therefore the small total number of lipid contacts, especially for hydrophilic and hydrophobic particles, all head group contacts are essentially symmetric ($N_-^{head}/N_+^{head,max} \sim 0$, panel (d)). The total tail group coordination number, itself presented as a fraction of the maximally attainable tail group coordination number across all chemistries at this size ($N_+^{tail}/N_+^{tail,max}$), shows membrane insertion for the C1, C3, and C5 particles (panel (e)) that is symmetric, as $N_-^{tail}/N_+^{tail,max} \sim 0$ (panel (f)). We thus conclude that the P8 particle is strongly adsorbed to the membrane, almost wrapped completely by lipid head groups, while the P7 particle is more weakly adsorbed, the C1, C3, and C5 particles are more or less symmetrically inserted in the membrane. For the other particles, NP-membrane interaction is unfavorable.

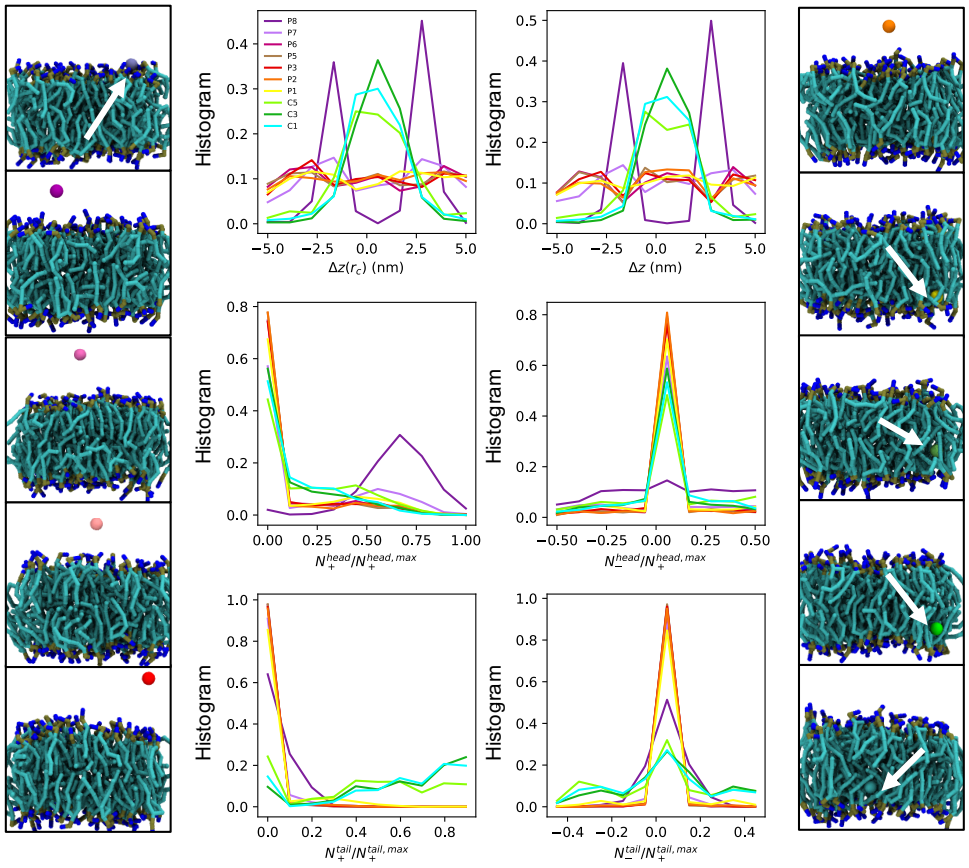

Figure 6.2: Order parameter analysis of ∼0.5 nm NP-membrane interactions. Shown here are the local displacement $\Delta z(r_c)$, global displacement Δz, head group coordination number N_+^{head}, head group coordination asymmetry number N_-^{head}, tail group coordination number N_+^{tail}, and tail group coordination asymmetry number N_-^{tail} for the ∼0.5 nm NP-membrane interactions, flanked by the final simulation snapshots. Due to their small, nondisruptive nature, these small particles show minimal differences between $\Delta z(r_c)$ and Δz, and coordination metrics are generally symmetric.

6.4.2 ∼10 nm particle-membrane thermodynamics

Next, we study large/colloidal-scale ∼10 nm NPs to explore behaviors commonly predicted with continuum elastic membrane models.

Figure 6.3 shows the probability distribution summary of the order parameter analysis now for these larger particles across all chemistries. For this size of NP, we use a 32768-lipid/∼104x104 nm bilayer. $\Delta z(r_c)$ (again, panel (a)) shows positive offset for P8 particles and negative offset for most others. The several reasons for these observations. The P8 particle is positively offset because of its full wrapping with the membrane from above it; the wrapping process brings the membrane around the particle to the extent that the particle's center of mass passes below that of the local membrane environment, and further below that of the full membrane (Δz, panel (b) for P8). The global displacement coordinate (calculated here with a 50 nm in-plane radial cutoff) also more clearly shows how the P7 particle is wrapped with the bilayer as well. The P6 particle is more adsorbed than wrapped, and as such, $\Delta z(r_c)$ and Δz for P6 are negative (the particle center of mass is above that of the membrane). Particles P5 through P1 do not enter the membrane over the course of the simulation, and barely come in contact with it; also, their diffusion in the bulk implicit solvent is slow. As such, these particles' displacements show an offset from the membrane, but broadly so due to the short time scale of the simulation. Particles C1, C3, and C5 show slight negative displacements, less so in the global displacement, indicative not of bilayer wrapping but membrane insertion or wrapping by the lipid monolayers (with the tail groups in contact with the particle). The differences between $\Delta z(r_c)$ and Δz demonstrate the influence of large-scale membrane deformations. The coordination metrics shine further light on these interaction modes. $N_+^{head}/N_+^{head,max}$ shows (panel (c)) indeed that the P8 and P7 particles are wrapping with the head groups, and that the P6 particle is docking to the membrane. $N_-^{head}/N_+^{head,max}$ provides

differentiation (panel (d)) between P8 full wrapping and P7 partial wrapping in that the metric is approximately zero for the former and offset from zero for the latter (< 0, as the lower particle hemisphere is disproportionally coordinating with the membrane). P6 adsorption also corresponds to a less negative $N_{-}^{head}/N_{+}^{head,max}$. $N_{+}^{tail}/N_{+}^{tail,max}$ shows (panel (e)) that the C1, C3, and C5 particles are indeed coordinating with the membrane tail groups. As a result of its strong and extensive head group binding, P8 displays non-negligible tail group binding as well. $N_{-}^{tail}/N_{+}^{tail,max}$ furthermore shows (panel (f)) that the coordination of the hydrophobes is potentially asymmetric, with preferential coordination of the particle lower hemisphere (which in all of the 9.87 nm hydrophobic particle trajectories here is a result of their membrane entrance from above it). This is consistent with these particles' slightly negative displacement, and may suggest that the particles are still inserting in the membrane and that much longer simulations may be prudent. We otherwise conclude that the P8 particle wraps fully, P7 wraps partially, P6 adsorbs, P5 through P1 freely diffuse, and C1, C3, and C5 wrap with the lipid monolayers.

To further explore the hydrophobic particle insertion processes, and also to explore whether or not bilayer and monolayer wrapped interfacially active and hydrophobic particles, respectively, would even bud or micellize respectively from the rest of the bilayer membrane, we uniformly extended the time of all ∼10 nm NP-membrane simulations to 1 μs (1000 ns). No major configurational changes were observed, suggesting either that the configurations have reached their stable states or that they were stuck in metastable states separated from their stable pinched states by prohibitively large thermodynamic barriers and/or dynamical limitations.

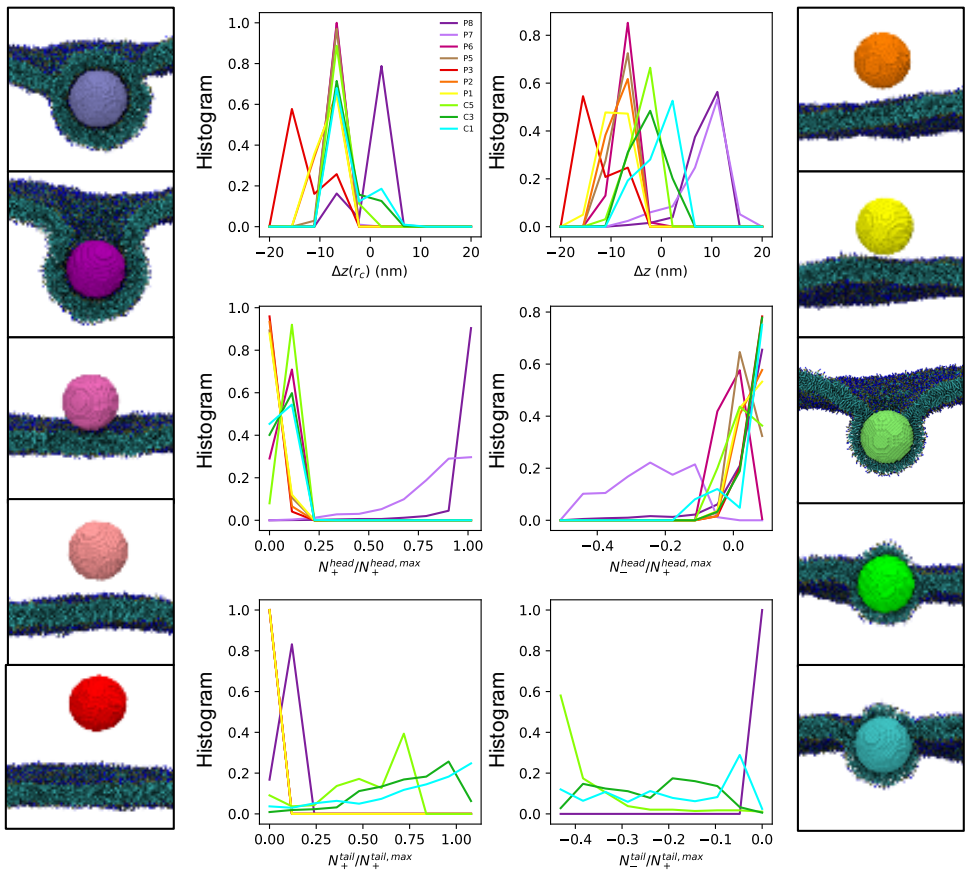

Figure 6.3: Order parameter analysis of ∼10 nm NP-membrane interactions. Shown here are the local displacement $\Delta z(r_c)$, global displacement Δz, head group coordination number N_+^{head}, head group coordination asymmetry number N_-^{head}, tail group coordination number N_+^{tail}, and tail group coordination asymmetry number N_-^{tail} for the ∼10 nm NP-membrane interactions, flanked by the final simulation snapshots. These larger particles invoke significant macroscopic membrane deformations; depending on their precise chemistry, they either wrap with the bilayer as a whole to interact with the lipid head groups or part the monolayers to interact with the tail groups.

6.4.3 ∼2 nm particle-membrane thermodynamics

Next, we study ∼2 and 4 nm NPs, whose interaction modes and mechanisms with lipid membranes are much less clear. For these two sizes of NPs, we use a 2048-lipid/∼26x26 nm bilayer.

Figure 6.4 shows the probability distribution summary of order parameters across all chemistries at ∼2 nm size. $\Delta z(r_c)$ (panel (a)) shows a slightly negative offset for P8 and P7 particles, which similar to the smaller ∼0.5 nm interfacially active particles appear to adsorb to the membrane, and is ∼0 for C1, C3, and C5 hydrophobes that appear to insert into the membrane core. The results for Δz (panel (b), calculated here with a 13 nm in-plane radial cutoff) are similar, with the exception of P8 whose global displacement is ∼0. This is likely due to large-scale membrane deformations that blur the local offset in a membrane adsorbed state. Particles P5 through P1 do not enter the membrane over the course of the simulation, and diffuse in the bulk. As for the ∼0.5 nm particles, $N_+^{head}/N_+^{head,max}$ shows (panel (c)) strong head group binding for P8 and weak binding for P7. $N_-^{head}/N_+^{head,max}$ provides differentiation (panel (d)) between P8 strong adsorption and P7 weak adsorption in that the metric is approximately zero for the former and offset from zero for the latter (< 0, as the lower particle hemisphere is disproportionally coordinating with the membrane). As was the case with the smaller particles, $N_+^{tail}/N_+^{tail,max}$ shows (panel (e)) that the C1, C3, and C5 particles are indeed coordinating with the membrane tail groups. As a result of the strong and extensive head group binding, P8 displays non-negligible tail group binding as well. $N_-^{tail}/N_+^{tail,max}$ shows (panel (f)) that C1, C3, and C5 particle membrane insertion is roughly symmetric. We conclude that P8 tightly binds to the membrane, P7 more loosely binds, P6 through P1 do not interact with the membrane and diffuse in the bulk, and C1, C3, and C5 hydrophobes symmetrically insert in the membrane.

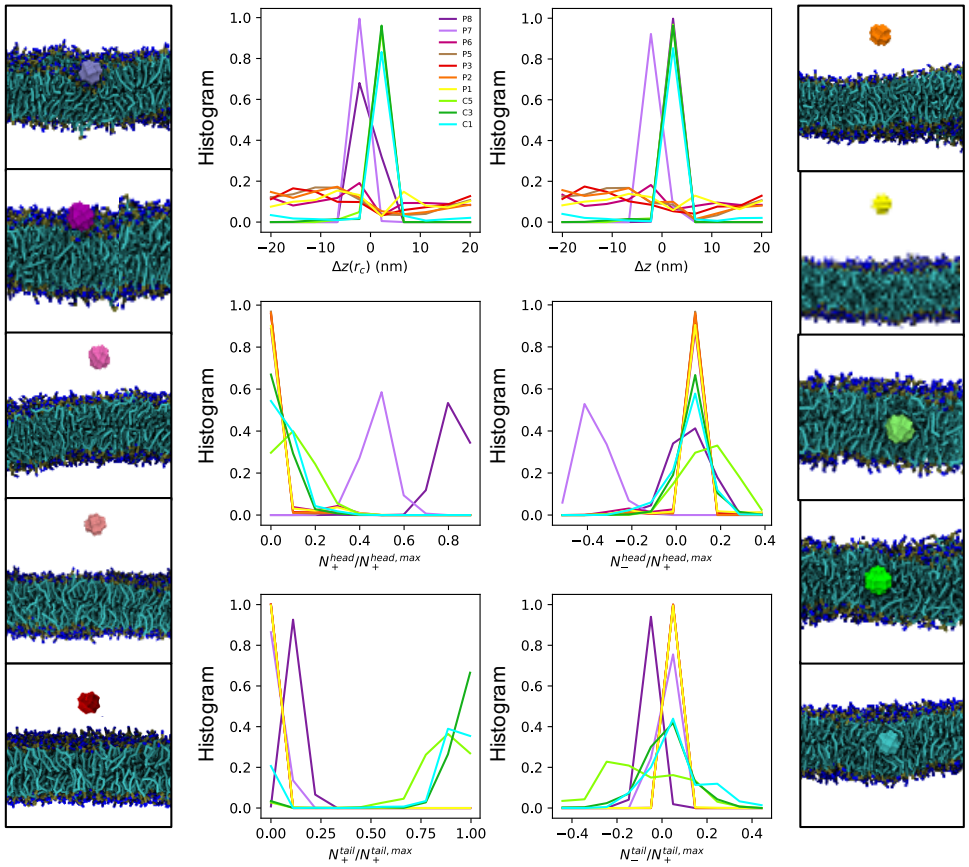

Figure 6.4: Order parameter analysis of ∼2 nm NP-membrane interactions. Shown here are the local displacement $\Delta z(r_c)$, global displacement Δz, head group coordination number N_+^{head}, head group coordination asymmetry number N_-^{head}, tail group coordination number N_+^{tail}, and tail group coordination asymmetry number N_-^{tail} for the ∼2 nm NP-membrane interactions, flanked by the final simulation snapshots. Relative to the ∼0.5 nm NP-membrane interactions, these larger NPs induce small membrane deformations to maximize the relevant lipid head or tail group interactions, resulting for some cases in small differences between $\Delta z(r_c)$ and Δz as well as minor asymmetries in the coordination metrics.

6.4.4 ∼4 nm particle-membrane thermodynamics

Figure 6.5 reports the probability distribution summary of order parameters across all chemistries at ∼4 nm size. Again, $\Delta z(r_c)$ (panel (a)) shows how full bilayer wrapping (here, in the P8 case as for the ∼10 nm P8 particle) results in a positive offset, as the particle center of mass drops below that of the local membrane environment. (Also, as for the ∼10 nm P8 case, the global displacement offset, panel (b) and calculated here also with a 13 nm in-plane radial cutoff, is more dramatic than the local displacement one, as the membrane is globally deforming to accomodate the wrapped complex.) The ∼4 nm P7 particle is more adsorbed than wrapped, and as such, $\Delta z(r_c)$ and Δz for P7 are slightly negative (the particle center of mass is above that of the membrane). Particles P6 through C5 do not enter the membrane over the course of the simulation, and diffuse–quite slowly–in bulk. Through $\Delta z(r_c)$ and Δz, C1 and C3 appear to insert *roughly* symmetrically into the membrane. $N_+^{tail}/N_+^{tail,max}$ shows (panel (e)) that the C1 and C3 particles are indeed coordinating with the membrane tail groups. However, their tail group coordination is uniquely *asymmetric*; as shown in panel (f), $N_-^{tail}/N_+^{tail,max}$ for C1 and C3 is offset and especially so for C1. The degree of asymmetry, ∼5% for the ∼4 nm C3 particle but almost 30% for C1, is much more definitive than for the large-scale ∼10 nm particles of corresponding chemistry. As for the ∼0.5 and ∼2 nm particles, $N_+^{head}/N_+^{head,max}$ shows (panel (c)) strong head group binding for P8 and weak binding for P7, and due to its unique configuration, a non-negligible head group coordination for C1. As for the other NP sizes, $N_-^{head}/N_+^{head,max}$ provides differentiation (panel (d)) between P8 full wrapping and P7 adsorption in that the metric is approximately zero for the former and offset from zero for the latter (< 0, as the lower particle hemisphere is disproportionally coordinate with the membrane). We conclude that P8 wraps fully with the membrane, P7 adsorbs, P6 through C5 freely diffuse, and C3 and C1 *asymmetrically*

insert into the membrane. In what follows, we explore the ∼4 nm C1 NP-membrane system in more detail, with much more extensive sampling. Given the differences between C3 and C1, it seems that this asymmetric insertion may be at least partly a function of the chemistry–asymmetry is more severe for C1, which has a larger lipid head group affinity. However, as we will show, this asymmetry is highly sensitive to several other design parameters.

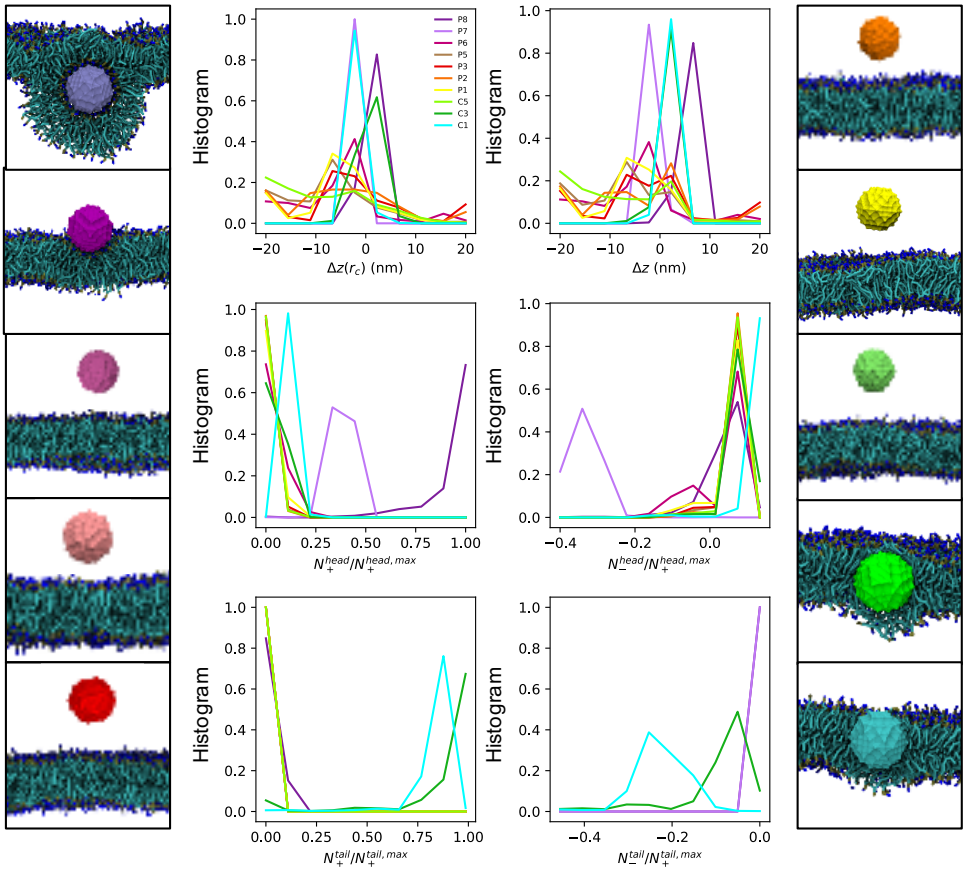

Figure 6.5: Order parameter analysis of ∼4 nm NP-membrane interactions. Shown here are the local displacement $\Delta z(r_c)$, global displacement Δz, head group coordination number N_+^{head}, head group coordination asymmetry number N_-^{head}, tail group coordination number N_+^{tail}, and tail group coordination asymmetry number N_-^{tail} for the ∼4 nm NP-membrane interactions, flanked by the final simulation snapshots. Relative to ∼2 nm NP-membrane interactions, these larger NPs induce still larger membrane deformations, with coordination asymmetries being sensitively dependent on the precise NP chemistry.

We report the completely novel and nontrivial asymmetric insertion and translocation mechanism of nanoscale (∼4 nm) hydrophobic, rough, crystalline nanoparticles (NPs) with a symmetric planar lipid bilayer membrane. In this mechanism, the NP rapidly inserts into the membrane, but with preference towards the proximal leaflet, resulting in the local formation of a proximal monolayer hydrophobic pre-pore and the global formation of bilayer curvature. Figure 6.6 shows that this asymmetric mode of insertion is characterized by a single-leaflet hole formation (panel (b)), whereby the upper membrane leaflet forms a discontinuous phase including a hole and the NP is exposed to the external solvent environment. The distal (lower) leaflet (panel (c)) appears to remain continuous, and wraps around the NP. In this configuration, the membrane actually bends towards the local particle displacement from the membrane–its bends upwards when the particle is displaced towards the upper leaflet. This mechanism is similar to wedging induced by integral membrane proteins, but here with a spherical NP that standing continuum theories would predict to symmetrically insert and with membrane curvature induced in the opposite direction due to the differences in area between the upper leaflet that is more laterally displaced than the lower leaflet.

For a better idea of the stability of this interaction configuration, we extended the original short 100 ns simulation to a massive 10 μs one. The quantify the asymmetry across this trajectory, we again use the N_{-}^{tail} coordination asymmetry metric (Figure 6.7, panel (a)). Asymmetric modes of insertion (in competition with symmetric insertion) are characterized by nonzero differences in coordination between the upper and lower hemispheres of the particle, initially in the negative direction due to the approach of the particle from the top and therefore the preferential lipid tail group coordination of the lower hemisphere of the particle. The initial asymmetric insertion in the upper leaflet is long-lived (O(100 ns-1 μs)). The transition to the equivalent stable equilibrium conformation in the opposite leaflet takes place through collective lipid motions. A

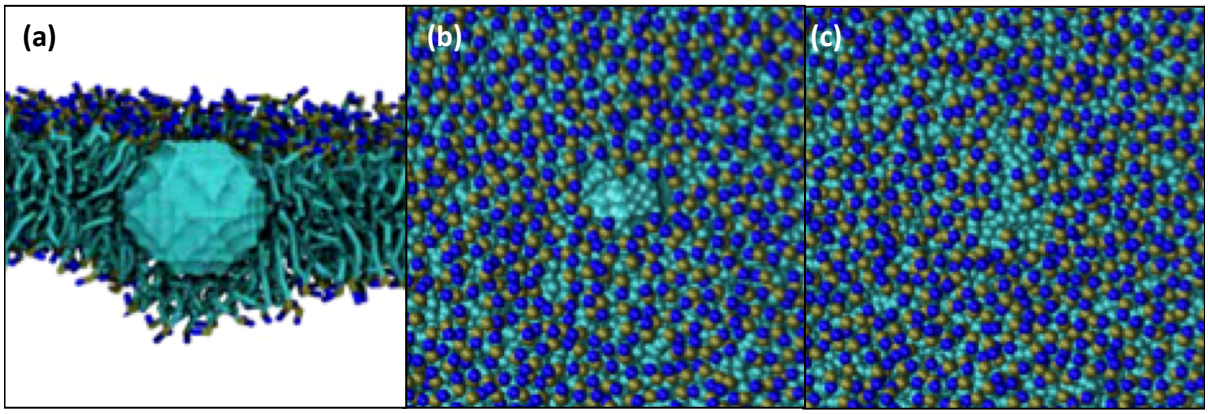

Figure 6.6: Simulation snapshots of the asymmetric membrane insertion of ∼4 nm hydrophobic NPs. Shown here are simulation snapshots after 100 ns of simulation time of the (a) side, (b) top, and (c) bottom views of the 4.23 nm C1 NP-membrane interaction mode. Asymmetry is evident in the slightly negative displacement of the NP relative to the local bilayer height, as well as a hydrophobic hole in the upper membrane leaflet while the lower leaflet wraps around the particle.

metastable state of symmetric insertion also exists. The NP attempts to symmetrize several times, remaining at symmetry for several nanoseconds at a time before returning back to the original leaflet. Several symmetry formation and breakage events occur with fleeting residence in the opposite symmetry breaking configuration. Finally, at around 7 μs, the NP "flips" to the other leaflet, remaining there for O(1 μs). The dynamical simulation is summarized in a putative potential of mean force (PMF) in the 2D space of total tail group coordination number N_+^{tail} and the tail group coordination asymmetry, discarding the initial membrane insertion data (0 to ∼10 ns) and therefore presumably capturing a equilibrium sampling distribution (panel (b)). This appears to prove the stability of an asymmetric insertion configuration, as the two equivalent asymmetric states should be degenerate and equally favorable. Indeed, the PMF is triple-welled, suggesting two equivalent asymmetric insertion states and a central symmetric insertion (at 0). All stable and metastable insertion states are separated by subtle free energy differences within the range of thermal fluctuations.

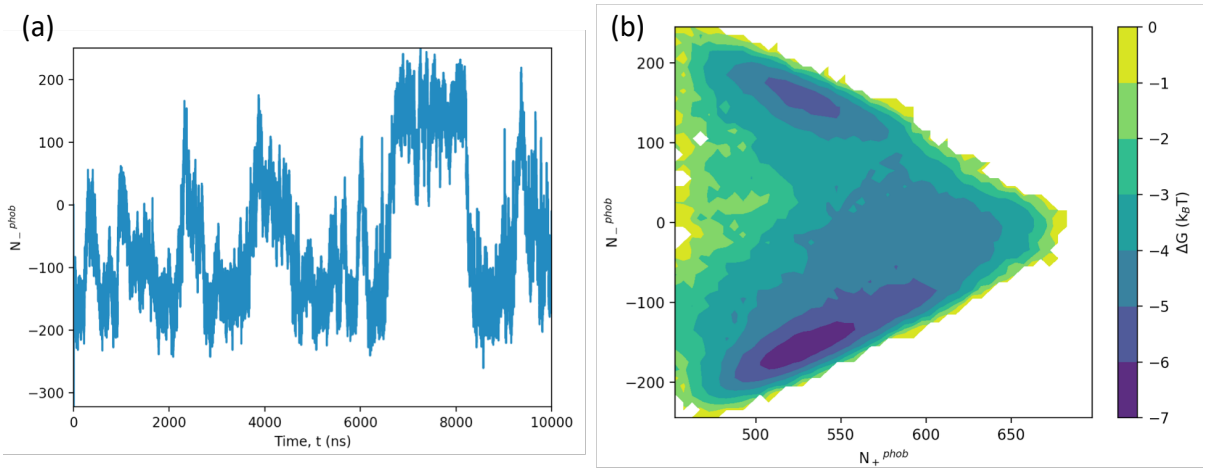

Figure 6.7: Simulation dynamics and thermodynamics of the asymmetric membrane insertion of ~4 nm hydrophobic NPs. Shown here for the 4.23 nm C1 NP-membrane system are the (a) tail group coordination asymmetry metric N_{-}^{tail} trajectory and (b) putative free energy landscape in N_{-}^{tail} and N_{+}^{tail}, both across the extended 10 μs simulation. Hopping is evident from asymmetric state to asymmetric state, with intermediate occupation of the symmetric state, resulting in free energy basins for the two asymmetric states and a very subtle basin for the symmetric one.

We have thoroughly probed this asymmetric insertion phenomenon to prove its stability. Additional stability and kinetic trapping tests have included: (1) variation of initial condition and (2) forced symmetry through external biasing. In terms of (1), a NP initialized below the membrane (at equal and opposite initial displacement) rapidly inserts and remains preferentially inserted in the opposite, lower leaflet for hundreds of nanoseconds. In terms of (2), we forced symmetry through combined use of an umbrella restraint on the NP-bilayer center of mass separation and individual out-of-plane position restraints on each lipid; after symmetrizing the insertion and releasing both restraints, the NP returned to asymmetry within nanoseconds.

This interaction mechanism is highly sensitive to NP design–increased particle size, lipid head and tail group affinity, average surface roughness, and crystallinity (vs. amorphous structure) appear to promote asymmetry (Figure 6.8). The size effect is expected to

be a result of the sensitivity of the system to NP-bilayer mismatch–when the particle diameter and membrane thickness are of comparable length scales, the membrane may reorganize to either match the precise particle length scale or reorganize itself completely. We are in the process of studying many intermediate particle sizes at the same chemistry, roughness, and crystallinity–0.94, 1.41, 2.35, 3.29, 3.76, and 4.7 nm. It appears that asymmetry may be more and more common for larger particle sizes, but the precise interaction mechanism and thermodynamic stable state for a given particle size is at the present unclear. Chemistry, specifically an attraction to both lipid head and tail groups, could be essential to asymmetry, as shown by the differences between the ∼4 nm C1 and C3 particle results. We find that roughness is also a significant factor. Particularly, the length scale of the asperities relative to the length scale of the coarse-grained lipids appear to be determinate in the overall mode of NP-membrane interaction. In our model, we can modulate roughness by the intra-bead spacing in the particles, which varies metrics like the RMSD roughness. We are in the process of studying smoother particles at the same size and crystallinity, and for increasing tail group attraction, we have observed a more trivial transition in interaction states from no interaction to symmetric insertion to symmetric wrapping with the lipid monolayers. Interestingly, we find in preliminary data that, while average surface roughness does matter, the exact arrangement (i.e. crystalline or amorphous arrangement) at constant particle size, chemistry, and average surface surface roughness may not –amorphous rough NPs seem to prefer the asymmetric insertion state. As the mechanism is implicated with membrane undulations, the asymmetry is also sensitive to system size, and amplified for larger and larger membranes.

6.5 Preliminary conclusions and future work

In these preliminary results, we have found the following:

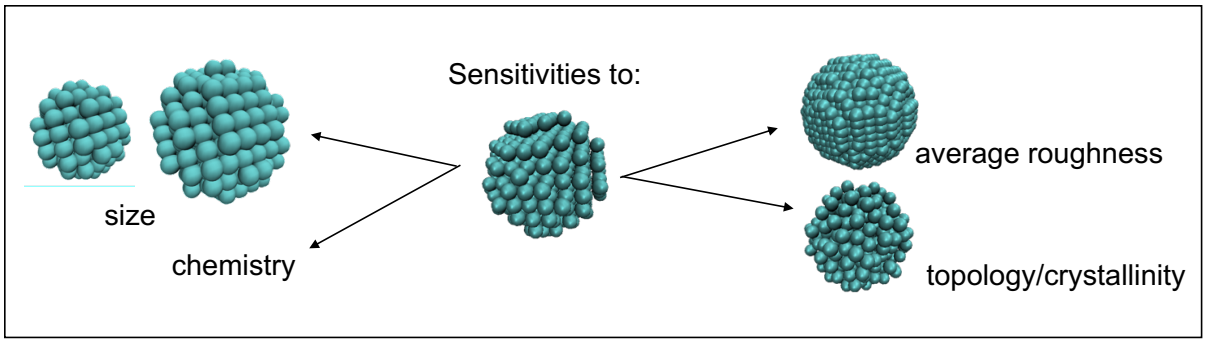

Figure 6.8: Sensitivity of asymmetric membrane insertion to NP design. From our initial simulations, there is evidence to show that asymmetric NP insertion is strongly dependent on NP size, chemistry, roughness, and topology. Asymmetry disappears or diminishes for reduced head group affinity, reduced roughness, and amorphous NPs, whereas for size, asymmetry could be a more general feature of large-scale hydrophobic NP-membrane interactions.

- For ∼0.5 nm NPs, the inhomogeneous solubility-diffusion model suffices to describe the free energy and dynamical landscapes (as we found in Chapter 3), and therefore the suite of thermodynamic and dynamic properties, of the interactions with and transport across simplistic DPPC lipid bilayer membranes. In previous chapters, we were furthermore able to reduce this information to structure-property and structure-kinetic relationships for the steady-state and apparent membrane permeability, respectively.

- For ∼10 nm NPs, existing elastic theories appear to describe some discrete states of interaction (e.g. bilayer and monolayer wrapping of large interfacially active and hydrophobic particles, respectively) well, but there is no surefire reaction coordinate for a given chemistry, let along a diffusion model and any analysis of dynamic effects.

- For ∼2 nm NPs, the inhomogeneous solubility-diffusion model breaks down across a wide range of particle chemistries. While in Chapter 3, we found that the local displacement gives a more intuitive thermodynamic picture than the global displacement, the mechanistic reaction coordinate for particles of ∼2 nm size is

unclear. There is evidence in this range, and sometimes for smaller particles, for anomalous diffusion effects and dynamic effects. The potential for dynamic effects further complicates the search for a mechanistic coordinate, and demotivates it due to the potential "cancellation of errors" anyway in that particles may still appear to follow the global displacement coordinate without systematic deviations in membrane shape and NP orientation, amongst other slow variables.

- For ∼4 nm NPs, there are many complications to the development of thermodynamic let alone mechanistic models. Simple solubility-diffusion models certainly break down due to the slower particle orientational dynamics and membrane disruption caused by any non-negligible NP-membrane chemical affinities, but there is no intuitive framework for building an elastic model. Traditional elastic models fail to capture the nanoscale effects of, for example, high-curvature bilayer wrapping around interfacially active particles and, perhaps most interestingly, the asymmetric, "inverse-membrane-curvature-inducing" of hydrophobic particles. A modified, separate-leaflet and monolayer-based asymmetry elastic model may work for describing the stability of the latter configuration, but the mechanistic and dynamical picture is very unclear. Furthermore, sensitivities to orthogonal NP design parameters like roughness and crystallinity as well as membrane size effects (molecular packing, fluctuations, and entropic effects) further muddle the picture.

Future work to close this exploratory study on ∼1-10 nm NP-membrane interactions, principally for varying NP size and surface chemistry, should involve a summary of simulation-validated and continuum theoretically-summarized stable interaction states and a thermodynamic model explaining the boundaries of stability. The hope is to arrive at a picture like the one shown below (Figure 6.9). Traditional simulation order parameters, plus the ones we have developed, provide a clearcut method to quantitatively

characterize diverse NP-membrane interactions. First and foremost, from the preliminary order parameter analysis, one can divide the NP size-chemistry space into distinct qualitative and quantitative regions of continuum pictures of interaction. Rigorously, this can be achieved through a clustering analysis of the simulation results, but the hope is that, more simply, the above order parameter analysis can be used to draw clear and intuitive separation between different characteristic interaction modes whose molecular thermodynamic driving forces if not continuum thermodynamic driving forces (e.g. leveraging membrane elasticity theory) can then be defined.

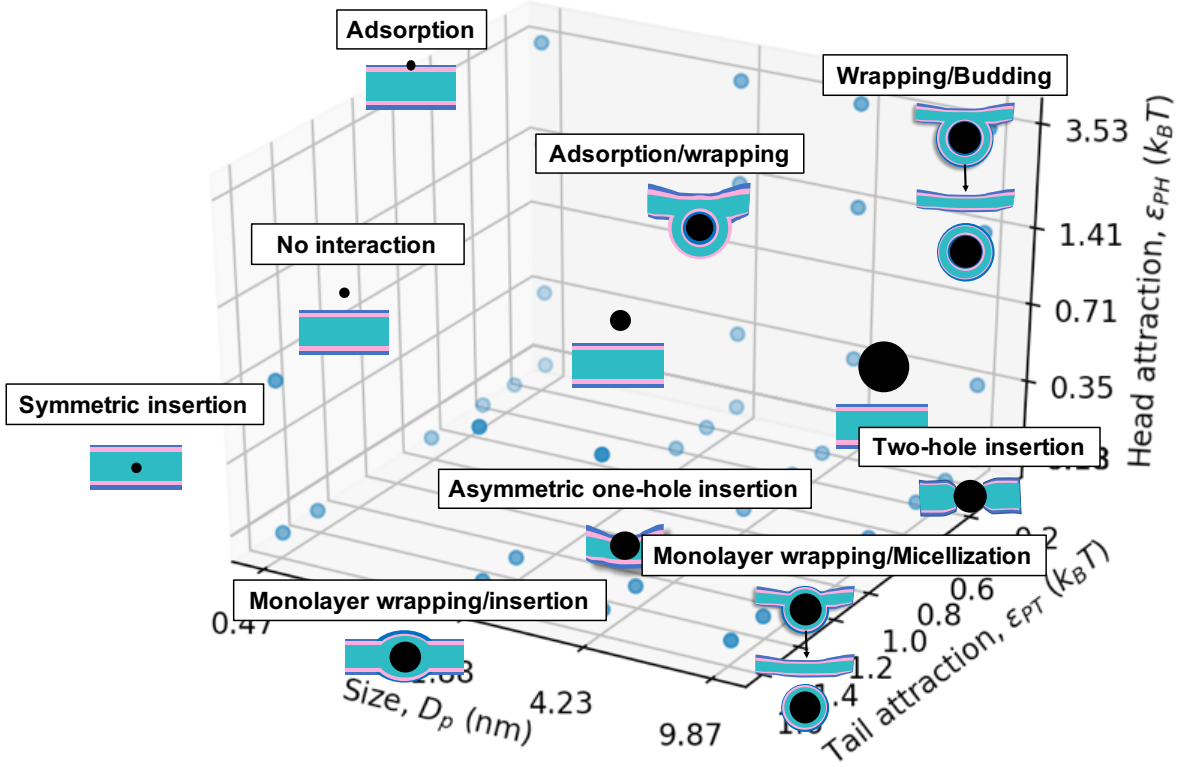

Figure 6.9: Hypothetical thermodynamic summary of particle size and chemistry effects on NP-membrane interactions

We have been constructing continuum elastic models to provide physical intuition behind the driving forces and therefore stability of interactions. In our preliminary

continuum theoretical modeling, it appears that many characteristic NP-membrane interaction modes can still be described by elasticity theories of the bilayer or individual monolayer shapes or modified versions thereof. A finishing goal is to determine if this size-chemistry space can be fully mapped with the current continuum models on-hand, or whether or not certain remaining regions require a more in-depth continuum theory or just a fully-molecular one. At this point, the relevance of small-wavelength membrane elasticity theories to these systems is still unclear. In the closing of gaps in this simulation analysis, the field-theoretic analysis of molecular simulations that we have built, analyzing the height, thickness, and local orientational fields of the membrane to drive the use of existing continuum theories or development of new ones, will be essential. However, it may be that the most practical means of understanding and summarizing the driving forces, in certain regions of design space, is to directly calculate them in the molecular simulations. For this, rigorous sampling (e.g. umbrella sampling) and free energy calculations can be leveraged where necessary.

The hope is that, long-term, this fundamental study can be used to define boundaries of behaviors between model NP-membrane systems and, ultimately, a toxicological understanding of the analogous yet more complex biological systems. For example, if above a critical affinity the particles are known to wrap with the bilayer, insert between monolayers, adsorb to the membrane, or asymmetrically insert in it, amongst other possibilities, and the size-dependence of that critical affinity can be defined, then these critical affinities can be used to define preliminary toxicity limits and, more directly, can be defined in more experimentally relevant terms like surface energies and zeta potentials. The dynamical analysis of Chapters 4 and 5 can also be of tremendous help to designing transient principles, up to structure-property, structure-kinetic, and structure-activity relationships, for the membrane activity and broader biodistribution behavior of this novel range of ∼1-10 nm NPs.

Chapter 7

Conclusions and future prospects

7.1 Summary

This work uses a novel multiscale physics-based modeling platform to characterize the interactions of NPs with model lipid membranes in a key underexplored particle size range. Through designing a custom multiscale platform, we have been able to directly link the physicochemical properties of a NP-membrane system, primarily focusing on the influence of NP properties of size and surface chemistry, to dynamic biodistribution outcomes, first in the context of a model membrane transport problem.

Table 7.1 outlines the major concepts addressed in this thesis. First, we designed a custom coarse-grained molecular model to support the study of a wide range of ∼1-10 nm NP-membrane interactions. The model is sufficiently specific to correspond to the chemistry and physics of a well-known phospholipid bilayer membrane, sufficiently generic to span a wide range of effective organic and inorganic NP chemistries, and an optimal resolution for the accurate and efficient simulation of a range of small- to large-scale studies of NP-membrane phenomena.

Table 7.1: Major concepts addressed in this thesis

Concept Addressed	Chapter 3	Chapter 4	Chapter 5	Chapter 6
Sub-nanometer particle-membrane interactions	x	x	x	
Nanoscale/large NP-membrane interactions	x			x
Sub-nanometer particle membrane transport kinetics	x	x	x	
Steady-state analysis	x	x	x	
Transient analysis and experimental comparison		x	x	
Quantitative structure-permeability/structure-kinetic relationships		x	x	
Effects of NP size and surface chemistry	x	x	x	x
Exploration of alternative mechanisms and coordinates	x			x
Free energy calculations	x			x
Continuum thermodynamic analysis				x
Membrane field theoretic analysis	x			x
Effects of NP surface roughness and crystallinity				x
Effects of membrane size	x			x

After establishing the model, we surveyed the space of NP size and surface chemistry. Chapter 3 baselines the molecular model and establishes a continuum theoretical foundation for sub-nanometer particles in the context of the membrane permeability metric and over two decades of simulation efforts for small molecules. In this chapter, we show through rigorous importance sampling and free energy calculations that the over-century-old structure-property correlation Overton's Rule, approximating a fluctuating, anistoropic lipid bilayer as a homogeneous slab, is overly simplified in quantitatively capturing the lipid membrane permeability of a wide range of sub-nanometer particles and the chemistry-dependence of the permeability. A major contribution of this chapter was the mechanistic validation of the more detailed and continuum mechanical model that is the inhomogeneous solubility-diffusion model. We demonstrated that this model was mechanistically reasonable, partly because of the simplicity of the NP model and confinement of the membrane, but also with quantitative structural analysis of the membrane and dynamical analysis of the particle dynamics. We also show the physical limits of the inhomogeneous solubility-diffusion model, specifically that it breaks down due to its assumptions of quasistatic, adiabatic dynamics along solely a translational coordinate transverse to the plane of the membrane and slow degrees of freedom like NP orientation and large-scale membrane deformations or undulations. This aggregate work, through baselining with a family of model particle transport problems, contextualizes the vast simulation literature on molecular-scale lipid membrane transport, cautions the community on sampling issues that can be indicative of larger problems with hidden free energy barriers and the mechanistic model for transport, and establishes a general paradigm for future evaluation and the mechanistic modeling of nanometer-scale particles, including a suite of alternative, physically-promising order parameters and rigorous rare events methods for determining mechanistic reaction coordinates.

Chapters 4 and 5 then build upon Chapter 3 in that they answer some residual

questions from the initial study. Specifically, Chapter 4 establishes a multiscale paradigm linking continuum theory and systems-level or multi-compartment modeling for closing the gap between simulation- and experimentally-calculated permeabilities. The multiscale platform is anchored by previous findings that experimental permeability assays can suffer from several complexity and reproducibility issues, the most influential of which include unstirred water layers, or diffusive boundary layers sandwiching the lipid membrane, and transient effects due to the initial accumulation of particles in the membrane and equilibration of the donor and receiver compartments. Both effects can combine for major deviations between simulation predictions at steady-state and experiment. By providing highly system-specific correction factors, our platform provides a first-of-its-kind, rigorous, and general means of closing the gap between simulation and experiment.

While Chapter 4 is carried out in the context of a simple microscopic hydrophilicity-hydrophobicity chemistry scale, Chapter 5 broadens the range of effective chemistries by constructing a novel structure-property correlation that directly links the physicochemical properties of the sub-nanometer particle data set in Chapter 3 (i.e. chemistry) to the membrane permeability and that is vastly superior to Overton's Rule. Because it fits the free energy and diffusivity profiles rigorously calculated in the molecular simulations and subsequently uses these fits to parameterize the multi-compartment models, the study in Chapter 5 additionally links the molecular-scale picture to the continuum theory and systems-level modeling, carrying the simulator from the design of the study for a given compound of interest to the final simulation permeability-prediction with experimentally-relevant transient corrections. In other words, Chapter 5 establishes a method to screen sub-nanometer compounds and produce the relevant values for one-to-one comparison with experiment. Both Chapters 4 and 5 additionally seek to establish design rules for sub-nanometer permeants.

Chapter 6 takes the next steps in extending the aforementioned multiscale paradigm

to ∼1-10 nm NPs, for which even a basic thermodynamic picture of NP-membrane interactions, let alone a picture of the biodistribution in a dynamical, model membrane setting, is lacking. By leveraging our detailed simulation foundation, we are able to explore size and surface chemistry space and try to reduce complex, size-, chemistry-, and other design-specific behaviors to a continuum mechanical picture that is otherwise hard to intuit between small-molecule and large colloidal regimes. Figure 7.1 shows the long-term potential benefit of this platform. The future of this platform is bright, and with the baselining of the platform on the sub-nanometer scale and scanning of the ∼1-10 nm regime, we can parsimoniously and deliberately lay out the predictable behaviors of ∼1-10 nm NP-membrane interactions and explore the unpredictable ones in much more depth, harnessing importance sampling and rare events strategies as well as high-performance computing. In and of itself, the information from this analysis provides critical insight into the thermodynamic consequences of NP-membrane interaction–namely, how a given particle is expected to deform and destabilize the membrane. The molecular mechanistic understanding can further be used via continuum theory to parameterize systems-level model that describe the transient dynamics of particles, from a model membrane problem or permeability assay to a complex biological setting.

7.2 Future prospects

There are many future prospects of this robust multiscale platform, including:

- Testing the transferability of the developed QSPRs and QSKRs:
  - Across a wider range of small-scale, ∼spherical, ∼homogeneous chemistries: as necessary, we can augment PMF models to account for more complicated transmembrane free energies and particularly repulsive interactions across the

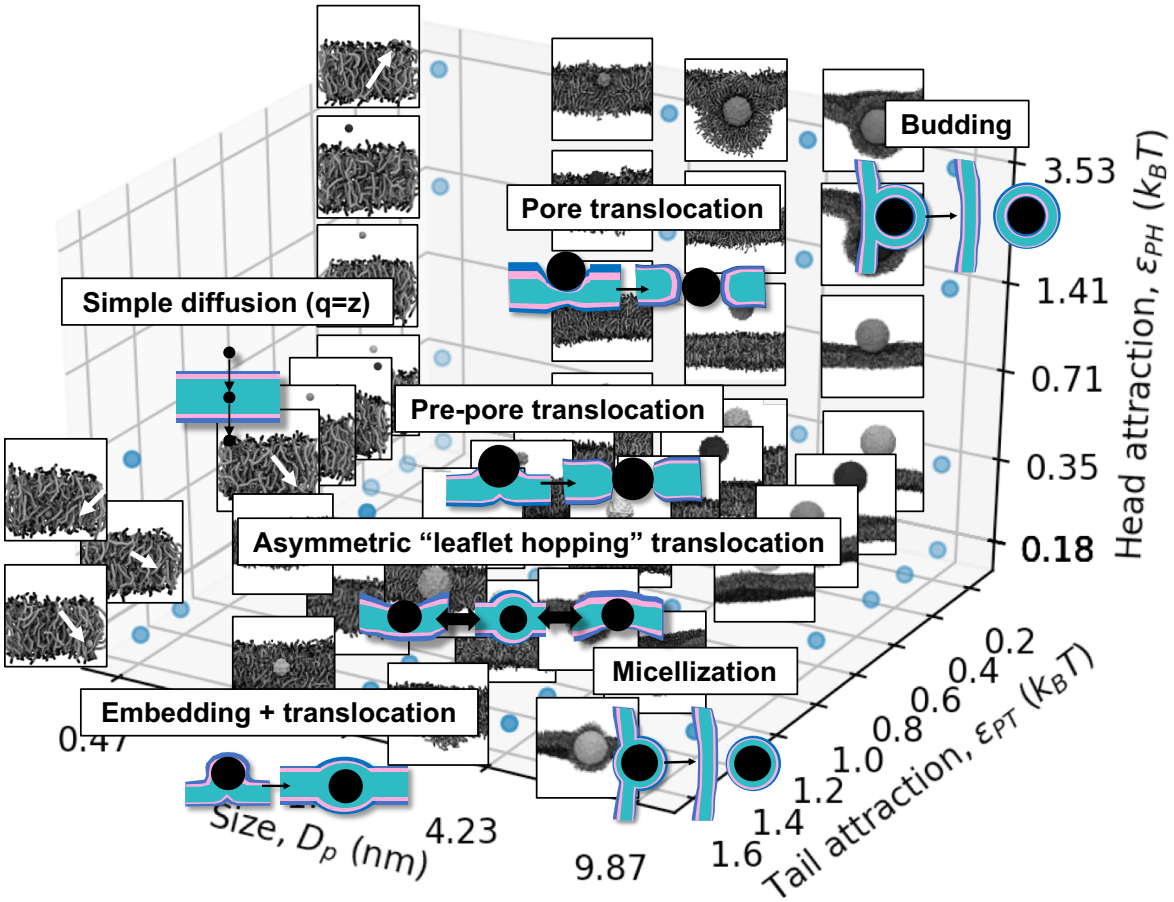

Figure 7.1: Mechanistic hypotheses of particle size and chemistry effects on NP-membrane interactions

membrane transport process.

  - Across different lipid membranes: we can explore different membrane compositions and phases, and incorporate lipidomics and proteomics for insights into relevant compositions.

- Exploring alternative mechanisms: starting from the approaches of Chapter 3 and exploiting additional importance sampling and rare events methods, this platform can potentially outline the mechanistic models for particles that, for example, wrap with the membrane or cross via membrane pore formation.

- Exploring a wider range of NP designs: our platform can easily allow for examination into the effects of NP shape, softness, roughness, and crystallinity.

- NP concentration effects: our platform can also handle multi-particle non-additivites, including particle aggregation inside or outside the membrane and membrane interactions with NP aggregates. Using importance sampling and rare events methods, we can potentially outline mechanistic models for these multi-particle systems as well.

- Effect of lipid diversity: as mentioned above, we can easily tune the cell membrane model to reflect lipidomics and proteomics and therefore the composition of a specific cell type or tissue in the body like the blood-brain barrier.

- Other aspects of existing systems-level and PBPK models: with our multiscale platform, we can handle much more detail than existing PBPK models and programs. For increased connectivity and relevance to those models, however, we can incorporate factors that are already built into them, including:

  - Dissolution of formulation in aqueous solution

- Membrane protein binding
- Cellular effects
    - Caco-2 cells in the corresponding permeability assay
    - Gastrointestinal absorption
    - Blood-brain barrier permeability

Ideally, future explorations with this platform should be guided by the experimental motivation. With the proper guidance, this platform has the potential to function accurately, efficiently, and robustly and make large impacts in the problem of interest.

Appendix A

Best practices for molecular simulations of lipid bilayer membranes

The content in this chapter has been reproduced in part with permission from:

D. J. Smith, J. B. Klauda, and A. J. Sodt. "Simulation Best Practices for Lipid Membranes." *Living Journal of Computational Molecular Science*, 2018. doi: 10.33011/livecoms.1.1.5966

A.1 Introduction

Here, we establish a reliable and robust standardization of settings and setup strategies for practical molecular dynamics (MD) simulations of pure and mixed (single- and multi-component) lipid bilayer membranes. In lipid membranes research, particle-based molecular simulations are a powerful tool alongside continuum theory, lipidomics, and model, *in vitro*, and *in vivo* experiments that can provide precise and reproducible

spatiotemporal (atomic- and femtosecond-level) information about membrane structure, mechanics, thermodynamics, kinetics, and dynamics. Yet the simulation of lipid membranes can be a daunting task, given the uniqueness of lipid membranes relative to conventional liquid-liquid and solid-liquid interfaces, the immense and complex thermodynamic and statistical mechanical theory, the diversity of multiscale lipid models, limitations of modern computing power, the difficulty and ambiguity of simulation controls, finite size effects, competitive continuum simulation alternatives, and the desired application (including vesicle experiments and biological membranes). These issues can complicate an essential understanding of the field of lipid membranes, and create major bottlenecks to simulation advancement. In this document, we hope to clarify these issues and arrive at a linear, consistent, thorough, prioritized, and user-friendly framework for the design of state-of-the-art lipid membrane MD simulations that bridges the gap between a first-timer and world expert.

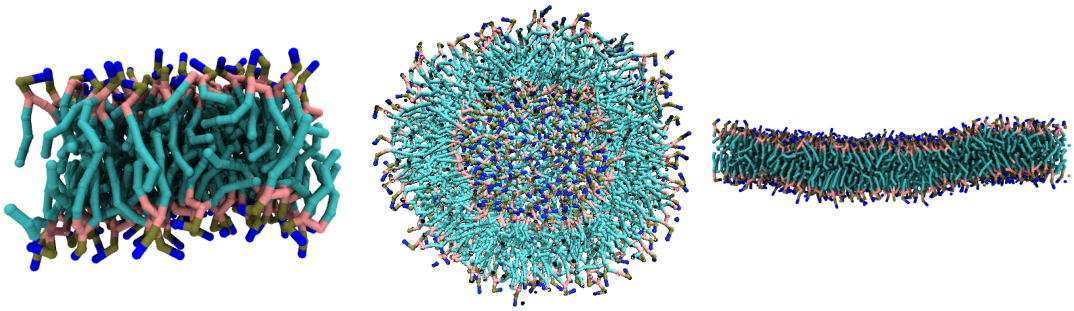

In the recommendations that follow, we seek to establish robust guidelines for equilibrium simulations of lipid bilayer membranes. We focus on dilute lamellar bilayer membranes in water (i.e. at high hydration), particularly the membrane fluid (liquid-crystalline, L_α) phase and, where relevant, gel (L_β or $L_{\beta'}$) and liquid-ordered (L_o) phases. While we do not dictate the choice of MD package for simulation, we draw heavily on tools available in the GROMACS package,[1] which has several built-in routines and add-on patches[2–4] and is the default for several multiscale lipid membrane models.[5–9] NAMD,[10]

CHARMM,[11] and AMBER[12] are well established for lipid membrane simulations as well. Where direct reading, writing, and analysis of the MD trajectories is deemed necessary, we recommend the Python-based packages MDtraj (`http://mdtraj.org/`) and MDanalysis (`https://www.mdanalysis.org/`).

Some good textbooks for statistical mechanical and thermodynamic background on membranes include:

- Safran, Samuel A. "Statistical Thermodynamics of Surfaces, Interfaces, and Membranes." 2003: Westview Press.
- Nelson, David R., et al. "Statistical Mechanics of Membranes and Surfaces." 2004: World Scientific Publishing Company.
- Boal, David. "Mechanics of the Cell." 2012: Cambridge University Press, New York.

Good papers and textbooks for computational and simulation guidance on membranes include:

- Sundararajan, V. "Computational Modeling of Membrane Bilayers, Volume 60 (Current Topics in Membranes)." 2008: Academic Press.
- Tieleman, Marrink, and Berendsen. *Biochimica et Biophysica Acta,* 1997.

In this document, we also assume basic proficiency with MD simulation. Where necessary, we refer simulators to other best practices documents for introductory guides:

- MD basics `https://github.com/MobleyLab/basic_simulation_training`
- MD setup, biomolecular setup `https://github.com/michellab/BioMolSetupPaper`
- Transport properties `https://github.com/ejmaginn/TransportCheckList`
- Statistical error and uncertainty analysis `https://github.com/dmzuckerman/Sampling-Uncertainty`

A.2 Simulation checklist

Here, we provide a checklist for the four major steps in the lipid membrane simulation process: (1) model selection, (2) pre-simulation considerations (selection of MD settings), (3) preparation of initial configurations, and (4) post-simulation considerations (property validation).

A.2.1 Model selection

As with other systems, model selection for lipid membranes is crucial. Lipid membrane models are relatively diverse–resolution can range from all-atom to united atom to coarse-grained and from explicit to implicit solvent. Furthermore, the lipid model may ultimately be implicated in some more complicated application (e.g. small solute transport, peptide-induced pore formation, embedded proteins). The model selection process for a given physical problem can at times be daunting, especially for an undergraduate, experimentalist, or otherwise newcomer. The main goal for a lipid membrane model study should be to correctly capture the correct structural, mechanical, thermodynamic, and/or dynamic properties (whatever is relevant) at the relevant length and timescales and the correct equilibrium conditions (thermodynamic, temperature, pressure, etc.) and/or

nonequilibrium conditions (thermal/mechanical/chemical/other gradients). However, accuracy must be balanced with efficiency. Generally speaking, the simulation time t_{sim} is a function of the (1) model, (2) system size, (3) computing resources, and (4) MD package, amongst other factors. These contributions are often overlapping, but can be deconvoluted in some simple scaling laws (cf. below for more details). In general, force field developers seek to first capture structural and thermodynamic properties, then address dynamical properties. This balance can be tricky, especially with all-atom force fields, as parameters that work for thermodynamics may not accurately match dynamical properties. Rigorous models are validated via their properties through experimental comparison, and with the proper corrections and normalization (most importantly, due to finite size effects in periodic simulations).[13,14] The discussion of model selection, including a comprehensive survey of force fields (including their advantages and disadvantages) at various resolutions, is continued below.

Efficiency is a major concern in virtually any lipid membrane simulation. In the MD loop, the most expensive step involves the pairwise force evaluations, and therefore the number of particles in your system N and the system density $\rho_{model} \propto 1/a_{model}^3$, where a_{model} is the average spacing between sites in the model. Exact simulation time t_{sim} scalings depend on the force field, and can range from $N\rho_{model}$ for short-ranged/mean field types of force fields to $NlogN$ (e.g. PME) to N^2 for long-ranged/rigorous pairwise interactions. Since the number of particles can be related to the system density ρ_{model} and the system length scale L (e.g. for a cubic box):

$$N = \begin{cases} \rho_{model} L^3 & (explicit\ solvent) \\ \rho_{model} L^2 & (implicit\ solvent). \end{cases} \tag{A.1}$$

This scaling incorporates the model resolution ρ_{model} and system size L/nature of solvent,

respectively. Thus, for short-ranged interactions:

$$t_{sim} \propto \begin{cases} \rho_{model}^2 L^3 & (explicit\ solvent) \\ \rho_{model}^2 L^2 & (implicit\ solvent) \end{cases} \tag{A.2}$$

and for long-ranged:

$$t_{sim} \propto \begin{cases} \rho_{model}^2 L^6 & (explicit\ solvent) \\ \rho_{model}^2 L^4 & (implicit\ solvent). \end{cases} \tag{A.3}$$

There is additionally a system size contribution (added to the geometric one) that accounts for sufficient sampling. This accounts for the largest wavelength undulations that are the slowest degree of freedom, and scale as L^3.[15] This is based on the theory of Zilman and Granek, modeling the membrane structure factor based on its approximation as a thin structureless sheet in viscous fluid.[16,17] Thus, the overall scaling in system size can be from L^5 up to L^9, depending on the range of interactions and presence/absence of solvent. In other words, at a minimum, an order of magnitude increase in membrane length scale leads to five order of magnitude increase in computational expense! Coarser models may contribute to higher accessible time scales in two ways: (a) by increasing the time scale of the fastest (vibrational) mode (i.e. $t_{sim} \propto \Delta t_{model}$) and (b) by also inherently smoothening the free energy landscape, and therefore enhancing dynamics across it (e.g. via a simple scale factor). Computing resources and the specific MD package can be viewed as (a) affecting the range of possible parallelization schemes (described in speedup by e.g. Amdahl's Law,[18] but convoluted with the specific MD scheme, e.g. domain decomposition) and (b) contributing to some intrinsic scale factor related to the hardware type (e.g. CPUs vs. GPUs) and software type.

Survey of lipid membrane models

In general, there is a very diverse range of models that can be leveraged for simulations of lipid bilayer membranes. An extensive summary of prominent lipid membrane force fields, along with the notable pros and cons of each, is presented in Table A.1.

Atomistic (all-atom, or AA) models are the "gold standard," as is the case with MD simulations of most other systems. The quality of AA MD simulations of lipid bilayers has improved dramatically since their initial development in the early 1990s.[19] AA models can have hundreds of atomic sites per lipid molecule. United atom (UA) force fields remove hydrogen atoms for an increase in efficiency (factor of ∼2-3),[20] and are competitive with AA force fields in accuracy. AA and UA can therefore easily reach the 100 ns time scale and 5 to 10 nm length scales,[21] but with the appropriate resources and GPU-enabled codes, microsecond timescales are attainable. Well-validated force fields include CHARMM36 (AA),[22] Slipids (AA),[6] AMBER Lipid14 (AA),[23] and GROMOS 54A7 (UA).[5] Alternatively, coarse-grained (CG) models are well-developed for the efficient, large-scale simulation of lipid membranes, often where the interest is in mechanical and qualitative behaviors and less in the quantitative and chemical detail. That said, systematic CG models can still retain some level of chemical specificity (e.g. the types of lipids that they represent). CG models can be bottom-up, parameterizing CG parameters with atomistic data; top-down, parameterizing to capture certain macroscopic quantities or qualitative phenomena; or a combination of the two. CG models can easily reach 1000 ns (1 μs) time scales and ∼20 nm length scales,[21] but can go beyond this toward the 100 μs with the proper resources. One of the best-known CG models for membranes is the Martini force field,[7,8] which via a 4:1 heavy (non-hydrogen) atom mapping reduces to about ten pseudoatom sites per lipid. Because the aqueous solvent can contribute up to 90 percent of the force evaluations,[9] implicit solvent (IS) simulations can be much more efficient and potentially advantageous.

Examples of IS CG models include the Dry Martini force field,[9] the implicit solvent analog of ("wet") Martini; the five-site model of Brannigan and Brown;[24] and the three-site model of Cooke, Kremer, and Deserno.[25] For proper dynamical correlations and conservation of momentum, CG models (particularly IS) are sometimes executed with a fluctuating hydrodynamics[26,27] or dissipative particle dynamics (DPD)[28] thermostat. These models extend the range of accessible scales even further to 100 μs and 100 nm[21]

In Table A.1, we do not include polarizable force fields that can account for problems with molecules parameterized in water that may also enter the vastly different dielectric environment of the membrane, thereby more accurately capturing energies and partitioning. However, the dielectric permittivity in the membrane interior is generally low, and polarizability effects are thus minimal. Furthermore, dipole relaxations can significantly slow down simulations, impacting efficiency and making polarizable force fields completely impractical for large-scale membrane simulation studies. For more information, see force fields like AMOEBA[29] and CHARMM Drude.[30]

Table A.1: Lipid membrane force fields: a survey

Force field (FF)	**Notable pros**	**Notable cons**
Atomistic (AA)	***"Gold standard": Full chemical detail of lipids and optimized against various experimental measures***	***Expensive, and therefore impractical for many large-scale membrane applications; does not typically account for polarizability***

CHARMM36[22]	Accurately represents many key bilayer properties: area per lipid, volume per lipid, electronic density profile, structure factor; operable in tensionless state; useful for membranes with cholesterol and studies of flip-flop; most diverse of AA FF with sphingolipids, ceramides, glycolipids, etc.; accurate with variations in temperature and phase changes;[31,32] compatible with CHARMM parameters for carbohydates, proteins, and nucleic acids;[33,34] used extensively with membrane proteins;[33] implemented and available in a variety of conventional MD packages (CHARMM, NAMD, GROMACS, etc.);[20] compatible with $CHARMM-GUI$	Results currently dependent on cutoffs used for FF development (1-1.2 nm); inaccurate dipole potential drop with fixed charge models; some inaccuracies with ion FF parameters

Slipids[6,35,36]	Captures experimental area per lipid, NMR order parameters and structure factors, and temperature dependencies thereof; able to reproduce structural properties of single- and double-component membranes without surface tension application; generally amenable to the NPT ensemble; many lipid types, including sphingomyelin, cholesterol, and polyunsaturated lipids;[37] compatible carbohydrate force field; parameterization of small molecules available;[33] compatible with AMBER FF and its amino acid and drug-related compounds[20]	Optimization approach similar to CHARMM36, yet not necessarily superior to it; less diverse options in lipids compared to CHARMM36
Lipid14[23]	Captures experimental area per lipid, volume per lipid, lipid thickness, NMR order parameters, scattering data, and lateral lipid diffusion; allows tensionless NPT simulations of a number of lipid types and cholesterol;[33] compatible with AMBER protein, nucleic acid, carbohydrate, and small molecule force fields[20]	Limited to a few lipids and less diverse compared to Slipids and CHARMM36 (saturated, monounsaturated, PC and PE lipids)

OPLS-AA[38]	Captures experimental area per lipid and X-ray form factors; captures deuterium order parameters overall; compatible with OPLS for organic liquid molecules, proteins, nucleic acids, carbohydrates, and drug molecules[20]	Limited range of lipids covered (lowest for AA lipid FFs); discrepancies with experimental deuterium order parameters for first carbon along acyl chains[20]
United Atom (UA)	***Detailed, and yet 2-3 times more efficient that AA simulations without explicitly including non-polar hydrogens***	***Still expensive and impractical for large-scale membrane simulations; does not account for polarizability***
GROMOS (e.g. 45A3,[39] 53A,[40] 54A,[5] Berger modification[41])	Focus on capturing enthalpies and free energies of solvation; diverse options of lipids similar to the level of diversity in CHARMM36; compatible with GROMOS parameter sets for proteins, carbohydrates, and nucleic acids; parameterization available for small molecules (e.g. Automated Topology Builder[42])[20,33]	Problems in representing proper gel phase of bilayer at temperatures below melting point[20]

Explicit solvent coarse-grained (CG)	***At least an order of magnitude more efficient than AA and UA, and can therefore access larger length and time scales, specifically larger-scale membranes and phenomena like undulations, self-assembly, phase transformations, phase coexistence, and interactions with macromolecules and nanoscale compounds***	***Less accurate; sometimes semiquantitative or just qualitative; sometimes distorted dynamics due to smoothened free energy landscape***

Martini[7,8]	Combined bottom-up and top-down model, using atomistically-derived bonded parameters and nonbonded parameters that capture enthalpies, free energies of solvation; repository for a host of lipid types similar to CHARMM36 level of diversity; compatible with Martini protein and peptide, carbohydrate, and nucleic acid models; lots of tools available on website;[20,33] broad range of applications; hydrodynamics thermostats in development;[26] compatible with $CHARMM-GUI$[43]	No major repulsive interactions/mostly soft attractive; molecular polarity can be difficult to capture; aphysical water model (4:1 molecule mapping), the first of which freezes at standard temperatures (must incorporate "antifreeze" particles); later solvent models capture polarity and polarizability,[44] but with drop in efficiency; interactions are shifted and truncated, and therefore short-ranged[20]
ELBA[45]	Good for electrostatics (includes dipoles into both lipid molecules and water beads)[33]	Limited lipid types available[33]

Implicit solvent coarse-grained (IS CG)	***O(10^0-10^3) times more efficient than AA and UA, and can therefore access the largest length and time scales of all particle-based simulations; useful for studying phenomena like undulations, self-assembly, phase transformations, phase coexistence, and interactions with macromolecules and nanoscale compounds***	***Less accurate; sometimes semiquantitative or just qualitative; fluid phase may be unstable or require stabilization; some have problems with self-assembly;[46] further distorted dynamics due to smoothened free energy landscape and lack of solvent***

Dry Martini[9]	Up to 10^3 times faster than atomistic models;[9] combined bottom-up and top-down model; captures experimental area per lipid, bilayer thickness, bending modulus, and liquid order-disorder coexistence; significant speedup permitting study of multicomponent, large-scale membranes; host of lipid types; compatible with other molecular models and broad range of applications; hydrodynamics thermostats in development with minimal computational overhead (still 4 times more efficient than explicit solvent "wet" Martini;[9,20,26] compatible with $CHARMM-GUI$[43]	No major repulsive interactions/mostly soft attractive; molecular polarity can be difficult to capture; no explicit water dynamics and physics in general; difficulty in capturing solvent-mediated effects; energetically-dominated/inaccurate energy-entropy breakdown
PLUM[47–49]	Contains parameters for lipids and proteins; describes protein folding[33]	Limited to a few lipids

Models of Izvekov and Voth[50,51]	Models available at various resolutions; efficient; multiscale coarse-graining (MS-CG) method bottom-up, and therefore preserves certain microscopic properties of system; coarse-graining method incorporates both energetic and entropic driving forces; reproduces fluid lipid bilayer with accurate structural and elastic properties[50]	Limited to a few lipids
Model of Brannigan and Brown[24]	Efficient (one head bead, one interface bead, three tail beads, and implicit solvent); relative to Cooke model, treats hydrocarbon groups at membrane interface differently from those at membrane core; self-assembles; experimentally reasonable fluid and elastic properties; tunable properties[24,52]	Generic/unclear chemical mapping; semiquantitative results; general overprediction of experimental and explicit solvent simulation bending moduli[53]

Model of Cooke, Kremer, and Deserno[46]	Very efficient (one head bead, two tail beads, and implicit solvent); competitive with and up to 5 times faster than DPD simulations of similar resolution; displays correct large-scale elastic behavior; tunable physical properties; stable fluid and gel phases; self-assembles; can model mixed-lipid systems;[46] compatible with hydrodynamics thermostats[27]	Generic/unclear chemical mapping; treats hydrocarbon groups at membrane interface the same as those at membrane core;[52] semi-quantitative results; general underprediction of experimental and explicit solvent simulation bending moduli[53]

For lipid membranes, there is also an extensive subcommunity that uses continuum mechanical theory and field-theoretic simulations that are sometimes in fact the preferred approach at larger length scales (100 nm to 100 μm) due to their efficiency.[21,54,55] These approaches are predicated on the above continuum theoretical framework, and can be performed on the basis of energy minimization of a continuum Hamiltonian and dynamical evolution of a continuum equation of motion for near-flat membranes; a surface-of-evolution approach for axisymmetric membrane shapes or deformations; direct numerical minimization for both axisymmetric and non-axisymmetric shapes; Fourier Space Brownian Dynamics (which has been applied to protein mobility on membranes and the effect of cytoskeletal pinning on membrane dynamics);[52,54,56,57] dynamically triangulated Monte Carlo for irregular, fluctuating membranes; and Monte Carlo on a lattice.[58,59] It is often crucial to compare with these techniques wherever possible. If

some of the above conditions motivating the use of molecular simulations are not met, it is useful to evaluate whether or not a continuum approach would be better.

It should be evident from the thermodynamic and statistical mechanical framework above that there are some crucial considerations for any lipid membrane model, regardless of resolution, including: (1) composition, (2) other thermodynamic constraints, (3) model size, and (4) model geometry.

Composition

It is generally important to consider the chemical mapping of the model to the real system, especially for multicomponent membranes. The desired heterogeneity and particular lipids may determine the model one ultimately chooses. In early simulations of lipid membranes (for both AA/UA and CG resolutions), the canonical lipid of choice was DPPC (dipalmitoylphosphatidylcholine, with two fully saturated 16-carbon chains) in water. DPPC is a common choice for vesicle experiments and is a major component of pulmonary surfactant. PC in general is the most abundant head group in mammalian and yeast membranes.[60,61] DPPC/water is typically the system for which new force fields are first tested. However, DPPC is sometimes not preferred in experiments, due to its high melting point (from the gel to liquid-crystalline state). A more relevant lipid is the 14-carbon chain DMPC or one that has a chain with a single double bond (unsaturation) like POPC.

The recent progression in the field is to go beyond single-component membranes toward more realistic membrane mixtures.[62] For multicomponent membranes, there is a well-established body of literature. For phase coexistence studies, typical model experiments consists of a ternary mixture of cholesterol and both saturated and unsaturated lipids,[63] but more biologically-relevant studies include greater than three lipid types.[62] In fact, for biologically-relevant simulations, we advise caution in the selection and relative

composition of lipids in the membrane model. While there are good guidelines for the contributions of major lipid head and tail groups to biological membranes via major progress in lipidomics,[60,61] composition can potentially vary across different domains and even between the two leaflets,[64] and the best choice for a given model will depend highly on the analogous experimental system. The development of biologically-relevant membranes is at the forefront of the field for AA and CG models,[62,65] and in probing biological processes, one must ensure a membrane of the appropriate phase and composition (e.g. proteins may function best in their native lipid environment, with certain lipid types).

When simulating a lipid membrane, ions may be required to match conditions in experiment and/or model systems. The ion concentration in a typical human environment is 0.15 M. If a membrane has negatively-charged lipids, then to maintain electroneutrality small counter ions are needed such as K^+ or Na^+.

Other thermodynamic constraints

Given a membrane's composition, the thermodynamic constraints of temperature and tension (or area) will largely determine phase behavior. As discussed above, simulations are sometimes amenable to different constraints from experiments (Section A.2.2), but the appropriate experimental conditions can be achieved in a corresponding simulation ensemble. It is worth noting that certain models, both AA and CG alike, sometimes experience difficulty in capturing phase transition temperatures and even entire phases (for example, subgel and ripple for Martini).[34,66]

Model size

Whether or not the membrane physically reflects the experimental setup also depends largely on the dimensions of the model. It has been shown for membranes that finite size effects can play a significant role for thermodynamic (especially mechanical) and

dynamical properties.[13,19,67,68] This refers not only to the in-plane dimensions, but also for the out-of-plane one; despite the quasi-two-dimensional structure of membranes and two-dimensional approximation at larger length scales, hydrodynamic theoretical models for periodic systems have shown that the thickness of the water layer(s) matter as well in convergence to macroscopic system dynamics.[13] In determining the model dimensions, one should search for the emergent length scales in the experimental system that can serve as the periodicity length scales in the simulation. For biological membranes, there is experimental evidence to show that an appropriate in-plane length scale is around 150-500 nm. This is set by the cortical cytoskeletal mesh, which pins membrane proteins and therefore constrains lipid motion (anchored protein picket model).[69,70] This is too large for most molecular simulations, but if a highly resolved picture of biological membranes is still desired, different subsystems can be simulated. If you're not going to simulate the experimentally relevant size (of the overall experimental system or a relevant subsystem), then you need to be able to normalize your results with respect to the difference in sizes.

Model geometry

In many cases, experimental vesicles are modeled with planar bilayer simulations. This may raise questions about the meaning of the results, as vesicular membranes are the result of a balance of positive strain on the outer leaflet and negative strain on the inner leaflet, while planar membranes have on average zero strain on each leaflet. Furthermore, vesicles often have a different number of outer and inner leaflet lipids. Rigorously speaking, there are mathematical transformations to convert data between vesicles and the corresponding planar bilayer. Luo and Maibaum have derived an approximate relationship between planar and spherical membranes for a model-free comparison of structure factors (Fourier transform of the density autocorrelation function) of the same material in different geometries.[71] However, large enough vesicles are also locally flat, so a planar membrane

can be a good approximant. The extensivity of the experimental vesicles can be used as a guide for the simulation size (or the size to which you normalize your results).

A.2.2 Pre-simulation considerations (selection of MD settings)

Once the model is selected, the pre-simulation considerations mainly concern the thermodynamic conditions under which the membrane simulation is ultimately going to be run. Proper control over membrane phase behavior and mechanical tension often necessitates the use of thermostats and barostats. The relevant thermodynamic ensembles for the study of lipid membranes are the canonical (NVT), isobaric/isothermal (NPT) and multiphase ($NP_z\gamma T$) ensembles. Here, P_z is the pressure in the transverse or membrane out-of-plane direction. In general, now with well-tuned force fields the semi-isotropic $NP_zP_{xy}T$ ensemble (where $P_{xy} = P_x = P_y$ is pressure in the lateral or membrane in-plane directions) is recommended for planar bilayers with the constraint that the planar dimensions are equal ($x = y$). Alternatively, the NVT ensemble may be required to avoid cell dimension fluctuations, or the $NP_z\gamma T$ ensemble may be required to probe the effect of surface tension.

The target temperature should be guided by the experimental correspondence. For the ideal model, the simulation temperature would be set to match that of experiment. In reality, however, the imprecise energy-entropy breakdown in the membrane model may lead to shifted phase transition temperatures, and therefore the need to simulate at a higher or lower temperature, depending on the desired membrane phase. Force fields like CHARMM36[22] are well-tuned for phase changes within 5^oC, which has been determined through thorough simulations at a single temperature (i.e. no dynamical ramping of temperature).[31] The main transition temperature of interest is the gel-to-liquid phase transition temperature T_g, above which the membrane exists in a disordered liquid

crystalline L_α state and below which the membrane exists in a more ordered gel L_β state. Some models may accurately capture intermediate tilted gel $L_{\beta'}$, ripple $P_{\beta'}$, and interdigitated $L_{\beta I}$ phases whose relevance depends on the experiments you are trying to model. Most simulations approximate a cellular membrane as a fluid lipid bilayer to match biological conditions, and build chemical and mechanical heterogeneity in later.

For the multiphase and the isobaric/isothermal ensembles, pressure control will additionally be required. For membranes with the isobaric/isothermal ensemble, pressure control is often conducted in a semi-isotropic scheme ($NP_zP_{xy}T$) to incorporate the isotropic conditions in the bilayer plane. Since experimental and biological membranes often operate at negligible tension (as their conjugate variable, the area per lipid, is unconstrained and therefore used to minimize the free energy), tensionless membranes are currently the most common. For membranes, the definition of tension is a precarious one that might not be trivial to a newcomer. While there is an important distinction between the frame tension τ (conjugate to the membrane projected area) and the Laplace tension γ (conjugate to the membrane fluctuating contour area), it has been clearly shown through thermodynamic arguments that these tensions and areas are directly related, and therefore not independent.[72] The Laplace tension is defined to a first approximation as:[73]

$$\gamma = 0.5 L_z \Big(P_z - P_{xy} \Big) \tag{A.4}$$

where L_z is the transverse length scale (in the membrane out-of-plane direction). Both tensions reduce to zero when the component pressures are set to be equal.

In general, most MD settings come with the model/force field. For other appropriate simulation settings, see Section A.2.2 and `https://github.com/MobleyLab/basic_simulation_training`

Technically, NVE (pure MD) is the correct ensemble for all MD simulations, and is

strictly the only ensemble in which pure dynamics are observed (cf. `https://github.com/MobleyLab/basic_simulation_training`). To roughly conserve energy and prevent drift, the integration settings (time step, etc.) matter. Since periodic center of mass removal can hide integrator artifacts, removal should ideally only occur at the start of the simulation.[26] However, as mentioned earlier, proper control over membrane phase and tension often necessitates the use of thermostats and barostats. In some cases, this (as well as the method for calculation of long-range electrostatics) can lead to significant drift when the center of mass motion is not removed.[26] It has been shown, however, that weak-coupling thermostats and barostats and periodic center of mass motion removal have a negligible role on lipid membrane dynamics, and that these thermodynamic controls rigorously correspond to the associated statistical ensemble.[13]

Additionally, thermostats can potentially affect hydrodynamic interactions. In general, MD thermostats that periodically randomize velocities disrupt velocity correlations, and therefore hydrodynamic flows.[26] For membranes, this can significantly affect in-plane lipid correlations and perturb lipid lateral diffusivities. In particular, the Langevin thermostat (sometimes recommended for implicit solvent coarse-grained/IS CG models to nonspecifically account for otherwise absent solvent collisions) does not technically conserve momentum.[74] Other stochastic dynamics thermostats do conserve momentum, and have been built to accurately capture long-range hydrodynamics for coarse-grained and implicit solvent models,[26,27] while DPD thermostats conserve momentum as well.[75]

There are some additional subtleties to barostat compressibilities for lipid membrane simulations. Inverse to some other interfacial simulations (e.g. self-assembled monolayer on an inorganic surface in water), where the in-plane compressibilities are set to zero to preserve hydrocarbon area per molecule, tilt, and density, membrane simulations are usually set to be compressible in the xy plane, and sometimes even incompressible in z (especially for IS CG models).

A.2.3 Preparation of initial configurations

Lamellar lipid bilayers exist for a variety of concentrations of water to lipid ratios. All force fields will produce single bilayers if conditions are at full hydration (∼30 waters per lipid) or above. For a planar bilayer, the desired number of lipids or membrane size in the xy-plane can be estimated from one another if the area per lipid is roughly known:

$$N_l = \frac{2L_xL_y}{a_l} \quad (planar) \tag{A.5}$$

where N_l is the total number of lipids, L_x and L_y are the lateral box dimensions in the x and y directions, and a_l is the area per lipid. The factor of two comes from the fact that there are two leaflets. If a mixed lipid component bilayer, then the a_l is the composition-weighted average. The amount of solvent can be independently varied by changing the box z-dimension L_z. The number of solvent molecules can be estimated from the following:

$$N_{solv} = L_xL_y(L_z - D_B)\rho_{solv} \quad (planar) \tag{A.6}$$

where N_{solv} is the number of solvent molecules, D_B is the bilayer thickness, and ρ_{solv} is the estimated or known bulk number density of the solvent model. Similarly, for a vesicle, the number of lipids/membrane size and amount of solvent can be estimated via:

$$N_l = \frac{8\pi R^2}{a_l} \quad (vesicular) \tag{A.7a}$$

$$N_{solv} = (L_xL_yL_z - 4\pi R^2 D_B)\rho_{solv} \quad (vesicular) \tag{A.7b}$$

where R is the vesicle radius defined from the center to the bilayer midplane. It is important to note that the leaflet lipid numbers will be equal and the above equations will be exactly only in the limit of an infinitely large vesicle. For finite-sized vesicles and especially nanoscale ones, the inner leaflet lipid number will be significantly lower than that of the outer leaflet, and the above equations will break down. In this scenario, membrane builder programs like $CHARMM-GUI$ can be of assistance.

For a vesicle, the total membrane area must be smaller than the smallest plane in periodic box; otherwise, the lipids will form a planar bilayer to minimize the free energy. (The cost of forming a vesicle from a planar membrane incurs at least a bending and Gaussian curvature energetic penalty.) Furthermore, simulating a membrane area smaller than the smallest plane in the periodic box does not ensure the formation of a stable vesicle; in fact, a pancake structure (bilayer patch with splayed edges) can be more stable up to a critical size on the order of a 10 nm radius, and therefore 10^3 to 10^4 total lipids[28]!

Membrane construction

Once the number of lipids and solvent molecules and periodic box dimensions are determined, there are two main methods for putting them all together: (1) "templating" and (2) self-assembly. These two methods are introduced below, and are further discussed, along with alternatives, in Section A.2.3

In the templating method, the lipids are pre-arranged in a planar or vesicular bilayer, close to the final equilibrated structure. Due to potential core overlaps for both planar and vesicular bilayers and the desired leaflet number asymmetry for vesicles (especially at smaller radii), existing packages and routines are recommended. CHARMM-GUI (`http://www.charmm-gui.org/`) is an excellent resource, and the most common for setting up membranes in a variety of configurations and for a variety of models/force fields.[76–79] CHARMM-GUI provides input files compliant with the GROMACS, NAMD,

Amber, OpenMM, and CHARMM MD packages, amongst others, but is limited in force fields to CHARMM36[33] and the Martini force fields.[43] Once the membrane is templated, it can then be solvated. Due to the fluctuating nature and molecular scale roughness of lipid membranes, a trial-and-error solvation routine (placing test particles in various locations, checking for steric overlap based on van der Waals radii, and removing particles if overlap is significant) may be preferred over appending solvent "slabs" to each side of the membrane due to the potentially long equilibration time of full head group solvation. The GROMACS *g_solvate* routine is one such example of a trial-and-error approach, whereas $CHARMM-GUI$ uses a slab-based approach.

In the self-assembly method, the lipids are dispersed in solvent, and allowed to dynamically and spontaneously arrange into their final equilibrium structure. The initial stages are normally fast, and involve the formation of lipid micellar aggregates followed by the bridging of micelles to form larger, lamellar aggregates. The rate-limiting step is believed to be the elimination of water pores in the membrane, sealing over 10 to 10^2 ns during which lipids may exchange across leaflets.[80] The proof-of-concept approach is more scientifically satisfying, but not necessarily reasonable for higher resolution models and/or larger length scale simulations due to the long time scale of assembly (discussed more in A.2.3). Again, care should be taken to generate a vesicle or bilayer, and not a pancake or other structure. Because the system will always proceed to minimize its total free energy, the initial box dimensions are crucial to the outcome of the self-assembly approach. For a planar bilayer, the in-plane box dimensions must be initialized near their intended end state (which can be predicted with the number of lipids and area per lipid), and for a vesicle, all box areas must be significantly larger than the corresponding planar bilayer with the same number of lipids (otherwise, the lipids will form a planar bilayer and not a vesicle). For one example of the self-assembly technique, you can visit the Martini website (`http://www.cgmartini.nl/index.php/tutorials-general-introduction/bilayers`).

Preparation procedure

After the building step, the system should be energy minimized to remove potential bad site contacts (steric overlap) generated during the original placement of molecules. Minimization routines like steepest descent are perfectly reasonable, and are available in conventional MD packages.

Then, the system should be gradually annealed from 0 K to the target temperature in the relevant thermodynamic ensemble (NVT or $NP_zP_{xy}T$, depending on whether or not a barostat will ultimately be used in the production run). In general, a short 100 ps to 1 ns run should suffice. The user may want to consider using position restraints during this process to prevent major lipid fluctuations, particularly if the templating method is used to initially build the bilayer. $CHARMM-GUI$ provides a pre-described set of equilibration scripts that have been tested on various bilayers to work well and is recommended based on their initial structure. For soft enough interactions, you may be able to skip this step.

In the case of self-assembly, a longer dynamical simulation is needed to allow for bilayer formation. For smaller ($\approx$ 128-lipid) membranes, this can take 10-100 ns, and can potentially take much longer for larger and vesicular ones. Visualization can be very helpful to track the assembly process. Care should still be taken after assembly is qualitatively confirmed to ensure quantitative equilibration.

Before the production run, the equilibrium structure can be further standardized for ease of analysis and comparison with external studies. Out of convention, for an open planar membrane, the membrane in-plane directions are often defined to be the x and y directions, while the out-of-plane direction is defined as z. All subsequent discussion assumes this directionality, but the choice of direction is otherwise arbitrary. In GROMACS, this can easily be achieved with the *editconf* command. For both open

planar and closed vesicular membranes, centering the membrane in the periodic box will largely prevent the jumping of bilayer leaflets and pieces across the periodic box, assuming drift does not occur. This will make subsequent visual observation and post-simulation analysis easier. Centering can also be achieved with *editconf*.

Before going into the details of production run, it should be noted that additional equilibration beyond the initial structure is needed and timescales depend strongly on the system complexity and size. For single-component lipid membranes in the liquid crystalline state, equilibration typically only requires 5-10 ns with a well educated initial setup of surface area per lipid. Membranes that have several lipids or conditions in more condensed phases can require 100+ ns of equilibration; the exact amount of time, however, will depend strongly on the composition and whether or not phase segregation is relevant. A typical first order method to determine equilibration is to track surface area per lipid as a function of time and verify that this has reached equilibrium via block averages and autocorrelation analysis.[19] However, all other key properties should also be verified–i.e., that they have stabilized and that reported averages are over equilibrated systems. This is especially true for lipid lateral clustering and radial distribution functions that depend on slowly relaxing diffusional degrees of freedom.

Guidelines for production run sampling

Finally, the initial estimation of the production run time is useful. You will ultimately want to incorporate an adequate amount of sampling for your phenomenon/phenomena of interest. In general, this means capturing several autocorrelation times for the relevant degrees of freedom. Lipid membranes are characterized by a hierarchy of time scales, including: bond vibrations (fs-ns), trans-gauche isomerization and rotation about chemical bonds (1-100 ps), rotation (axial diffusion) about the lipid axis and wobbling (1-100ns), lateral diffusion (1-100 μs), and flip-flop (1 ms-1 s for most lipids;[81–83] shorter for

cholesterol) and undulations (1 ms-1 s for experimental system sizes[81] and down to 100 ns-1 us for typical simulation[53]). Collective order fluctuations (e.g. undulations, flip-flop, lateral diffusion) are the longest timescale fluctuations in the system because they involve the coordination and motion of several lipids.[81] Even at equilibrium, area per lipid can fluctuate in simulations on the time scale of tens of nanoseconds.[19,84] However, if your study concerns more localized or molecular degrees of freedom (e.g. rotation about chemical bonds, trans-gauche isomerization, lipid axial diffusion, etc.) at constant membrane macroscopic shape and lipid leaflet number, then smaller sampling times may be permissible.

In terms of templating methods, $CHARMM-GUI$ is perhaps the most commonly used package. $CHARMM-GUI$ packs lipids from a library, then relaxes atom clashes on its own. During the building and equilibration schemes, $CHARMM-GUI$ performs internal checks for "disaster structures" that can range from ring penetration (molecular chains going through rings) to flipped chiralities of lipid backbones, and additionally includes built-in restraints to maintain chirality. $CHARMM-GUI$ has developed an estimate strategy for vesicles to determine the optimal number of lipids in the inner and outer leaflets for a given vesicle size; additionally, it can include water pores directly to facilitate flip-flop and lipid number equilibration, which can be important for vesicular geometries.[43] $CHARMM-GUI$ can also handle membrane-embedded proteins, which are often initialized with structures from the PDB. In all of this, the user should still perform spot checks and, if necessary, conduct more extensive structural analysis. One downside to $CHARMM-GUI$ is that it is slow–for Martini, $CHARMM-GUI$'s $MartiniMaker$ can take several minutes to a few hours, depending on the system size and server load.[43] This slow performance in part comes from the Monte Carlo procedure in determining the optimal arrangement of lipid head groups.[85] $MartiniMaker$ is not the best choice for large Martini systems, but programs like *insane.py*[85] (`http://www.cgmartini.nl/index.`

`php/downloads/tools/239-insane`) and *LipidWrapper* (discussed further below) may work better. Insane uses a scaling procedure to avoid bad structures, but does not require several cycles and/or parameter adjustments to yield a stable system, unlike *InflateGro* and *g_membed*.[85] Insane is well established in user controls, and largely prevents user errors in setup; the downside, therefore, is that it sacrifices user creativity and customizability.

Self-assembly, or even combining pre-existing bilayers to make a larger one, can result in lipid number asymmetric membranes. Thus, without repeated trials, self-assembly will not reliably generate balanced bilayers, in contrast to templating. In the absence of flip-flop, the leaflet composition of a self assembled bilayer is kinetically trapped. Given repeated trials of self-assembly, and assuming the end distribution samples the canonical ensemble (i.e., it is not influenced by kinetics) the distribution of compositions can be calculated (see, e.g., Ref.[86]). For example, consider a self assembled bilayer with $N_l = 200$ total lipids with $a_l = 65$ Å^2 and K_A=300 mN/m. The strain energy is equal to $\frac{K_A}{2} N_l a_l \epsilon^2$, where $\epsilon = \frac{A - A_0}{A_0}$, $A \approx a_l N_l/2$ is the self-assembled area of the system, and A_0 is the minimum free energy leaflet area, given the self-assembled lipid count. The leaflet imbalance is characterized by $\Delta = N_1 - N_2$, where N_1 (N_2) is the area of the one (the other) leaflet. Under these definitions the minimum free energy area of the first leaflet is $a_l N_1$. By periodic boundary conditions the two leaflets have the same projected area, A. Each leaflet will then have approximately the same strain magnitude: $|\epsilon| = \frac{\Delta}{N_l}$. The Boltzmann distribution is then

$$p(\Delta) = e^{-\frac{\beta K_A a_l}{4 N_l} \Delta^2}, \tag{A.8}$$

that is, a normal distribution with variance $\sigma_\Delta^2 = \frac{2 N_l}{a_l \beta K_A}$. Here the strain energies of the individual leaflets (each with leaflet K_A half that of the bilayer) have been summed. The

standard deviation for this example is 5 lipids at 298K. For larger systems the tension per leaflet ($\frac{K_A}{2}\epsilon$) goes to zero even as the expected imbalance increases.

Depending on the application, the two build methods (templating and self-assembly) can vary significantly in their efficiency and final outcomes. In Table A.2, we outline some major advantages and disadvantages of both.

Table A.2: Membrane building methods: a cross-comparison

Method	**Advantages**	**Disadvantages**
Templating	• Directly construct a sane-looking bilayer • Efficient • Developer support often available[33]	• Doesn't capture preferential segregation of multicomponent bilayers, which can be slow to emerge • You need to know what's in what leaflet, etc.; can lead to user bias if arrangement is not known • Performance can sometimes still be slow (code not optimized)[33] • Sometimes limited application to MD packages, force fields, and lipid types[33]

Self-Assembly	• "Natural": lets things assemble the way they want • Great if you know the overall system composition but not distribution (across leaflets, within leaflets, etc.) • Easy (at least with CG models) – scatter molecules and run simulation	• Less reproducible – bilayers won't necessarily be symmetric, and leaflets won't necessarily have same composition • Can be problematic with small systems • Relatively slow and expensive

Other/hybrid construction methods

One fairly simple alternative to building a membrane oneself is downloading a pre-equilibrated membrane from a lipid library.[33] Membranes from a library can either be used directly or to make larger membrane structures. Examples include *lipidbook* (`lipidbook.bioch.ox.ac.uk`), *NMRlipids* (`www.nmrlipids.fi`), and *zenodo* (`www.zenodo.org`). *NMRlipids* is a particularly new and comprehensive initiative launched by S. Ollila to compare membrane properties across 13 different force fields. The advantages of using a library are that the structures used are inherently validated by potentially more experienced researchers, and that the results one obtains can be directly compared with the previously published data associated with a given structure. The downsides are that libraries are still somewhat specialized and scattered on the web, and that the translation of structures files across force fields and packages can be a nontrivial process.[33]

The generation of curved membranes may be essential to the study of biological membranes and processes like membrane-protein interactions, membrane scission, and viral budding. *LipidWrapper*[87] is a multiscale Python-based utility particularly useful for generation of experimentally- and theoretically-relevant curved membranes that can generate membranes of arbitrary geometry and size. *LipidWrapper* builds larger membranes from pre-equilibrated small planar membrane triangulations, and appears compatible with several force fields. It is unclear exactly how efficient this procedure is, but the strategy of building membranes from membranes seems more efficient than $CHARMM-GUI$ and *insane*. Caution should be exercised with *LipidWrapper*, however, as improvements in generating the necessary leaflet number asymmetry for highly curved bilayers are still under development.[87] Generally speaking, building larger membranes from smaller ones (with methods like *LipidWrapper* or otherwise) puts restrictions on the resulting membrane composition,[85] so this should be kept in mind while developing the smaller membrane template. Especially for bilayers of low curvature, Section A.2.1 discusses how one can model a planar membrane and still transform the experimental vesicle data for one-to-one comparison.

Lastly, backmapping (or reverse transformation) converts coarse-grained membranes to atomistic ones. Wassenaar and coworkers have developed *backward.py*,[88] a robust Python-based backmapping procedure based on geometric projection and subsequent force field based relaxation (energy minimization and position-restrained MD) that requires only a list of particle correspondences for the two levels of resolution in the conversion. The method crosses various MD platforms, force fields, and lipid types, and can handle lipid membrane phases beyond planar bilayers as well as the solvent. For example, the method can successfully span the three-bead model of Cooke, Kremer, and Deserno to Martini and Martini to GROMOS, CHARMM, and AMBER. If necessary, backmapping is also useful for studying detailed molecular interactions in a large-scale membrane, in

that the membrane can be assembled and equilibrated on the coarse-grained level and, after backmapping, is presumably still at equilibrium. *backward.py* and its workflow *initram.sh* are available at `http://cgmartini.nl`.

For conversions between similarly-resolved models or lipid types if the lipid topologies are sufficiently similar, *Lipid Converter*[89] can be helpful. In some instances, it may be useful to combine different construction methods, e.g. *insane* then *backward* then *Lipid Converter*, in that it permits construction of a CG membrane, conversion of that CG membrane to an atomistic one, then conversion of that atomistic membrane to another atomistic one.

A.2.4 Post-simulation considerations (property validation)

Fluid lipid membranes are normally modeled as liquid-like laterally (no in-plane shear modulus) and solid-like transversely. Because of this, important properties include in-plane structure, elasticity, and dynamics and out-of-plane structure and elasticity.

Experimental reference data can be classified as either direct or indirect. Direct data includes experimentally measured properties (e.g. x-ray and neutron form factors from scattering experiments, NMR bond order parameter), while indirect data includes properties inferred from direct experimental data based on a given theoretical model (e.g. area per lipid, bilayer thickness, lipid diffusion coefficient). Ideally, force field and simulation validation should be based on the comparison of simulated data with direct experimental data, but this is not always possible.[84] Therefore, we discuss both types of data comparisons.

Perhaps the most important verification of any lipid membrane model involves the continuous structural and mechanical profiles in the out-of-plane ("transverse", or z) direction. The lipid bilayer membrane's internal structure and mechanics are crucial to its physics. These metrics include (1) the local density profile and (2) the stress profile.

Transverse local density profile

As for general liquid-liquid interfaces, the density profile $\rho(z)$ is a crucial structural metric for lipid bilayer membranes. A typical transverse local electron density profile is shown in Figure A.1. Various regional models have been proposed to characterize the membrane based on its component and overall densities. For atomistic models, the local density profile is explained by a four-region model. The region numbering scheme proceeds from the exterior water layer to the bilayer midplane, including (1) "perturbed water" (between where lipids protrude into the water layer and where lipid and water densities are comparable), (2) "interface" (where the water density disappears and the lipid and total density reaches a maximum), (3) "soft polymer" (a region of high tail density and partially ordered chains), and (4) "decane" (a region of low density and high free volume). The typical density hierarchy, from most to least dense, is therefore as follows: region 2 > region 3 > region 1 > region 4.[90,91] The local density can be calculated through most conventional MD packages, although care should be taken to ensure appropriate averaging, especially for larger, more appreciably fluctuating membranes. Be careful with programs that tabulate density averages based on absolute coordinates and not on relative positions (e.g. aligning profiles each frame by the apparent membrane center). When using *g_density* in GROMACS, be sure to use the -center flag. Relative positions can be valuable when there are even minor fluctuations. Failure to correct for this can result in smearing of the density profile; one possible outcome is that region 4 (local lipid density drop in center) is not properly captured when it may exist for a given model. For larger membranes with significant undulations, the order parameter for the density profile (i.e. the relative z-coordinate location) must be replaced with a more appropriate one that reflects the depth into the fluctuating interface. The local density profile can be directly compared with x-ray and neutron scattering experiments through conversion of atomic

density profiles to electron and neutron density profiles, respectively, and transformation of these profiles to Fourier space. Care should be taken here as well to account for geometric differences between planar and vesicular membranes (see Section A.2.1). For AA MD data comparisons, there are several thorough studies.[92,93] Electron densities proceed generally in the same trends as above.[22] For more information on techniques, the following reference is instructive.[84]

Transverse lateral stress profile

The lateral stress profile (in the transverse direction) $P_{xy}(z) - P_z$ quantifies the equilibrium balance of stresses (forces acting between regions) pointwise in a lipid bilayer. This breakdown is only unambiguous for a model whose forces are themselves defined pointwise (for example, a continuum model). However, these ranged forces can be projected onto a continuum model, a transformation that requires the specification of a path (the contour) between points. As shown in "Statistical mechanics of inhomogeneous fluids"[95] by Schofield and Henderson, section IV, observables that can be cast as resulting from a global deformation of the system can be computed unambiguously from the profile, including curvature derivatives (see Sodt 2016,[96] supplemental). Care must be taken, however, to interpret local features of the profile qualitatively. For example, it is appropriate to ask the question "Does the model capture the qualitative structure of the competing forces in lipid bilayer assembly and stability?" Despite its importance, however, the stress profile is often more difficult and expensive to calculate. One means of calculating is through GROMACS-LS, a customized version of the MD package GROMACS. GROMACS-LS can even calculate stress component profiles, including those arising from van der Waals and electrostatic interactions. For more information about package and theory: `http://mdstress.org/`.[97–100] As an important verifying metric of force field development, the stress profile can be thoroughly compared with existing

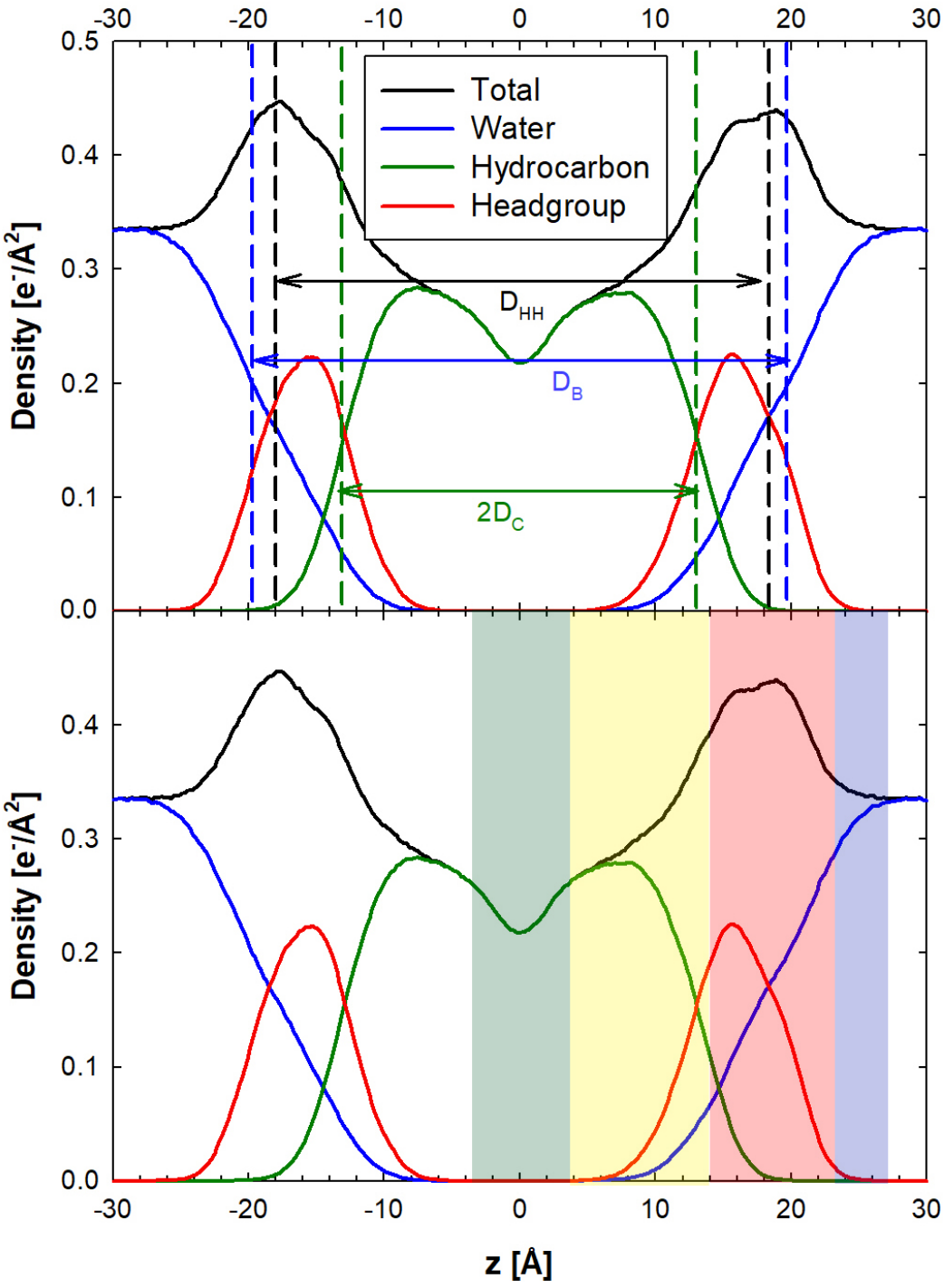

Figure A.1: Transverse local electron density profiles for DMPC/cholesterol bilayer. Shown here are local density profiles for different molecular/atomic groups along the lipid normal for a fluid DMPC bilayer with 5% cholesterol (top panel: different bilayer thickness definitions and bottom panel: four-region model with Regions 1, 2, 3, and 4 labeled as blue, red, yellow, and green, respectively). Data adapted from Boughter et al.[94]

atomistic simulation studies. There is no direct means of stress profile comparison with experiments, though as we will explain, properties calculated from the stress profile can be compared with experiment (Section A.2.4).

Bilayer thickness

The membrane thickness is a structural metric that is consequently calculated from the density profile. Three experimentally relevant definitions include (1) the Luzzati (total lipid) thickness D_B, (2) the head-to-head distance D_{HH}, and (3) the hydrocarbon thickness $2D_C$. The Luzzati thickness is relevant to neutron scattering, and is calculated as the distance between the two locations on each side of the bilayer where the water density drops to one half its bulk value. This thickness metric in reality is based on the spatial profile of protiated and deuterated water, and is physically indicative of the degree of water penetration into the bilayer.[84] The head-to-head distance is relevant to x-ray scattering, and calculated as the distance between the two peaks in the electron density profile. More simply, this can also be approximated as the distance between the maximal phosphate group densities in each leaflet (relevant to coarser lipid models).[84] The hydrocarbon thickness is also an important measure when comparing with transmembrane proteins and their length of surface exposure of the hydrophobic residues. All of these thickness calculations can be indirectly compared with experiment, which for example can be obtained from neutron scattering (specifically, the difference between repeat spacing of lipid lamellae in water and the thickness of the water layer) or x-ray scattering (the same definition as in simulation).[84] Typical values for phospholipid bilayers in simulation and experiment are around 3 to 5 nm.

Area per lipid and NMR order parameter

Two important structural parameters, complementary to one another, are (1) the area per lipid a_l (providing information about in-plane structure or lateral density) and (2) the deuterium NMR order parameter S_{CD} (for out-of-plane structure). Area per lipid and the deuterium NMR order parameter are shown schematically in Figure A.2.

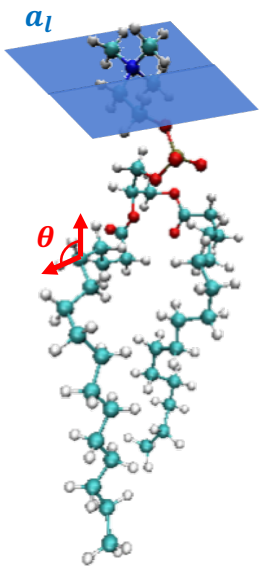

Figure A.2: Area per lipid and deuterium NMR order parameter definitions. Shown here for an all-atom DPPC phospholipid are the definitions of the area per lipid (blue plane) and an angle along one of the lipid acyl chains (red) used for the NMR order parameter calculation.

The area per lipid, or in-plane area occupied by a given lipid, is a critical target in force field parameterization of lipid membranes.[19,22] In simulation, the area per lipid is typically calculated via

$$a_l = \frac{L_x L_y}{n} \tag{A.9}$$

where $n = N_l/2$ is the number of lipids per leaflet.[84] This equation assumes a lipid number symmetric bilayer with negligible undulations, such that the contour (membrane) and projected (periodic box) areas are roughly equal.[19,22] However, for larger membranes, undulations will lead to significant differences between the contour and projected areas. Theoretically speaking, undulations will increase the ratio of contour area to the projected area, and this is specifically because the undulations reduce the projected areas.[19] The area per lipid is rigorously an intensive, or size-independent, quantity, so the appropriate steps should be taken to normalize for significant size effects when necessary before experimental comparison. This may warrant simulation of different membrane sizes, extrapolating results to zero system size to allow for convergence of contour area to frame area and arriving at a size-independent metric.[68] However, the area per lipid may not vary much across typical sizes of MD simulations, or even in experiments. In any event, care should be taken to ensure proper statistics. Even at equilibrium, the area per lipid can fluctuate on a time scale of 10-100 ns,[84] especially for complex bilayers and for those with many components. For multicomponent membranes, the membrane should be partitioned into individual values for each lipid species. Voronoi-based methods can be particularly useful for lipid mixtures in that they can partition the total bilayer area into individual area per lipid values for each species.[84] APL@Voro is a prominent Voronoi-based method for GROMACS trajectories, and supports projected area per lipid and bilayer thickness calculations for mixed lipid membranes and those including proteins.[3] Partial molar areas can be determined, but this requires that a range of concentration ratios be simulated. The area per lipid can be compared directly with other simulations; normalized size-independent metrics should be obtained where possible. The value for double-tailed phospholipids is generally larger than single-chain hydrocarbons in systems like self-assembled monolayers (60 Å^2/molecule versus 30-40 Å^2/molecule).

The deuterium P_2 NMR order parameter describes the alignment of lipid constituent

bonds with the global membrane normal (the z-direction for a bilayer assembled in the xy-plane), and will vary along the length of the lipid tail group chains and between liquid disordered and ordered or gel membranes. For phospholipids, the NMR order parameter can also be used validate the structure of the glycerol backbone and headgroup.[101] The metric is defined as:

$$S_{CD} = \frac{1}{2}\left\langle 3\cos^2\theta - 1 \right\rangle . \tag{A.10}$$

where θ is the angle between a given carbon-deuterium bond along the lipid molecule and the global membrane normal and the brackets specify an ensemble average. A value of 1 indicates perfect alignment of the chain with the global bilayer normal, while -0.5 indicates anti-alignment. This metric, however, can be ambiguous. For example, a value of zero can mean either that the lipids are isotropically disordered with respect to the bilayer normal, or that the lipids are perfectly oriented at a constant angle equal to the "magic angle" of 54.74°.[84] Computing error bars is tricky, but the *order_parameters* tool in LOOS[102] offers one approach; LOOS is compatible with files generated from multiple MD packages, including Amber, CHARMM, GROMACS, and NAMD. Since the area per lipid and NMR order parameter are tightly coupled, a similar magnitude of statistics (≈10-100 ns) is required for S_{CD} as well. Calculated metrics can be compared with other simulations and directly with quadrupolar NMR splitting experiments.[103] Figure A.3 shows typical order parameter profiles along the length of the lipid acyl chains for membranes of different lipid composition, and therefore different phase composition. Increasing cholesterol composition transitions a DMPC bilayer from a liquid-disordered bilayer to a liquid-ordered one. For a fluid phase bilayer from the top of the acyl chains to the bottom, values typically rise from about 0.17-0.20 to 0.20-0.22, then fall down to 0.10. Averages across the entire chains are therefore typically around 0.17.[19] Gel and

liquid-ordered phase bilayer values are systematically larger across the acyl chains due to enhanced packing and ordering.

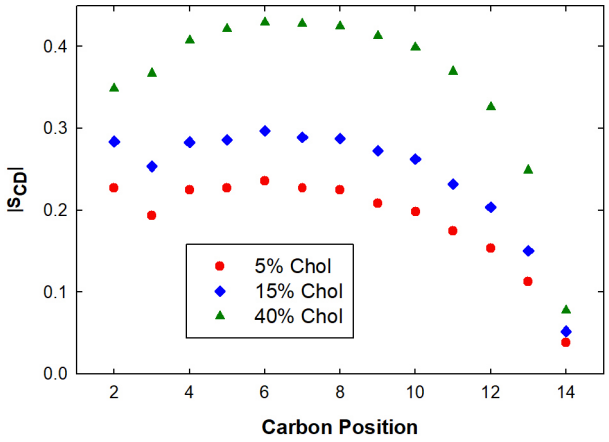

Figure A.3: Deuterium NMR order parameters for DMPC/cholesterol bilayers. Shown here are order parameter profiles along the lipid acyl chains for DMPC bilayers of increasing cholesterol composition, with values increasing from a L_d (5% cholesterol) to L_o (40% cholesterol) phase bilayer. Data adapted from Boughter et al.[94]

While the area per lipid cannot be directly compared with experiments, due to the complications of lateral and transverse structure fluctuations, it can usually be inferred from a theoretical model that sometimes involves S_{CD}. One example simply uses the lipid volume V_L and the Luzzati thickness: $a_l = 2V_L/D_B$. This assumes, however, that the lipid volume can be estimated accurately.[84] Another approach uses the deuterium NMR order parameter: $a/chain = 2V_{CH_2}/\Big((1+2S)b_{cc}\Big)$, where $a/chain$ is the area per tail group chain (of which there are two for double-tailed lipids), V_{CH_2} is the volume of a CH_2 group, S is the plateau value of S_{CD} (maximum described above) and b_{cc} is the projected C-C bond length along bilayer normal.[104] Practically, these comparisons are difficult because S_{CD} contains contributions from conformational disorder, local lipid tilting, and assorted collective motions.[19] While we do not recommend the above area per lipid models for the validation of lipid force fields, these models can at least be used for semiquantitative comparisons.

Lipid lateral diffusivity

The lipid lateral diffusivity D_l is used to characterize lipid mobility, to gain insight into collective lipid motion timescales, and also potentially to discriminate between liquid crystalline and gel phase lipids. The relevance of a diffusivity is predicated on the assumption of classical in-plane diffusion. As such, the diffusivity can be determined from the slope of the average lipid mean-squared displacement (MSD) plotted against lag time (equal to $4D_l$ for 2D diffusion). In the MSD calculation, the user should be careful of artifacts due to lipid molecules partially or fully jumping across periodic boxes; periodicity can be accounted for by reimaging where appropriate. For a homogeneous, single-component membrane, averages are normally taken over all lipids. Results typically fall around O(10^{-8} to 10^{-7} cm^2/s). Simulation results can vary significantly with the force field, system size, truncation scheme for long-range interactions, time step, and non-bonded interaction pair list update frequency.[84] Venable et al. recommends that, when reporting and comparing with other simulations, the system size in particular should be noted and accounted for. Given the hydrodynamic theory, the lateral and transverse dimensions would be even more explicit, and ideally, studies should report extrapolated infinite size values with a confidence interval.[13] The hydrodynamic theoretical framework has been extensively validated by Vögele and Hummer, who conducted MD simulations with up to 10^8 coarse-grained particles in half-micron-sized boxes.[105] Results can be indirectly compared with experiment. Experimental estimates can generally vary over three orders of magnitude, due to a number of reasons (cf. Section A.2.4 for more details).[84]

Mechanical/elastic properties

Mechanical properties for membranes can be calculated from a number of techniques that can be broadly classified by (1) equilibrium fluctuations, (2) stress profile, and (3) biased/active deformations. We discuss the merits of each umbrella of approaches in general terms in Section A.2.4. In this section, we merely attempt to recommend the best technique(s) for a given property. These mechanical properties include: (1) lateral tension, (2) area compressibility modulus, (3) bending modulus, (4) monolayer spontaneous curvature, (5) Gaussian curvature modulus, and (6) line tension.

(1) Calculation of the lateral tension γ from a membrane simulation is a way to calculate the variable conjugate to the membrane [contour] area in canonical simulations, and in tension control, a way to directly confirm the simulation controls for the intended ensemble. In model development, the tension is a parameter probed to capture the correct area per lipid (which should ideally occur at zero tension).[26] The tension is related to the zeroth moment of the stress profile, and can be easily approximated with the Kirkwood-Buff equation Equation A.4 above.

(2) The area compressibility modulus K_A determines a membrane's ability to compress and expand, and is another important property in force field parameterization.[19] The recommended way to calculate K_A is based on area fluctuations in the tensionless ensemble:

$$K_A^{app} = \frac{k_B T A_p}{\sigma^2_{A_p}} \tag{A.11}$$

where K_A^{app} is the apparent area compressibility modulus based on the fluctuations in projected area $A_p = L_x L_y$. This equation is fairly simple, but involves two major nuances. The first is that the calculation may take 100 ns to converge,[19] if not longer. The second is that this is an apparent value based on size-dependent projected area fluctuations, and is not the end point for characterizing the intensive, size-independent in-

plane compressibility. The recommended correction to deconvolute expansion-compression modes from undulatory modes is to simulate multiple membrane sizes and extrapolate the results to zero system size, where undulations no longer exist.[68] At smaller simulated system sizes, the result of not accounting for undulatory contributions can be negligible (∼5-10% correction with experiment), but becomes substantial and must be corrected for larger system sizes (where they can be ∼50% larger than experimental results).[19,68] Results typically vary between 100 and 400 mN/m,[19] and are often compared with micropipette aspiration experiments.[106] Results can also be compared with predictions from polymer brush theories, where K_A is sometimes related to the oil-water interfacial tension $\gamma^{o/w}$–for example, $K_A = 6\gamma^{o/w}$.[106]

(3) The bending modulus (bending rigidity/constant) κ determines the ability of the membrane to bend. The undulation spectrum method[107,108] is the traditional and well-established way to calculate κ. On the basis that at large enough scales, a membrane behaves as a two-dimensional surface, the free energy per lipid can be expanded in terms of the area per lipid and mean and Gaussian curvatures H and K_G respectively.[109] In the absence of external stresses, a membrane minimizes its free energy with respect to area (i.e. it is tensionless), and shape (i.e. curvature) fluctuations are more accessible than expansion-compression (area compressibility) fluctuations. Canham and Helfrich developed a membrane Hamiltonian on this phenomenological basis, that a membrane has a preferred morphology (dictated by its spontaneous curvature C_0) and has deviations from that preferred curvature,[110,111] resulting in:

$$\mathcal{H} = \int dS \left[\frac{\kappa}{2} (2H - C_0)^2 + \kappa_G K_G \right] \tag{A.12}$$

where $H \equiv (c_x + c_y)/2$ (c_x and c_y are the principal curvatures), κ_G is the Gaussian curvature modulus, and $K_G \equiv c_x c_y$. This integral is performed over the entire surface of

the membrane. The integral over the Gaussian curvature term depends on the membrane topology and boundary, and does not contribute to the membrane energetics when topology and boundary do not change (i.e. when there are no membrane fission/fusion events, no pores/pre-pores, etc.). In this definition, κ is the bare bending modulus, a "true bilayer property" and enthalpic/elastic quantity that represents a spring constant for curvature deformations. For small deformations of a bilayer of zero spontaneous curvature ($C_0 = 0$), the first term of the integral is often presented in terms of the Monge gauge (with the surface described with respect to the xy-plane at $z = 0$):[109]

$$\mathcal{H} = \int dxdy \left[\frac{\kappa}{2} \left(\nabla^2 h(x,y) \right)^2 \right] \tag{A.13}$$

where h is the membrane height function and x and y, as before, are the in-plane directions of the membrane. By introducing a Fourier representation for h and applying the Equipartition Theorem, one can derive the height-height undulation spectrum.[54] The spectrum describes the height-height correlations $|h_q|^2$ of the membrane continuum shape, and for a tensionless membrane, the large wavelength/small wavevector (q) behavior follows an inverse fourth power relation with a constant of proportionality that contains the bending modulus:[107,108]

$$\left\langle |h_q|^2 \right\rangle = \frac{k_B T}{\kappa q^4} \tag{A.14}$$

The undulation spectrum method, however, must be used over "mesoscopic" length scales (approximately ten times the bilayer thickness, or about 50 nm / 5000 lipids) that are out of reach for AA and most CG simulations. If simulations are too small, deviations to the undulation spectrum will result from individual lipid tilting (below ten thicknesses) and protrusions (below three thicknesses).[19] Also, there will simply not be a large enough range of wave vector magnitudes to fit the spectrum and obtain a bending modulus

estimate. For this reason, we recommend the lipid director field spectrum approach,[19,112] which analyzes thermal fluctuations of lipid orientation via a director vector field $\hat{n}_q$ (the vector from a lipid's head to its tail). Specifically, the longitudinal component of the director field $\hat{n}_q^{||}$ relates to the macroscopic bending modulus through an inverse second power relation in the wave vector:

$$\left\langle \left| \hat{n}_q^{||} \right| \right\rangle = \frac{k_B T}{\kappa q^2} \quad (recommended) \tag{A.15}$$

The lipid director field spectrum method works well for "modestly sized" membranes, down to approximately three bilayer thicknesses (≈12-15 nm); AA simulations of 648 lipids have been shown to be well converged. This general approach also provides a route to calculating bilayer tilt and twist moduli. Both the undulation and lipid director field spectrum approaches will take at least 100 ns to converge.[19]

Equations A.14 and A.15 above relate membrane fluctuations to the bending modulus. It is important to note that the κ resulting from these methods is actually an apparent/effective bending modulus, a free energetic quantity incorporating the effects of finite size (thermal fluctuations). The effective bending modulus is not a material property, and can be understood as a renormalization/correction from the bare value as first introduced by Peliti and Leibler. It is dependent on system size, and decreases at larger wavelengths λ as $\kappa(\lambda) = \kappa_0 - 3k_B T/4\pi ln(\lambda a)$, where κ_0 is the bare modulus and a is some constant.[113] The determination of the appropriate size renormalization is somewhat ambiguous, but the length scale of the relevant experimental system can be used as a guide. Furthermore, these techniques are only applicable in the small deformation/low curvature limit (i.e. in the absence of an external bending force). The bare bending modulus is a size-independent quantity applicable at larger deformations/higher curvatures where ground state energies are dominant and fluctuation effects are negligible, and therefore

may be more experimentally relevant. Several, more user-intensive approaches have recently been introduced to directly measure the bare bending modulus;[114–117] for more information, the interested reader is directed to those studies.

Bending modulus results typically vary between 10 and 40 k_BT,[19] and can be compared with a host of experimental techniques, including flicker spectroscopy and micropipette aspiration. See Section A.2.4 for more details. For more information on experimental and simulation approaches to calculating the bending modulus across various force fields, and particularly the inconsistencies in results, we direct the interested reader to Bochicchio and Monticelli.[53] Results can also be compared with polymer brush theory, which relates κ to K_A and the bilayer hydrophobic thickness h_{phob} via $\kappa = K_A h_{phob}^2/24$.[106] We do not recommend using polymer brush theory to obtain and report bending moduli, but recommend it as a point of comparison with bending moduli calculated from the techniques recommended above.

(4) While lipid bilayers (planar and vesicular) have a net zero bilayer spontaneous curvature C_0, their monolayers individually may have a propensity to curve. This propensity is quantified by the monolayer spontaneous curvature c_0, and is defined to be positive for a lipid that forms micelles and negative for one that forms inverted micelles.[19] Together with the monolayer bending modulus κ_m, c_0 is related to the first moment of the stress profile, integrated from the bilayer midplane to the upper edge of the simulation cell:[109]

$$\kappa_m c_0 = \int_0^{L_z/2} z[P_{xy}(z) - P_z]dz \tag{A.16}$$

Thus, if κ_m is known, then c_0 can be quantified. κ_m is predicted by elastic theory to be one half the bilayer value (κ). Monolayer spontaneous curvatures are typically calculated indirectly in experiment from studies in the completely different inverted hexagonal H_{II}

phase, where lipid monolayers are assembled in long, hexagonally-arranged water-filled tubes.[118] Results are then extrapolated to the lamellar phase. This is hard to study for lipids like DPPC that are more cylindrical in shape, but easier for those like DOPE that are more like inverted truncated cones (due to acyl chain unsaturation).[19,119]

(5) The Gaussian curvature modulus κ_G describes the propensity of the membrane to change topology, and is especially important for fission and fusion events.[115] In general, even simulation methods for calculating κ_G are controversial. The difficulty in calculating κ_G lies in controlling topology and boundary behaviors in which Gaussian curvature plays a role.[115] The stress profile approach, specifically involving the second moment, is not reliable here.[115,120] We recommend the patch closure method, which has shown promise in preliminary work.[115] Experimental analysis of the temperature dependence of the cubic to inverse hexagonal transition for N-monomethylated dioleoylphosphatidylethanolamine[?] is one of the few hints, with $\kappa_G/\kappa = -0.927$. Elasticity theories do offer predictions, for example, the simple approximation $\kappa_G \approx -\kappa$.[28,59,115]

(6) A line tension (edge energy) Γ is an energy per unit length that can describe lipid phase segregation and hole formation. Specifically for pores (hydrophilic holes, where lipids splay to connect the two leaflets), the line tension can be studied through simulation of a bilayer "strip" or "half-connected bilayer" (with exposed bilayer edges in one in-plane box dimension). The bilayer is thus periodic in one lateral dimension and exposed in the other, resulting in lipid splaying and therefore a rim on both sides. In this scenario, the line tension can be determined from the stress profile, specifically the lateral normal stresses. If the strip is periodic in y and non-periodic in x, then:

$$\Gamma = \frac{1}{2}\, L_x L_y (P_{xx} - P_{yy}) \tag{A.17}$$

and $P_{xx} = P_{zz}$.[121] Typical values are around 35 to 50 pN in simulation[121,122] and 5 to 30

pN in experiment,[123–125] the latter of which are typically determined through dynamical pore closure studies.

Leaflet-dependent properties

Lipid bilayers are made up of two molecularly-thick leaflets in a fluctuating membrane embedded in three dimensions. Identifying which lipid is in which leaflet at any given time is useful for identifying the local bilayer midplane, and therefore a host of bilayer and individual monolayer properties. While thickness, area per lipid, deuterium order parameter, and lipid lateral diffusivity calculations do not necessarily require leaflet identification, other metrics do. Leaflet identification and the relevant metrics are discussed in Section A.2.4.

Property validation summary

It is the responsibility of computationalists in the field of membranes and otherwise to adequately validate the physical properties resulting from their model. The method of calculation in experiment does matter to the method of calculation in simulation. For example, methods based on biased membrane perturbations may deviate significantly from those based on equilibrium fluctuations (e.g. micropipette aspiration versus flicker experiments).[19] Wherever possible, the theoretical basis for both the experimental and simulation property calculations should be used as a guide. A final point is that experimental results are not infallible. When simulation and experiment do not agree or there is large variation within experimental measurements for the same property and the computational procedure is sound, simulations can provide refinement to the experimental results.[19]

Nuances to diffusivity calculations

Subdiffusion, a distinct form of anomalous diffusive motion characterized by long-range correlations in time or space, has been recognized in many biological systems, including diffusion in the crowded cytoplasm, the internal dynamics of proteins, and the gating of ion channels.[126–129] The physical origin of subdiffusion, and whether it is truly present, remains controversial for some systems.[130] However, there is growing evidence for transient subdiffusion in the lateral dynamics of lipids in phospholipid bilayers.[131] The subdiffusive regime has been shown to exist between the ballistic and random (linear MSD) walk regimes, spanning as many as five orders of magnitude in time[132] and timescales reaching many seconds in multicomponent membranes.[131] While this potentially has crucial consequences for dynamical validation of membrane models, its application to a robust protocol for multiscale lipid models is at this point unestablished.

There is a major box size dependence for dynamic properties in MD simulation. In general, diffusive dynamics in confined, periodic simulation systems are perturbed relative to the macroscopic limit, and can be corrected through the application of hydrodynamic theories. Lateral diffusive dynamics in lipid membranes suffer from significant finite size effects (a factor of 3 to 4 for AA MD)[13,14] relative to bulk dynamics in a homogeneous fluid ($\sim$10-20%).[133] Because of longer-ranged hydrodynamic correlations for membranes, convergence is expected to be even slower than an inverse box length convergence in 3D.[134] Camley et al. has adapted the Periodic Saffman-Dellbrück theory describing hydrodynamics of a periodically-replicated membrane suspended in an infinite bulk fluid for cylinders spanning a single leaflet (i.e. lipids). The model additionally accounts for the influence of interleaflet friction. Crucially, it has been shown that not only the lateral dimension, but also the transverse dimension (solvent thickness) plays a large role in the convergence to macroscopic diffusive dynamics.[13] This hydrodynamic

framework has been extensively validated by Vögele and Hummer, who conducted MD simulations with up to 10^8 coarse-grained particles in half-micron-sized boxes.[105] The theory shows that typical simulation dimensions are much too small for macroscopic dynamical estimates, but allows for extrapolation and comparison with experiment. The theory also effectively implies a variational principle for capturing diffusivities with AA simulations of reasonably-sized systems: if the force field and other settings (integration, ensemble, long-range electrostatics, etc.) are correct, then the simulated diffusivities are expected to underestimate experiment.[13] However, if the desire is to compare to some biological system, it may be useful to normalize to a different finite system size. Experiments have shown that, through an anchored protein picket model, proteins anchored by the membrane cytoskeleton can slow effective lipid diffusion due to both steric hindrance and circumferential slowing, a hydrodynamic friction-like effect.[70] This has been found to be consistent with a characteristic domain size of 150-500 nm[69,70] (cf. Section A.2.1).

Experimental diffusivity estimates can vary for a number of reasons. First, diffusivities can be determined from a variety of methods, including fluorescence techniques (e.g. fluorescence recovery after photobleaching, FRAP, and fluorescence correlation spectroscopy, FCS), quasi-elastic neutron scattering, EPR, and NMR, amongst others. The length and time scale of study can vary significantly with different methods; for example, EPR and NMR (O(1 nm-100 μm),O(1 ns-1 ms))[135–138] and quasi-elastic neutron scattering (O(0.1-10 nm,<1 ns)).[84] (Furthermore, neutron spin echo spectroscopy has recently been shown to probe ∼100 ns and obtain membrane viscosity estimates that can be used to estimate in-plane diffusivity.[139]) While different regimes of diffusion may exist across different lag time scales (most notably, non-classical subdiffusion; see above), fits and comparisons from very different time scales can also be prone to significant statistical error. In some of these techniques (e.g. FCS, FRAP), the use of labeled lipids instead of

the normal lipids biases the calculations for lipid diffusion. In addition to the increased drag that the label introduces, dynamics can also be impacted by label concentration. Dynamics can be particularly slow for supported lipid bilayers, the physics of which can also be very different from those of the simulation due to interleaflet friction and increased drag from the solid support. Otherwise, results are highly dependent on temperature, hydration content, pH, ionic strength, and experimental setup.[84]

Evaluation of major techniques for mechanical property calculation

In general terms, we outline the merits of each umbrella of approaches for calculating mechanical properties (Table A.3).

Table A.3: Methods for calculating mechanical properties: a broad cross-comparison

Class of Methods	**Advantages**	**Disadvantages**
Equilibrium Fluctuations	• Theoretically consistent/rigorous and elegant (admitted directly from Landau-Ginzburg and related approaches, e.g. Canham-Helfrich) • No additional user input required (just run the simulation!) • Well documented and generally the preferred choice in the membrane theory and simulation community	• Can only study and apply results to small deformation limit; not necessarily relevant to strong deformations[114] • Can take a long time for statistics to converge / fluctuations to develop[116] • Low signal-to-noise ratio • Grid analysis in post-processing can be expensive

Local Thermodynamics / Stress Profile	• Theoretically motivated • No additional user input required (just run the simulation!) • Consistent with rationale for simulation pressure coupling scheme and Laplace tension (and therefore frame tension), i.e. equation for justifying tension settings in simulation is a specific case (Equation A.4) • The only route to calculating certain properties (tension, monolayer spontaneous curvature) • Profile also be used to understand local stresses and molecular driving forces	• Rigorous implementation (although codes exist); expensive voxel analysis in post-processing • Certain moments give you combinations of properties rather than individual ones, and are therefore dependent on other techniques • Slow convergence • Low signal-to-noise ratio (seeking small numbers often from largely-fluctuating ones)

Biased/Active Deformations	• Theoretically motivated • Applicable to large-scale deformations (potentially more physically relevant), with a broader range of permissible deformations overall; capable of addressing nonlinear and higher-order effects on mechanical properties at higher deformations[116] • Often more efficient/do not require long sampling times, due to probing of ground state energies over fluctuations[53,116] • Less sensitive to finite-size effects[116] • High signal-to-noise ratio (ground state energies dominant over thermal fluctuations)[53]	• Don't necessarily allow for pressure and lipid number asymmetry relaxation along the deformation process[53] • Limited to pure membranes due to the possibility of composition-curvature inhomogeneities otherwise[53] • In extreme circumstances, can induce phase transformations[53] • Requires additional user input: some biasing scheme and/or nontrivial simulation setup (e.g. tether) for the calculation

For most of our mechanical property method recommendations here, we focus on the "equilibrium fluctuations" and "stress profile" classes of techniques. However, there are several alternative methods based on "biased/active deformations" techniques. For the area compressibility modulus, the bilayer can be actively stretched via different simulations in the NP_zAT (constant area and transverse pressure) ensemble; the surface tension can be evaluated at each area, and K_A is calculated from the derivative $K_A^{app} = A_p(\partial\gamma/\partial A_p)_T$.[140,141] For the bending modulus, there are several techniques.[114,116,117,142] Umbrella sampling has been used to enforce large undulation modes,[117] but this study experienced difficulty separating bending contributions from those of stretching. The membrane tether stretching approach in general applies to larger curvature deformations, with radii of curvature down to the membrane thickness, and converges to undulation spectrum results in the small deformation limit. Most recently, the buckling technique was introduced to overcome limitations of membrane tether stretching techniques (including problems with handling explicit solvent), and provides insight into the enthalpy-entropy breakdown of bending contributions and therefore the local temperature dependence on κ.[114,142]

The bending modulus can be experimentally determined from a variety of techniques. This includes fluctuation analysis (e.g. flicker spectroscopy), micropipette aspiration and the low-tension stress-strain relationship, tether stretching (with magnetic fields or optical tweezers,[143,144] x-ray scattering, and neutron spin echo measurements. The bending modulus provides one example where parallel experimental and simulation calculation methods is useful. Simulation results from the undulation and lipid director spectra have been found to agree well with flicker experiments, as both are based on equilibrium fluctuations. These deviate significantly from micropipette aspiration, which is based on "biasing/active deformations".[19]

In the simulation community, as in most of the experimental community, bending

is treated as an elastic deformation, so the stress-strain relationship is independent of the rate at which the bending strain is applied. However, there have been various suggestions, with experiment evidence, that membranes may exhibit viscoelasticity with short-time transient responses.[144,145] Due to the complete lack of simulation infrastructure for assessing membrane viscoelasticity at this time, we defer any recommendations on studying it.

Techniques for leaflet identification & leaflet-dependent properties

One method to identify leaflets involves first determining the height function of the entire bilayer in high-resolution gridspace (cf. recommended procedure in Watson et al., Appendix C),[146] then going back and sorting into leaflets. However, this can be difficult, especially for membranes with large deformations and complicated morphologies. One analysis package that overcomes these complications is the Fast Analysis Toolbox for Simulations of Lipid Membranes (FATSLiM). FATSLiM[2] is a Python-based package designed to work with GROMACS that, for every simulation frame, can estimate the normal for every lipid via principal component analysis of each lipid and its neighbors. Therefore, it can approximate the membrane surface in a morphology-independent manner (e.g. can be applied to planar and vesicular membranes alike, unlike the packages APL@Voro,[3] MEMBPLUGIN,[147] and GridMAT-MD[4]), and can determine membrane leaflets, thickness, and area per lipid. FATSLiM is both efficient and low-memory-consuming (relative to APL@Voro), and documentation is available at: `http://pythonhosted.org/fatslim`.

One class of metrics that require leaflet identification are those associated with lipid coordination. The lipid coordination number can be used in phase transitions and coexistence to distinguish between fluid and gel phases, which have markedly different values, and to characterize the segregation of multicomponent bilayers (e.g. does cholesterol segregate with lipid X vs Y). The coordination number is rigorously determined from

cumulative integration of the in-plane (2D) radial distribution function to some coordination cutoff distance. Unless interested otherwise, histograms should be binned separately for each leaflet (otherwise, liquid and solid structural signatures are convoluted and lack meaning) by the in-plane 2D radial distance (as opposed to standard RDFs in 3D). (There are several other structural, thermodynamic, and dynamic techniques for detecting and characterizing phase transitions and coexistence outlined above, including thickness, area per lipid, the deuterium NMR order parameter, and lipid lateral diffusivity, amongst others.)

Other properties & relevant resources

In order to simulate biologically-relevant transmembrane voltage gradients, there are several possible simulation "tricks." The major problem is the need to use PBCs in simulations, which prevent the setup of a charge gradient. A well-accepted solution is to simulate two bilayers in a single simulation cell, separating the salt baths for the charge gradient. For more details, see the work of Sachs, Crozier, and Woolf.[148]

At present, free energy calculations and rare events & importance sampling methods are beyond the current scope of this document. We recognize that free energy calculations and advanced sampling strategies are extremely promising for studies of pore formation, membrane fusion and other collective phenomena of lipid membranes. For more information, see Smirnova et al.[21] and its references.[7,19]

A.3 Acknowledgements

DJS acknowledges the support of the Department of Defense Defense Threat Reduction Agency (HDTRA1-15-1-0045) and NSF (project DMR-1312548). The content of the publication does not necessarily reflect the position or policy of the Federal Government,

and no official endorsement should be inferred. DJS also acknowledges the Center for Bioengineering at the University of California, Santa Barbara, for the Crossroads Fellowship in Materials, Mechanics, and Medicine. JBK acknowledges the support from NSF (MCB-1149187 and CBET-1604576).

Bibliography

[1] Van Der Spoel D, Lindahl E, Hess B, Groenhof G, Mark AE, Berendsen HJC. GROMACS: Fast, flexible, and free. *Journal of Computational Chemistry.* 2005; 26(16): 1701–1718.

[2] Buchoux S. FATSLiM: a fast and robust software to analyze MD simulations of membranes. *Bioinformatics.* 2017; 33(1): 133–134.

[3] Lukat G, Krüger J, Sommer B. APL@Voro: A Voronoi-Based Membrane Analysis Tool for GROMACS Trajectories. *Journal of Chemical Information and Modeling.* 2013; 53(11): 2908–2925.

[4] Allen WJ, Lemkul JA, Bevan DR. GridMAT-MD: A grid-based membrane analysis tool for use with molecular dynamics. *Journal of Computational Chemistry.* 2009; 30(12): 1952–1958.

[5] Poger D, Van Gunsteren WF, Mark AE. A new force field for simulating phosphatidylcholine bilayers. *Journal of Computational Chemistry.* 2010; 31(6): 1117–1125.

[6] Jämbeck JPM, Lyubartsev AP. Derivation and Systematic Validation of a Refined All-Atom Force Field for Phosphatidylcholine Lipids. *The Journal of Physical Chemistry B.* 2012; 116(10): 3164–3179.

[7] Marrink SJ, Vries AH, Mark AE. Coarse Grained Model for Semiquantitative Lipid Simulations. *The Journal of Physical Chemistry B.* 2004; 108(2): 750–760.

[8] Marrink SJ, Risselada HJ, Yefimov S, Tieleman DP, Vries AH. The MARTINI Force Field: Coarse Grained Model for Biomolecular Simulations. *The Journal of Physical Chemistry B.* 2007; 111(27): 7812–7824.

[9] Arnarez C, Uusitalo JJ, Masman MF, et al. Dry Martini, a Coarse-Grained Force Field for Lipid Membrane Simulations with Implicit Solvent. *Journal of Chemical Theory and Computation.* 2015; 11(1): 260–275.

[10] Phillips JC, Braun R, Wang W, et al. Scalable molecular dynamics with NAMD. *Journal of Computational Chemistry.* 2005; 26(16): 1781–1802.

[11] Brooks BR, Brooks CL, Mackerell AD, et al. CHARMM: the biomolecular simulation program. *Journal of computational chemistry.* 2009; 30(10): 1545–614.

[12] Case D, Brozell S, Cerutti D, et al. AMBER 2018. 2018.

[13] Venable RM, Ingólfsson HI, Lerner MG, et al. Lipid and Peptide Diffusion in Bilayers: The SaffmanâĂŞDelbrück Model and Periodic Boundary Conditions. *The Journal of Physical Chemistry B.* 2017; 121(15): 3443–3457.

[14] Klauda JB, Brooks BR, Pastor RW. Dynamical motions of lipids and a finite size effect in simulations of bilayers. *The Journal of Chemical Physics.* 2006; 125(14): 144710.

[15] Watson MC, Brown FL. Interpreting Membrane Scattering Experiments at the Mesoscale: The Contribution of Dissipation within the Bilayer. *Biophysical Journal.* 2010; 98(6): L9–L11.

[16] Zilman AG, Granek R. Membrane dynamics and structure factor. *Chemical Physics.* 2002; 284(1-2): 195–204.

[17] Zilman AG, Granek R. Undulations and Dynamic Structure Factor of Membranes. *Physical Review Letters.* 1996; 77(23): 4788–4791.

[18] Hill MD, Marty MR. Retrospective on Amdahl's Law in the Multicore Era. *Computer.* 2017; 50(6): 12–14.

[19] Venable RM, Brown FL, Pastor RW. Mechanical properties of lipid bilayers from molecular dynamics simulation. *Chemistry and Physics of Lipids.* 2015; 192: 60–74.

[20] Lyubartsev AP, Rabinovich AL. Force Field Development for Lipid Membrane Simulations. *Biochimica et Biophysica Acta - Biomembranes.* 2016; 1858(10): 2483–2497.

[21] Smirnova YG, Fuhrmans M, Barragan Vidal IA, Müller M. Free-energy calculation methods for collective phenomena in membranes. *Journal of Physics D: Applied Physics.* 2015; 48(34): 343001.

[22] Klauda JB, Venable RM, Freites JA, et al. Update of the CHARMM All-Atom Additive Force Field for Lipids: Validation on Six Lipid Types. *The Journal of Physical Chemistry B.* 2010; 114(23): 7830–7843.

[23] Dickson CJ, Madej BD, Skjevik ÅA, et al. Lipid14: The Amber Lipid Force Field. *Journal of Chemical Theory and Computation.* 2014; 10(2): 865–879.

[24] Brannigan G, Philips PF, Brown FLH. Flexible lipid bilayers in implicit solvent. *Physical Review E.* 2005; 72(1): 011915.

[25] Cooke IR, Deserno M. Solvent-free model for self-assembling fluid bilayer membranes: Stabilization of the fluid phase based on broad attractive tail potentials. *The Journal of Chemical Physics.* 2005; 123(22): 224710.

[26] Zgorski A, Lyman E. Toward Hydrodynamics with Solvent Free Lipid Models: STRD Martini. *Biophysical Journal.* 2016; 111(12): 2689–2697.

[27] Wang Y, Sigurdsson JK, Brandt E, Atzberger PJ. Dynamic implicit-solvent coarse-grained models of lipid bilayer membranes: Fluctuating hydrodynamics thermostat. *Physical Review E.* 2013; 88(2): 023301.

[28] Deserno M. Mesoscopic Membrane Physics: Concepts, Simulations, and Selected Applications. *Macromolecular Rapid Communications.* 2009; 30(9-10): 752–771.

[29] Ponder JW, Wu C, Ren P, et al. Current Status of the AMOEBA Polarizable Force Field. *The Journal of Physical Chemistry B.* 2010; 114(8): 2549–2564.

[30] Vanommeslaeghe K, MacKerell A. CHARMM additive and polarizable force fields for biophysics and computer-aided drug design. *Biochimica et Biophysica Acta (BBA) - General Subjects.* 2015; 1850(5): 861–871.

[31] Khakbaz P, Klauda JB. Investigation of phase transitions of saturated phosphocholine lipid bilayers via molecular dynamics simulations. *Biochimica et Biophysica Acta - Biomembranes.* 2018; 1860(8): 1489–1501.

[32] Zhuang X, Dávila-Contreras EM, Beaven AH, Im W, Klauda JB. An extensive simulation study of lipid bilayer properties with different head groups, acyl chain lengths, and chain saturations. *Biochimica et Biophysica Acta - Biomembranes.* 2016; 1858(12): 3093–3104.

[33] Javanainen M, Martinez-Seara H. Efficient preparation and analysis of membrane and membrane protein systems. *Biochimica et Biophysica Acta - Biomembranes.* 2016; 1858(10): 2468–2482.

[34] Pluhackova K, Kirsch SA, Han J, et al. A Critical Comparison of Biomembrane Force Fields: Structure and Dynamics of Model DMPC, POPC, and POPE Bilayers. *Journal of Physical Chemistry B.* 2016; 120(16): 3888–3903.

[35] Jämbeck JPM, Lyubartsev AP. An Extension and Further Validation of an All-Atomistic Force Field for Biological Membranes. *Journal of Chemical Theory and Computation.* 2012; 8(8): 2938–2948.

[36] Jämbeck JPM, Lyubartsev AP. Another Piece of the Membrane Puzzle: Extending Slipids Further. *Journal of Chemical Theory and Computation.* 2013; 9(1): 774–784.

[37] Ermilova I, Lyubartsev AP. Extension of the Slipids Force Field to Polyunsaturated Lipids. *The Journal of Physical Chemistry B.* 2016; 120(50): 12826–12842.

[38] Maciejewski A, Pasenkiewicz-Gierula M, Cramariuc O, Vattulainen I, Rog T. Refined OPLS All-Atom Force Field for Saturated Phosphatidylcholine Bilayers at Full Hydration. *The Journal of Physical Chemistry B.* 2014; 118(17): 4571–4581.

[39] Chandrasekhar I, Kastenholz M, Lins RD, et al. A consistent potential energy parameter set for lipids: dipalmitoylphosphatidylcholine as a benchmark of the GROMOS96 45A3 force field. *European biophysics journal : EBJ.* 2003; 32(1): 67–77.

[40] Oostenbrink C, Villa A, Mark AE, Gunsteren WF. A biomolecular force field based on the free enthalpy of hydration and solvation: the GROMOS force-field parameter sets 53A5 and 53A6. *Journal of computational chemistry.* 2004; 25(13): 1656–76.

[41] Berger O, Edholm O, Jähnig F. Molecular dynamics simulations of a fluid bilayer of dipalmitoylphosphatidylcholine at full hydration, constant pressure, and constant temperature. *Biophysical journal.* 1997; 72(5): 2002–13.

[42] Malde AK, Zuo L, Breeze M, et al. An Automated Force Field Topology Builder (ATB) and Repository: Version 1.0. *Journal of Chemical Theory and Computation.* 2011; 7(12): 4026–4037.

[43] Qi Y, Ingólfsson HI, Cheng X, Lee J, Marrink SJ, Im W. CHARMM-GUI Martini Maker for Coarse-Grained Simulations with the Martini Force Field. *Journal of Chemical Theory and Computation.* 2015; 11(9): 4486–4494.

[44] Yesylevskyy SO, Schäfer LV, Sengupta D, Marrink SJ. Polarizable Water Model for the Coarse-Grained MARTINI Force Field. *PLoS Computational Biology.* 2010; 6(6): e1000810.

[45] Orsi M, Essex JW. The ELBA Force Field for Coarse-Grain Modeling of Lipid Membranes. *PLoS ONE.* 2011; 6(12): e28637.

[46] Cooke IR, Kremer K, Deserno M. Tunable generic model for fluid bilayer membranes. *Physical Review E.* 2005; 72(1): 011506.

[47] Bereau T, Deserno M. Generic coarse-grained model for protein folding and aggregation. *The Journal of Chemical Physics.* 2009; 130(23): 235106.

[48] Wang ZJ, Deserno M. A Solvent-Free Coarse-Grained Model for Quantitative POPC Bilayer Simulations. *Biophysical Journal.* 2009; 96(3): 365a.

[49] Bereau T, Wang ZJ, Deserno M. More than the sum of its parts: Coarse-grained peptide-lipid interactions from a simple cross-parametrization. *The Journal of Chemical Physics.* 2014; 140(11): 115101.

[50] Izvekov S, Voth GA. A Multiscale Coarse-Graining Method for Biomolecular Systems. *The Journal of Physical Chemistry B.* 2005; 109(7): 2469–2473.

[51] Srivastava A, Voth GA. Hybrid Approach for Highly Coarse-Grained Lipid Bilayer Models. *Journal of Chemical Theory and Computation.* 2013; 9(1): 750–765.

[52] Brannigan G, Lin LCL, Brown FLH. Implicit solvent simulation models for biomembranes. *European Biophysics Journal.* 2006; 35(2): 104–124.

[53] Bochicchio D, Monticelli L. The membrane bending modulus in experiments and simulations: A puzzling picture. *Advances in Biomembranes and Lipid Self-Assembly.* 2016; 23(April): 117–143.

[54] Brown FL. Elastic Modeling of Biomembranes and Lipid Bilayers. *Annual Review of Physical Chemistry.* 2008; 59(1): 685–712.

[55] Sapp K, Shlomovitz R, Maibaum L. Seeing the Forest in Lieu of the Trees. In *Annual Reports in Computational Chemistry*; Vol. 10 47–76 2014.

[56] Lin LC, Brown FL. Dynamic simulations of membranes with cytoskeletal interactions. *Physical Review E - Statistical, Nonlinear, and Soft Matter Physics.* 2005; 72(1): 1–15.

[57] Lin LCL, Brown FLH. Brownian dynamics in Fourier space: Membrane simulations over long length and time scales. *Physical Review Letters.* 2004; 93(25): 1–4.

[58] Brannigan G, Brown FL. A Consistent Model for Thermal Fluctuations and Protein-Induced Deformations in Lipid Bilayers. *Biophysical Journal.* 2006; 90(5): 1501–1520.

[59] Ramakrishnan N, Sunil Kumar P, Radhakrishnan R. Mesoscale computational studies of membrane bilayer remodeling by curvature-inducing proteins. *Physics Reports.* 2014; 543(1): 1–60.

[60] Van Meer G, Voelker DR, Feigenson GW. Membrane lipids: Where they are and how they behave. *Nature Reviews Molecular Cell Biology.* 2008; 9(2): 112–124.

[61] Sampaio JL, Gerl MJ, Klose C, et al. Membrane lipidome of an epithelial cell line. *Proceedings of the National Academy of Sciences.* 2011; 108(5): 1903–1907.

[62] Khakbaz P, Klauda JB. Probing the importance of lipid diversity in cell membranes via molecular simulation. *Chemistry and Physics of Lipids.* 2015; 192: 12–22.

[63] Berkowitz ML. Detailed molecular dynamics simulations of model biological membranes containing cholesterol. *Biochimica et Biophysica Acta (BBA) - Biomembranes.* 2009; 1788(1): 86–96.

[64] Ingólfsson HI, Melo MN, Eerden FJ, et al. Lipid Organization of the Plasma Membrane. *Journal of the American Chemical Society.* 2014; 136(41): 14554–14559.

[65] Monje-Galvan V, Klauda JB. Modeling Yeast Organelle Membranes and How Lipid Diversity Influences Bilayer Properties. *Biochemistry.* 2015; 54(45): 6852–6861.

[66] Rodgers JM, Sørensen J, Meyer FJM, Schiøtt B, Smit B. Understanding the Phase Behavior of Coarse-Grained Model Lipid Bilayers through Computational Calorimetry. *The Journal of Physical Chemistry B.* 2012; 116(5): 1551–1569.

[67] Castro-Román F, Benz RW, White SH, Tobias DJ. Investigation of Finite System-Size Effects in Molecular Dynamics Simulations of Lipid Bilayers. *The Journal of Physical Chemistry B.* 2006; 110(47): 24157–24164.

[68] Waheed Q, Edholm O. Undulation Contributions to the Area Compressibility in Lipid Bilayer Simulations. *Biophysical Journal.* 2009; 97(10): 2754–2760.

[69] Ritchie K, Iino R, Fujiwara T, Murase K, Kusumi A. The fence and picket structure of the plasma membrane of live cells as revealed by single molecule techniques (Review). *Molecular Membrane Biology.* 2003; 20(1): 13–18.

[70] Morone N, Fujiwara T, Murase K, et al. Three-dimensional reconstruction of the membrane skeleton at the plasma membrane interface by electron tomography. *The Journal of Cell Biology.* 2006; 174(6): 851–862.

[71] Luo Y, Maibaum L. Relating the structure factors of two-dimensional materials in planar and spherical geometries. *Soft Matter.* 2018; 14(27): 5686–5692.

[72] Diamant H. Model-free thermodynamics of fluid vesicles. *Physical Review E.* 2011; 84(6): 061123.

[73] Kirkwood JG, Buff FP. The Statistical Mechanical Theory of Surface Tension. *The Journal of Chemical Physics.* 1949; 17(3): 338–343.

[74] Goga N, Rzepiela AJ, Vries AH, Marrink SJ, Berendsen HJC. Efficient Algorithms for Langevin and DPD Dynamics. *Journal of Chemical Theory and Computation.* 2012; 8(10): 3637–3649.

[75] Soddemann T, Dünweg B, Kremer K. Dissipative particle dynamics: A useful thermostat for equilibrium and nonequilibrium molecular dynamics simulations. *Physical Review E.* 2003; 68(4): 046702.

[76] Jo S, Lim JB, Klauda JB, Im W. CHARMM-GUI Membrane Builder for Mixed Bilayers and Its Application to Yeast Membranes. *Biophysical Journal.* 2009; 97(1): 50–58.

[77] Cheng X, Jo S, Lee HS, Klauda JB, Im W. CHARMM-GUI Micelle Builder for Pure/Mixed Micelle and Protein/Micelle Complex Systems. *Journal of Chemical Information and Modeling.* 2013; 53(8): 2171–2180.

[78] Wu EL, Cheng X, Jo S, et al. CHARMM-GUI Membrane Builder toward realistic biological membrane simulations. *Journal of computational chemistry.* 2014; 35(27): 1997–2004.

[79] Jo S, Kim T, Iyer VG, Im W. CHARMM-GUI: A web-based graphical user interface for CHARMM. *Journal of Computational Chemistry.* 2008; 29(11): 1859–1865.

[80] De Vries AH, Mark AE, Marrink SJ. Molecular Dynamics Simulation of the Spontaneous Formation of a Small DPPC Vesicle in Water in Atomistic Detail. *Journal of the American Chemical Society.* 2004; 126(14): 4488–4489.

[81] Vermeer LS, Groot BL, Réat V, Milon A, Czaplicki J. Acyl chain order parameter profiles in phospholipid bilayers: computation from molecular dynamics simulations and comparison with 2H NMR experiments. *European Biophysics Journal.* 2007; 36(8): 919–931.

[82] König S, Sackmann E. Molecular and collective dynamics of lipid bilayers. *Current Opinion in Colloid & Interface Science.* 1996; 1(1): 78–82.

[83] Leftin A, Brown MF. An NMR database for simulations of membrane dynamics. *Biochimica et Biophysica Acta (BBA) - Biomembranes.* 2011; 1808(3): 818–839.

[84] Poger D, Caron B, Mark AE. Validating lipid force fields against experimental data: Progress, challenges and perspectives. *Biochimica et Biophysica Acta (BBA) - Biomembranes.* 2016; 1858(7): 1556–1565.

[85] Wassenaar TA, Ingólfsson HI, Böckmann RA, Tieleman DP, Marrink SJ. Computational Lipidomics with insane : A Versatile Tool for Generating Custom Membranes for Molecular Simulations. *Journal of Chemical Theory and Computation.* 2015; 11(5): 2144–2155.

[86] Park S, Beaven AH, Klauda JB, Im W. How Tolerant are Membrane Simulations with Mismatch in Area per Lipid between Leaflets? *Journal of Chemical Theory and Computation.* 2015; 11(7): 3466–3477.

[87] Durrant JD, Amaro RE. LipidWrapper: An Algorithm for Generating Large-Scale Membrane Models of Arbitrary Geometry. *PLoS Computational Biology.* 2014; 10(7): e1003720.

[88] Wassenaar TA, Pluhackova K, Böckmann RA, Marrink SJ, Tieleman DP. Going backward: A flexible geometric approach to reverse transformation from coarse grained to atomistic models. *Journal of Chemical Theory and Computation.* 2014; 10(2): 676–690.

[89] Larsson P, Kasson PM. Lipid Converter, A Framework for Lipid Manipulations in Molecular Dynamics Simulations. *Journal of Membrane Biology.* 2014; 247(11): 1137–1140.

[90] Tieleman D, Marrink S, Berendsen H. A computer perspective of membranes: molecular dynamics studies of lipid bilayer systems. *Biochimica et Biophysica Acta (BBA) - Reviews on Biomembranes.* 1997; 1331(3): 235–270.

[91] Marrink SJ, Berendsen HJC. Simulation of water transport through a lipid membrane. *The Journal of Physical Chemistry.* 1994; 98(15): 4155–4168.

[92] Braun AR, Brandt EG, Edholm O, Nagle JF, Sachs JN. Determination of Electron Density Profiles and Area from Simulations of Undulating Membranes. *Biophysical Journal.* 2011; 100(9): 2112–2120.

[93] Klauda JB, Kučerka N, Brooks BR, Pastor RW, Nagle JF. Simulation-Based Methods for Interpreting X-Ray Data from Lipid Bilayers. *Biophysical Journal.* 2006; 90(8): 2796–2807.

[94] Boughter CT, Monje-Galvan V, Im W, Klauda JB. Influence of Cholesterol on Phospholipid Bilayer Structure and Dynamics. *The Journal of Physical Chemistry B.* 2016; 120(45): 11761–11772.

[95] Schofield P, Henderson JR. Statistical Mechanics of Inhomogeneous Fluids. *Proceedings of the Royal Society A: Mathematical, Physical and Engineering Sciences.* 1982; 379(1776): 231–246.

[96] Sodt AJ, Venable RM, Lyman E, Pastor RW. Nonadditive Compositional Curvature Energetics of Lipid Bilayers. *Physical Review Letters.* 2016; 117(13): 1–6.

[97] Torres-Sánchez A, Vanegas JM, Arroyo M. Geometric derivation of the microscopic stress: A covariant central force decomposition. *Journal of the Mechanics and Physics of Solids.* 2016; 93: 224–239.

[98] Torres-Sánchez A, Vanegas JM, Arroyo M. Examining the mechanical equilibrium of microscopic stresses in molecular simulations. *Physical Review Letters.* 2015; 114(25): 1–5.

[99] Vanegas JM, Torres-Sánchez A, Arroyo M. Importance of force decomposition for local stress calculations in biomembrane molecular simulations. *Journal of Chemical Theory and Computation.* 2014; 10(2): 691–702.

[100] Ollila OHS, Risselada HJ, Louhivuori M, Lindahl E, Vattulainen I, Marrink SJ. 3D Pressure Field in Lipid Membranes and Membrane-Protein Complexes. *Physical Review Letters.* 2009; 102(7): 078101.

[101] Botan A, Favela-Rosales F, Fuchs PF, et al. Toward Atomistic Resolution Structure of Phosphatidylcholine Headgroup and Glycerol Backbone at Different Ambient Conditions. *Journal of Physical Chemistry B.* 2015; 119(49): 15075–15088.

[102] Romo T, Grossfield A. LOOS: An extensible platform for the structural analysis of simulations. In *2009 Annual International Conference of the IEEE Engineering in Medicine and Biology Society*: 2332–2335IEEE 2009.

[103] Ollila OH, Pabst G. Atomistic resolution structure and dynamics of lipid bilayers in simulations and experiments. *Biochimica et Biophysica Acta - Biomembranes.* 2016; 1858(10): 2512–2528.

[104] Nagle J. Area/lipid of bilayers from NMR. *Biophysical Journal.* 1993; 64(5): 1476–1481.

[105] Vögele M, Köfinger J, Hummer G. Hydrodynamics of Diffusion in Lipid Membrane Simulations. *Physical Review Letters.* 2018; 120(26): 268104.

[106] Rawicz W, Olbrich K, McIntosh T, Needham D, Evans E. Effect of Chain Length and Unsaturation on Elasticity of Lipid Bilayers. *Biophysical Journal.* 2000; 79(1): 328–339.

[107] Goetz R, Gompper G, Lipowsky R. Mobility and Elasticity of Self-Assembled Membranes. *Physical Review Letters.* 1999; 82(1): 221–224.

[108] Lindahl E, Edholm O. Mesoscopic Undulations and Thickness Fluctuations in Lipid Bilayers from Molecular Dynamics Simulations. *Biophysical Journal.* 2000; 79(1): 426–433.

[109] Safran SA. *Statistical Thermodynamics of Surfaces, Interfaces, and Membranes.* Boca Raton, FL: Westview Press 2018.

[110] Canham P. The minimum energy of bending as a possible explanation of the biconcave shape of the human red blood cell. *Journal of Theoretical Biology.* 1970; 26(1): 61–81.

[111] Helfrich W. Elastic properties of lipid bilayers: theory and possible experiments. *Zeitschrift fur Naturforschung. Teil C: Biochemie, Biophysik, Biologie, Virologie.* 1981; 28(11): 693–703.

[112] Watson MC, Brandt EG, Welch PM, Brown FLH. Determining Biomembrane Bending Rigidities from Simulations of Modest Size. *Physical Review Letters.* 2012; 109(2): 028102.

[113] Peliti L, Leibler S. Effects of Thermal Fluctuations on Systems with Small Surface Tension. *Physical Review Letters.* 1985; 54(15): 1690–1693.

[114] Diggins P, Deserno M. Determining the bending modulus of a lipid membrane by simulating buckling. *The Journal of Chemical Physics.* 2013; 138(21): 214110.

[115] Hu M, Briguglio JJ, Deserno M. Determining the Gaussian Curvature Modulus of Lipid Membranes in Simulations. *Biophysical Journal.* 2012; 102(6): 1403–1410.

[116] Harmandaris VA, Deserno M. A novel method for measuring the bending rigidity of model lipid membranes by simulating tethers. *The Journal of Chemical Physics.* 2006; 125(20): 204905.

[117] Otter WK, Briels WJ. The bending rigidity of an amphiphilic bilayer from equilibrium and nonequilibrium molecular dynamics. *The Journal of Chemical Physics.* 2003; 118(10): 4712–4720.

[118] Gruner SM, Parsegian VA, Rand RP. Directly measured energy of phospholipid HII hexagonal phases . *Faraday Discuss.Chem.Soc..* 1986; 81: 29–37.

[119] Israelachvili JN. *Intermolecular and Surface Forces.* Waltham, MA: Elsevier 2011.

[120] Hu M, Jong DH, Marrink SJ, Deserno M. Gaussian curvature elasticity determined from global shape transformations and local stress distributions: a comparative study using the MARTINI model. *Faraday Discuss..* 2013; 161: 365–382.

[121] Tolpekina TV, Otter WK, Briels WJ. Simulations of stable pores in membranes: System size dependence and line tension. *The Journal of Chemical Physics.* 2004; 121(16): 8014.

[122] Wohlert J, Otter WK, Edholm O, Briels WJ. Free energy of a trans-membrane pore calculated from atomistic molecular dynamics simulations. *The Journal of Chemical Physics.* 2006; 124(15): 154905.

[123] Brochard-Wyart F, Gennes P, Sandre O. Transient pores in stretched vesicles: role of leak-out. *Physica A: Statistical Mechanics and its Applications.* 2000; 278(1-2): 32–51.

[124] Moroz J, Nelson P. Dynamically stabilized pores in bilayer membranes. *Biophysical Journal.* 1997; 72(5): 2211–2216.

[125] Zhelev DV, Needham D. Tension-stabilized pores in giant vesicles: determination of pore size and pore line tension. *Biochimica et Biophysica Acta (BBA) - Biomembranes.* 1993; 1147(1): 89–104.

[126] Nagle J. Long tail kinetics in biophysics? *Biophysical Journal.* 1992; 63(2): 366–370.

[127] Weiss M, Elsner M, Kartberg F, Nilsson T. Anomalous Subdiffusion Is a Measure for Cytoplasmic Crowding in Living Cells. *Biophysical Journal.* 2004; 87(5): 3518–3524.

[128] Kou SC, Xie XS. Generalized Langevin Equation with Fractional Gaussian Noise: Subdiffusion within a Single Protein Molecule. *Physical Review Letters.* 2004; 93(18): 180603.

[129] Goychuk I, Hänggi P. Fractional diffusion modeling of ion channel gating. *Physical Review E.* 2004; 70(5): 051915.

[130] Saxton MJ. Wanted: A Positive Control for Anomalous Subdiffusion. *Biophysical Journal.* 2012; 103(12): 2411–2422.

[131] Munguira I, Casuso I, Takahashi H, et al. Glasslike Membrane Protein Diffusion in a Crowded Membrane. *ACS Nano.* 2016; 10(2): 2584–2590.

[132] Flenner E, Das J, Rheinstädter MC, Kosztin I. Subdiffusion and lateral diffusion coefficient of lipid atoms and molecules in phospholipid bilayers. *Physical Review E - Statistical, Nonlinear, and Soft Matter Physics.* 2009; 79(1): 1–11.

[133] Yeh IC, Hummer G. System-Size Dependence of Diffusion Coefficients and Viscosities from Molecular Dynamics Simulations with Periodic Boundary Conditions. *The Journal of Physical Chemistry B.* 2004; 108(40): 15873–15879.

[134] Camley Ba, Brown FLH. Diffusion of complex objects embedded in free and supported lipid bilayer membranes: role of shape anisotropy and leaflet structure. *Soft Matter.* 2013; 9(19): 4767.

[135] Jeschke G. DEER Distance Measurements on Proteins. *Annual Review of Physical Chemistry.* 2012; 63(1): 419–446.

[136] Sahu ID, Lorigan GA. Site-Directed Spin Labeling EPR for Studying Membrane Proteins. *BioMed Research International.* 2018; 2018(1): 1–13.

[137] Vaz W, Almeida P. Microscopic versus macroscopic diffusion in one-component fluid phase lipid bilayer membranes. *Biophysical Journal.* 1991; 60(6): 1553–1554.

[138] Shin YK, Ewert U, Budil DE, Freed JH. Microscopic Versus Macroscopic Diffusion in Model Membranes by Electron-Spin-Resonance Spectral-Spatial Imaging. *Biophysical Journal.* 1991; 59(4): 950–957.

[139] Nagao M, Kelley EG, Ashkar R, Bradbury R, Butler PD. Probing elastic and viscous properties of phospholipid bilayers using neutron spin echo spectroscopy. *Journal of Physical Chemistry Letters.* 2017; 8(19): 4679–4684.

[140] Feller SE, Zhang Y, Pastor RW. Computer simulation of liquid/liquid interfaces. II. Surface tensionâĂŘarea dependence of a bilayer and monolayer. *The Journal of Chemical Physics.* 1995; 103(23): 10267–10276.

[141] Zhang Y, Feller SE, Brooks BR, Pastor RW. Computer simulation of liquid/liquid interfaces. I. Theory and application to octane/water. *The Journal of Chemical Physics.* 1995; 103(23): 10252–10266.

[142] Shiba H, Noguchi H. Estimation of the bending rigidity and spontaneous curvature of fluid membranes in simulations. *Physical Review E.* 2011; 84(3): 031926.

[143] Pontes B, Monzo P, Gauthier NC. Membrane tension: A challenging but universal physical parameter in cell biology. *Seminars in Cell & Developmental Biology.* 2017; 71: 30–41.

[144] Wu SH, Sankhagowit S, Biswas R, Wu S, Povinelli ML, Malmstadt N. Viscoelastic deformation of lipid bilayer vesicles. *Soft Matter.* 2015; 11(37): 7385–7391.

[145] Brown FLH. Continuum simulations of biomembrane dynamics and the importance of hydrodynamic effects. *Quarterly Reviews of Biophysics.* 2011; 44(04): 391–432.

[146] Watson MC, Penev ES, Welch PM, Brown FLH. Thermal fluctuations in shape, thickness, and molecular orientation in lipid bilayers. *The Journal of Chemical Physics.* 2011; 135(24): 244701.

[147] Guixà-González R, Rodriguez-Espigares I, Ramírez-Anguita JM, et al. MEMBPLUGIN: Studying membrane complexity in VMD. *Bioinformatics.* 2014; 30(10): 1478–1480.

[148] Sachs JN, Crozier PS, Woolf TB. Atomistic simulations of biologically realistic transmembrane potential gradients. *The Journal of Chemical Physics.* 2004; 121(22): 10847.

Appendix B

Validation of Dry Martini Lipid Membrane Model

The membrane transverse density profile is a critical structural metric that can determine chemical and mechanical partitioning effects for NP-membrane interactions (Fig. B.1), calculated from a 15 ns simulation of the confined membrane. Here, the use of an implicit solvent model precludes the existence of an aqueous solvent phase (referred to as region 1 in the typical lipid bilayer membrane four-region model[1]). Region 2 (the "interface"/"interphase"), normally the densest, is also affected by the lack of solvent. Otherwise, however, the model captures typical local density variations from all-atom models in the membrane interior–namely, the larger density in the "soft polymer" region (3) relative to the "decane" region (4). The local free volume (local density drop) in the membrane center is a critical qualitative feature in solute-membrane interactions that can, depending on the solute, lead to a singular stable insertion state in the membrane center.[2] Figure B.1 also shows the local density of the lipid choline head and acyl chain tail groups, the dominant lipid chemical groups and those whose interaction with the NPs is tuned.

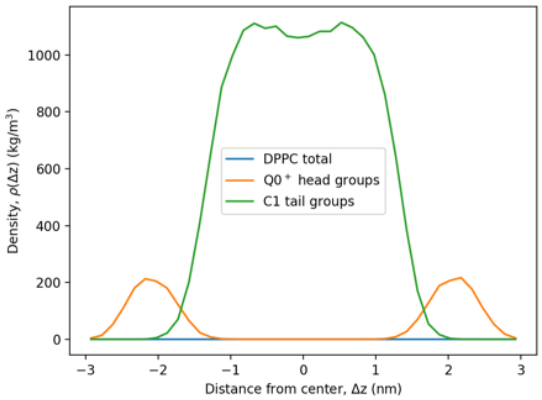

Figure B.1: Membrane Transverse Density Profile. The density profile is calculated via binning in the z-direction, averaging across the xy-plane. Local density calculations are centered every simulation frame such as to avoid smearing in simulation averages, particularly across the local density drop in the membrane center; Dry Martini DPPC, while devoid of solvent, captures the critical local free volume in the membrane center.

We further validate Dry Martini DPPC with structural, dynamical, and mechanical properties that can be both directly and indirectly compared with analogous atomistic model systems and experiments (Table B.1)).

Structural and dynamical property calculation techniques are broadly outlined in Poger et al.[3] The equilibrium area per lipid is a critical target in a lipid force field parameterization.[4] Area per lipid for Dry Martini DPPC is slightly larger than for the CHARMM36 atomistic model for DPPC; it larger than in some experiments, but is also within range of others. The lipid P2 NMR order parameter is defined in Appendix A Dry Martini values here are around 0.36, which is just slightly more ordered, and larger than those for CHARMM36 and experiment. That said, simulations in this study are conducted at 341 K, which should be well above the gel-to-liquid phase transition temperature. Lateral lipid diffusivity values for Dry Martini are larger than for CHARMM36, but on the same order of magnitude; the difference could be attributed to a number of factors, not limited to but including system size effects, long-range electrostatics, and thermostatting. Dry Martini DPPC in this study is simulated at larger sizes, which should

increase diffusivities relative to typical atomistic system sizes towards the macroscopic limiting values, but dynamics in this study should also be perturbed by truncation of electrostatics and the stochastic Langevin thermostat. Experimental diffusivities span multiple orders of magnitude, and are highly dependent on technique; that said, Dry Martini and experimental values overlap.

The area compressibility modulus and bending modulus were calculated via the methods outlined in Venable et al.,[4] with the bending modulus specifically calculated using the undulation spectrum. Perhaps remarkably, Dry Martini area compressibility and bending moduli are within range of atomistic simulations and experiments. There are basically no notable size variations in properties for the two membranes studied here–confidence intervals, where present, overlap–and better control of errors and resolution of finite size effects could potentially be achieved through large increases in sampling.[4,5]

As a result, we can preliminarily conclude that Dry Martini reasonably captures membrane structural and mechanical properties and, roughly, dynamics.

Table B.1: Dry Martini Membrane Property Validation. Structural, dynamic, and mechanical properties were calculated from short 15 ns simulations of the confined and modest-sized membranes, and compared with atomistic DPPC simulations and DPPC experiments. Despite large uncertainties for certain metrics and variety of techniques used for property calculations, Dry Martini compares quite reasonably with atomistic simulations and experiments. *From modest-sized membrane only [@]303 K; fluid phase for this force field[6] [$]variety of fluid phase temperatures and experimental methods[3] [%]"Plateau values"[4] [#]variety of experimental techniques at 323 K, with results spanning several orders of magnitude[3]

Property (Units)	**Dry Martini DPPC, This Study (Confined / Modest)**	**CHARMM36 Atomistic DPPC**	**Experimental DPPC (Method)**
Area per lipid, a (nm^2)	0.6581 +/- 0.0014 / 0.6545 +/- 0.0003	0.629[@]	0.65 +/- 0.04[$]; 0.630
P2 NMR order parameter, S_{CD}	0.361 / 0.360	∼0.15-0.26; 0.203-0.217[%]	∼0.14-0.26

Lipid lateral diffusivity, D_l (10^{-5} cm^2/s)	0.0833 +/- 0.0001 / 0.0815 +/- 0.0062	0.01835	0.03 +/- 0.04[#]
Area compressibility modulus, K_A (mN/m)	206 +/- 55 / 273 +/- 35	236 +/- 31	231
Bending modulus, κ (k_BT)	30 +/- 10*	35.4 +/- 0.9	33.6

Bibliography

[1] Tieleman D, Marrink S, Berendsen H. A computer perspective of membranes: molecular dynamics studies of lipid bilayer systems. *Biochimica et Biophysica Acta (BBA) - Reviews on Biomembranes.* 1997; 1331(3): 235–270.

[2] MacCallum JL, Tieleman DP. Computer simulation of the distribution of hexane in a lipid bilayer: Spatially resolved free energy, entropy, and enthalpy profiles. *Journal of the American Chemical Society.* 2006; 128(1): 125–130.

[3] Poger D, Caron B, Mark AE. Validating lipid force fields against experimental data: Progress, challenges and perspectives. *Biochimica et Biophysica Acta (BBA) - Biomembranes.* 2016; 1858(7): 1556–1565.

[4] Venable RM, Brown FL, Pastor RW. Mechanical properties of lipid bilayers from molecular dynamics simulation. *Chemistry and Physics of Lipids.* 2015; 192: 60–74.

[5] Waheed Q, Edholm O. Undulation Contributions to the Area Compressibility in Lipid Bilayer Simulations. *Biophysical Journal.* 2009; 97(10): 2754–2760.

[6] Klauda JB, Venable RM, Freites JA, et al. Update of the CHARMM All-Atom Additive Force Field for Lipids: Validation on Six Lipid Types. *Journal of Physical Chemistry B.* 2010; 114(23): 7830–7843.